Acoustic Logging in Fractured and Porous Formations

by

Xiaoming Tang

M.S., Graduate School of Chinese Academy of Sciences (1984)
B.S., Beijing University (1982)

Submitted to the Department of Earth, Atmospheric, and Planetary Sciences
in partial fulfillment of the requirements for the degree of

Doctor of Sciences

at the

MASSACHUSETTS INSTITUTE OF TECHNOLOGY

June 1990

Signature of Author .....
Department of Earth, Atmospheric, and Planetary Sciences
June, 1990

Certified by .....
M. Nafi Toksöz
Professor of Geophysics
Thesis Advisor

Certified by .....
Chuen H. Cheng
Principal Research Scientist
Thesis Co-Advisor

Accepted by .....
Thomas H. Jordan
Chairman
Department of Earth, Atmospheric, and Planetary Sciences

Acoustic Logging in Fractured and Porous Formations

by

Xiaoming Tang

Submitted to the Department of Earth, Atmospheric, and Planetary Sciences
on June, 1990, in partial fulfillment of the
requirements for the degree of
Doctor of Sciences

Abstract

This thesis is concerned with the dynamic fluid transport properties of fractures and porous media and their application to the estimation of formation hydraulic properties using borehole acoustic logging techniques. In the first part of the thesis, the dynamic response of a viscous fluid in a borehole fracture to the oscillatory pressure excitation of borehole acoustic waves is investigated, which leads to the theory of fracture dynamic conductivity. The distinction between this dynamic conductivity and the conventional cubic law conductivity is whether the viscous skin depth, $\delta = (2\nu/\omega)^{1/2}$, is large or small compared to the thickness of the fracture. Although this characteristics of dynamic fluid flow is obtained using the simple plane parallel fracture model, the physics involved is universally true for dynamic fluid flow in hydraulic conduits of rocks. The theory of fracture dynamic conductivity is compared with the theory of dynamic permeability of a general porous medium. It is found that the latter theory, when applied to the the fracture case, is in excellent agreement with the theory of fracture conductivity. This points to the general behavior of frequency-dependent fluid motion through conduits in rocks, regardless whether they are fractures or pores. Consequently, in acoustic logging measurements performed in a typical frequency range of [2-20] kHz, the dynamic fluid flow theory, instead of the conventional Darcy's law, is the appropriate theory for the fluid flow in the formation induced by logging acoustic waves.

In the second part of the thesis, the concept of dynamic permeability is applied to the important problem of acoustic logging in a permeable porous formation using borehole Stoneley waves. The interaction of the Stoneley wave with the porous formation is decomposed into two parts. The first is the interaction of the Stoneley with an equivalent elastic formation composed of the saturated porous matrix. The second is the interaction with pore fluid flow governed by the dynamic permeability. In this manner, a simple dynamic model is obtained for the Stoneley propagation in permeable boreholes. This simple model is compared with the complete model of the Biot-Rosenbaum theory for the effects of a porous formation on the Stoneley

propagation characteristics. It is found that the results from the two models agree very well for a hard formation, although they differ at higher frequencies for a soft formation because of the increased formation compressibility. The simple model is also tested with recently published laboratory experimental data of Stoneley wave measurements. The theory and experiment are in excellent agreement. As a result, the application of the dynamic fluid flow theory not only clearly points to the physical process involved in wave propagation in permeable boreholes, but also yields a much simplified Biot-Rosenbaum model that can be applied to the problem of acoustic logging in porous formations, especially to an inverse problem to extract formation permeability from Stoneley wave measurements.

In the third part, the problem of acoustic logging in a fluid-filled borehole with a vertical fracture is investigated both theoretically and experimentally. The Stoneley wave is used to probe the borehole. The propagation of this wave excites fluid motion in the fracture and the resulting fluid flow at the fracture opening perturbs the fluid-solid boundary condition at the borehole wall. The dynamic conductivity is applied to measure the fluid flow into the fracture and a boundary condition perturbation technique is developed to study the effects of the change in the boundary condition on the Stoneley propagation. The results indicate that the fracture has significant effects on the Stoneley waves, especially in the low frequency range. Significant Stoneley wave attenuation is produced and the Stoneley phase velocity is drastically decreased with decreasing frequency. Ultrasonic experiments are performed to measure Stoneley propagation in laboratory fracture borehole models. Cases of both hard and soft formations are studied. For both formations, the experimental results are found to agree well with the theoretical predictions. The important result of this study is that, a quantitative relationship between the Stoneley propagation and the fracture character is found. This relationship can be used to provide a method for characterizing a vertical borehole fracture by means of Stoneley wave measurements.

In the last part, the guided wave propagation in a fluid-filled borehole with a horizontal fracture is investigated. For the solution of the problem, a hybrid method is used to generate wave modes for the two regions separated by the fracture. The modes are then summed to match the boundary conditions at the fracture surfaces. A singularity problem arises in matching the surface conditions and is regularized by balancing borehole fluid flow across and into the fracture. The latter flow is characterized using the fracture dynamic conductivity. The results show that at low frequencies, the Stoneley wave attenuation across a fracture is controlled by the fluid flow into the fracture. As frequency increases, mode conversion at the fracture becomes important. Above the cut-off frequency of the first pseudo-Rayleigh mode, the Stoneley wave is strongly coupled with pseudo-Rayleigh waves, which is demonstrated by synthetic microseismograms. The pseudo-Rayleigh wave is strongly attenuated and reflected by thin as well as thick fractures. These effects are more pronounced towards the cut-off frequencies than away from the frequencies. Consequently, in acoustic logging measurements, the lack of wave energy across a borehole fracture may be a very good

indication of the existing fracture. The substantial effects of a fracture on pseudo-Rayleigh waves have been verified in the laboratory by experimenting with thin and thick fracture models. The experimental results demonstrate the guided wave characteristics across a fracture and confirm the theoretical analysis on these effects. The wave characteristics in the vicinity of a fracture, as described in this study, can be used to provide useful information for the detection and characterization of borehole fractures using acoustic logging techniques.

Thesis Advisor: M. Nafi Toksöz
Title: Professor of Geophysics

Thesis Co-Advisor: Chuen H. Cheng
Title: Principal Research Scientist

Acknowledgments

I would like to thank my advisor Nafi Toksöz for his advice and guidance throughout my study at MIT. His scientific insight and broad knowledge in geophysical research have guided me in the right direction and taught me how to become a better scientist. I enjoyed talking with him not only about science but also about life, things on China and the world, etc. I also like to thank my co-advisor Arthur Cheng for his advice, constant help, and friendship. His experience in acoustic logging has been a continuous source of information and ideas to me. His sense of humor makes working with him enjoyable.

The Earth Resources Laboratory at MIT is a stimulating environment. I thank the staff and students at ERL for making it an enjoyable and rewarding place for all. Roger Turpening 'lured' me into the fracture business by showing me his VSP data, although the fracture I settled down to work with is only a small part of the fracture he's being trying to explore. Roy Wilkens generously provided help when I first arrived in Boston, and constant advice and friendship during my first year graduate study. Sara Brydges reviewed my papers for the consortium report and helped me improve my English writing skills. Tien-when Lo, Karl Coyner, Perrie Tarif, Fatih Güler, Philippe Guerendel, and Craig Schultz shared with me their experience in ultrasonic modeling and laboratory measurements. Karl Ellefsen, Jeff Meredith, Deny Schmitt, Rick, Gibson, Bob Cicerone, Jack Foley, Joe Matarese, Arcangelo Sena, Delaine Thompson, Lisa Block, Al Taylor, Jean Maloof, Carol Caravana, and many others have always been helpful with using computer and technical discussions. Chatting with Jim Mendelson, Ed Reiter, Ted Charette, and Bata Mandal has always been fun and enjoyable. Sara Brydges, Naida Buckingham, Liz Henderson, and Sue Turbak have provided help in administrative matters.

I need to thank several people who, with their experiences in teaching and research, have provided advice and help during my graduate study at MIT. I am indebted to Brian Evans and Ted Madden of the department. Brian was my academic advisor

during my first year at MIT and helped me with selecting graduate courses. Ted taught me inversion theory and provided useful comments and discussions. Thanks also go to Albert Hsui, who, as a visiting professor from university of Illinois, provided advice and help in my pre-generals research. Discussions with Vernon Cormier, Aton Dainty, Michael Bucoun are also gratefully acknowledged.

I wish to thank my Chinese fellow students in the department: Peizheng Zhang, Danan Dong, Changsheng Chen, Shuntai Zhou, Ningya Cheng, Wenjie Dong, Chengbin Peng, who have shared with me the common experiences and interests as foreign students from main land China.

My greatest thanks go to my wife Xiaomin Zhao, whose understanding, encouragement, and sacrifice made it possible to complete this thesis. No oral expression can express my deepest appreciation. I also want to thank my child, Tony Tang who has always been a cheerful boy and brought happiness to me. In addition, he also taught me how to use my time efficiently. I owe many thanks to my parents and in-laws in China, whom I should have been in accompany with in their retired lives. Their expectation and constant encouragement have always inspired me throughout this endeavor.

Contents

Chapter 1

Introduction

1.1 The Subject of the Thesis

One of the prominent features of the earth's upper crust is the presence of fractures and joints of all scales. In addition, many rocks in the upper crust have porosity and are characterized as porous, permeable media. The determination of fluid-flow properties of sedimentary as well as crystalline rocks are of great importance for basic scientific studies, ground water hydrology, environmental problems, and the evaluation of the hydraulic conductivity of reservoir rocks in petroleum production. One technique which can directly measure the fracture and porous medium properties is acoustic logging in a borehole that penetrates such formations. This logging measurement involves acoustic waves that are generated by a source in the borehole and propagate along the borehole. The focus of this thesis is to study the response of a viscous fluid, saturating fractures and pores of the formation, subject to a borehole wave excitation, and the determination of hydraulic conductivity using borehole guided waves.

In the study of formation hydraulic properties using acoustic logging, one must bear in mind that the fluid flow in the formation fracture or pore system due to a borehole wave is dynamic in nature, because acoustic logging is usually performed in

a typical frequency range of [2-20] kHz. The nature of dynamic fluid flow in fractures and porous media must be understood before it can be applied to study its effects on borehole acoustic waves. On the other hand, the incorporation of the flow effects into the borehole propagation problem is a non-trivial task. In addition to the fluid flow effects, the borehole waves may also be subject to such effects as the coupling with the elastic properties of the formation and the scattering and mode conversion at the fracture surfaces, etc. For example, in the case of logging in a porous formation, the motion of the borehole wall includes both the elastic deformation of the wall and the fluid flow through the wall, while in the presence of a vertical fracture along the borehole, in addition to the effects of elastic wall motion and fluid flow, axial symmetry is lost because the fluid flow occurs at a small part of the borehole wall. Furthermore, in the presense of a horizontal fracture, the wave phenomenon becomes more complicated. The borehole waves leak their energy into the fracture and are scattered at the fracture surfaces. For each particular problem, this thesis develops specific techniques to find the solutions and analyzes the borehole wave propagation characteristics. Ultrasonic borehole fracture model experiments are also performed to study wave propagation in these models and to test the theoretical predictions. To this end, the thesis provides the physical insight into the various problems associated with acoustic logging in fractured and porous formations and illustrates some useful applications.

1.2 Background

During the propagation in a fluid-filled borehole, seismic waves interact with the formation and the effects of this interaction are recorded by a receiver in the borehole. The time series of the entire recorded wave trains displayed for successive measured depths are known as full waveform acoustic logs. The first arrival of the full waveform acoustic log is the compressional head wave which propagates along the borehole

wall. Following the head wave are borehole guided waves: the pseudo-Rayleigh and Stoneley waves. Because a large portion of strain energy of these waves is trapped in the borehole, they are the prominent arrivals on an acoustic log. The pseudo-Rayleigh wave exists above a certain frequency called the cut-off frequency. The onset of this wave arrives at the shear wave velocity of the formation and the wave is strongly coupled with the formation shear strength. Therefore, the pseudo-Rayleigh wave is sensitive to the formation fractures that are filled with fluid with zero shear strength. The Stoneley wave is an interface wave borne in borehole fluid. This wave exists for all frequencies but is most effectively excited at low frequencies. Because this wave is effectively associated with borehole fluid pressure, the Stoneley wave tends to drive the fluid into the formation through fractures and pores that are open to the borehole wall. The hydraulic exchange results in the change in the Stoneley wave velocity and attenuation. Thus the Stoneley is sensitive to the formation permeability and fracture conductivity.

The study of acoustic wave propagation in a cylindrical borehole appeared in the 1950's and 1960's, and has undergone a rapid development in the past ten years. The theoretical foundation was laid by Biot (1952), who presented a derivation of the period equation for borehole guided waves and their dispersion characteristics. White and Zechman (1968) computed synthetic microseismograms for a borehole containing a rigid tool in the center. Roever et al. (1974) studied the the wave propagation in terms of modal theory and a ray-type expansion, which led to the discovery of the laws of amplitude decay of borehole head waves as a function of distance. These geometric decay laws were in agreement with later work of Winbow (1980), Zhang and Cheng (1984), and White and Tongtaow (1981). Using a branch cut integration technique, Tsang and Rader (1979) gave the form of the pressure response for the early part of the signal with the head wave arrivals. Peterson (1974) studied the full waveform as a sum of guided waves by generating synthetics via pole and branch cut integration in the complex wavenumber plane. Rosenbaum (1974) investigated

the effect of formation permeability on high frequency acoustic wave train by using Biot (1956a,b) theory for a porous solid to model a permeable formation surrounding a borehole. Although there was not much interest following the publication of the work, the topic pioneered by this work has now become an important topic of intense research in the past few years, and will be discussed in more detail in Chapter 3. In the past decade, borehole acoustic logging studies have gained significant progress in both theoretical development and field applications. Cheng and Toksöz (1981) applied the discrete wavenumber technique to generate synthetics for various formations. They also investigated the effect of an elastic tool along the borehole axis on the wave characteristics. Cheng et al. (1982) found that the Stoneley wave in a soft formation is influenced strongly by the formation shear velocity . This allows the use of this wave as an indirect method for obtaining the formation shear velocity (Cheng and Toksöz, 1983; Chen and Willen, 1984; Liu, 1984; Stevens and Day, 1986). Cheng et al. (1982) applied the sensitivity analysis of borehole guided waves to the determination of in-situ attenuation from full waveform acoustic logs. This technique has later been further developed by Burns (1986) for the radially layered geometry which occurs when an altered zone is present in the formation or casing is introduced into the borehole. For the layered geometry, Schoenberg et al. (1981) studied synthetic waveforms in conjunction with laboratory scale model waveforms. Tubman et al. (1984, 1986) computed synthetic microseismograms in cased boreholes. In addition to the increasingly complex geometry, complexities in formation physical properties have also been introduced. White and Tongtaow (1981) investigated the case of a borehole surrounded by a transversely isotropic formation. Recently, Elleffsen (1990) has studied the problem using perturbation and variational methods and inverted formation anisotropic properties using Stoneley waves. Chan and Tsang (1983) treated the case of multiple radial layers, the elastic constants of each layer being transversely isotropic. Schmitt (1989) investigated the more complicated case of a borehole surrounded by multiple porous layers with anisotropy in both elastic

constants and permeabilities. Problems that involve bed-boundaries have also been treated. Stephen et al. (1986) have computed finite-difference synthetic microseismograms for such problems. Recently, Tsang (1985, 1987) has treated the transient acoustic logging problem for a borehole with a horizontal bed boundary separating two formations. The technique he used was a hybrid method. This method is a useful tool for studying wave propagation in waveguides with discontinuities, and will be described in more details in Chapter 5.

In the past ten years, full waveform acoustic logging has found an important application in the detection and characterization of borehole fractures. Through field observations, Paillet (1980) was able to recognize the effects of fractures intersecting the borehole on the logging waveforms. Since then, studies based on field data (Paillet, 1983; Hsu et al., 1983; Arditty and Staron, 1987; Hardin et al., 1987; Brie et al., 1988), theoretical modeling (Bhashvanija, 1983; Stephen et al., 1985; Mathieu, 1984, Tang and Cheng, 1989; Hornby et al., 1989), and ultrasonic laboratory models (Güler and Toksöz 1987; Lakey, 1985; Poeter, 1987; Hornby et al., 1989) have been used to relate acoustic log characteristics to fracture properties. All studies show that full waveform acoustic logs are attenuated by fractures. The magnitudes of attenuation have been different. The field results show significant attenuation in some cases and little attenuation in others. Theoretical results, obtained using different techniques and different assumptions in formulating the problem, have yielded different results. The theoretical studies have been concerned with fluid-flow in a fracture. The problem of fluid-flow in a fracture has been studied by many workers starting from Boussinesq (1868). The analogy of parallel planar plates is commonly adopted to represent the fracture surfaces and the fluid-flow is assumed laminar. Snow (1966), Romm (1966), Louis (1969), and Bear (1972) have derived the basic equations describing the flow through a fracture. These workers have shown that the hydraulic conductivity of a fracture is proportional to its aperture cubed. Witherspoon et al. (1980) performed experiment to evaluate the validity of the cubic law and found that this law is valid

even for a closed fracture where the surfaces are in contact. Later numerical simulations of Brown (1987) and Rothman (1988) have substantiated this experimental observation. Because the cubic law is well established, several workers tried to apply it to characterize in-situ fracture properties using seismic measurements. For example, Beydoun et al. (1985) applied the cubic law to relate the borehole tube waves and the fluid-flow in a borehole fracture intersecting the borehole. Mathieu (1984) formulated the problem of Stoneley wave attenuation across a plane-parallel fracture by assuming that the fluid flow in the fracture is governed by viscous forces and that the conduction of fluid obeys cubic law. His result, however, when applied to the laboratory modeling data, would predict the almost complete attenuation of the Stoneley waves. But the laboratory data show that Stoneley waves can cross fractures as thick as the borehole radius and still has significant amplitude (Güler and Toksöz, 1987). It is this discrepancy between theory and experiment that leads the study of dynamic fluid-flow effects in Chapter 2. The earliest modeling of wave propagation across a horizontal fracture was based on the direct calculation of waveform time series using finite-difference models containing boreholes and fractures (Bhashvanija, 1983; Stephen et al., 1985). These calculations require large fracture apertures in the modeling because of the number of nodal points needed to resolve the effects of the fracture. In addition, because of the overlap of different wave components (such as pseudo-Rayleigh and Stoneley waves) in the time domain, the response of the fracture on each wave component is difficult to resolve. In Chapter 5, this problem is treated in the frequency domain using the hybrid method of Tsang (1985, 1987), and the effects of the fracture on borehole guided waves are studied.

Although horizontal and inclined fractures are a common phenomenon in acoustic logging, vertical fractures are frequently encountered in many situations. For example, the fractures resulting from hydraulic fracturing in oil production are often vertical. Borehole Stoneley waves are found to attenuate along such fractures (Cheng, personal communication). Laboratory modeling of Güler and Toköz (1987) has also

demonstrated this phenomenon. However, theoretical modeling was not available to help understand the cause of this phenomenon. In Chapter 4, this problem will be handled using a boundary condition perturbation theory in conjunction with the dynamic flow theory developed in Chapter 2 of this thesis.

1.3 Outline of Thesis

This thesis is divided into six chapters. Chapter 1 defines the subject of the thesis, reviews the background work concerning acoustic logging in fractured and permeable formations, and outlines the studies covered by this thesis.

Chapter 2 studies the dynamic fluid flow effects in a fracture filled with a Newtonian viscous fluid. On the basis of the analysis, the theory of dynamic conductivity of a fracture is derived, and is applied to obtain a simple model for Stoneley wave propagation across a fracture. Comparison is then made between the theory of fracture dynamic conductivity and the theory of dynamic permeability of a porous medium. The comparison reconciles the two theories and illustrates the general behavior of dynamic fluid motion in hydraulic conduits of rocks, be they fractures or pores.

Chapter 3 illustrates a successful application of the dynamic fluid flow theory to the important problem of logging in porous formations. This chapter begins by briefly reviewing currently existing models for Stoneley propagation in permeable boreholes and their similarities and differences. These are some quasi-static models and the complete model of Biot-Rosenbaum theory. The differences arise because the dynamic effects of pore fluid flow were not taken into account in the quasi-static models. By characterizing the dynamic pore fluid flow using the concept of dynamic permeability, this chapter presents a very simple dynamic model which yields practically the same results as those from the Biot-Rosenbaum model in the presence of a permeable hard formation. Comparison is also made between laboratory experimental data and the simple theory and there is an excellent agreement between theory and experiment.

The study of this chapter provides a useful simple model which can be applied to the estimation of formation permeability using Stoneley wave measurements.

In Chapter 4, the problem of logging in a vertically fractured borehole is investigated both theoretically and experimentally. The borehole is probed using the Stoneley wave, whose propagation excites dynamic fluid flow in the fracture. The dynamic conductivity is then used to measure the amount of fluid flow into the fracture. A boundary condition perturbation technique is developed for the borehole situation and is used to study the effects of the fracture on the Stoneley wave propagation. Cases of both hard and soft formations are studied. Ultrasonic experiments are performed to measure Stoneley propagation in laboratory fracture borehole models using aluminum and lucite as the hard and the soft formation, respectively. The experimental procedure and data processing are described. The results are compared with theoretical predictions. This chapter provides the relationship between the Stoneley propagation and the fracture character. This relationship can be used to provide a method for characterizing a vertical fracture by means of Stoneley wave measurements.

Chapter 5 treats the problem of guided wave propagation in a fluid-filled borehole intersected by a horizontal fracture. A hybrid method is employed to generate wave modes in the two regions separated by the fracture. The coupling of the modes with the boundary conditions at the fracture surfaces results in the transmission and reflection of the incident borehole wave. A singularity problem arises in matching the surface conditions and is regularized by balancing the fluid flow across and into the fracture. The latter flow is measured using the fracture dynamic conductivity. The effects of the fracture on the borehole Stoneley and pseudo-Rayleigh waves are analyzed and are compared with the results from the ultrasonic experimental modeling. The guided wave characteristics in the vicinity of a fracture as described in this chapter may be used to provide useful information for the detection and characterization using acoustic logging technique. Chapter 6 summarizes the important results and

major conclusions of this thesis.

Chapter 2

Dynamic Fluid Flow in Fractures and Porous Media

2.1 Introduction

There is an increasing interest in fracture characterization in using both full waveform acoustic logs and vertical seismic profiling (VSP) surveys (Paillet, 1980; Hsu et al., 1985; Beydoun et al., 1985; Hardin et al., 1987). In full waveform logging, a model by Mathieu (1984) has been used to model Stoneley wave attenuation across a fracture. Although qualitative correlations were found between the model and field data (Hardin et al., 1987), this model is imperfect because it is a kinematic rather than a dynamic model. In VSP surveys, a model by Beydoun et al. (1985) has been used to study tube wave generation by a borehole fracture. In both models, however, fluid flow in the fracture was treated as quasi-static, and the "cubic law" (Snow, 1965) for steady flow was assumed. Since both models deal with dynamic wave phenomena, the validity of this law under dynamic conditions is subject to question. One of the major goals of this chapter is to investigate the behavior of fluid motions in a fracture under dynamic wave excitations. The results will lead to the theory of dynamic conductivity of a fracture, which is an extension of the cubic law into the dynamic regime. As

will be shown later in this chapter, the distinction between high- and low-frequency behaviors of the fracture fluid motion is whether the viscous skin depth, $\delta = \sqrt{2\nu/\omega}$, is large or small compared to the aperture of the fracture. When δ is large compared to fracture aperture, fluid flow is diffusive, while when the reverse is true, fluid flow becomes a propagational wave motion.

Analogous to the dynamic fracture fluid flow and conductivity, the fluid motion in a porous medium possesses similar properties. The conventional static permeability of a porous medium is analogous to the cubic law conductivity of a fracture. Under dynamic wave excitation, the pore fluid flow also exhibits frequency-dependent behaviors, and is characterized as the "slow wave" in Biot's (1956a,b, 1962a,b) theory for a porous medium. Basically, Biot's theory predicts three distinct types of waves in a fluid-saturated porous medium (Biot, 1956a,b), the "fast" compressional and shear waves, and the the slow compressional wave. The former waves are analogous to the P and S waves in an elastic solid, while the latter wave is a dilatational wave primarily associated with the motion of the pore fluid. Cleary (1978, 1980) pointed out that the slow wave does not contribute appreciably to the stress associated with the low frequency disturbance and can not be easily detectable in low permeability materials because of its diffusive nature. In high permeability materials such as sintered glass beads, the slow wave was observed as a propagation wave (Plona, 1980), and calculations show that the measured properties are entirely consistent with the Biot theory (Dutta, 1980). Using Biot theory, Schmitt (1985, 1986) has made a thorough study on the behaviors of these three waves and their variations with permeability, porosity, and saturant fluid, etc. Of the three waves, the slow wave is the most sensitive to these parameters. The slow wave exhibits strong frequency-dependent behaviors. At low frequencies, the slow wave motion is diffusive, and the amount of fluid flow driven by this motion is well described by the static Darcy's law. At high frequencies, however, this wave is a propagational wave and the fluid flow is no longer governed by this law. To address this frequency-dependent fluid transport problem, Johnson et al.

(1987) developed the theory of dynamic permeability for fluid-saturated porous media based on these low- and high-frequency behaviors of the pore fluid motion. Because of the similarity between the the theory of dynamic conductivity of a fracture and that of the dynamic permeability of a porous medium, it is instructive to compare the two theories and obtain a reconciliation for the theories. It will be shown in this chapter that dynamic permeability, when applied to the fracture case, is in excellent agreement with the exact dynamic conductivity. The success of this comparison will further demonstrate the general applicability of the dynamic permeability to porous media, whatever the pore shape and sizes.

There are two major parts in this chapter. In the first part, dynamic wave equation for a viscous fluid are solved in conjunction boundary conditions at the fracture surface. This leads to a characteristic equation which governs the relative importance of viscous shear effects and wave propagation effects. Based on these solutions and Darcy's law, the fracture dynamic conductivity is derived to characterize fluid conduction under dynamic conditions. Then the dynamic flow theory is used to study Stoneley wave attenuation across a borehole fracture. Relevance to previous Stoneley wave attenuation theories will also be discussed. In the second part, the theory of dynamic permeability is tested with the exact fracture dynamic conductivity in the case of a fracture. The relation between dynamic permeability and Biot's slow compressional wave is also demonstrated. By using dynamic permeability, an equation that governs the dynamic pore fluid flow is derived, which will be applied to study wave propagation in permeable boreholes in Chapter 3.

2.2 Dynamic Fluid Flow in a Fracture and Dynamic Conductivity

In this section, the dynamic response of a viscous fluid in a borehole fracture to the oscillatory pressure excitation of borehole Stoneley waves at the fracture opening will

be studied. In a viscous fluid, a small-amplitude wave motion is governed by the equation of motion (i.e., the Navier-Stokes equation, see Landau and Lifshitz, 1959) and the equation of continuity, which are written as

$$\rho\left(\frac{\partial\vec{v}}{\partial t}+\vec{v}\cdot\nabla\vec{v}\right)=-\nabla p+\mu\nabla^2\vec{v}+\frac{\mu}{3}\nabla\nabla\cdot\vec{v}\ , \tag{2.1}$$

$$\frac{\partial\rho}{\partial t}+\nabla\cdot(\rho\vec{v})=0\ , \tag{2.2}$$

respectively, where t is time, $\vec{v}$ is the fluid particle velocity, p is the pressure perturbation, and μ is viscosity. The density of the fluid, ρ, can be written as

$$\rho=\rho_0+\rho'\ , \tag{2.3}$$

where ρ_0 is the density at equilibrium and ρ' is the density perturbation. Neglecting thermal effects in the fluid, one has the relation between pressure and density perturbations:

$$p=\alpha_f^2\rho'\ , \tag{2.4}$$

where α_f is the acoustic velocity of the fluid. This relation follows from the constitutive equation of fluid $\rho'/\rho=p/K_f$, where $K_f=\rho_0\alpha_f^2$. Substituting equation 2.3 and 2.4 into equations 2.1 and 2.2 and using the fact that $\vec{v}$ is also a perturbation, one can linearize equations 2.1 and 2.2 by taking only the first order perturbation. In the frequency domain, the linearized equations are

$$-i\omega\vec{v}+\frac{1}{\rho_0}\nabla p = \nu\nabla^2\vec{v}+\frac{\nu}{3}\nabla\nabla\cdot\vec{v}\ , \tag{2.5}$$

$$-i\omega p+\rho_0\alpha_f^2\nabla\cdot\vec{v} = 0\ , \tag{2.6}$$

where ω is angular frequency and $\nu=\mu/\rho_0$ is the kinematic viscosity. Using vector decomposition, one can write $\vec{v}$ as

$$\vec{v}=\nabla\phi+\nabla\times\vec{\psi}\ , \tag{2.7}$$

where ϕ is the acoustic wave potential and $\vec{\psi}$ is the viscous shear potential (Landau and Lifshitz, 1959). Substitution of equation 2.7 into equations 2.5 and 2.6 gives

$$\nabla^2\phi+\frac{\omega^2}{\alpha_f^2-\frac{4}{3}i\omega\nu}\phi = 0\ , \tag{2.8}$$

$$\nabla^2\vec{\psi} + \frac{i\omega}{\nu}\vec{\psi} = 0 \ . \tag{2.9}$$

Equations 2.8 and 2.9 can now be applied to study the fluid motion inside a horizontal borehole fracture, which is modeled as a plane-parallel channel of thickness L_0 and of infinite extent. A fracture of finite extent can also be modeled in this way as long as its extension is large compared to the wavelength. One considers cylindrical coordinates (r, φ, z) where r is the distance from the borehole axis, φ is the polar angle, and z is the vertical coordinate, with $z = 0$ at the center of the fracture opening. Assuming axial symmetry of the problem, one can chose $\vec{\psi} = \psi\vec{e}_\varphi$, where $\vec{e}_\varphi$ is the unit vector along the increasing φ direction. Equations 2.8 and 2.9 may thus be written as

$$\frac{\partial^2\phi}{\partial r^2} + \frac{1}{r}\frac{\partial\phi}{\partial r} + \frac{\partial^2\phi}{\partial z^2} + \frac{\omega^2}{\alpha_f^2 - \frac{4}{3}i\omega\nu}\phi = 0 \ , \tag{2.10}$$

$$\frac{\partial^2\psi}{\partial r^2} + \frac{1}{r}\frac{\partial\psi}{\partial r} - \frac{\psi}{r^2} + \frac{\partial^2\psi}{\partial z^2} + \frac{i\omega}{\nu}\psi = 0 \ . \tag{2.11}$$

By separation of variables, solutions of equations 2.10 and 2.11 are found to be

$$\phi = H_0^{(1)}(kr)[A\cos(fz) + B\sin(fz)] \ , \tag{2.12}$$

$$\psi = H_1^{(1)}(kr)[C\cos(\bar{f}z) + D\sin(\bar{f}z)] \ , \tag{2.13}$$

where

$$f^2 = \frac{\omega^2}{\alpha_f^2 - \frac{4}{3}i\omega\nu} - k^2 \ , \tag{2.14}$$

$$\bar{f}^2 = \frac{i\omega}{\nu} - k^2 \ , \tag{2.15}$$

$H_0^{(1)}$ and $H_1^{(1)}$ are outgoing Hankel functions of order zero and one, $k = \omega/\bar{c}$ is the wavenumber of the fracture fluid, and A, B, C, and D are parameters to be determined.

2.2.1 Characteristic Equation

One can now determine the parameters in equations 2.12 and 2.13 with the boundary conditions at the fracture surface. Because of the axial symmetry, the fluid particle

velocity has only two components. According to equation 2.7, they are

$$\begin{aligned} v_r &= \frac{\partial \phi}{\partial r} - \frac{\partial \psi}{\partial z} \\ &= -H_1^{(1)}(kr)[Ak\cos(fz) + Bk\sin(fz) - C\bar{f}\sin(\bar{f}z) + D\bar{f}\cos(\bar{f}z)] \ , \end{aligned} \tag{2.16}$$

$$\begin{aligned} v_z &= \frac{\partial \phi}{\partial z} + \frac{\partial \psi}{\partial r} + \frac{\psi}{r} \\ &= H_0^{(1)}(kr)[-Af\sin(fz) + Bf\cos(fz) + Ck\cos(\bar{f}z) + Dk\sin(\bar{f}z)] \ . \end{aligned} \tag{2.17}$$

It is now assumed that the formation is rigid. This is appropriate when the fracture is in a hard formation whose elastic moduli and density are much larger than those of the fluid. The non-rigid formation case will be addressed later in section 2.4 of this chapter. For the rigid fracture surfaces, the viscous non-slip boundary condition at the fracture surface gives

$$v_r = v_z = 0 \ , \ (\text{at} \ \ z = \pm\frac{L_0}{2}) \ . \tag{2.18}$$

Substitution of equations 2.16 and 2.17 into equation 2.18 results in a system of homogeneous equations:

$$\mathbf{Gx} = 0 \ , \tag{2.19}$$

where:

$$\mathbf{x}^T = [A \ B \ C \ D] \ , \tag{2.20}$$

and $\mathbf{G}$ is a 4×4 matrix whose elements are given by the terms such as $k\cos(f\frac{L_0}{2})$, $\bar{f}\sin(\bar{f}\frac{L_0}{2})$, etc. (equations 2.16 and 2.17). For $\mathbf{x}$ to have a non-trivial solution, the determinant of $\mathbf{G}$ must vanish and this leads to the following characteristic equation

$$k^2\tan(\bar{f}\frac{L_0}{2}) + f\bar{f}\tan(f\frac{L_0}{2}) = 0 \ . \tag{2.21}$$

This is an important equation because it relates both viscous shear and acoustic propagation effects in the fracture. As a result, $k = \omega/\bar{c}$ is no longer the free space

wavenumber, wave dispersion and attenuation will both occur. When k is found by solving this complex equation the velocity dispersion is determined and the quality factor of the fracture fluid is given by

$$Q_f = \frac{Re\{k\}}{Im\{k\}} \quad . \tag{2.22}$$

Figure 2-1 plots the wave velocity and Q_f versus frequency for different fracture widths. The fluid is water (ρ=1 g/cm^3, μ=0.01 gs^{-1}cm, and α_f=1500 m/s). As seen from this figure, the velocity and Q_f are substantially reduced with decreasing aperture and frequency. This can be understood because viscous shear is mostly a boundary layer effect (Burns, 1988). The thickness of the boundary layer is measured by the viscous skin depth $\delta = \sqrt{2\nu/\omega}$. When the 2δ is comparable to the fracture aperture, the viscous shear effects become dominant and the fluid motion exhibits the diffusive nature, as can be seen from the decrease in both velocity and quality factor in Figure 2-1. On the other hand, when δ is small compared to the fracture thickness, the viscous shear effects are minimal and the fluid motion is a propagating wave with its phase velocity approaching the free space velocity. In fact, these behaviors can be obtained by asymptotically solving equation 2.21 at low and high frequencies or small or large fracture apertures. When the argument of the tangent functions in equation 2.21 is small (this condition can be satisfied by requiring either low frequencies or small flow apertures), the tangent functions can be expanded in a Taylor series

$$\tan(f\frac{L_0}{2}) \sim f\frac{L_0}{2} + \frac{1}{3}(f\frac{L_0}{2})^3 + \cdots \quad , \tag{2.23}$$

$$\tan(\bar{f}\frac{L_0}{2}) \sim \bar{f}\frac{L_0}{2} + \frac{1}{3}(\bar{f}\frac{L_0}{2})^3 + \cdots \quad . \tag{2.24}$$

Substitution of the above equations into equation 2.21 results in

$$k^2 + f^2 + \frac{L_0^2}{12}\bar{f}^2 k^2 + \frac{L_0^2}{12} f^4 \approx 0 \quad . \tag{2.25}$$

Solving this equation, one finds

$$k^2 = \left(\frac{\omega^2}{\alpha_f^2 - \frac{4}{3}i\omega\nu} + \frac{12}{L_0^2}\right)\left(2 + \frac{\alpha_f^2 - \frac{4}{3}i\omega\nu}{i\omega\nu}\right)^{-1} \quad . \tag{2.26}$$

As will be shown in the following, the term $\omega\nu/\alpha_f^2$ is a small quantity for ordinary fluids. It can also be readily seen that $(\omega L_0/\alpha_f)^2$ is a very small number at low frequency or small fracture apertures (alternatively, one may interpretate this as that the acoustic wavelength is much larger compared to the fracture aperture). Therefore, the second term in both the numerator and the denominator of equation 2.26 is much larger than the first term. This results in

$$k^2 \approx \frac{12i\omega\nu}{L_0^2\alpha_f^2} \quad , \quad (\delta \gg L_0) \quad . \tag{2.27}$$

Equation 2.27 agrees with Rayleigh's (1945) results for sound propagation in an exceedingly narrow aperture. To show the high-frequency behavior of equation 2.21, one rewrites it as

$$\tan\left(\frac{L_0\omega}{2\bar{c}}\sqrt{\frac{\bar{c}^2}{\alpha_f^2[1-4i\omega\nu/(3\alpha_f^2)]}-1}\right)\sqrt{\frac{\bar{c}^2}{\alpha_f^2[1-4i\omega\nu/(3\alpha_f^2)])}-1}$$
$$+\tan\left(\frac{L_0}{2\delta}\sqrt{2i-\frac{2\omega\nu}{\bar{c}^2}}\right)\left(\sqrt{\frac{i\bar{c}^2}{\omega\nu}-1}\right)^{-1}=0 \quad , \tag{2.28}$$

where $\delta = \sqrt{2\nu/\omega}$ is the viscous skin depth, and $\bar{c}$ is the wave velocity in fracture. It can be shown that $\omega\nu/v^2$ (v can be either $\bar{c}$ or α_f) is a very small quantity even for very viscous fluids and ultrasonic frequencies. As an example, one can take $\nu = 10^{-3}$ m^2/s (this is 10^3 times as viscous as water), $\omega = 2\pi \times 10^6$ Hz, and $\alpha_f \sim \bar{c} \sim 1500$ m/s. For this case, $\omega\nu/v^2$ is on the order of 0.003. Thus for moderately high frequencies and for fluids of ordinary viscousity, this quantity is generally very small. One now considers the second term of equation 2.28. When the fracture aperture is considerably larger than the viscous skin depth so that $L_0/(2\delta) \gg 1$ (this condition requires that either ω or L_0 be large), the tangent approaches i, a finite value. But the denominator is a large quantity. The second term is therefore a small quantity. To make the first term a small quantity, $\bar{c}$ must be close to α_f (note that $4i\omega\nu/3\alpha_f^2 \ll 1$). Expanding the tangent of the first term in series and taking the first order, one finds from equation 2.28 that

$$\bar{c} \approx \alpha_f(1-\sqrt{\frac{i}{2}}\frac{\delta}{L_0}) \quad . \tag{2.29}$$

Since $\delta/L_0 \ll 1$, one has $\bar{c} \sim \alpha_f$. Thus

$$k = \frac{\omega}{\bar{c}} \approx \frac{\omega}{\alpha_f} \ , \ (L_0 \gg \delta) \ . \tag{2.30}$$

The asymptotic solutions of equation 2.21, as given in equations 2.27 and 2.30, will be used to illustrate the low- and high-frequency behaviors of the dynamic fluid conduction in a fracture in the following section.

2.2.2 Dynamic Conductivity of a Fracture

It is well known that fluid conduction in a fracture under a static pressure gradient obeys the cubic law (Snow, 1965). The fluid conduction in a fracture under dynamic pressure excitations is of particular interest of this section. By using k determined from equation 2.21, a non-trivial solution of $\mathbf{x}$ in equation 2.20 can be found, whose elements are specifically given as

$$\begin{aligned} B &= 0 \ , \\ C &= 0 \ , \\ D &= -\frac{k\cos(f\frac{L_0}{2})}{\bar{f}\cos(\bar{f}\frac{L_0}{2})}A \ . \end{aligned} \tag{2.31}$$

Therefore, only one parameter (say A) needs to be found, and it is determined by pressure continuity at the fracture opening. By using equations 2.6, 2.7, and 2.12, pressure in the fracture is found to be

$$p = \frac{i\omega\rho_0 A}{1-(4i\omega\nu)/(3\alpha_f^2)} H_0^{(1)}(kr)\cos(fz) \ . \tag{2.32}$$

At the fracture opening $r = R$, equation 2.32 is averaged over the fracture width L_0 to match the borehole fluid pressure $p(\omega, R)$, which is taken to be independent of z because L_0 is small compared with the Stoneley wave wavelength (Hardin et al., 1987). By so doing, A is determined as

$$A = \frac{p(\omega,R)[1-4i\omega\nu/(3\alpha_f^2)]fL_0/2}{i\omega\rho_0 H_0^{(1)}(kR)\sin(fL_0/2)} \ . \tag{2.33}$$

Once A is known, the fluid motion in the fracture is completely specified by equations 2.16 and 2.17. One can therefore find the fluid flow conducted into the fracture opening, which is given by

$$q^{(F)} = 2\pi R \int_{-\frac{L_0}{2}}^{\frac{L_0}{2}} v_r dz \ , \quad (\text{at } r = R)$$

$$= -\frac{i\omega L_0}{k^2 \alpha_f^2 \rho_0} \left[-p(\omega, R) k \frac{H_1^{(1)}(kR)}{H_0^{(1)}(kR)} \right] 2\pi R \ . \tag{2.34}$$

By differentiating equation 2.32 with respect to r and using equation 2.33, it is readily shown that the term in square brackets in equation 2.34 is the pressure gradient $\frac{\partial p}{\partial r}$ averaged over L_0 and evaluated at the borehole radius $r = R$. Comparing equation 2.34 with Darcy's (1856) law

$$q = -\bar{C} | \bigtriangledown p | \ , \tag{2.35}$$

where q is now the flow rate per unit fracture length (analogous to $q^{(F)}/2\pi R$ in equation 2.34) and $\bar{C}$ is the hydraulic conductivity for the steady state case, one can see that the term in front of the square brackets in equation 2.34 is analogous to $\bar{C}$, and is therefore defined as the dynamic conductivity of the fracture:

$$\bar{C} \equiv \frac{i\omega L_0}{k^2 \alpha_f^2 \rho_0} \ , \tag{2.36}$$

where k is given by the solution to equation 2.21. It should be emphasized that, although equations 2.21 and 2.36 are obtained with a borehole geometry, they are also valid in general fracture fluid flow problems. The asymptotic behaviors of $\bar{C}$ at low and high frequencies (or small and large flow apertures) can be readily obtained. Substituting equations 2.27 and 2.30 into equation 2.28, one has

$$\bar{C} = \frac{L_0^3}{12\mu} \ , \quad (\delta \gg L_0) \tag{2.37}$$

$$\bar{C} = \frac{iL_0}{\omega \rho_0} \ , \quad (\delta \ll L_0) \tag{2.38}$$

Equation 2.37 is exactly the cubic law (Snow, 1965). Thus the definition in equation 2.36 is consistent with this well defined law at low frequencies. Whereas at high

frequencies, $\bar{C}$ becomes a purely imaginary quantity, decreasing with frequency as ω^{-1}. This means that the fluid conduction will be largely reduced as $\omega \to \infty$. Figure 2-2 plots the amplitude (a) and phase (b) of the dynamic conductivity for different flow apertures. The amplitudes reach the highest value given by the cubic law at the zero frequency, and decreases with increasing frequency. The larger the aperture, the faster they decrease, as indicated in Figure 2-2a. Figure 2-2b is a complement to Figure 2-2a showing that the phase of $\bar{C}$ approaches $\pi/2$ as frequency increases. The larger the aperture, the faster the phase approaches this value, at which $\bar{C}$ becomes an imaginary quantity.

2.2.3 Application to Stoneley Wave Attenuation across a fracture

In this section, the fracture fluid flow model is applied to study Stoneley wave attenuation across a single horizontal borehole fracture. Using the same cylindrical coordinates described previously, the borehole fluid pressure due to Stoneley waves can be written as (Biot, 1952; Cheng and Toköz, 1981)

$$p^{(l)} = E^{(l)} I_0(nr) e^{\pm i\kappa z} \quad , \tag{2.39}$$

where I_0 is the zeroth order modified Bessel function of the first kind and $E^{(l)}$'s are as yet undetermined coefficients. Equation 2.39 includes Stoneley waves incident on ($l = I$, $e^{\pm i\kappa z} \to e^{+i\kappa z}$), reflected back from ($l = R$, $e^{\pm i\kappa z} \to e^{-i\kappa z}$), and transmitted across ($l = T$, $e^{\pm i\kappa z} \to e^{+i\kappa z}$) the fracture opening; and

$$n^2 = \kappa^2 (1 - \frac{c^2}{\alpha_f^2}) \quad , \tag{2.40}$$

where $\kappa = \omega/c$ and c is the Stoneley wave phase velocity along the z axis. The axial particle velocity in the borehole fluid is given by

$$v_z^{(l)} = \frac{1}{i\omega\rho_0} \frac{dp^{(l)}}{dz} \quad , \quad (l = I, R, T) \quad . \tag{2.41}$$

Since fracture width L_0 is generally small, no significant pressure drop will occur across the fracture. Pressure continuity gives

$$p^{(I)} + p^{(R)} = p^{(T)} \quad , \quad (at \ z = 0) \quad . \tag{2.42}$$

Substituting equation 2.39 into equation 2.42, one obtains

$$E^{(T)} = E^{(I)} + E^{(R)} \quad . \tag{2.43}$$

Under dynamic conditions, volume conservation of fluid flow is governed by equation 2.6. Integrating this equation over a small volume ΔV and applying the divergence theorem, one gets

$$-\oint_S \vec{v} \cdot d\vec{S} = \frac{i\omega}{\rho_0 \alpha_f^2} \int_{\Delta V} -p dV \quad , \tag{2.44}$$

where $\Delta V = \pi R^2 L_0$ is a flat cylinder of height L_0 and radius R located at the fracture opening, and S is the surface enclosing ΔV. The normal to S is pointed outwards from ΔV. Equation 2.44 has the simple physical meaning that the net flow into ΔV equals the dynamic volume compression of ΔV. In previous models of Mathieu (1984) and Hornby et al. (1989), this dynamic effect was not taken into account. However, this effect is generally not significant since L_0 is small. The net flow into ΔV is

$$-\oint_S \vec{v} \cdot d\vec{S} = q^{(I)} + q^{(R)} - q^{(T)} - q^{(F)} \quad , \quad (at \ z \approx 0) \tag{2.45}$$

where

$$q^{(l)} = 2\pi \int_0^R v_z^{(l)} r dr \quad , \quad (l = I, R, T) \tag{2.46}$$

and $q^{(F)}$ is the flow away from ΔV into the fracture, as given by equation 2.34. If one approximates the pressure inside ΔV by the transmitted pressure $p^{(T)}$, the volume integral in equation 2.44 is given by

$$\int_{\Delta V} p^{(T)} dV = 2\pi L_0 \frac{R}{n} I_1(nR) E^{(T)} \quad , \tag{2.47}$$

where I_1 is the first order modified Bessel function of the first kind. When the integration in equation 2.46 is completed using equations 2.39 and 2.41, equations 2.44 and 2.47 are combined to give

$$q^{(F)} = \frac{2\pi R}{\rho_0 cn} I_1(nR) \left[E^{(I)} - E^{(R)} - (1 - \frac{i\omega c L_0}{\alpha_f^2}) E^{(T)} \right] \quad . \tag{2.48}$$

Equating the pressure at the fracture opening (i.e., $p(w, R)$ in equation 2.34) to $p^{(T)}(\omega, R)$, one has

$$p(\omega, R) = E^{(T)} I_0(nR) \quad . \tag{2.49}$$

Equations 2.44 and 2.48, together with equations 2.34, 2.47, and 2.49, are solved to give the reflection and transmission coefficients of the waves. They are:

$$R_{ef} = \frac{E^{(R)}}{E^{(I)}} = -\frac{Y}{1+Y} \quad , \tag{2.50}$$

$$T_{rs} = \frac{E^{(T)}}{E^{(I)}} = \frac{1}{1+Y} \quad , \tag{2.51}$$

where:

$$Y = \frac{\rho_0 c}{2} \bar{C} \left[kn \frac{I_0(nR)}{I_1(nR)} \frac{H_1^{(1)}(kR)}{H_0^{(1)}(kR)} - k^2 \right] \quad , \tag{2.52}$$

where $\bar{C}$ is the dynamic conductivity given by equation 2.36. Thus it can be seen that when a Stoneley wave comes across a borehole fracture, part of the wave is reflected at the fracture opening, resulting in the attenuation of the wave amplitude of the transmitted wave. Figure 2-3 shows the amplitude of the transmission coefficient $|T_{rs}|$ as the function of fracture width L_0 for different frequencies. The borehole diameter is 7.62 cm. The borehole fluid is water (α_f=1500 m/s), and the Stoneley wave velocity is taken to be $0.95\alpha_f$. The general behavior of $|T_{rs}|$ decreases with L_0 and increases with frequency. The simple Stoneley attenuation model derived here will be compared with a more elaborate model in Chapter 5.

2.2.4 Relevance to Existing Stoneley Attenuation Models

In previous sections of this chapter, the fluid motion inside a fracture with rigid walls is rigorously solved by relating both viscous shear effect and acoustic propagation

effect. The relative importance of these two effects is governed by a complex equation (equation 2.21). When the former effect dominates, the fluid motion is diffusive, while when latter effect dominates, the motion is propagational. A qualitative criterion is the viscous skin depth $\delta = \sqrt{2\nu/\omega}$. For example, taking $\omega = 2\pi \times 1000$ Hz, the skin depths for water and mud ($\mu_{mud} \approx 100\mu_{water}$, Burns, 1988) are about 20 μm and 200 μm, respectively. It has been shown in Figure 2-1 that when $L_0 > 100$ μm, the velocity dispersion is not very significant (the fluid is water.). Also, as has been shown in Figure 2-2, the dynamic conductivity for the small aperture (L_0 =10 μm) curve is nearly constant (the cubic law). The conductivity decreases with increasing frequency when the flow aperture is large. These examples demonstrate that, for fractures with large apertures, fluid flow is mainly a propagational effect. However, when the flow aperture is the order of 2δ, viscous effects will control the fluid motion.

The relevance of the present Stoneley attenuation model to previous models of Mathieu (1984) and Hornby et al. (1987) can now be discussed. In Mathieu's model, flow in the fracture was assumed diffusive and the fracture conductivity was given by the cubic law. In addition, pressure excitation at the borehole opening was treated as quasi-static by averaging it over the half cycle. An important parameter of this model is the fluid diffusivity in the diffusion equation (Mathieu, 1984)

$$b = \frac{L_0^2}{12\gamma\mu} \quad , \tag{2.53}$$

where $\gamma = \rho^{-1}(\partial\rho/\partial p)_T$ is the fluid compressibility. It can be shown that $i\omega/b$ is the k^2 in equation 2.27 at low frequencies. One uses the thermodynamic relation,

$$(\frac{\partial\rho}{\partial p})_T = \frac{C_p}{C_v}(\frac{\partial\rho}{\partial p})_S \quad , \tag{2.54}$$

where S denotes entropy while T denotes temperature. For fluid, the ratio of the heat capacities $C_p/C_v \approx 1$. Thus $\gamma \approx \rho^{-1}(\partial\rho/\partial p)_S = \rho^{-1}\alpha_f^{-2}$. This immediately gives

$$\frac{i\omega}{b} = \frac{12i\omega\nu}{\alpha_f^2 L_0^2} \quad , \tag{2.55}$$

agreeing with equation 2.27, where $k^2 \propto i\omega$ implies that the wave motion is diffusive. Thus the present model reduces to Mathieu's model at low frequencies or small apertures. However, Mathieu (1984) modeled the pressure excitation as a step function in the time domain, which is inconsistent with the present dynamic model. In addition, Mathieu's model predicts that the transmission coefficient is minimally dependent on frequency, whereas the present one can be strongly dependent on frequency. This implies that when using the present model to determine flow aperture, this frequency dependency has to be taken into account. Moreover, in order to produce a specific attenuation, the present model generally requires a larger flow aperture than Mathieu's model does.

In the Hornby et al. (1989) model, the fluid motion in a fracture is purely propagational. This is valid when the fracture fluid has very low viscosity (such as water), the fracture aperture is not very small, and the frequency is high. In fact, under the above mentioned conditions, the fracture fluid wavenumber, as determined by equation 2.21, approaches the free space wavenumber, and the fluid motion becomes propagational. Therefore, under these conditions, the present model is almost identical to Hornby et al. (1989) model. However, as shown previously, at 1 kHz, the viscous skin depth is of the order of 20 to 200 μm, depending on the viscosity. In situ fracture apertures of the order of 100 μm are not uncommon. In VSP's, lower frequency means that the skip depth is even greater, of the order of 500 μm or more, and thus one must take the viscous effect into account for this to be a complete theory. The present model is a complete theory valid for any flow aperture, fluid viscosity, and frequencies.

2.3 Dynamic Permeability of porous media and Fracture Dynamic Conductivity

Under an oscillatory presure gradient, the motion of a viscous fluid that saturates the pore space of a porous medium exhibits strong frequency-dependent behaviors. As

in the fracture case, the distinction between high- and low-frequencies is whether the viscous skin depth, $\delta = \sqrt{2\nu/\omega}$, is small or large compare to the size of the pores. For a homogeneous, isotropic, porous solid saturated with a Newtonian viscous fluid, Johnson et al. (1987) developed the theory of dynamic permeability to characterize the frequency-dependent behavior of the pore fluid flow. This theory is constructed based on the high- and low-frequency behaviors of the pore fluid motion and a simple model that satisfies certain analytical properties required by causality and reality for a complex frequency. Detailed derivation of the theory is referred to the original article of Johnson et al. (1987). Assuming that the solid frame is rigid, they derived the complex permeability as

$$\kappa(\omega) = \frac{\kappa_0}{[1 - 4i\alpha^2\kappa_0^2\rho_0\omega/(\mu\Lambda^2\phi^2)]^{1/2} - i\alpha\kappa_0\rho_0\omega/(\mu\phi)} \quad , \tag{2.56}$$

where κ_0 is the static Darcy permeability, ω is the angular frequency, α is the high frequency limit of the dynamic tortuosity, which is a parameter describing the tortuous, winding pore spaces, ρ_0 and μ are fluid density and viscosity, respectively, and ϕ is porosity. The symbol Λ is a measure of pore size. If one models the pores as a set of non-intersecting tubes, Λ is then given as (Johnson et al., 1987)

$$\Lambda \approx \left(\frac{8\alpha\kappa_0}{\phi}\right)^{1/2} \quad . \tag{2.57}$$

In the case of a fracture, Λ is the fracture aperture and the number 8 in equation 2.57 is replaced by 12. For general porous media, one can use the relation in equation 2.57 for the value of Λ in equation 2.56. The low- and high-frequency behaviors of $\kappa(\omega)$ are readily derived from equation 2.56. At low frequencies, $\kappa(\omega) \rightarrow \kappa_0$; at high frequencies, $\kappa(\omega) \rightarrow i\mu\phi/(\alpha\rho_0\omega)$, varying inversely proportional to ω. Since $\kappa(\omega)$ is a very important parameter that will be applied to the problem of logging in permeable formations in the next chapter, it is desirable to test its validity and accuracy against a simple model with known results.

In the first part of this chapter, the fracture dynamic conductivity has been obtained based on the study of frequency-dependent fluid flow properties of a single

fracture. It is now ready to compare the fracture conductivity given in equation 2.36 with the dynamic permeability of a porous medium in equation 2.56. In order to do so, one needs to use appropriate parameters for the permeability and deduce from it a fracture conductivity that can be directly compared with the one given in equation 2.36. For the fracture case, the parameters in equation 2.56 are chosen as: $\alpha = 1$, $\Lambda = L_0$, $\kappa_0 = L_0^2/12$ and $\phi = 1$. By Darcy's law, the fracture conductivity and permeability are related via $C = \kappa L_0/\mu$. Therefore, the fracture dynamic conductivity derived from equation 2.56 is

$$C(\omega) = \frac{L_0^3/12\mu}{[1 - i\rho_0\omega L_0^2/(36\mu)]^{\frac{1}{2}} - i\rho_0\omega L_0^2/(12\mu)} \quad . \tag{2.58}$$

It is obvious that the low- and high-frequency behaviors of equation 2.58 are exactly those of the fracture dynamic conductivity, as given in equations 2.37 and 2.38. Thus at low and high frequencies the two theories are in agreement. A complete comparison between equation 2.36 and equation 2.58 is illustrated in Figure 2-4 for a set of fracture apertures ranging from 10 μm to 100 μm. The fluid is water with $\mu = 1$ cp. The reason for choosing different apertures is that the fracture fluid motion is controlled by the viscous skin depth $\delta = \sqrt{2\nu/\omega}$. For water, the skin depth is about 20 μm at 1 kHz and 8 μm at 5 kHz. For apertures which are small compared to 2δ the fluid motion is dominated by diffusion. While for apertures which are large compared to δ, the motion is mostly propagational. Thus the comparison of $C(\omega)$ and $\bar{C}(\omega)$ from small to large apertures will fully illustrate their compatibility in frequency ranges from quasi-static to dynamic regimes. Figure 2-4a shows the amplitudes of $C(\omega)$ (solid curves) and $\bar{C}(\omega)$ (dashed curves) in the frequency range of [0-5] kHz. The conductivities are normalized by their zero frequency value $L_0^3/(12\mu)$. An excellent agreement of $C(\omega)$ with the exact $\bar{C}(\omega)$ is seen from the quasi-static regime (the lower frequency part of the $L_0 = 10$ μm curves), through the transition regime (the $L_0 = 30$ and 60 μm curves), to the dynamic regime (the higher frequency part of the $L_0 = 100$ μm curves). Figure 2-4b shows that not only their amplitudes but also their phases are in excellent agreement. Thus the general formula of equation 2.56,

when applied to the special case of a fracture, agrees extremely well with the exact solution of equation 2.36. In fact, equation 2.56 has been successfully tested with large tube lattices with randomly varying radii (Johnson et al., 1987). The present test, together with the previous test, further reflects the general applicability of the theory of dynamic permeability to the modeling of frequency-dependent fluid flow properties of porous media.

2.3.1 Relation Between Dynamic Permeability and Biot's Slow Wave

It has been shown that the frequency-dependent transport property of porous media can be expressed in terms of the dynamic permeability. It is appropriate here to demonstrate the relation between dynamic permeability and Biot's slow compressional waves and derive an equation that will later be used in the borehole propagation problem. For a fluid-saturated porous medium, the equation of continuity for the pore fluid is

$$\nabla \cdot (\rho \phi \vec{v}) + \frac{\partial}{\partial t}(\phi \rho) = 0 \ , \tag{2.59}$$

where t is time, $\vec{v}$ is the macroscopic fluid velocity through the porous medium. For a small amplitude fluid motion, the density ρ can be written as

$$\rho = \rho_0 + \rho' \ , \tag{2.60}$$

where ρ' is the density perturbation which is related to the pressure disturbance P as

$$\frac{\rho'}{\rho_0} = \frac{P}{K_f} \ , \tag{2.61}$$

where $K_f = \rho_0 \alpha_f^2$ is the fluid modulus. At this stage, elasticity of the solid frame is ignored and only pore fluid flow that results from the pore pressure gradient and permeability is considered. Therefore, one can still use Darcy's law

$$\phi \vec{v} = -\frac{\kappa(\omega)}{\mu} \nabla P \ . \tag{2.62}$$

However, an important modification to the conventional Darcy's law is that the static permeability κ_0 is now replaced by the dynamic permeability $\kappa(\omega)$ given by equation 2.56. Transforming equation 2.59 into the frequency domain, then substituting equations 2.60, 2.61, and 2.62 into it and taking the first order perturbation terms, one obtains a linearized equation for the pore fluid pressure

$$\nabla^2 P + \frac{i\omega}{D_0} P = 0 \ , \tag{2.63}$$

where

$$D_0 = \frac{\kappa(\omega) K_f}{\phi \mu} \tag{2.64}$$

is the pore fluid diffusivity for the rigid frame case. A plane wave solution to equation 2.63 has a wave number $k = \sqrt{i\omega/D_0}$. Using the dynamic permeability given in equation 2.56 and substituting it into D_0 given in equation 2.64, one obtains the low- and high-frequency behaviors of this wave motion. At low frequencies, $D_0 \sim const.$ and $k \propto \sqrt{i\omega}$, indicating that this motion is diffusive. At high frequencies, $D_0 \propto (i\omega)^{-1}$ and $k \propto \omega$, implying that this motion becomes a propagational wave. Therefore, based on the theory of dynamic permeability, equation 2.63 correctly predicts the general behavior of Biot's slow compressional waves.

One can now relax the assumption that the solid frame is rigid and make a correction for the effects due to its elasticity. Based on Biot's theory, Chang et al. (1988) as well as Norris (1989) showed that at low frequencies, if the frame elasticity is taken into account, the diffusivity given in equation 2.64 should be corrected to become

$$D = D_0 (1 + \xi)^{-1} \ , \tag{2.65}$$

with ξ given by

$$\xi = \frac{K_f}{\phi(K_b + \frac{4}{3}N)} \left\{ 1 + \frac{1}{K_s} \left[\frac{4}{3} N (1 - \frac{K_b}{K_s}) - K_b - \phi(K_b + \frac{4}{3}N) \right] \right\} \ , \tag{2.66}$$

where K_s is the solid grain bulk modulus, K_b and N are the solid frame bulk and shear moduli, respectively. It should be noted that in Chang et al.'s (1988) formula,

the permeability in D_0 was the static permeability κ_0. Here κ_0 has been replaced with $\kappa(\omega)$, but the correction term ξ given in equation 2.66 is used to account for the frame elasticity. Because $\kappa(\omega) \rightarrow \kappa_0$ as $\omega \rightarrow 0$, equation 2.65 is identical to Chang et al.'s (1988) diffusivity at low frequencies. As frequency increases, the frequency-dependent fluid flow is accounted for by $\kappa(\omega)$, and the effects due to frame elasticity will be compensated by the correction term ξ. With this correction, equation 2.63 becomes

$$\nabla^2 P + \frac{i\omega}{D} P = 0 \quad . \tag{2.67}$$

The wavenumber of the slow wave is now given by

$$k^2 = i\omega/D = \frac{i\omega\phi\nu}{\kappa(\omega)\alpha_f^2(1+\xi)^{-1}} \quad . \tag{2.68}$$

The complex slow wavenumber determined from equation 2.68 is in complete agreement with that from the exact Biot formulation (for an example of this formulation, see Chang et al.'s (1988) article) in the low-frequency region of the Biot theory. In the high-frequency region, the two wavenumbers are slightly different depending on porosity and permeability. As will be shown in Chapter 3, the application of equation 2.67 to borehole logging problem yields satisfactory results, even in the high-frequency region of the Biot theory.

2.4 Discussion

In section 2.3.1, the effect of solid elasticity on the fluid motion in a porous medium is addressed. It is seen that this effect does not change the dynamic permeability $\kappa(\omega)$ that governs the fluid transport property, but only modifies the wavenumber of Biot's slow wave. In fact, as pointed out by Johnson et al. (1987), the quantity $\kappa(\omega)$ is independent of the elastic property of the solid. Because of the similarity between $\kappa(\omega)$ and the fracture dynamic conductivity $\bar{C}(\omega)$, it is reasonable to assume that, when the fracture is bounded by an elastic solid, the dynamic conductivity $\bar{C}(\omega)$

is independent of the elastic property of the solid, and that the effect of the solid elasticity is only to change the the wavenumber of the fracture fluid wave motion. For the fracture case, k^2 in equation 2.68 can be written as

$$k^2 = \frac{i\omega L_0}{\bar{C}(\omega)\rho_0 v_e^2} \ , \tag{2.69}$$

where $\phi = 1$ and $\kappa(\omega) = \mu\bar{C}(\omega)/L_0$ have been used in equation 2.68, and v_e^2 here is analogous to $\alpha_f^2(1+\xi)^{-1}$ in equation 2.68. The free space velocity α_f has now been modified by the solid elasticity to become an effective velocity v_e. Accordingly, the definition of $\bar{C}$ given by equation 2.36 should also be modified to become

$$\bar{C} \equiv \frac{i\omega L_0}{k^2 v_e^2 \rho_0} \ . \tag{2.70}$$

A candidate for v_e can be obtained by neglecting the viscousity of the fluid and solving a fracture dispersion equation that results from the coupling of an inviscid fluid with the elastic solid. This equation is given in equation 4.24 in Chapter 4. The effective velocity can be equated with the velocity of the fundamental wave mode in the fracture, since this mode is the extension of the dynamic fluid flow in the presence of the elastic fracture wall. In the high-frequency region where $L_0 \gg \delta$, such that the viscous effect is minimal, this choice of v_e can be readily justified. Because the effect of solid elasticity is to reduce the effective velocity from α_f to v_e, the squared wavenumber k^2 in equation 2.69 is simply ω^2/v_e^2, and the dynamic conductivity in equation 2.70 becomes $\bar{C} = iL_0/(\omega\rho_0)$, agreeing with with the high-frequency behavior of the dynamic conductivity in the rigid fracture case, as given in equation 2.38. In the low-frequency region where $\delta \gg L_0$, this choice of v_e may not be adequate because the fundamental mode velocity determined from equation 4.24 goes to zero as L_0 and ω decrease (Ferrazzini and Aki, 1987; Tang and Cheng, 1989). In this case, a further study is needed to investigate the fracture fluid motion that involves the coupling between a viscous fluid and an elastic solid. For the acoustic logging studies, however, the typical frequency band is [2-20] kHz and fracture thickness of interest is on the order of millimeter to centimeter. Under these conditions, the

applications are often in the high-frequency region of the fracture dynamic flow theory. Therefore, the high-frequency expressions for the fracture dynamic conductivity and wavenumber are used in the study of effects of a major fracture on the propagation of borehole acoustic waves.

2.5 Conclusions

In this chapter, fluid motion in a narrow aperture has been treated by considering both viscous shear and wave propagation effects. A characteristic equation has been obtained (equation 2.21), which governs the relative importance of the two effects. The viscous fluid flow is important for very narrow apertures or high viscosity fluids, especially at low frequencies. Outside of these situations, fluid motion is mostly propagational. Under dynamic pressure excitations, fluid conduction in a fracture is characterized by the dynamic conductivity (equation 2.36), which reduces to the cubic law at low frequencies or small flow apertures. This dynamic flow law, instead of the cubic law, can be applied to dynamic flow problems in a fracture. The present flow model has been used to obtain Stoneley wave attenuation across a borehole fracture, which will be compared with a more elaborate model in Chapter 5.

The theory of dynamic permeability of a porous medium has been compared with the theory of fracture dynamic conductivity. The excellent agreement of the two theories reflects the general behavior of frequency-dependent fluid motion in fluid-saturated conduits of rocks, regardless whether they are fractures or pores. It has also been shown that the dynamic permeability, together with a simple correction for the solid elasticity, is a very good description of Biot's slow wave. Analogous to the dynamic wave motion in a porous medium, a correction for the effect of solid elasticity on the fracture wave motion has been obtained, and its validity in the high-frequency region has been justified. The dynamic flow theory studied in this chapter will be applied in the following chapters to study the effects of porous formations, a vertical

fracture, and a horizontal fracture on the propagation of borehole acoustic waves.

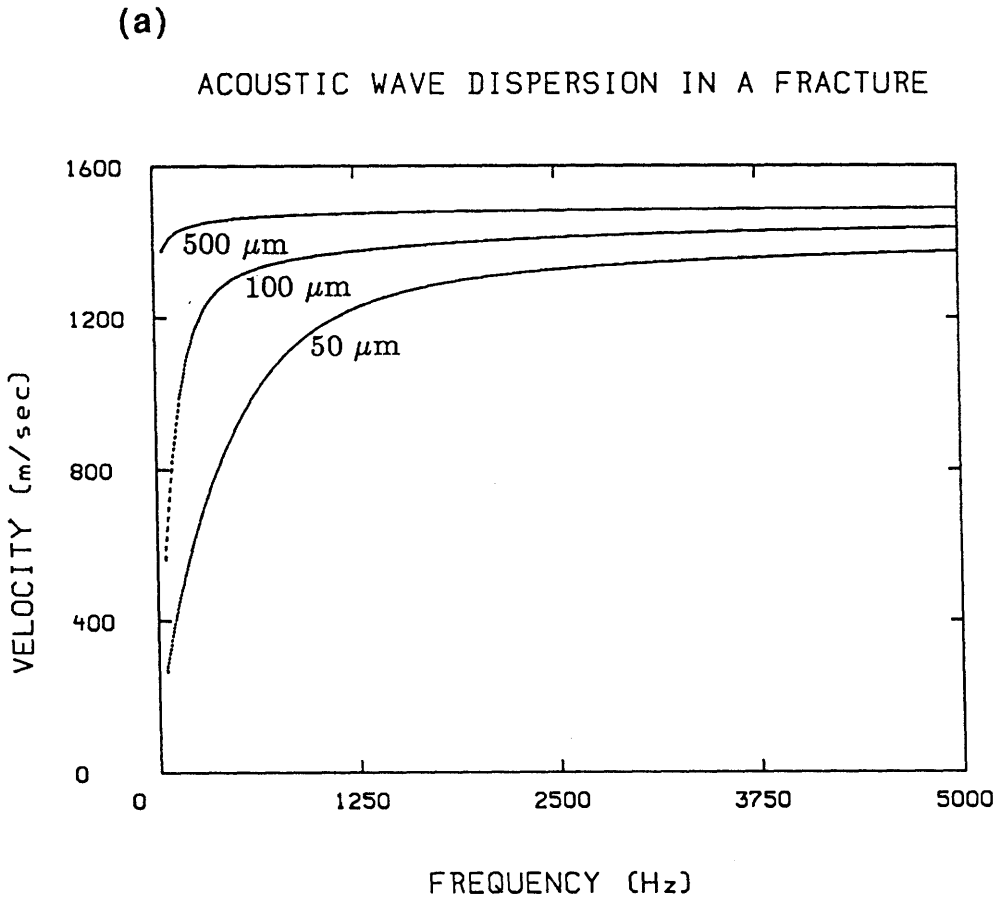

Figure 2-1: (a) Velocity dispersion (b) and attenuation of a viscous fluid wave motion in a fracture. In both (a) and (b), the curves are plotted for a set of fracture widths of 50, 100, and 500 μm. The fracture fluid is water.

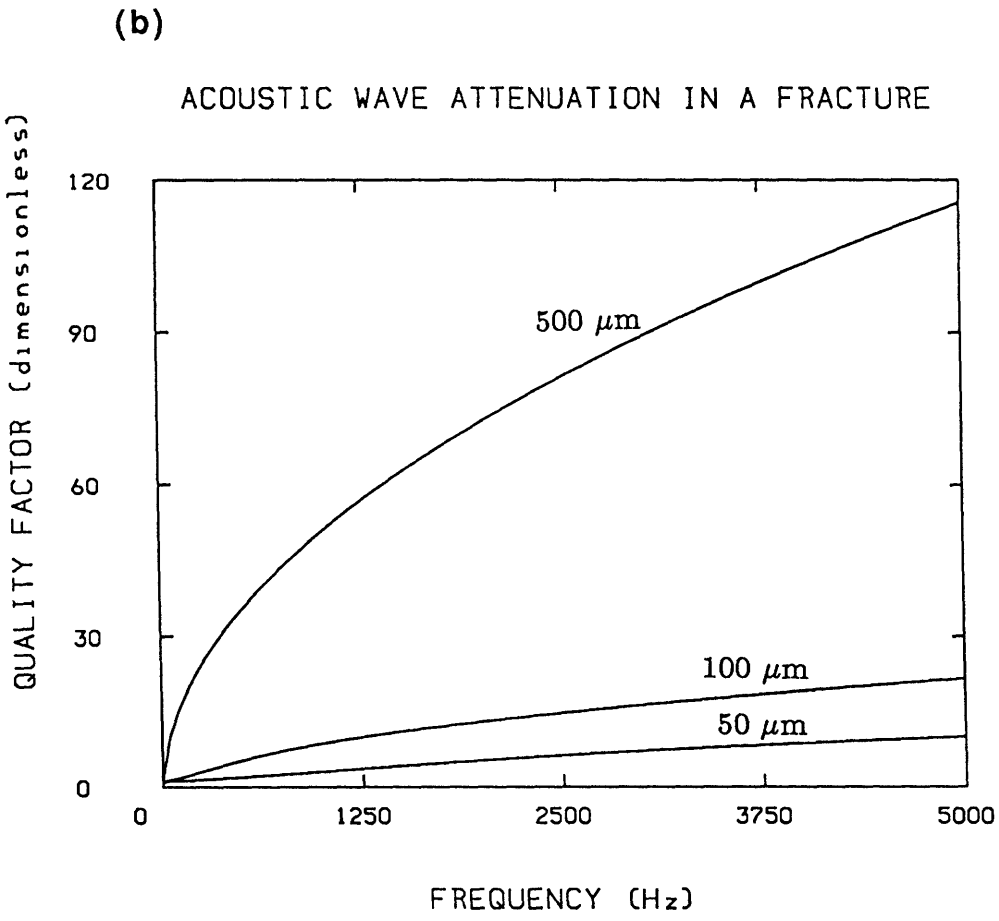

Figure 2-1: (b) Attenuation (plotted as quality factor) of the fracture wave motion.

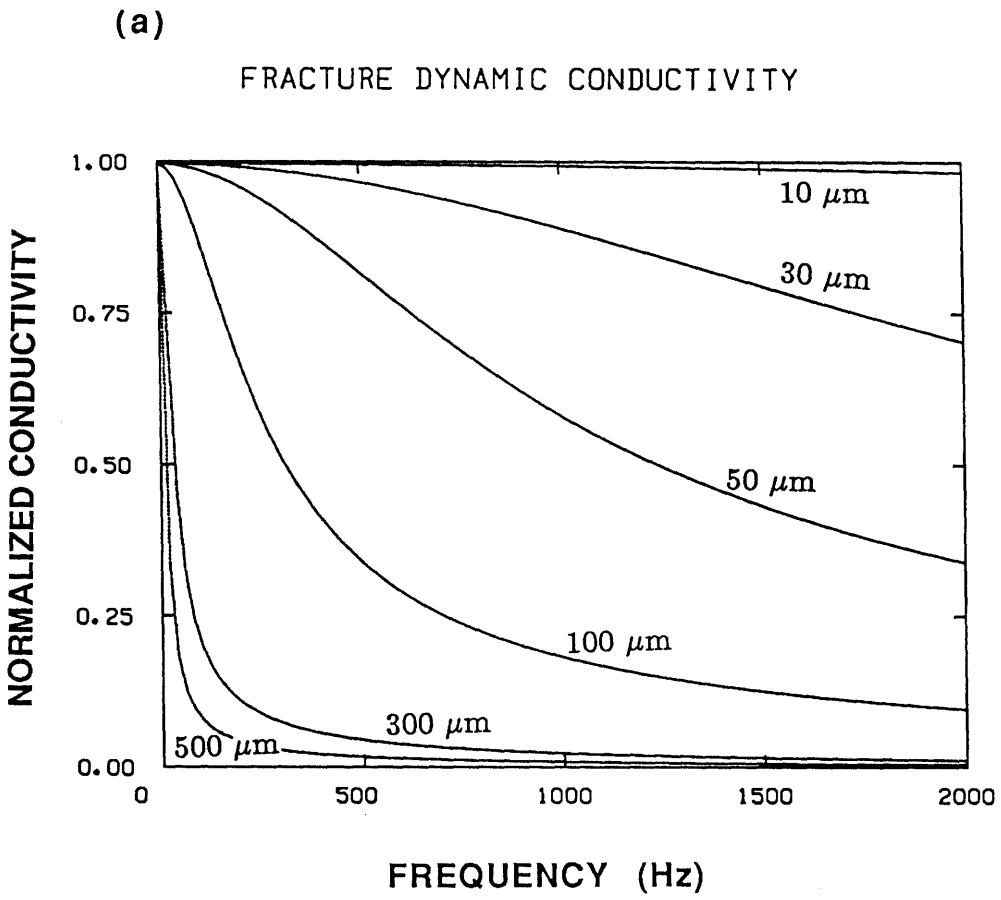

Figure 2-2: (a) Amplitude of the dynamic conductivity versus frequency for different fracture widths. The amplitudes are normalized by their zero-frequency value $L_0^3/12\mu$ (the cubic law).

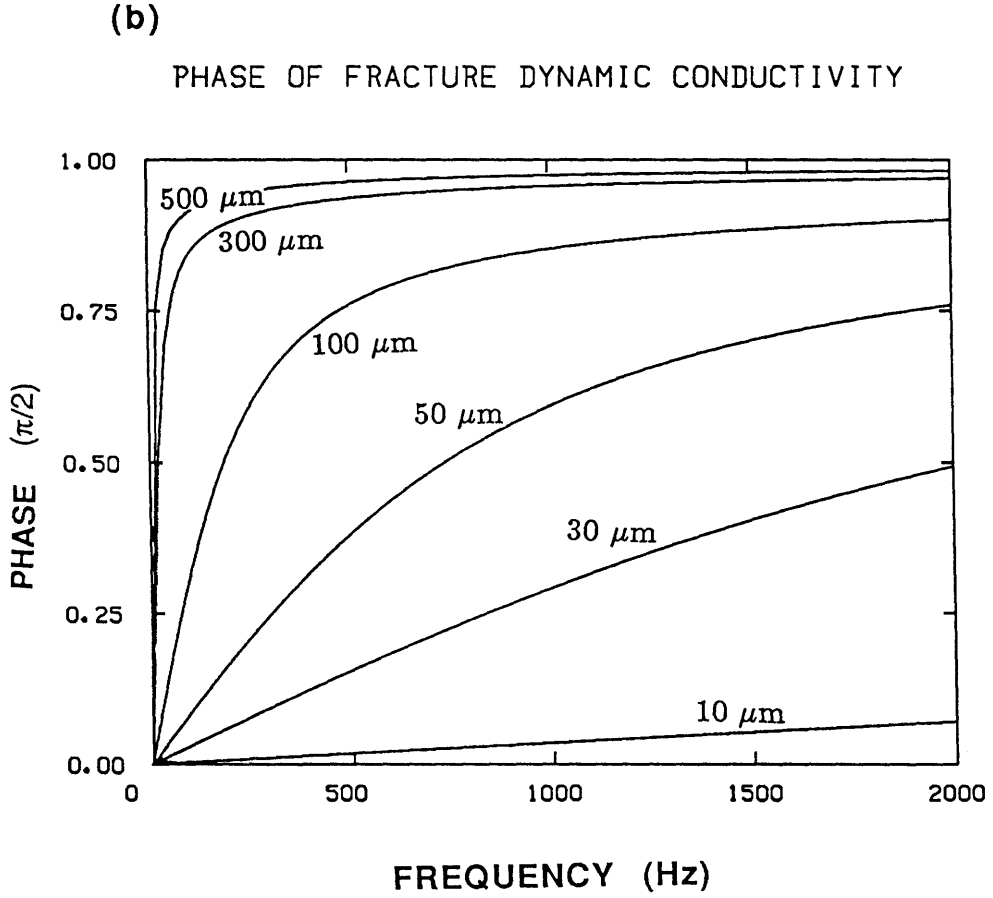

Figure 2-2: (b) Phase of the dynamic conductivity (normalized by $\pi/2$) versus frequency for different fracture widths.

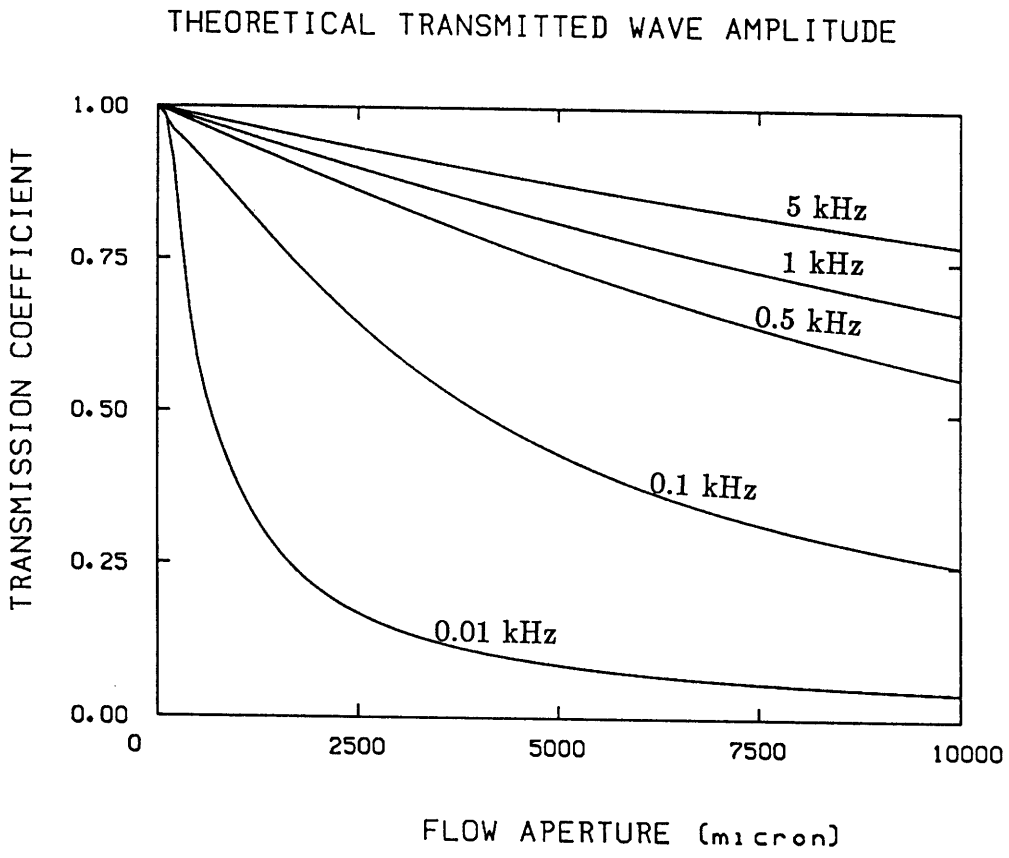

Figure 2-3: Amplitude of the theoretical transmission coefficient versus fracture width for different frequencies. The parameters are $R = 3.81$ cm, $\alpha = 1500$ m/s, and $c = 0.95\alpha_f$.

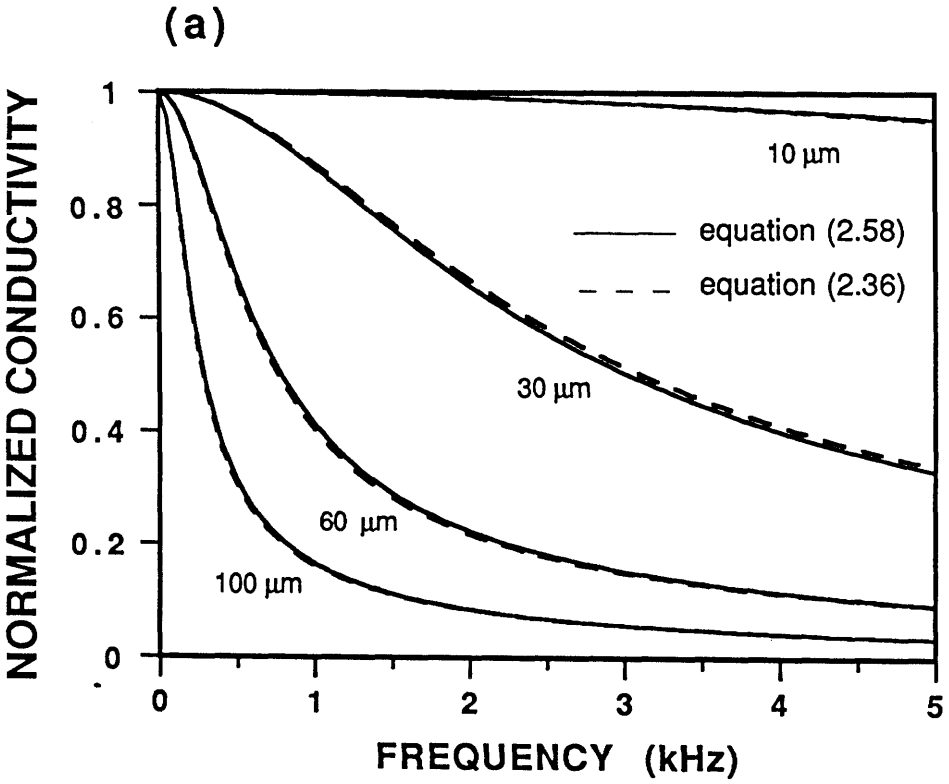

Figure 2-4: Comparison between the theory of fracture dynamic conductivity and the theory of dynamic permeability applied to the fracture case. The two theories are respectively evaluated using equation 2.36 (dashed curves) and equation 2.58 (solid curves) for fracture aperture L_0 equals 10, 30, 60, and 100 μm, as indicated on the curves. The amplitudes in (a) are normalized by their zero frequency value $L_0^3/12\mu$. Both amplitudes (a) and phases (b) of the two theories are in excellent agreement for all apertures and frequencies.

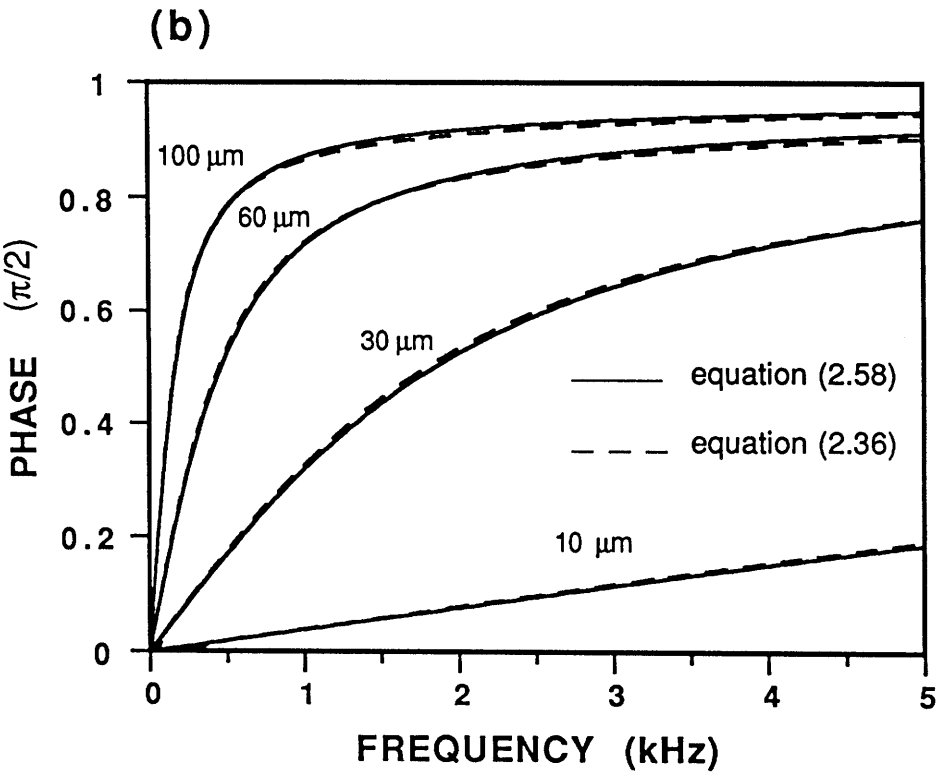

Figure 2-4: (b) Comparison of phases of the two conductivities (normalized by $\pi/2$).

Chapter 3

Application of Dynamic Fluid Flow Theory to Acoustic Logging in Porous Formations

3.1 Introduction

In Chapter 2, the general characteristics of dynamic fluid flow in fractures and porous media were studied. The dynamic permeability was shown to be a very good measure of the fluid conduction under dynamic wave excitations. An equation (equation 2.67) which governs the dynamic fluid pressure in a porous medium was also obtained. In this chapter, the theory of dynamic fluid flow in porous media will be applied to study the Stoneley wave propagation in permeable boreholes. The concept of dynamic permeability will be used to characterize the fluid flow excited by the Stoneley wave at the borehole wall. A simple dynamic model of Stoneley wave propagation will be derived. The same problem was formulated by Rosenbaum (1974) using Biot (1956a,b) theory for a porous and permeable medium. This model has been referred to as Biot-Rosenbaum model (Cheng et al., 1987). As will be shown later in this chapter, the theoretical predictions from the simple model agree well with those from the

complete model of the Biot-Rosenbaum theory, but the formulation and calculation are much simplified. Therefore, this chapter provides a simple and useful theory that can be easily applied to the estimation of formation permeability from Stoneley wave measurements.

In the following, models concerning acoustic logging in porous formations will be reviewed to give some background materials that are relevant to the development of the present theory. Next, the theoretical formulation of the simple model is presented. The results from this model are then compared with those from the Biot-Rosenbaum model and the experimental results available from Winkler et al. (1989). Finally, the conditions under which the simple model is valid or inadequate will be discussed.

3.2 Background

In the past few years, the estimation of rock permeability from borehole acoustic logging measurements has become a topic of intense research. Field measurements clearly indicated the effects of formation permeability on borehole Stoneley waves (Bamber and Evans, 1967; Staal and Robinson, 1977; Williams et al., 1984; Zemanek et al., 1985). A convincing example is the published data of Williams et al. (1984) which shows excellent correlation between the Stoneley wave velocity and attenuation and core measured permeability. On the other hand, theoretical models were developed to study the correlation between permeability and Stoneley propagation. White (1983) and Hsui and Toksöz (1986) developed low-frequency models of Stoneley wave propagation and predicted this correlation, although these models are not accurate at high frequencies. Rosenbaum (1974) was the first to use Biot's (1956) theory for a porous solid to model acoustic logging in a porous formation and investigated the effects of permeability on high-frequency borehole acoustic waves. This model is therefore termed the Biot-Rosenbaum model. Using this model, Burns and Cheng (1986) inverted in-situ permeability from Stoneley wave velocity and attenuation and

found a good agreement between the inverted permeability and core measurements. Cheng et al. (1987) applied this model to the medium frequency range of [0-8] kHz, in which the Stoneley wave is effectively excited. They found substantial influence of permeability on Stoneley propagation and a good agreement of the theory with field observations. Schimtt et al. (1988) extended the model to study the permeability effects on the Stoneley and other borehole waves (e.g., pseudo-Rayleigh waves). Winkler et al. (1989) performed laboratory model experiments on borehole Stoneley wave propagation to evaluate the applicability of the Biot theory to logging in porous formations. The theory was found to be in excellent agreement with the experiment. In addition, Chang et al. (1988) and Norris (1989) derived low-frequency asymptotics of the Biot-Rosenbaum theory for the Stoneley wave and showed that the White (1983) and Hsui and Toksöz (1986) models are the low-frequency representation of the theory when the frame of the solid is very rigid. In summary, it has become clear that the Biot-Rosenbaum model is the appropriate basic theory for wave propagation in a borehole penetrating a porous formation.

As summarized briefly in Chapter 2, there are three types of waves which can propagate independently in a fluid-saturated porous medium (Biot, 1956a,b, 1962a,b). The fast compressional wave and shear wave are primarily associated with the motion of the solid matrix, but modified by the presence of the pore fluid. The slow compressional wave is associated primarily with the motion of the pore fluid, but modified by the presence of the solid matrix. In the case of Stoneley wave propagation in a permeable borehole, the borehole wave will excite all three types of Biot waves in the formation. The Biot-Rosenbaum model deals with the interaction between the borehole propagation and these three waves by rigorously solving a set of coupled partial differential equations in connection with boundary conditions at the borehole wall (Rosenbaum, 1974). Although such an approach is complete and accurate, the mathematics and computation involved make the model complicated. Particularly in an inverse problem to extract formation permeability from Stoneley wave measure-

ments, this model is not convenient to use. In this chapter, a much simpler alternative approach is taken to handle this problem. The interaction between the Stoneley wave and a porous formation is decomposed into two parts. The first is the interaction of the Stoneley with the formation shear and fast compressional waves in the absence of the slow wave. This problem is equivalent to the one with a formation having effective elastic moduli corresponding to the first two waves, for which the solutions are known. On the basis of the first step, the second step is to add the interaction between the Stoneley and the formation slow wave, for which the dynamic permeability is applied to measure the loss of Stoneley energy that is carried away by the slow wave into the formation. Since the correlation between Stoneley attenuation and permeability is largely due to this latter interaction (Schmitt, 1988; Winkler et al., 1989), the final results of the present approach are expected to be consistent with those from the Biot-Rosenbaum theory, as long as the frequency-dependent transport property of the porous formation is correctly accounted for. The success of this effort will not only further verify the Stoneley attenuation mechanism in permeable boreholes, but will also provide a much simplified useful model that is of sufficient accuracy in applications to both forward and inverse problems concerning borehole Stoneley wave propagation in a porous formation.

3.3 Theoretical Formulation of the Simple Model

For a fluid-filled borehole, the cylindrical coordinates (r, θ, z) can be used, where z is along the borehole axis, r is the radial distance from the axis, and θ is the polar angle. The borehole fluid displacement potential Ψ satisfies the following wave equation:

$$\nabla_t^2 \Psi + \frac{\partial^2 \Psi}{\partial z^2} + \frac{\omega^2}{V_f^2} \Psi = 0 \ , \tag{3.1}$$

where V_f is the acoustic velocity of the fluid, ω is the angular frequency, and

$$\nabla_t^2 = \frac{\partial^2}{\partial r^2} + \frac{1}{r} \frac{\partial}{\partial r}$$

is the two dimensional Laplace operator. In the present formulation, the azimuthal symmetry is assumed thus the θ-dependencies are dropped. In terms of Ψ, the borehole fluid pressure P and radial displacement U are given by

$$P = \rho_0 \omega^2 \Psi \ , \tag{3.2}$$

$$U = \frac{\partial \Psi}{\partial r} \ . \tag{3.3}$$

For a Stoneley wave propagating along the borehole, Ψ, P, and U can be written as

$$\begin{aligned} \Psi(r,z) &= \psi(r)\exp(ik_z z) \ , \\ P(r,z) &= p(r)\exp(ik_z z) \ , \\ U(r,z) &= u(r)\exp(ik_z z) \ , \end{aligned} \tag{3.4}$$

where k_z is the axial Stoneley wavenumber. Using equations 3.2, 3.3, and 3.4, one can relate the potential ψ and its radial derivative through the equation

$$\frac{\partial \psi}{\partial r} - (\rho_0 \omega^2 \frac{u}{p})\psi = 0 \ , \tag{3.5}$$

which, when evaluated at the borehole boundary $r = R$, becomes the boundary condition for ψ. Consequently, ψ is given by the following boundary value problem

$$\begin{cases} \nabla_t^2 \psi + \nu^2 \psi = 0 \\ \partial_r \psi = \rho_0 \omega^2 (u/p)\psi \quad , \quad (\text{at } r = R) \end{cases} \tag{3.6}$$

where ∂_r denotes taking derivative with respect to r and $\nu = \sqrt{\omega^2/V_f^2 - k_z^2}$ is the radial wavenumber. The wall conductance (inverse of impedance) (u/p) is the ratio of the displacement u and pressure p evaluated at the borehole boundary $r = R$. When the borehole wall is permeable, u includes two contributions. The first is the elastic displacement of the wall, given by u_e. The second is the fluid flow into pores that are open to the borehole wall, given by ϕu_f, where ϕ is the porosity of the formation. As illustrated by a diagram in Figure 3-1, the present problem can be decomposed into two problems. The first problem is equivalent to that of a borehole with an equivalent elastic formation consisting of the porous skeleton and fluid. In the first step, only P

and S waves in such a formation need to be considered. They are analogous to Biot's fast compressional and shear waves. Whereas for the second problem, one is mainly concerned with pore fluid flow, which is Biot's slow compressional wave. Splitting the problem of equation 3.6 into two, one can write ψ and ν^2 as

$$\psi = \psi_e + \psi_f \ , \tag{3.7}$$

$$\nu^2 = \nu_e^2 + \nu_f^2 \ , \tag{3.8}$$

where ψ_e satisfies the following boundary value problem

$$\begin{cases} \nabla_t^2 \psi_e + \nu_e^2 \psi_e = 0 \\ \partial_r \psi_e = \rho_0 \omega^2 (u_e/p) \psi_e \quad , \quad (\text{at } r = R) \end{cases} \tag{3.9}$$

and ψ_f and ν_f^2 are perturbations to ψ_e and ν_e^2, respectively. They result from the fluid flow at the borehole wall. The solution to the elastic problem (equation 3.9) is known. The boundary condition in equation 3.9 leads to a borehole dispersion equation (see equation 4.9 in Chapter 4). Given the effective elastic moduli or P and S wave velocities of the equivalent elastic formation as well as its effective density, one can solve the dispersion equation to find ν_e^2, from which the Stoneley wavenumber k_{ze} without the flow effects is obtained as $k_{ze} = \sqrt{\omega^2/V_f^2 - \nu_e^2}$. The calculation of the effective moduli and the velocities are described in the next section. To find ν_f^2, one substitutes equations 3.7 and 3.8 into equation 3.6 and obtains a boundary value problem for ψ_f

$$\begin{cases} \nabla_t^2 \psi_f + \nu_e^2 \psi_f = -\nu_f^2 \psi \\ \partial_r \psi_f = \rho_0 \omega^2 (u_e/p) \psi_f + \rho_0 \omega^2 \phi (u_f/p) \psi \quad , \quad (\text{at } r = R) \ . \end{cases} \tag{3.10}$$

To this end, one can see that the fluid flow at the borehole wall is to modify the boundary condition corresponding to the equivalent elastic formation, so as to change the fluid displacement potential from ψ_e to ψ, and the wavenumber from k_{ze} to k_z . Therefore, a boundary condition perturbation technique (Jackson, 1962; Morse and Feshbach, 1953) can be applied to incorporate the fluid flow effects and to find the

resulting changes in wave propagation. The condition at the borehole boundary and its effects over the borehole area are related through the two-dimensional Green's theorem

$$\iint_A [\psi_e \nabla_t^2 \psi_f - \psi_f \nabla_t^2 \psi_e] dA = \oint_S [\psi_e \frac{\partial \psi_f}{\partial r} - \psi_f \frac{\partial \psi_e}{\partial r}] dS \ , \tag{3.11}$$

where

$$A : \text{borehole area}; \quad S : \text{borehole boundary } r = R \ .$$

Applying equation 3.11 to equations 3.9 and 3.10 and using their respective boundary conditions, one gets

$$\nu_f^2 = -\rho_0 \omega^2 \phi (\frac{u_f}{p}) \left[\frac{\oint_S \psi \psi_e dS}{\iint_A \psi \psi_e dA} \right] \ . \tag{3.12}$$

To evaluate ν_f^2, one needs to find the flow conductance (u_f/p) and the ratio of integrals in equation 3.12. As a first order perturbation, this ratio is approximately the ratio of bore perimeter to bore area

$$\frac{\oint_S \psi \psi_e dS}{\iint_A \psi \psi_e dA} \sim \frac{2}{R} \ . \tag{3.13}$$

To find (u_f/p), one can make use of equations 2.67 and 2.62, as derived in Chapter 2. The first equation governs the dynamic pressure in the porous formation through the use of the dynamic permeability $\kappa(\omega)$ (equation 2.56) in the fluid diffusivity D (equation 2.65). The second equation is the modified Darcy's law, in which the dynamic permeability is used to measure the fluid transport driven by a dynamic pressure gradient. Under the excitation of a borehole propagation $e^{ik_z z}$, the formation pore fluid pressure has the form

$$P(r,z) = p(r) e^{ik_z z} \ , \ \ (r \geq R) \ . \tag{3.14}$$

In the previously mentioned quasi-static, low-frequency models, the term $e^{ik_z z}$ was ignored (see White, 1983 for example). This is valid when the wavelength is large compared to the borehole radius. However, at higher frequencies, the pore fluid motion is coupled with the borehole propagation and this term should be included.

Substitution of equation 3.14 into equation 2.67 results in a Bessel's equation for p

$$\frac{d^2p}{dr^2} + \frac{1}{r}\frac{dp}{dr} + (\frac{i\omega}{D} - k_z^2)p = 0 \ , \quad (r \geq R) \tag{3.15}$$

for which the solution is

$$p(r) = p(R)\frac{K_0(r\sqrt{-i\omega/D + k_z^2})}{K_0(R\sqrt{-i\omega/D + k_z^2})} \ , \tag{3.16}$$

where $p(R)$ is the borehole pressure at the wall and K_0 is the second kind modified Bessel function of order zero. By differentiating equation 3.16 with respect to r and using the modified Darcy's law given by equation 2.62 (note that $v = -i\omega u_f$ in this equation), the wall conductance due to flow is found to be

$$\frac{u_f}{p} = \frac{i\kappa(\omega)}{\omega\mu\phi}\sqrt{-i\omega/D + k_z^2}\frac{K_1(R\sqrt{-i\omega/D + k_z^2})}{K_0(R\sqrt{-i\omega/D + k_z^2})} \ , \tag{3.17}$$

where K_1 is the second kind modified Bessel function of order one. It is a very good approximation to replace k_z in equation 3.17 by k_{ze}, since the amplitude of their difference is considerably smaller than that of k_{ze}. Using equations 3.12, 3.13, and 3.17, and a relation following from equation 3.8

$$\nu_f^2 = \nu^2 - \nu_e^2 = k_{ze}^2 - k_z^2 \ ,$$

one gets a final expression for the Stoneley wavenumber

$$k_z = \sqrt{k_{ze}^2 + \frac{2i\rho_0\omega\kappa(\omega)}{\mu R}\sqrt{-\frac{i\omega}{D} + k_{ze}^2}\frac{K_1(R\sqrt{-i\omega/D + k_{ze}^2})}{K_0(R\sqrt{-i\omega/D + k_{ze}^2})}} \ . \tag{3.18}$$

In this manner, a simple, explicit formula for calculating Stoneley wave propagation in permeable boreholes is obtained. The Stoneley phase velocity and attenuation are calculated using

$$\begin{aligned} V_{ST} &= \omega/Re(k_z) \ , \\ Q^{-1} &= 2Im(k_z)/Re(k_z) \ . \end{aligned} \tag{3.19}$$

Equation 3.18 is the central result of this chapter. Before comparing this simple model with the complete model of the Biot-Rosenbaum theory, it is instructive to

point out the relevance of the present model to other simple low-frequency models. At low frequencies, one has in equation 3.18 that $i\omega/D \gg k_z^2$, $\kappa(\omega) \rightarrow \kappa_0$, and $k_{ze}^2 \rightarrow \rho_0\omega^2(1/K_f + 1/N)$. With these relations it can be readily seen that the present model reduces identically to Chang et al. (1988) and Norris (1989) quasi-static models. When the solid is taken as rigid, the present model reduces to the White (1983) and Hsui and Toksöz (1986) models. It is emphasized here that the major improvements of these quasi-static models by the present simple model are the use of the dynamic permeability and the Stoneley wavenumber corresponding to an equivalent elastic formation. The former parameter takes into account the frequency-dependent effects of the pore fluid flow at the borehole wall, while the latter parameter, the effects of the formation elasticity on borehole Stoneley waves. In addition, as will be shown later, the use of the latter parameter can even allow one to model Stoneley propagation in the presence of intrinsic attenuation due to the anelasticity of the formation and borehole fluid.

3.4 Comparison With Biot-Rosenbaum Model

In this section, the simple model derived in the previous section will be compared with the Biot-Rosenbaum model for the effects of frequency, permeability, porosity, and intrinsic attenuation. The cases of a hard and a soft formation will also be studied to check the applicability and limitations of the simple model. A parameter in the Rosenbaum (1974) formulation is the borehole acoustic pressure impedance factor κ . When $\kappa = 0$, the borehole fluid pressure and the formation pore fluid pressure are equal, this case being referred to as the open hole case, in which fluid flow occurs through pores that are open to the wall. With increasing κ, the pressure communication between the two fluids decreases. As κ goes to infinity there is no hydraulic exchange at the wall and this is referred to as the sealed borehole case. All examples in this study will assume the open hole case, except that the relationship

between the two models for the sealed hole case will be briefly mentioned in the following. In both models the solid frame bulk and shear moduli are calculated using (Schmitt et al., 1988; Norris, 1989)

$$K_b = (1-\phi)\rho_s(V_p^2 - 4V_s^2/3) \ , \tag{3.20}$$

$$N = (1-\phi)\rho_s V_s^2 \ , \tag{3.21}$$

where ρ_s is the density of the solid frame, V_p and V_s are the compressional and shear velocities of the dry rock. For the equivalent elastic formation, the effective P and S velocities are calculated using

$$\bar{V}_p = \sqrt{(K_e + 4N/3)/\rho_e} \ , \tag{3.22}$$

$$\bar{V}_s = \sqrt{N/\rho_e} \ , \tag{3.23}$$

where the effective density ρ_e and bulk modulus K_e of the formation are given by the Gassmann equations (Gassmann, 1951):

$$\rho_e = \phi\rho_f + (1-\phi)\rho_s \ , \tag{3.24}$$

$$K_e = K_b + \frac{(1-K_b/K_s)^2}{[\phi/K_f + (1-\phi)/K_s - K_b/K_s^2]} \ . \tag{3.25}$$

Equation 3.25 indicates that the effective bulk modulus equals the bulk modulus of the skeleton plus a fluid-dependent term. The elastic formation Stoneley wavenumber k_{ze} in equation 3.18 is calculated by substituting the above given $\bar{V}_p$ and $\bar{V}_s$, and ρ_e into the borehole dispersion equation given in equation 4.9 of Chapter 4. Interestingly, the Stoneley wavenumber k_{ze} so obtained is almost equivalent to the wavenumber corresponding to the sealed borehole case of the Biot-Rosenbaum theory. This equivalence will later be demonstrated in section 3.5, where the Stoneley velocity calculated using the above procedure is in close agreement with the velocity calculated for a non-permeable wall using the Biot-Rosenbaum theory. This is not surprising since Biot's (1956a, b, 1962a, b) theory for a porous solid is formulated on the basis of Gassmann's (1951) theory by adding fluid flow and dissipation effects (White, 1983). Without flow at the borehole wall, the Stoneley wave primarily

interacts with the fast compressional and shear waves in the formation. These two waves are little affected by the pore fluid flow effects associated with their motions, although these effects are predicted by the Biot-Rosenbaum model (see Schmitt et al., 1988), which yields some (negligibly small) attenuation for the Stoneley wave. Thus, for the sealed hole case, the above calculated k_{ze} is adequate to determine the borehole Stoneley propagation. In the open hole case, k_{ze} is substituted into equation 3.18 to calculate the Stoneley wavenumber with the fluid flow effects. The whole procedure is straightforward and much simpler than solving the borehole dispersion equation corresponding to the Biot-Rosenbaum theory (Rosenbaum, 1974). Especially in an inversion procedure where extensive computation of the forward model is required, using the present model will be much simpler and faster than using the Biot-Rosenbaum theory. In cases where one approximately knows the velocity of the Stoneley wave and only wants to know the effects of a given permeability on Stoneley waves, the calculation of k_{ze} using equation 4.9 can even be omitted. Since the velocity dispersion of the Stoneley wave due to the borehole is relatively not very significant (Cheng and Toksöz, 1981), one can substitute k_{ze} by ω/V_{ST}, where V_{ST} is a roughly measured or estimated Stoneley velocity. The Stoneley wavenumber k_z calculated in this way reflects the permeability effects relative to other effects, such as intrinsic attenuation.

In the following, the present simple model and the Biot-Rosenbaum model will be compared by numerically evaluate the models for a given set of model parameters. In all examples, the grain modulus $K_s = 3.79 \times 10^{10}$ Pa, the solid density $\rho_s = 2650$ kg/m^3, the borehole radius $R = 10$ cm, and the borehole and formation pore fluid is water with $\rho_0 = 1000$ kg/m^3, $\mu = 0.001$ Pa.s (1 cp), and $V_f = 1500$ m/s. The tortuosity α for both models is taken to be 3 (the α in equation 2.56 is equivalent to Morse's dynamic fluid-solid coupling factor E in the Rosenbaum (1974) formulation). Other parameters that vary from example to example are summarized in Table 3.1.

3.4.1 Hard Formation

A hard formation is the one whose shear wave velocity is greater than the borehole fluid velocity. This formation is important because many permeable reservoir rocks, such as sandstone, fall into this category. Another reason for studying this case is that in this formation, the rock is less compressible than the pore fluid, so that the fluid-solid coupling is not pronounced and the simple correction for the frame elasticity in the fluid diffusivity D (equation 2.66) is expected to be adequate.

The effects of the dynamic permeability in equation 3.18 are first studied, since this parameter is a major quality by which the present model differs from other quasi-static, low-frequency models. These effects can be illustrated by respectively using the dynamic permeability $\kappa(\omega)$ and the static permeability κ_0 in equation 3.18 and comparing the results against those of the Biot-Rosenbaum theory. In this comparison, a permeability $\kappa_0 = 10$ Darcy is used in the calculations. Although this value is rather high for common reservoir rocks, it serves to demonstrate the dynamic effects of $\kappa(\omega)$ in equation 3.18. Other parameters involved are given in Table 3.1. For this value of κ_0, Biot's critical frequency $f_c = \mu\phi/(2\pi\kappa_0\alpha\rho_0)$ (at f_c the viscous and the dynamic effects are comparable) is only about 1.3 kHz. But the dynamic effects occur before this frequency is reached. Figure 3-2a shows the dynamic permeability in the frequency range of [0-8] kHz. The amplitude of $\kappa(\omega)$ (solid curve) is normalized by κ_0, and its phase (dashed curve) by $\pi/2$. The static Darcy permeability (solid line) is also plotted. As seen from this figure, the amplitude decreases, and the phase increases with frequency, this behavior of $\kappa(\omega)$ being substantially different from the constant κ_0. Figure 3-2b shows the Stoneley wave attenuations calculated using equation 3.18 with $\kappa(\omega)$ (solid curve marked 'dynamic') and κ_0 (solid curve marked 'quasi-static'), respectively. The results are compared against that of the Biot-Rosenbaum model (dashed curve). Surprisingly, the result from the simple dynamic model fits that from the complete theory very well, simply because of the use of $\kappa(\omega)$. Whereas the result from using κ_0 agrees with the theory only at the low-frequency limit. It largely

over-predicts the attenuation at frequencies above 2 kHz. The difference between the dynamic and quasi-static results can be qualitatively explained by the behavior of $\kappa(\omega)$ shown in Figure 3-2a. That is, because of the decrease of $\kappa(\omega)$ with frequency, the formation is less permeable under high-frequency excitations than it is under low-frequency excitations. Figure 3-2c shows the Stoneley wave dispersions associated with Figure 3-2b. To one's satisfaction, the simple dynamic model (solid curve marked 'dynamic') agrees with the complete theory (dashed curve) fairly well, the velocity of the simple model being slightly lower than that of the Biot-Rosenbaum model. The velocity from using κ_0 is significantly lower than that of the dynamic models. This difference can be explained as follows: For the high permeability used, the dynamic (or inertial) effects of pore fluid flow are increased, which tends to decouple the borehole propagation from the formation (Schmitt et al., 1988) and the Stoneley wave velocity tends to reach the free space fluid velocity. Since these effects are accounted for by the dynamic permeability, the simple dynamic model correctly shows this tendency (i.e., the increase of Stoneley velocity). However, the use of κ_0 assumes that the pore fluid flow is still governed by viscous forces and therefore maintains significant borehole-formation coupling, resulting in lower Stoneley velocity than that of the dynamic models.

Next, the two models are compared versus frequency for a representative range of permeabilities and porosities found from typical reservoir rocks (Table 3.1). Note that the permeability here refers to the static Darcy permeability (i.e., κ_0 in equation 2.56). Figure 3-3a shows the Stoneley wave attenuations predicted by the simple model (solid curve) and the Biot-Rosenbaum model (dashed curve). The frequency range is [0-10] kHz. This is a range in which most field Stoneley wave measurements are made. A general good agreement between the two models is obtained for formations ranging from low (curve A), medium (curve B), to high (curve C) permeabilities and porosities. Figure 3-3b shows the Stoneley wave phase velocities predicted by the two models. Again, the agreement is quite good between the two models. For the

low and medium permeability (porosity) cases A and B, the agreement is excellent. For the high permeability (porosity) case C, the simple model predicts slightly lower velocity at higher frequencies than the Biot-Rosenbaum model does. This difference should be expected since the effect of fluid-solid coupling due to the relative motion of the two phases may become significant when permeability and porosity are increased. But this effect is not taken into account in the present simple model. However, these differences, as well as those shown in Figure 3-3a for the attenuation, are only of academic importance because in practice they are well within the error of Stoneley wave measurements made in the field or even in the laboratory.

As the third example, the Stoneley wave attenuations and dispersions from the two models are compared versus permeability. Figure 3-4 shows the results at 1, 2, and 5 kHz for a sandstone with 15 percent porosity. In Figure 3-4a, the agreement between the two models is quite good throughout the permeability range of [0-1000] mD for the three frequencies. The attenuations from the simple model (solid curve) and from the Biot-Rosenbaum model (dashed curve) are fairly close and show the same increasing tendency with permeability. In Figure 3-4b, the velocities from the two models are almost identical in the low permeability range up to 100 mD. This range corresponds to curves A and B in Figure 3-3b. As permeability further increases, they begin to show some differences because of the increase of the inertia coupling effect between fluid and solid in the Biot-Rosenbaum model. These differences can also be reflected in curve C of Figure 3-3b. However, as explained above, the differences of this kind are of little practical importance. What is interesting in Figure 3-4b is that the simple model even shows a complex feature of the Biot-Rosenbaum model, i.e., the increase of Stoneley velocity with permeability (an effect due to the increased pore fluid mobility, as explained above). This feature can be seen from the high permeability end of the 2 and 5 kHz curves. Although the comparisons are shown only for the permeability range of common reservoir rocks, the agreement between the two models will continue at higher permeabilities. This has been demonstrated

by the agreement shown in Figure 3-2, where $\kappa_0 = 10^4$ mD was used. Again, in complement to Figures 3-2 and 3-3, the comparison shown in Figure 3-4 confirms the validity of the simple model.

As a last example for the hard formation case, the validity of the simple model is demonstrated in the presence of intrinsic body-wave attenuation in the fluid acoustic wave and the formation shear and compressional waves. Because in the field the measured Stoneley wave attenuation is coupled with the intrinsic attenuation (Cheng et al., 1987), the latter effect must be considered for the present model to be applicable under field conditions. In the Biot-Rosenbaum model, the effects of intrinsic attenuation are taken into account by using the complex body-wave velocities. In the present model, this problem can treated in much the same way. In calculating the elastic formation Stoneley wavenumber k_{ze} in equation 3.18, one can simply introduce the effect of intrinsic attenuation by using the transformation

$$V_\gamma \rightarrow V_\gamma/(1 + i/2Q_\gamma) \ ,$$

where subscript γ can be each one of the subscripts p, s, and f, and V_γ and Q_γ correspond to V_p, V_s, V_f and their respective Q's. The anelastic body-wave dispersion can also be added as necessary. Here this minor effect is neglected. Figure 3-5 shows the comparison between the two models for the intrinsic attenuation effect. Formation and borehole fluid quality factors are taken to be $Q_p = 100$, $Q_s = 50$, and $Q_f = 20$. Other parameters involved are the same as those of curve C in Figure 3-3a, given in Table 3.1. The Stoneley attenuation due to intrinsic effects is also shown, which is nearly constant throughout the frequency range, consistent with the results of analyzing partition coefficients (Cheng et al., 1982). The total attenuation curves from the simple model (solid curve) and the Biot-Rosenbaum model (dashed curve) are seen to agree quite well, showing only slight difference in the higher frequency range. In fact, the total attenuations are almost equal to the respective sums of the attenuations due to flow (curves C of Figure 3-3a) with the intrinsic attenuation in Figure 3-5. From this example, it is seen that the effects of intrinsic attenuation are

properly handled by using the complex-valued wavenumber k_{ze} in the simple model.

3.4.2 Soft Formation

A soft formation has a shear wave velocity smaller than the fluid acoustic velocity. Because of this, the solid may have a compressibility closer to that of the pore fluid and the dynamic coupling between the two phases becomes strong, especially at high frequencies. As a result, the simple model that ignores this coupling effect may not be adequate under such conditions. This case is studied here in order to show the differences between the simple model and the Biot-Rosenbaum model in the presence of a soft formation, so that one will be aware of these differences when applying the simple model to such conditions.

Figure 3-6 shows the comparison between the simple model (solid curves) and Biot-Rosenbaum model (dashed curves) for three different soft formations given in Table 3.1. The permeabilities and porosities are the same as those used in Figure 3-3 and the curves A, B, and C have the same correspondence as in Figure 3-3. Because the effective Stoneley excitation will be shifted to a lower frequency range in the soft formation case (Cheng et al., 1982), the results in Figure 3-6 are shown only in the frequency range of [0-6] kHz. Although the attenuations in Figure 3-6a predicted by the two models are identical at low frequencies and all decrease with increasing frequency, the attenuation from the simple model is significantly over-predicted at high frequencies, compared with the attenuation from the Biot-Rosenbaum model. This indicates that the fluid flow effects are less pronounced for the soft formation case, than they are for the hard formation case. Figure 3-6b shows the Stoneley wave phase velocity from the two models. Compared to the attenuation in Figure 3-6a, the difference between the two models is less apparent from the velocities. Only the high-permeability curves C show some meaningful differences. Despite these differences, the simple dynamic model may still be a reasonably good model if one applies it to the low-frequency range (e.g., < 2 kHz in this particular case), because in the soft

formation case the Stoneley wave energy is located in a narrower low-frequency range than it is in the presence of a hard formation.

The two models are now compared versus permeability for three different frequencies of 1, 2, and 5 kHz. The porosity of the formation is 30 percent. Figure 3-7a shows the attenuations from the simple model (solid curves) and from the Biot-Rosenbaum model (dashed curves). Both attenuations increase with increasing permeability, with the simple model results higher than those of the other model. For the 1 kHz case, both results are in reasonably good agreement. As frequency increases, they begin to differ significantly. These effects can also be seen from Figure 3-6a. Figure 3-7b shows the velocities associated with Figure 3-7a. The velocities from the two models are very close at low permeabilities. They begin to differ as permeability increases. This difference also appears on curves C of Figure 3-6b. Again, the comparison in Figure 3-6 shows the applicability of the simple model at low frequencies. At higher frequencies, this model over-predicts the Stoneley attenuation, especially at high permeabilities.

3.5 Comparison With Laboratory Experimental Results

In a recently published paper, Winkler et al. (1989) showed the experimental results on the Stoneley wave propagation in permeable materials. These experiments were performed to evaluate the applicability of Biot's theory to acoustic logging in porous formations using Stoneley wave measurements. Excellent agreement was found between theory and experiment. In their experiments, they used formation materials with different permeabilities, velocities, and porosities, and fluids with high and low viscosities. By varying these parameters, they were able to conduct the experiments in both low- and high-frequency regions of Biot's theory, as well as in the intermediate transition zone. Thus, in addition to the comparison with Biot-Rosenbaum theory in the previous section, these experiments provide a further test of the simple model and

its validity in different frequency regions of Biot theory, as well as its applicability to porous materials with different properties. Four samples were measured in their experiments. Three were synthetic materials made of resin-cemented glass beads. One was a rock sample made of a Berea sandstone. All these samples were cylindrical in shape, having a diameter of 21.6 cm. A borehole was drilled along the sample axis, the diameter of the hole was 0.95 cm for the synthetic samples and 0.93 cm for the rock sample, respectively. The sample and fluid properties are given in Table 1 of Winkler et al. (1989), and are summarized in Table 3.2 of this chapter for reference. One can see from the properties given in Table 3.2 that all the samples belong to the hard formation case because their shear velocities are higher than fluid velocities. The present model has been shown to be applicable to such a formation. In Winkler et al.'s (1989) article, the experimental results were given for the Stoneley phase velocity and attenuation, which can be directly compared with the theoretical results calculated from equations 3.18 and 3.19. In the experiments, P and S velocities and density of the fluid-saturated samples were also measured, as listed in Table 3.2. One can therefore use these parameters as the effective elastic formation properties to directly calculate the elastic Stoneley wavenumber k_{ze} in equation 3.18. In addition, although the present model is for the borehole with a formation of infinite radial extent, the results still hold true for the laboratory models of finite size. This comes from the fact that the Stoneley wave is a guided wave trapped in the borehole, so that it is not sensitive to the large outer boundary of the samples, as long as the radius of this boundary (10.8 cm) is much bigger than the borehole radius (0.47 cm).

The comparison begins with sample A, saturated with high-viscosity silicon oil with $\mu = 96$ cp (Table 3.2, sample A). With this high viscosity, the pore fluid motion is controlled by viscous effects. This puts one in the low-frequency region of Biot theory. Figure 3-8a shows Stoneley velocity versus frequency. The experimental data were digitized from the published figures of Winkler et al. (1989). The theoretical curve (solid curve) is calculated using equation 3.18. The theory fits the data extremely

well. A copy of Winkler et al.'s (1989) Figure 4 is shown in Figure 3-8c and d. The theoretical curve shown in Figure 3-8c goes slightly above the data points, although this is insignificant for the confirmation of the theory. The dashed curve in Figure 3-8a is the Stoneley velocity corresponding to the sealed borehole case, which is calculated from the given parameters of the fluid-saturated sample (Table 3.2). This curve fits almost exactly with the original curve shown in Figure 3-8c which is calculated with a non-permeable borehole wall using the complete Biot-Rosenbaum theory. This is also the case for the remaining three examples. This fit indicates that when the borehole wall is sealed, the formation acts like an equivalent elastic formation with effective properties given by equations 3.22 through 3.25. The corresponding Stoneley attenuation data as $1/Q$ versus frequency are shown in Figure 3-8b. Again, the theory fits the experimental data excellently.

For the next example, the theory and experiment are compared for a sample saturated with low-viscosity fluid (Table 3.2, sample C). This low viscosity (0.818 cp) puts the experimental bandwidth in the high-frequency region of Biot theory. As seen from Figure 3-9a, the open hole Stoneley velocity crosses the sealed hole velocity at about 17 kHz. This high-frequency behavior due to the permeability effects, as predicted by Biot-Rosenbaum theory, is seen to be also predicted by the simple model, although this crossing is less significant than what is shown on Winkler et al.'s (1989) theoretical curve (Figure 3-9c), and the high-frequency portion of the simple theoretical curve goes slightly below the measured data, while the curve of Winkler et al. (Figure 3-9c) goes slightly above the measured data in the high-frequency range. The scatter of the data around 20 kHz was attributed to the mode interference due to the finite size of the sample (Winkler et al., 1989). In spite of the scatter, the theory fits the experiment very well. For the Stoneley attenuation shown in Figure 3-8b, both theory and experiment show the strong increase of attenuation as frequency decreases. The simple model predicts slightly higher attenuation than the theory of Winkler et al. (1989) shown in Figure 3-9d. However, the agreement

between the simple theory and experiment is still very good.

The third case (Table 3.2, sample B) is a sample having an intermediate viscosity. This places the experimental bandwidth in the intermediate transition region of Biot theory. The velocity and attenuation data are shown in Figure 3-10. In this case, the agreement between the theory and experiment is not as good as in the previous two examples, the same as what is shown in Winkler et al.'s (1989) results (Figure 3-10c,d). In their case, the theoretical velocity (Figure 3-10c) crosses the data at about 35 kHz and the sealed velocity at 50 kHz. Thus it is not able to fit the data. The simple model fits the high-frequency portion of the data, although the misfit in the low-frequency portion persists. The theoretical attenuation shown in Figure 3-10b is very close to that of Winkler et al. (1989) shown in Figure 3-10d. But the discrepancy between the theory and experiment is significant. The discrepancies of Figure 3-10 were attributed by Winkler et al. as due to the undetected heterogeneities in the sample or perhaps due to the behaviors of the porous material in the transition region that are not well defined in Biot theory.

The last example (Table 3.2, sample Berea S.S.) is a Berea sandstone saturated with silicone oil ($\mu = 9.34$ cp). Since this is the only case where a reservoir rock was measured, the results for this case are especially important, because a useful theory must eventually work in rocks. The properties of the sample given in Table 3.2 put the experimental bandwidth in the low-frequency range of Biot theory (Winkler et al., 1989), which is relevant to most field situations. The theoretical velocity and attenuation predicted by the simple model (shown in Figure 3-11a,b) are very close to Winkler et al.'s (1989) results (shown in Figure 3-11c,d). For both velocity and attenuation, there is an excellent agreement between theory and experiment.

The above examples show that, in general, the laboratory experimental results are in excellent agreement with the simple Stoneley propagation theory developed in this chapter. These examples substantially confirm the validity of the simple theory and its general applicability to porous media with different properties.

3.6 Discussion

In this section, the cause of disagreement between the simple model and the Biot-Rosenbaum model in the presence of a soft formation will further be explored. Discussion will also be made to show how one can incorporate the effects of a borehole logging tool into the present model.

In the formulation of the simple model, the interaction between the borehole propagation and the porous formation was split into two parts, i.e., the one due to formation elasticity and the other due to pore fluid flow. By this separation, it was implied that the pore fluid flow associated with the motion of the slow wave is not strongly coupled with the motion of the solid matrix. Strictly speaking, this is true only if the latter motion is small compared to the former motion. In fact, in a Biot solid, the effective moving fluid volume is proportional to the relative motion between the two phases

$$v \propto \phi(u_f - u_s) \ ,$$

where u_s is the displacement of the solid associated with the slow wave motion. An example of the relative motion and the associated solid displacement has recently been shown by the finite difference modeling of Zhu and McMechan (1989). In a hard formation, or in the very low frequency range in which viscous fluid flow dominates (for either a hard and a soft formation case), u_s is small compared to u_f, so that the moving volume v is dominated by the contribution from u_f. This point has been demonstrated by the agreement of the simple model with the Biot-Rosenbaum model in the presence of a hard formation and in the low-frequency range of the soft formation case. This can also be seen from Zhu and McMechan's (1989) finite difference modeling in the low-frequency region of the Biot theory, in which the solid displacement associated with the slow wave motion is indeed considerably small compared with the relative motion between fluid and solid. However, in the presence of a soft formation, the increased compressibility results in a larger u_s, hence the relative motion $u_f - u_s$ is reduced

and the effective flow volume v decreased. In terms of borehole Stoneley waves, this means that less energy will be carried away and that the attenuation will be less severe. In the Biot-Rosenbaum theory, this coupling process is modeled in the form of coupled partial differential equations. Therefore, for given porosity, permeability and pore fluid, the high-frequency Stoneley wave attenuation for a soft formation will be less pronounced than that for a hard formation (for example, one can compare the Biot-Rosenbaum results shown on Figure 3-3a and Figure 3-6a). However, in the simple model, the relative motion $u_f - u_s$ is still taken as u_f. Although the frequency dependent behavior of u_f is accounted for by using the dynamic permeability, which is independent of the solid elasticity (Johnson et al., 1987), and the effects of solid elasticity on u_f have been corrected (equation 2.65), the resulting flow volume v is still larger than it actually is because of the missing term u_s. As a result, the predicted Stoneley wave attenuation is higher than the correct result. This is indeed what one has seen in Figure 3-6a.

In the presence of a logging tool of radius a in the borehole, the present model needs two simple modifications. The first is the ratio of the boundary integral of $\psi\psi_e$ to the area integral of $\psi\psi_e$ in equation 3.12. Without the tool, this ratio is approximately the ratio of bore perimeter to bore area (i.e., $2/R$ in equation 3.13). With the tool, the area becomes that of the fluid annulus and equation 3.13 is now written as

$$\frac{\oint_S \psi\psi_e dS}{\iint_A \psi\psi_e dA} \sim \frac{2R}{R^2 - a^2}$$

Thus the resulting correction is to replace the term $2/R$ in equation 3.13 with $2R/(R^2 - a^2)$. Another modification is calculating the elastic formation Stoneley wavenumber k_{ze} in conjunction with the logging tool. This procedure has been described by Cheng and Toksöz (1981). It is worthwhile to note that in a soft formation, the presence of a logging tool will push the agreement between the simple model and the Biot-Rosenbaum model to a higher frequency range, simply because the tool reduces the effective borehole area and the wave propagation is approximately similar

to that of a borehole with smaller radius (Cheng and Toksöz, 1981).

3.7 Conclusions

In this chapter, the theory of dynamic fluid flow has been applied to the important problem of acoustic logging in porous formations. A simple dynamic theory has been developed to model Stoneley wave propagation in permeable boreholes. This model is formulated based on the dynamic hydraulic exchange between the Stoneley wave and formation pore fluid, in which the concept of dynamic permeability is used to measure the frequency-dependent fluid transport into the formation. This formulation clearly points to the physical process involved in the problem. The simple model has been compared with the exact model of the Biot-Rosenbaum theory for the effects of frequency, porosity, permeability, intrinsic attenuation, and formation type (hard or soft). It has been shown that both models yield practically the same result in the hard formation case. In a soft formation, the simple model over-predicts the Stoneley wave attenuation at higher frequencies, because the increased coupling between the solid and fluid is not fully accounted for. However, since many important permeable reservoir rocks belong to the hard formation category, this model will be of significant applicability to the estimation of formation permeability using Stoneley wave measurements, because of its simplicity and validity in the hard formation case. Comparison with the available experimental data showed the excellent agreement between the simple model and the data and further confirmed this simple theory. A further study on this theory is perhaps the application of it to formulate an inverse problem, analyze its sensitivity to each model parameter, and finally invert for the parameters (particularly the permeability) using available Stoneley measurement data.

Figure	V_p (m/s)	V_s (m/s)	ϕ (%)	κ_0 (mD)
3-2	3800	2200	25	10^4
3-3	3800	2200	5,15,25	10, 10^2, 10^3
3-4	3800	2200	15	
3-5	3800	2200	25	10^3
3-6	2300	1200	5,15,25	10,10^2, 10^3
3-7	2300	1200	30	

Table 3.1: Parameters used for comparison with Biot-Rosenbaum model. Biot's structural constant is $\sqrt{8}$, and tortuosity α is 3. Borehole and pore-fluid is water with $\rho_0 = 1000$ kg/m^3, $V_f = 1500$ m/s, and $\mu = 0.001$ Pa·s. The solid grain density ρ_s =2650 kg/m^3 and modulus K_s =37.9 GPa. The borehole radius is 10 cm.

Sample	A	B	C	Berea S.S.
ϕ (%)	26.5	22.9	22.3	21.0
κ_0 (mD)	3600	2300	1300	220
α	2.4	2.4	2.4	3.2
ρ_s (kg/m^3)	2300	2270	2290	2650
K_s (GPa)	50	50	50	37
ρ_0 (kg/m^3)	960	934	818	934
μ (cp)	96	9.34	0.818	9.34
V_f (m/s)	1014	999	926	999
Fluid-saturated sample:				
ρ_e (kg/m^3)	1940	1960	1970	2090
$\bar{V}_p$ (m/s)	2850	2930	2822	3208
$\bar{V}_s$ (m/s)	1680	1610	1665	2005

Table 3.2: Physical properties of the samples and fluids in Winkler et al.'s (1989) experiment.

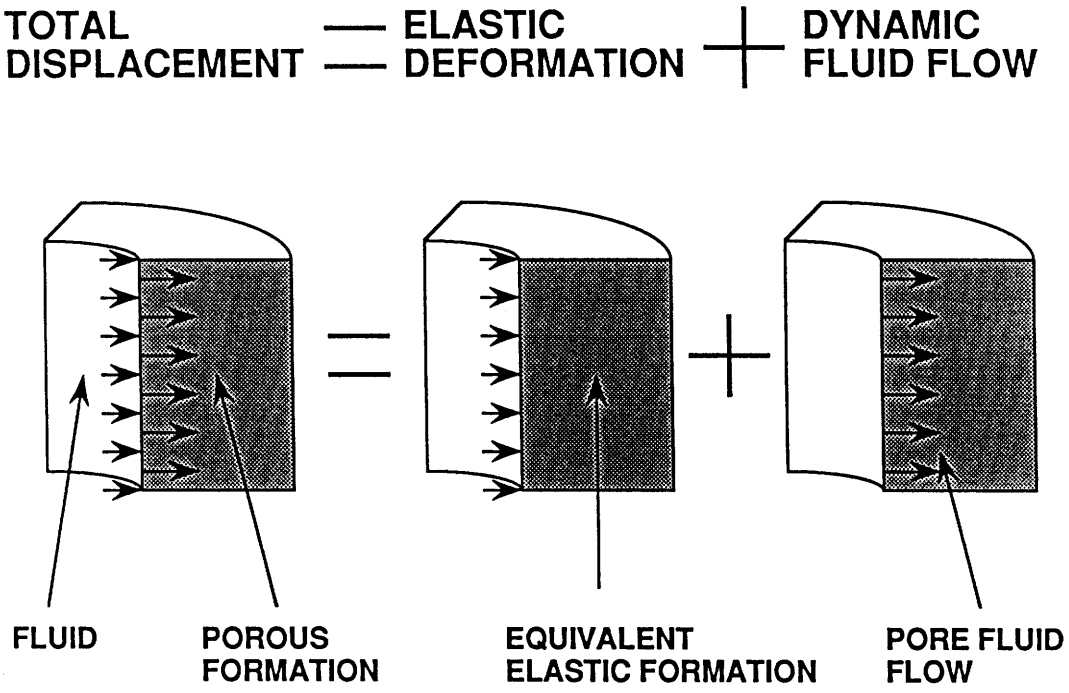

Figure 3-1: Diagram showing the two contributions to the displacement of the borehole wall. The first is the contribution due to the elastic deformation of the formation. The second is the contribution due to the dynamic fluid flow.

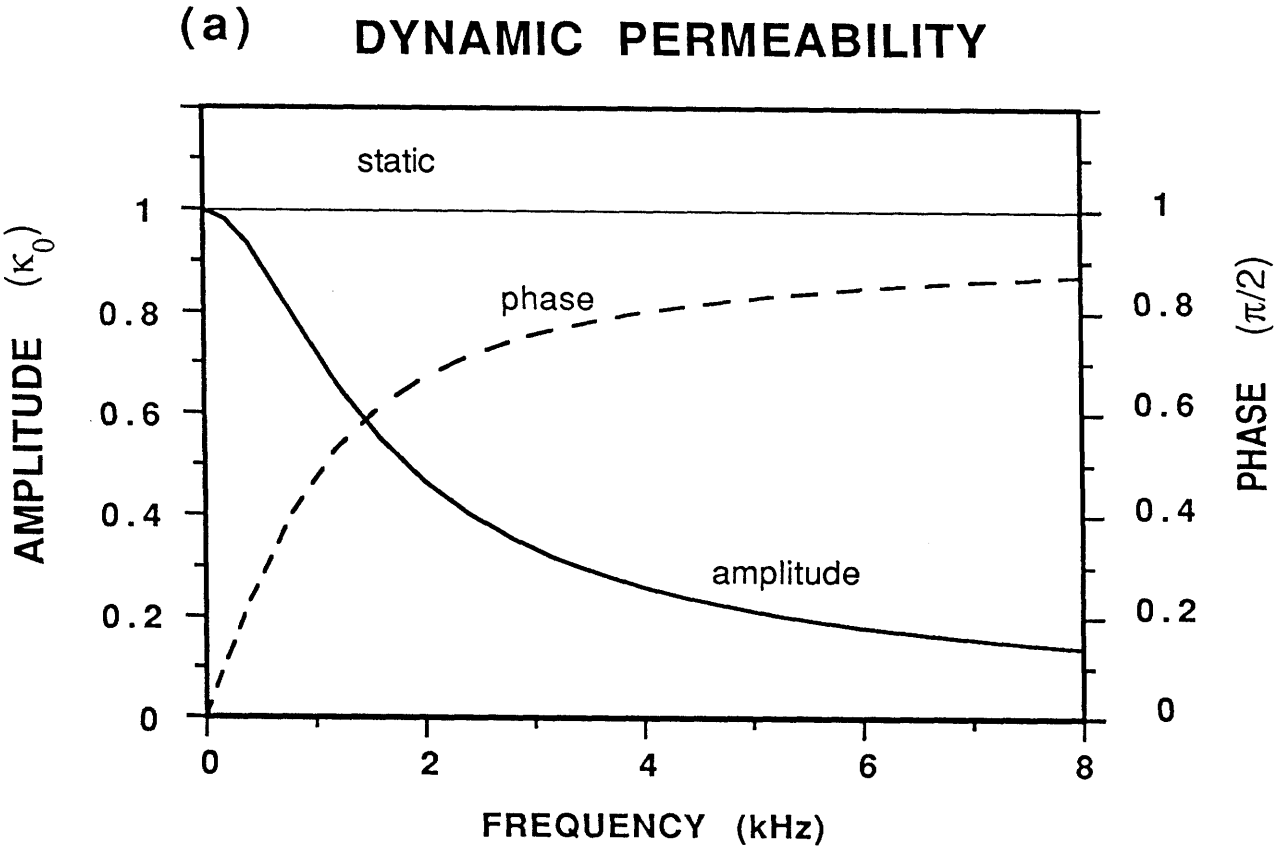

Figure 3-2: Test of effects of dynamic permeability against Biot-Rosenbaum model. (a) The dynamic permeability $\kappa(\omega)$ as a function of frequency. Its static value $\kappa_0 = 10^4$ mD. The amplitude is normalized by κ_0 and phase by $\pi/2$.

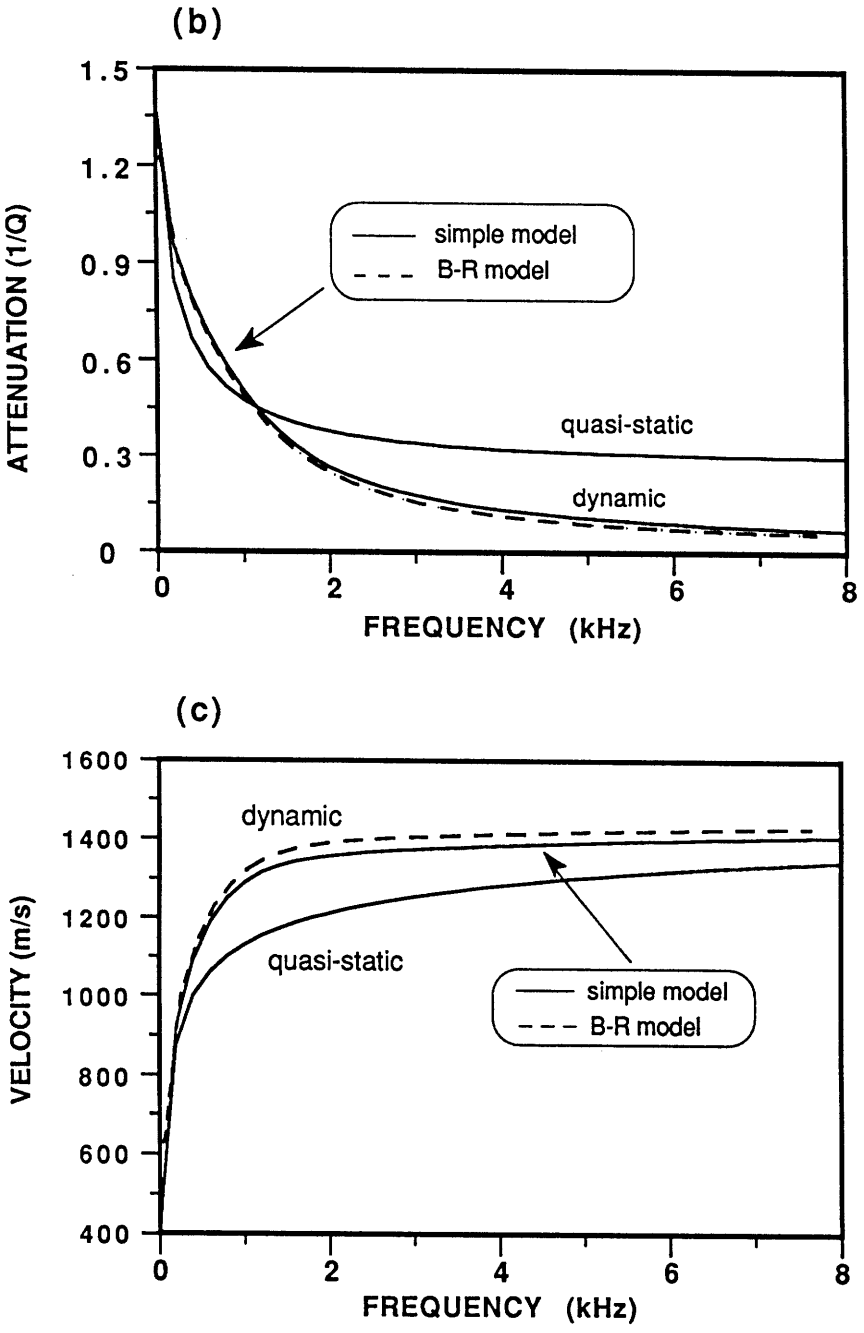

Figure 3-2: (b) Stoneley wave attenuations calculated from equation 3.18 using $\kappa(\omega)$ (solid line marked 'dynamic') and κ_0 (solid line marked 'quasi-static'), respectively. The result from the Biot-Rosenbaum theory (dashed line) is also plotted, which agrees with the simple dynamic model very well. (c) Stoneley phase velocities associated with (b). This figure shows also the agreement of the simple dynamic model with the full theory and the disagreement of the quasi-static results.

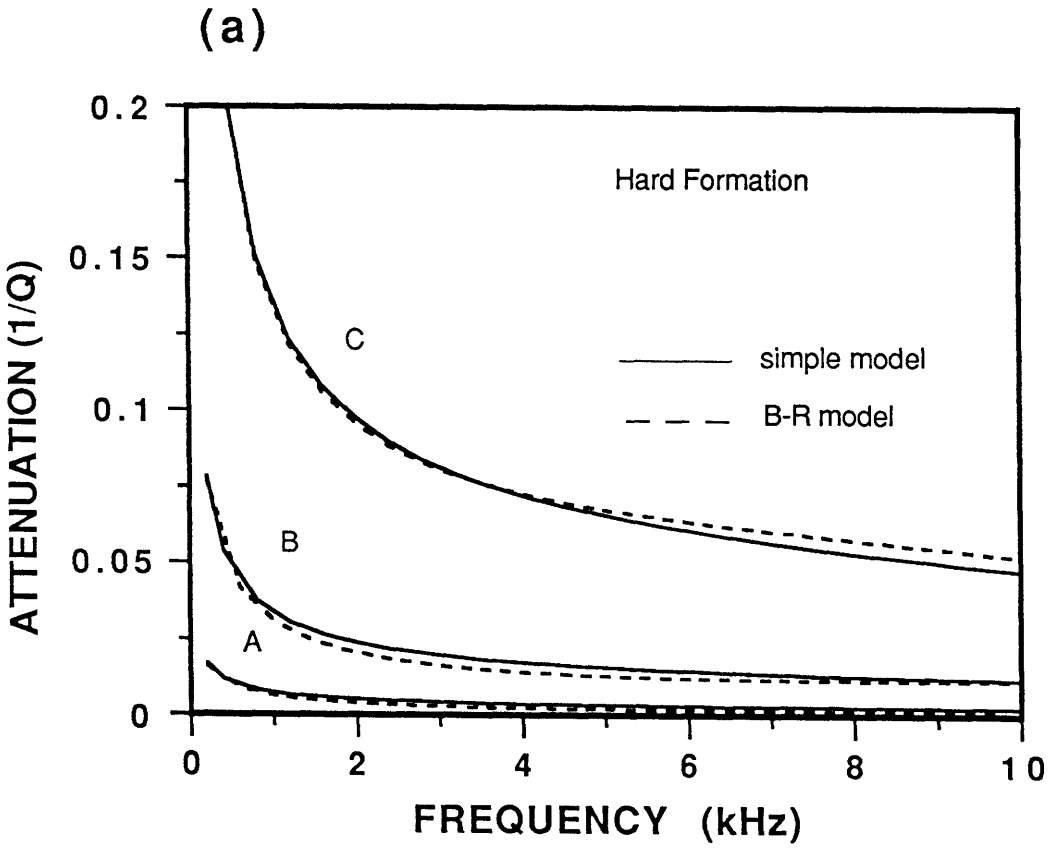

Figure 3-3: Comparison between the simple dynamic model (solid curves) and the Biot-Rosenbaum model (dashed curves) for three different (hard) formations (see Table 3.1) in the frequency range of [0-10] kHz. In both (a) and (b), curves A are for a formation with $\phi = 0.05$ and $\kappa_0 = 10$ mD, curves B are for $\phi = 0.15$ and $\kappa_0 = 100$ mD, and curves C are for $\phi = 0.25$ and $\kappa_0 = 1000$ mD. Both the Stoneley attenuation (a) and phase velocity (b) show the good agreement of the two models.

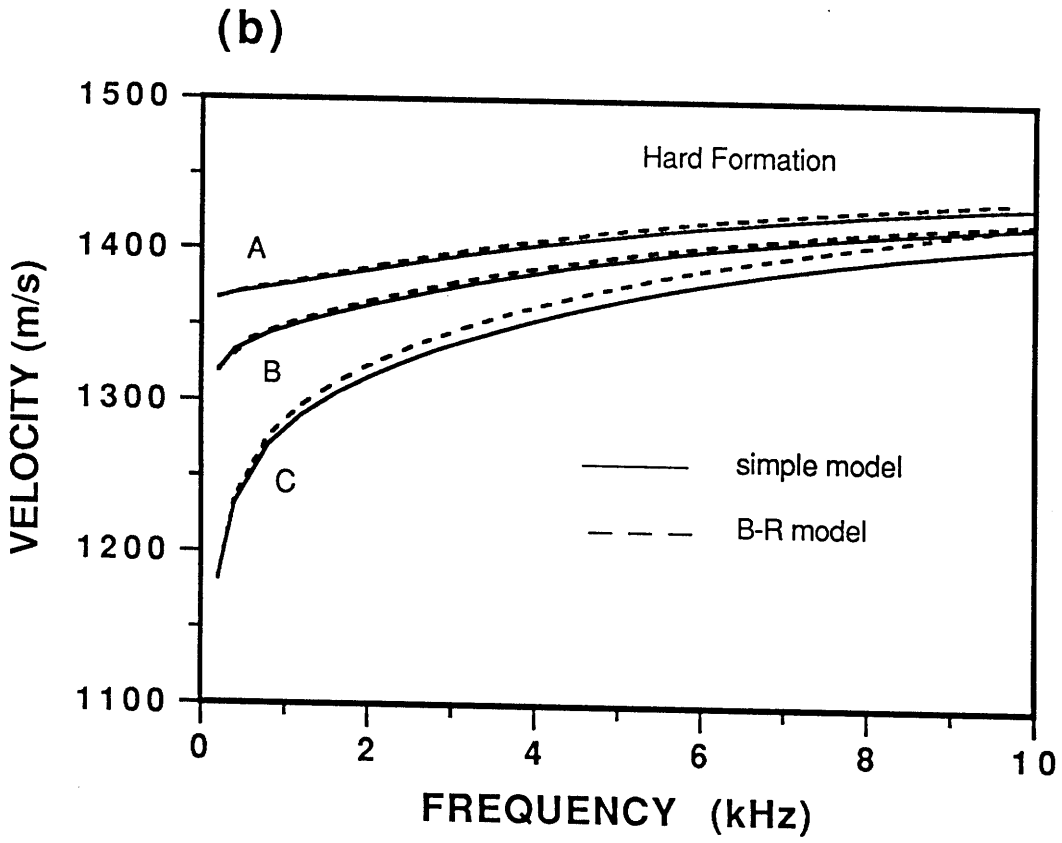

Figure 3-3: (b) Phase velocity associated with (a).

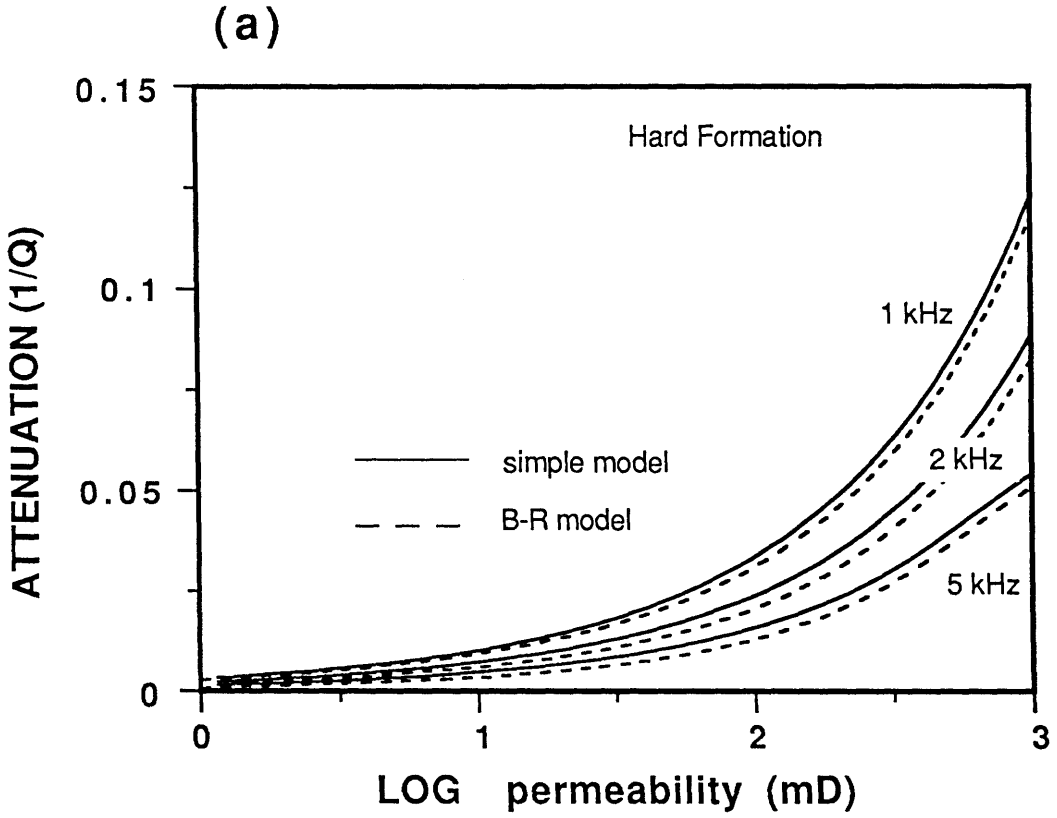

Figure 3-4: Comparison of the simple model with the Biot-Rosenbaum model versus permeability κ_0 for different frequencies. The formation is a sandstone with $\phi = 0.15$. (a) Stoneley wave attenuation. (b) Stoneley wave phase velocity. In both (a) and (b), the two models agree quite well.

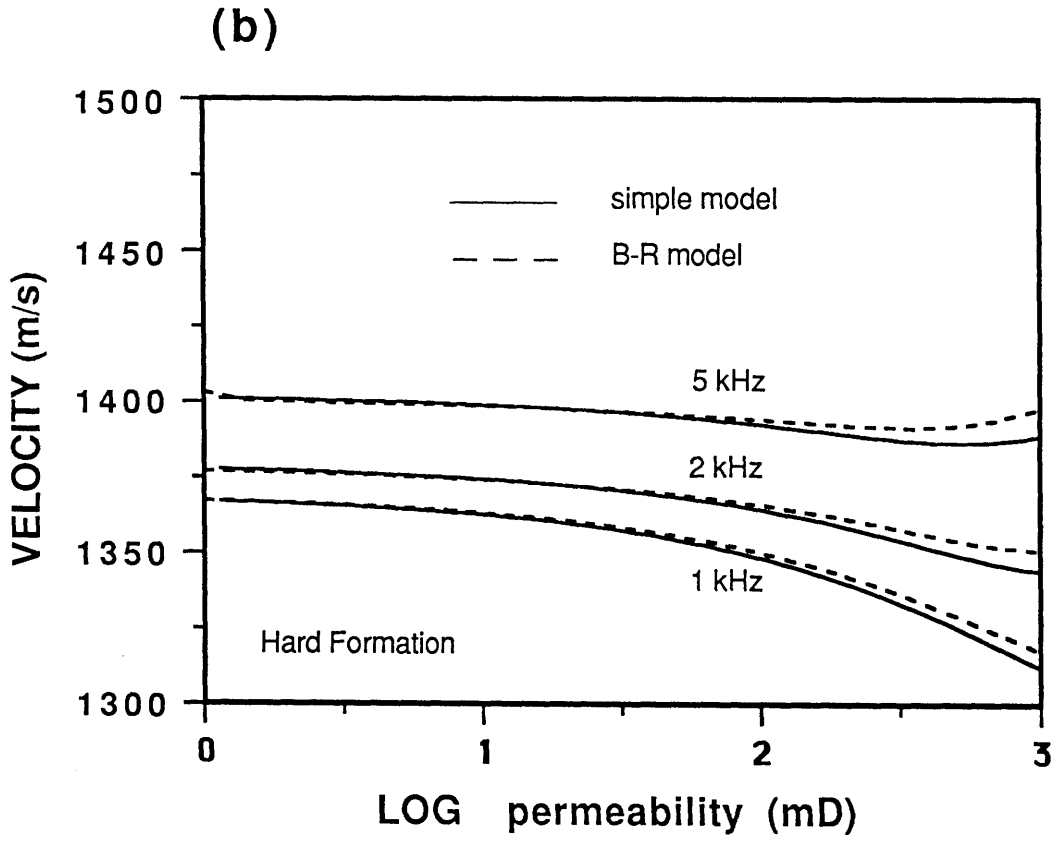

Figure 3-4: (b) Phase velocity associated with (a). Note that in (b) the simple model can even model the the slight increase of velocity with permeability (see the 5 kHz curve), a complex feature predicted by the Biot-Rosenbaum theory.

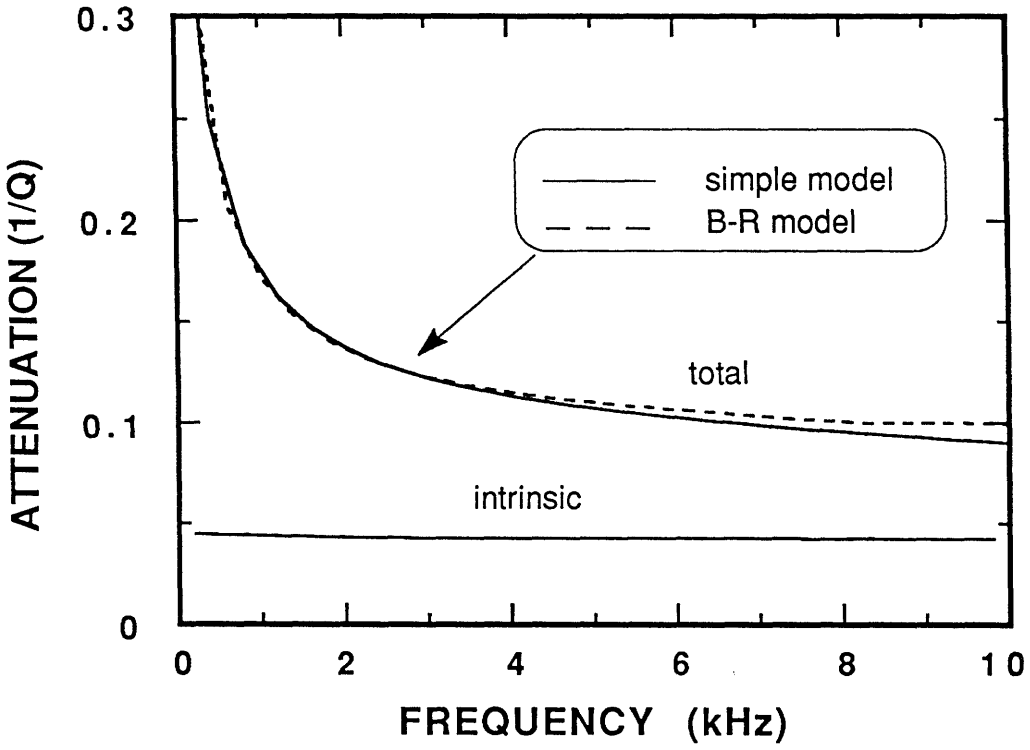

Figure 3-5: Comparison between the two models in the presence of intrinsic attenuation for a hard formation with $\phi = 0.25$ and $\kappa_0 = 1000$ mD. Intrinsic Q values are $Q_p = 100$, $Q_s = 50$, and $Q_f = 20$. The total attenuation of the simple model (solid curve) and that of the Biot-Rosenbaum model (dashed curve) are the sum of the intrinsic attenuation curve and their respective predicted attenuations due to fluid flow. The two results agree well.

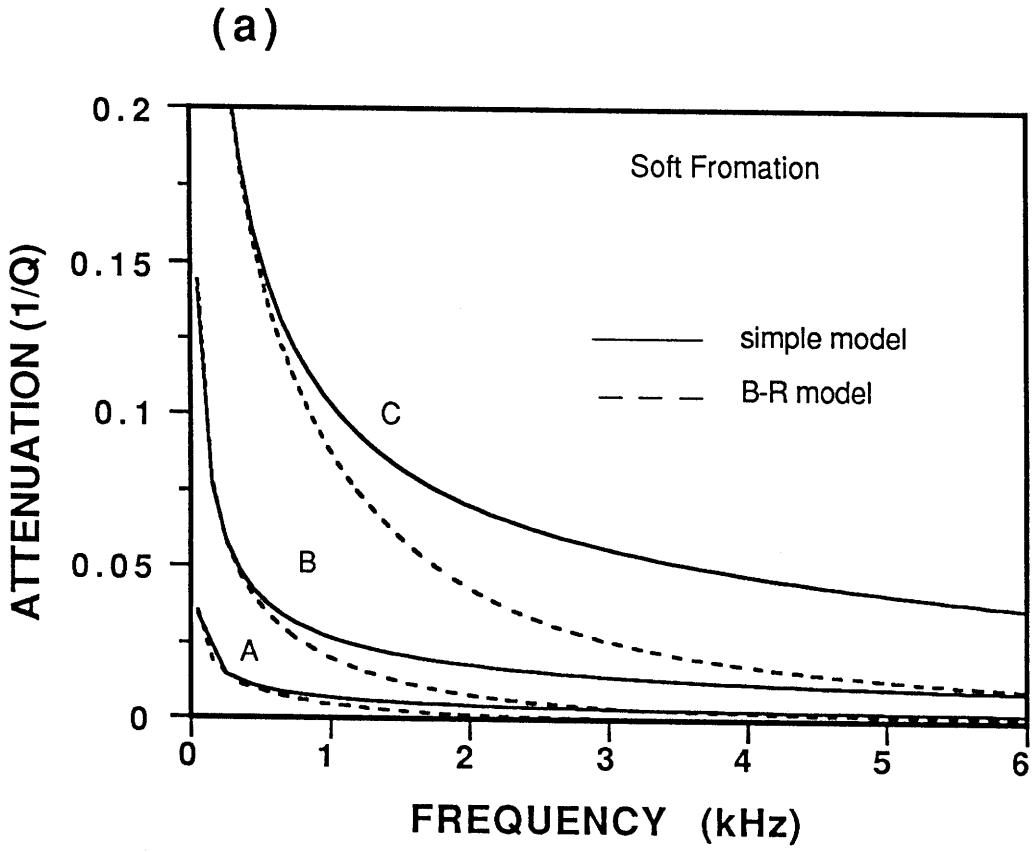

Figure 3-6: Comparison of the two models versus frequency for three different soft formations (properties given in Table 3.1). In both (a) and (b), curves A are for a formation with $\phi = 0.05$ and $\kappa_0 = 10$ mD, curves B are for $\phi = 0.15$ and $\kappa_0 = 100$ mD, and curves C are for $\phi = 0.25$ and $\kappa_0 = 1000$ mD. In (a), the attenuations from the simple model (solid curves) coincide with those from the Biot-Rosenbaum model at low frequencies, but differ from them at higher frequencies.

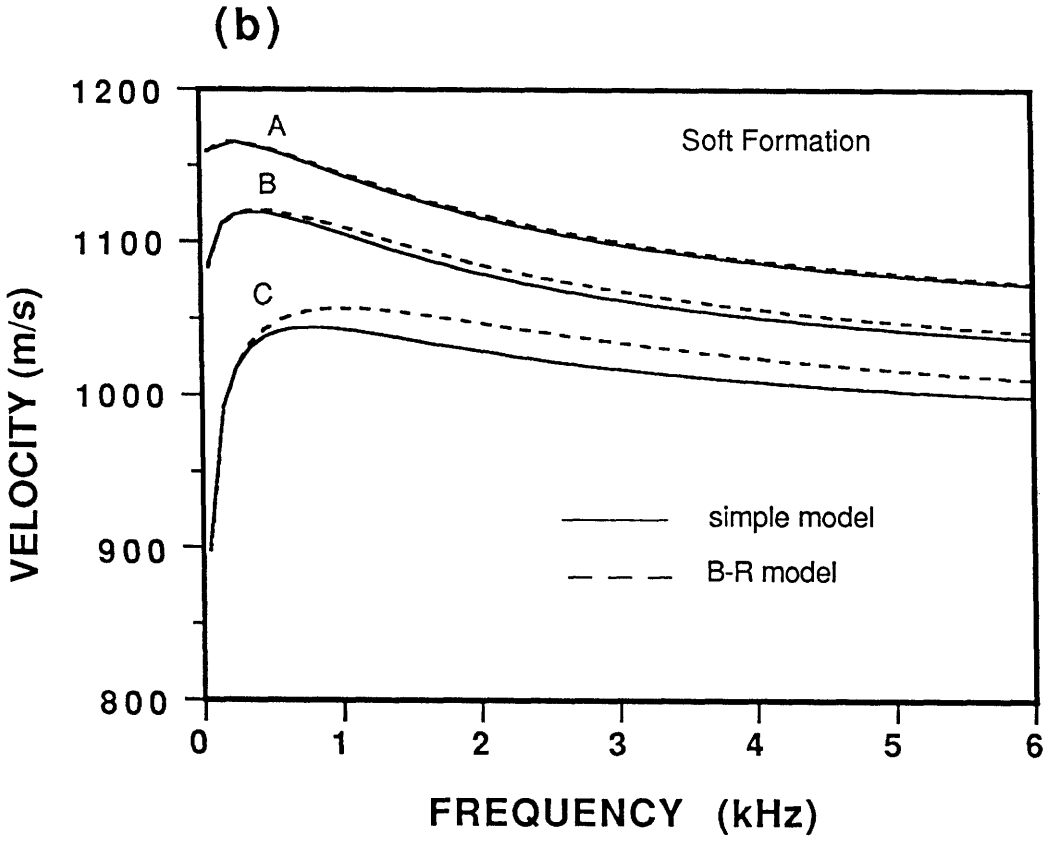

Figure 3-6: (b) Phase velocity associated with (a). The velocities from the two models agree fairly well for low permeability cases A and B. For high permeability case C, two models differ at higher frequencies.

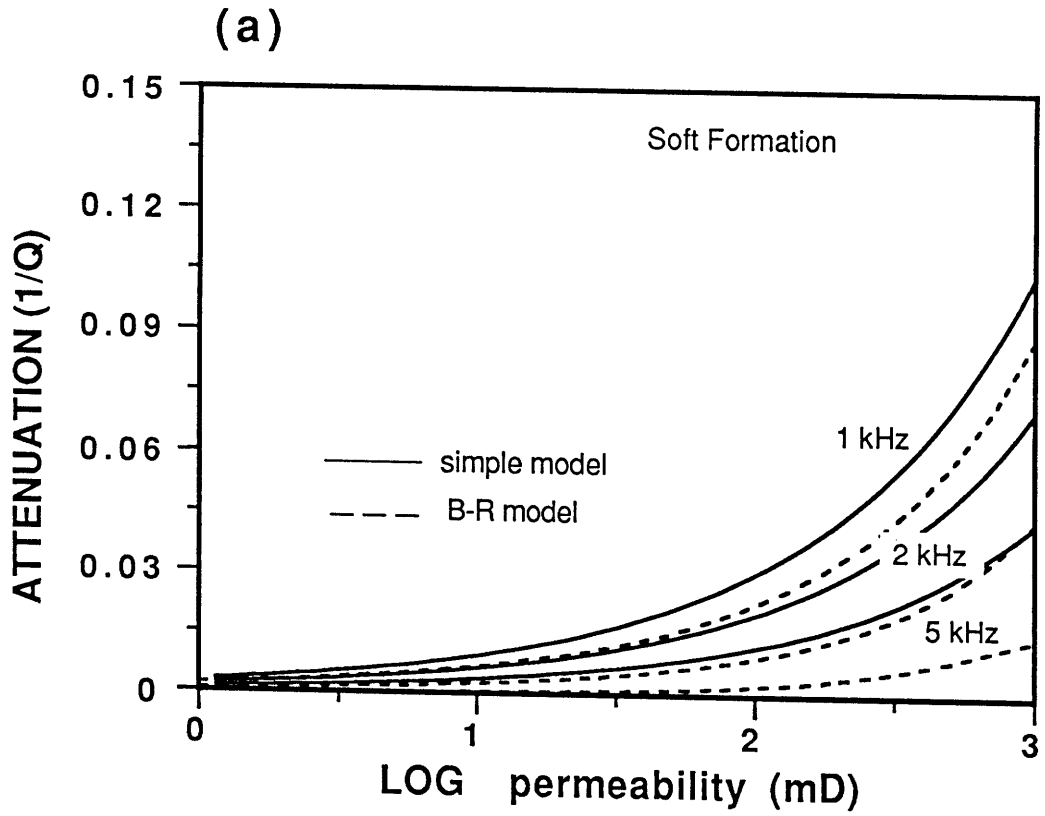

Figure 3-7: Comparison of the two models versus permeability for a soft formation case. The formation has a porosity of 30 percent. In (a), the Stoneley attenuations from the simple model (solid curves) differ from those from the Biot-Rosenbaum model, especially at higher permeabilities and frequencies.

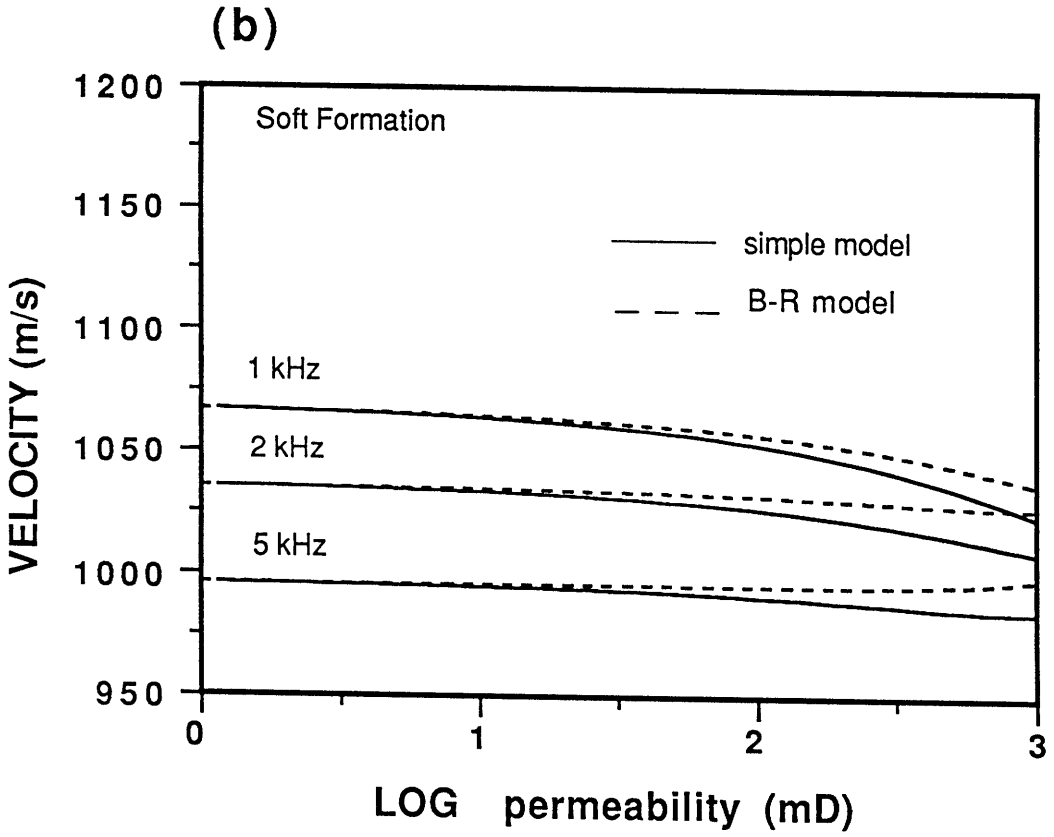

Figure 3-7: (b) Phase velocity associated with (a). The Stoneley velocities from the two models fit at low permeabilities, but begin to differ as permeability increases.

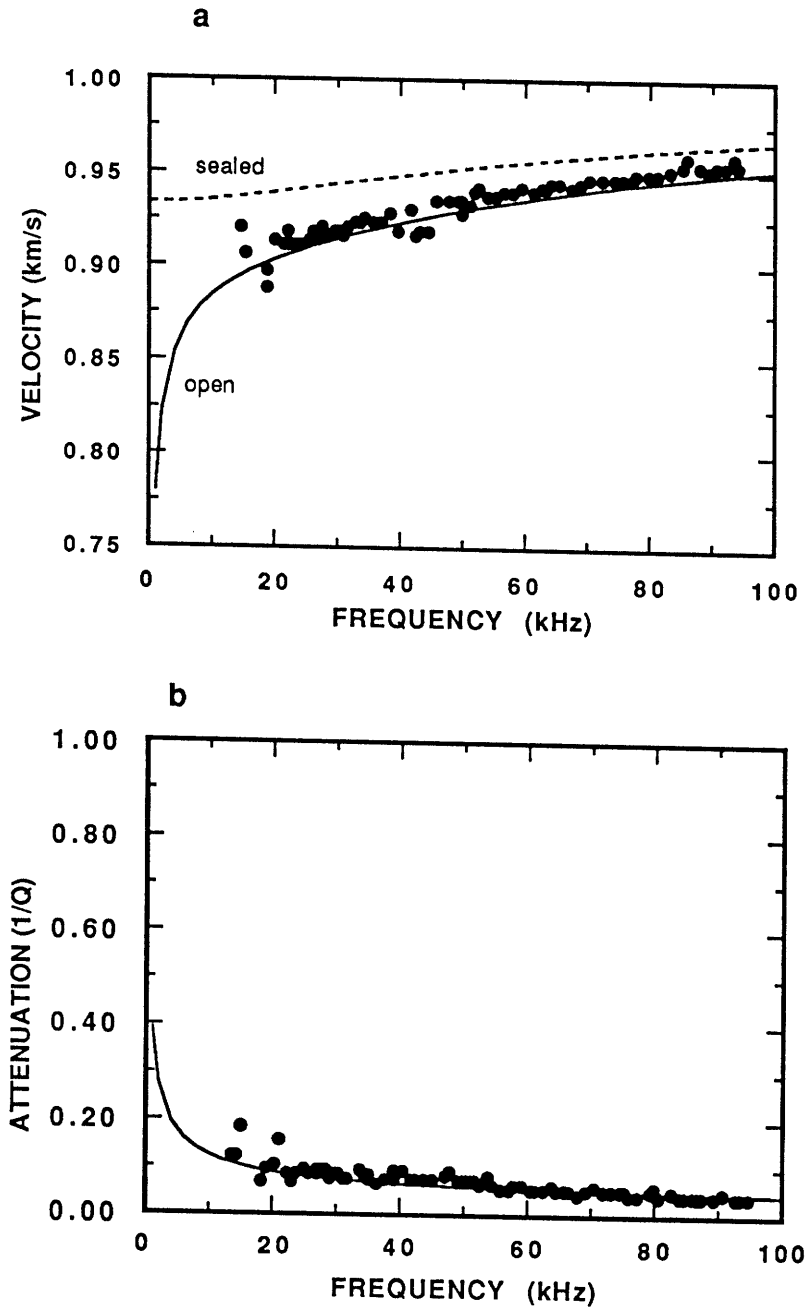

Figure 3-8: Stoneley velocity (a) and attenuation (b) versus frequency for sample A. Dots are experimental results. Solid curves are theoretical predictions from the simple model. The dashed curve in (a) is Stoneley velocity corresponding to a sealed borehole wall.

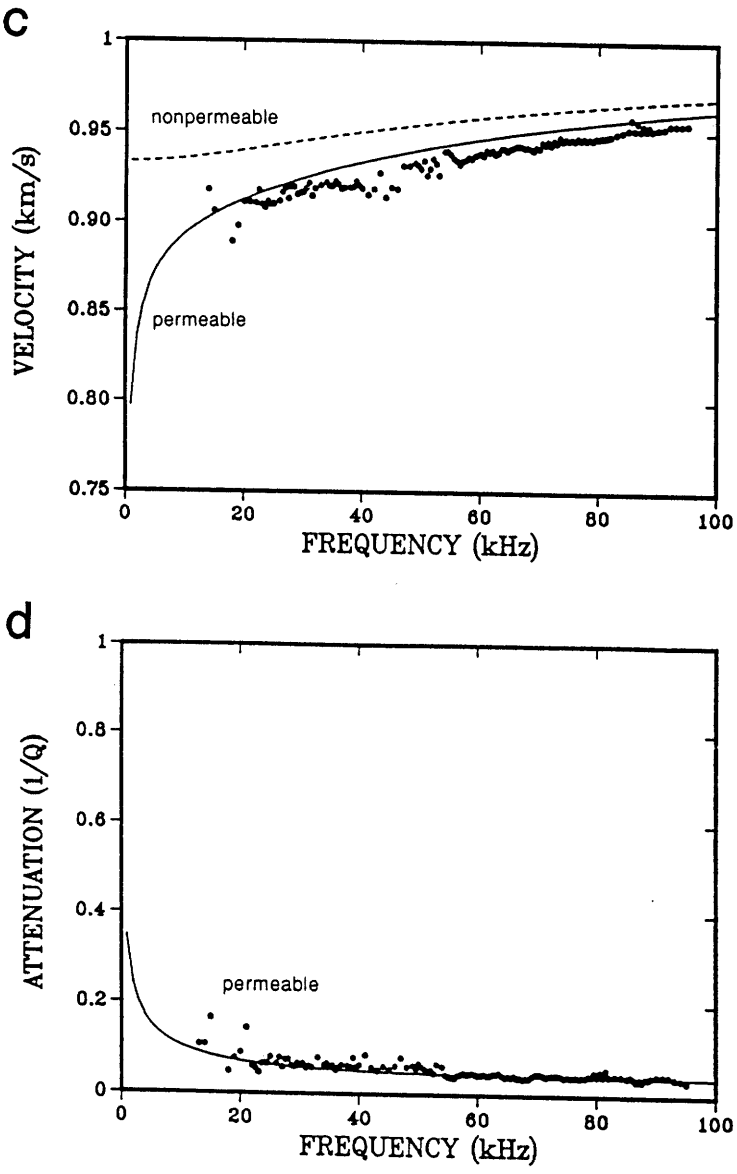

Figure 3-8: (c) and (d) Original results of Winkler et al. (1989) for sample A.

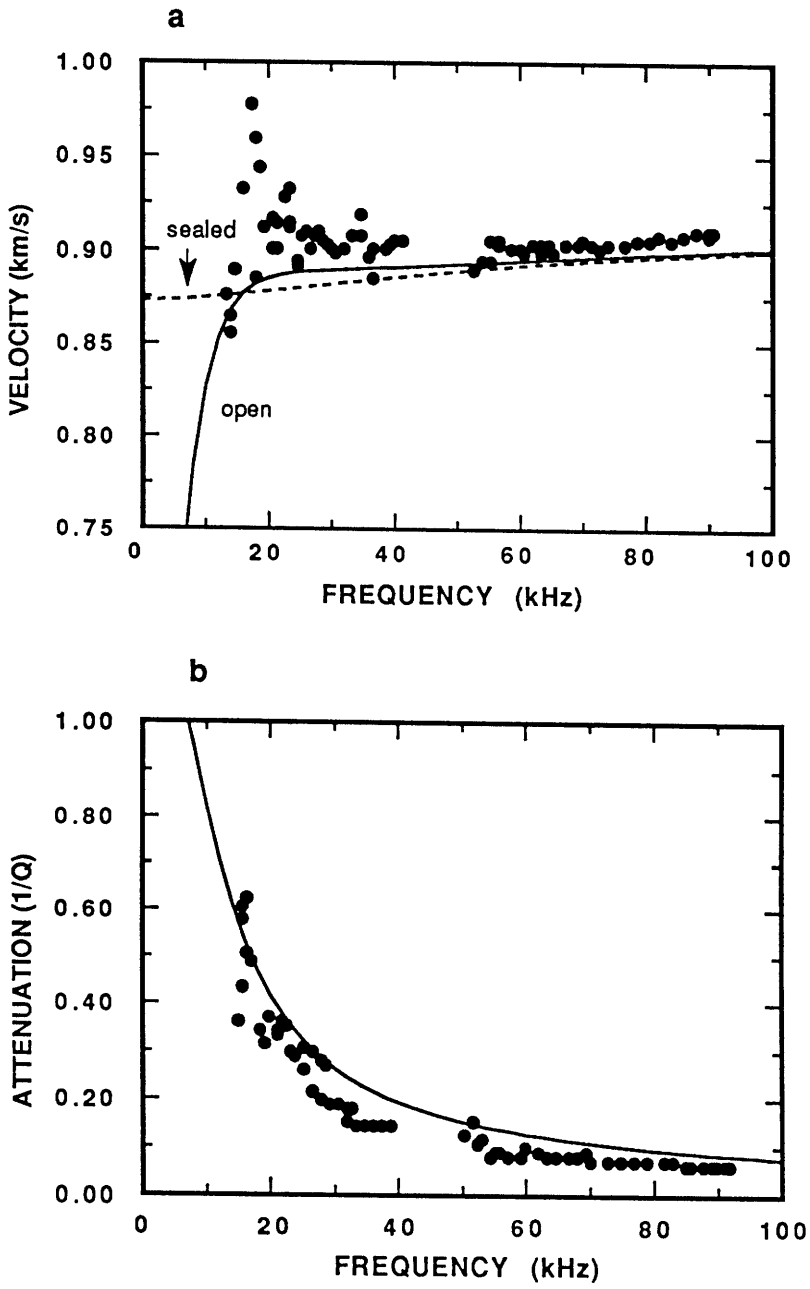

Figure 3-9: Stoneley velocity (a) and attenuation (b) versus frequency for sample C. Dots are experimental results and solid curves are theoretical predictions. The dashed curve is the sealed-hole Stoneley velocity.

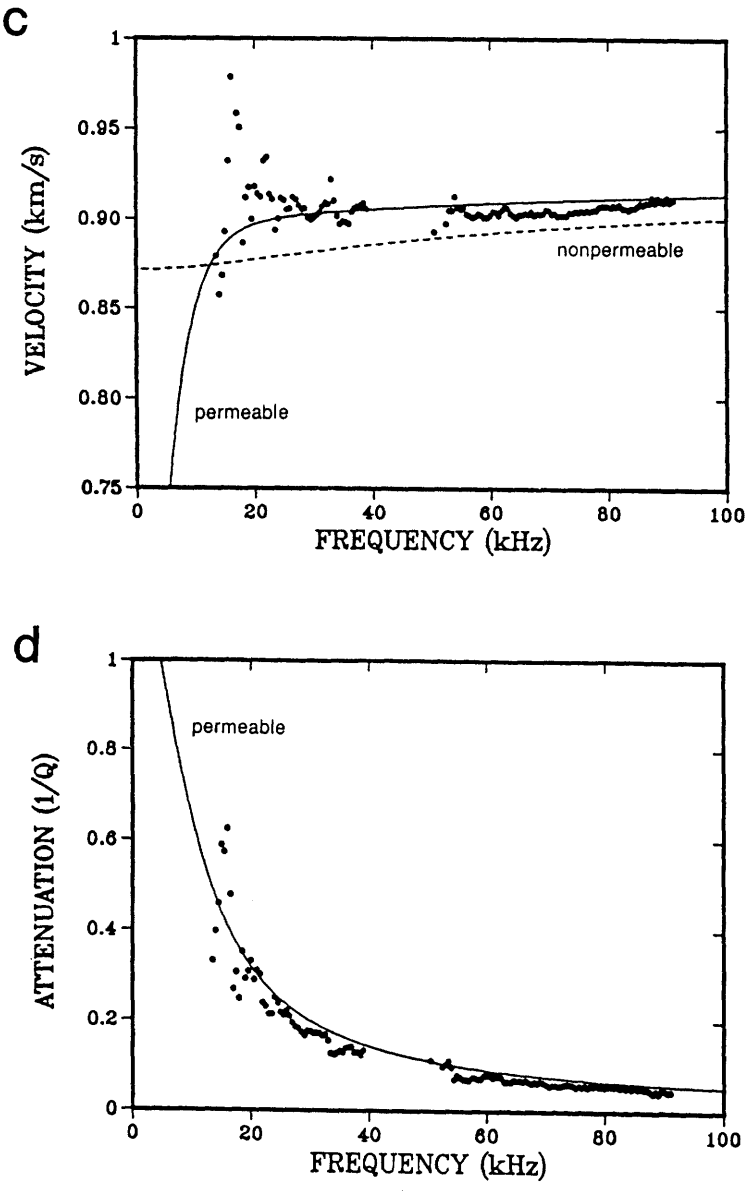

Figure 3-9: (c) and (d) Winkler et al.'s (1989) results for sample C.

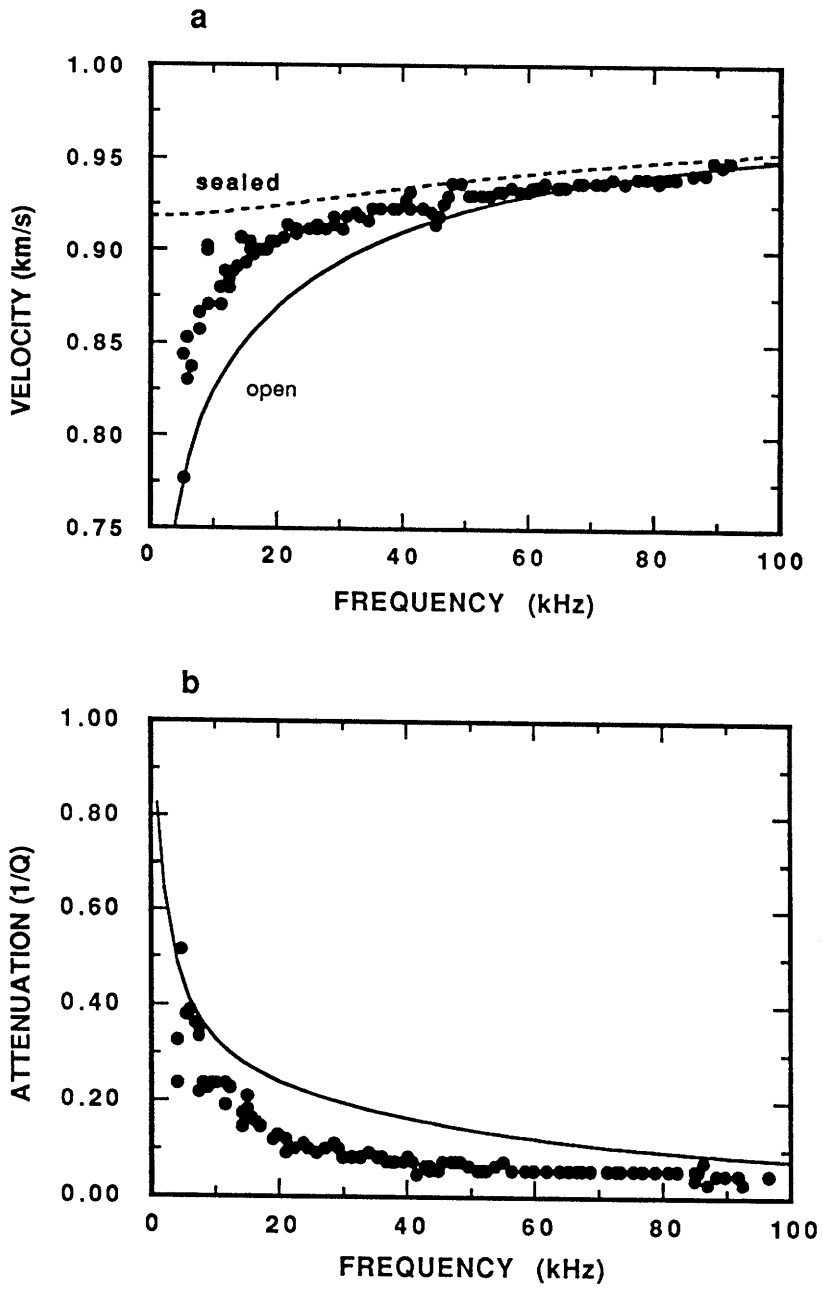

Figure 3-10: Stoneley velocity (a) and attenuation (b) versus frequency for sample B. Dots are experimental results and solid curves are theoretical predictions. The dashed curve is the sealed-hole Stoneley velocity. The data are in the transition region of Biot theory.

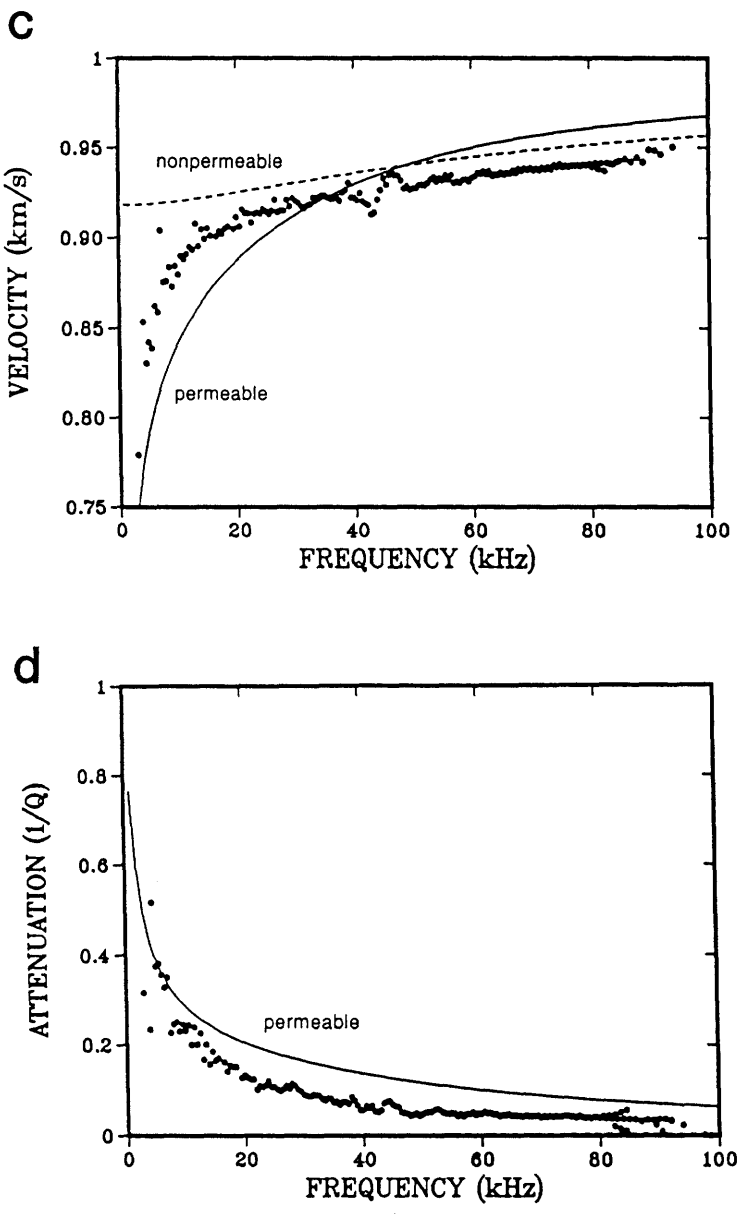

Figure 3-10: (c) and (d) Winkler et al.'s (1989) results for Sample B.

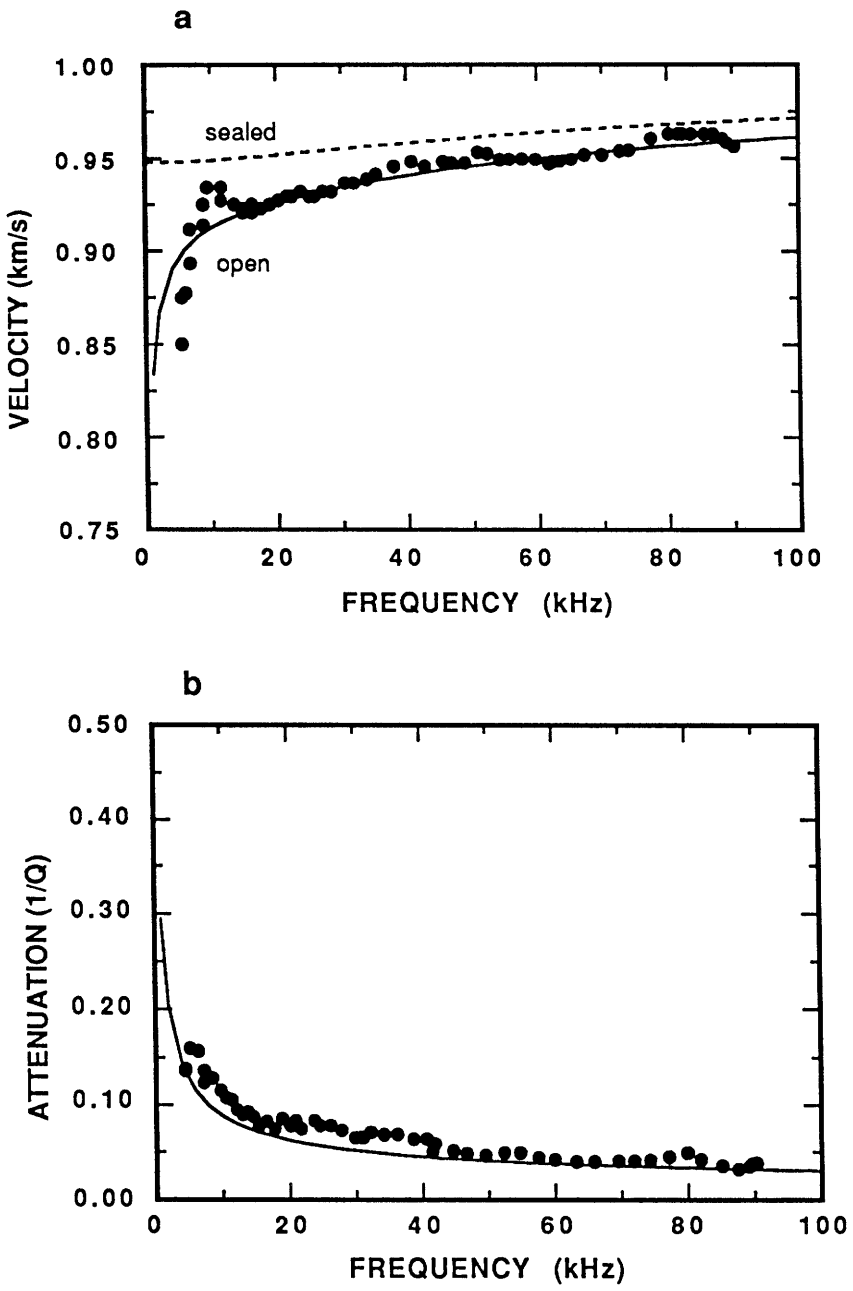

Figure 3-11: Stoneley velocity (a) and attenuation (b) versus frequency. The sample is made of a Berea sandstone. Dots are experimental results and solid curves are theoretical predictions. The dashed curve is the sealed-hole Stoneley velocity.

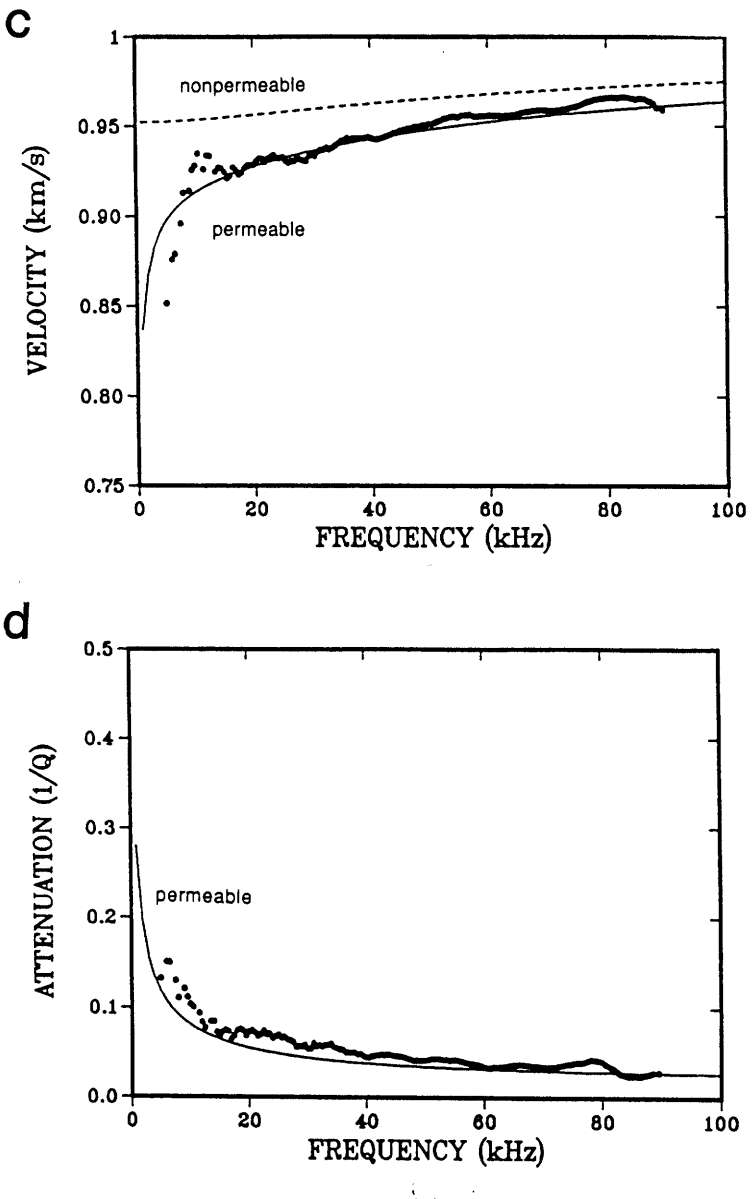

Figure 3-11: (c) and (d) Winkler et al.'s (1989) results for sample B.S.

Chapter 4

Stoneley Wave Propagation in a Fluid-filled Borehole With a Vertical Fracture

4.1 Introduction

An important application of full waveform acoustic logging is the detection of open borehole fractures. Although horizontal and inclined fractures are a common feature encountered in borehole acoustic logging, vertical fractures are of particular interest in certain situations. For example, a fracture resulting from hydraulic fracturing in oil production is often vertical, and its aperture is an important parameter that governs the amount of fluid conducted into (or away from) the borehole. The Stoneley wave has been explored as a means of fracture detection and characterization. In many situations, this wave mode is the most recognizable wave in the full waveform acoustic logs because of its relatively large amplitude and slow velocity. Based on field observations, Paillet and White (1982) have suggested that the Stoneley wave may be the portion of the full waveform which is most indicative of fracture characteristics. If the quantitative relationship between Stoneley propagation and the fracture character

can be found, it will provide a method for estimating fracture characteristics by means of Stoneley wave measurements. The objective of the study in this chapter is to develop a quantitative analysis of Stoneley propagation in the presence of a vertical borehole fracture and to provide the theoretical basis for its application to fracture detection and characterization.

Apart from its practical importance, this problem points to an interesting "leaky" wave-guide phenomenon. Because of a fracture along the borehole wall, the wave propagation is attenuated as a result of the leakage of wave energy into the fracture. Since the leakage occurs at the fractured part of the borehole wall, it is expected that the problem does not have an axial symmetry and one needs to consider azimuthal distribution of borehole wave motions. Driven by the pressure associated with the borehole waves, dynamic fluid flow occurs at the fracture opening. The amount of the flow conducted into the fracture is measured by the fracture dynamic conductivity given in Chapter 2 (equation 2.36). On the other hand, the fluid flow at the fracture opening is connected with the fluid motion in the fracture. The characteristics of the fracture fluid motion subject to the excitation of propagating borehole acoustic waves must also be understood in order to study its effects on the borehole propagation. There are two characteristics for the fracture wave motion. The first is the nature of the "slow" wave in a fracture. Ferrazzini and Aki (1987) have recently studied the dynamic wave motion in a fluid-filled fracture between two elastic solids. One significant result of their study is the nature of the slow wave existing in a fracture. Essentially, the slow wave is the fundamental mode of the fracture and is analogous to the borehole Stoneley wave. But unlike the Stoneley wave which has a finite velocity at zero frequency, the slow wave velocity goes to zero as frequency decreases. This behavior has been observed by Tang and Cheng (1988) in their laboratory experimental study. The fluid conduction in the case of an elastic fracture has been discussed in section 2.4 of Chapter 2. The modified fracture dynamic conductivity is given by equation 2.70 and will be employed to measure the dynamic fracture fluid

flow in this chapter. The second characteristic is that the fracture wave motion in the present problem propagates in two dimensions. One is in horizontal direction away from the borehole, and the other is in vertical direction complying with the borehole propagation. These characteristics and their effects on the borehole propagation will be studied in this chapter.

Owing to a discontinuity in the formation surrounding the borehole, seeking an exact solution will be a formidable task. This study therefore turns to the use of a perturbation theory. A boundary condition perturbation technique will be developed to treat the problem. This technique has been employed to treat acoustic problems involving perturbation of boundary conditions from the ideal "hard" (Neumann) or "soft" (Dirichlet) extremes (Morse and Feshbach, 1953). In the borehole propagation problem, however, the technique needs to be further developed because the boundary condition at the borehole wall is neither ideally hard nor ideally soft, due to the coupling between the borehole fluid and the elastic formation. In fact, an example of this kind was demonstrated in Chapter 3, where the boundary condition perturbation technique was applied to study the effects of fluid flow at the borehole wall. The wall was modeled as elastic. Then the elastic boundary condition was perturbed by adding the fluid flow effects. Because of the axial symmetry of that problem, the first order perturbation sufficed to yield satisfactory results. In the present problem, however, because of its non-axial-symmetric nature, the development of full perturbation series is needed to obtain convergent solutions for the azimuthal as well as axial borehole fluid motions induced by the fracture.

In the following text of this chapter, the problem is first described. Next, the elastic motion of the wall as a boundary condition in the absence of the fracture is determined. In the presence of the fracture, the fracture fluid motion excited by the borehole propagation is studied and its effect is incorporated into the boundary condition. Then the problem is formulated and solved by developing a boundary condition perturbation technique for the borehole situation. Following the solution of

the problem, numerical examples are presented for a hard and a soft formation case. Finally, the laboratory experiments are carried out and the experimental results are compared with the theoretical predictions.

4.2 Statement of the Problem

Consider a fluid-filled circular cylindrical borehole with a vertical fracture. The fracture is a vertical formation discontinuity having an aperture L, is filled with fluid, and intersects the borehole diametrically (Figure 4-1). The formation outside the borehole consists of a homogeneous isotropic elastic solid with density ρ, compressional velocity V_p, and shear velocity V_s. The borehole and the fracture are filled with the same fluid with density ρ_f and acoustic velocity V_f. The formation can be either hard ($V_p > V_s > V_f$) or soft ($V_p > V_f > V_s$) with respect to the borehole fluid.

A cylindrical coordinate system (r, θ, z) will be used, with z coinciding with borehole axis that is taken to be vertical, r is the radial distance from the center of the borehole, and θ the angle measured from the radial direction that points into the fracture (Figure 4-1). In the borehole fluid, the fluid displacement potential Ψ satisfies the wave equation

$$\frac{1}{r}\frac{\partial}{\partial r}(r\frac{\partial \Psi}{\partial r}) + \frac{1}{r^2}\frac{\partial^2 \Psi}{\partial \theta^2} + \frac{\partial^2 \Psi}{\partial z^2} + k_0^2 \Psi = 0 \ , \tag{4.1}$$

where $k_0 = \omega / V_f$ is the acoustic wavenumber of the fluid and ω is the angular frequency. This equation is similar to equation 3.1 in Chapter 3, but now the second derivative of Ψ with respect to θ is considered in order to account for the azimuthal fluid motion induced by the fracture. The fluid displacement $\vec{U}$ and pressure P are given by

$$\vec{U} = \nabla \Psi \ , \tag{4.2}$$

$$P = \rho_f \omega^2 \Psi \ . \tag{4.3}$$

For a propagation along the positive z direction, Ψ can be written as:

$$\Psi(r,\theta,z) = \psi(r,\theta)\exp(ik_z z) \ , \tag{4.4}$$

where k_z is axial wavenumber. Substitution of equation 4.4 into equation 4.1 results in

$$\nabla_t^2 \psi + \kappa^2 \psi = 0 \ , \tag{4.5}$$

where

$$\nabla_t^2 = \frac{1}{r}\frac{\partial}{\partial r}(r\frac{\partial}{\partial r}) + \frac{1}{r^2}\frac{\partial^2}{\partial \theta^2} \tag{4.6}$$

is the two-dimensional Laplace operator, and $\kappa = \sqrt{k_0^2 - k_z^2}$ is the radial wavenumber. Equation 4.5 will be solved in conjunction with the boundary condition at the borehole wall.

In the absence of a vertical discontinuity in the elastic formation, solutions have long been available for wave motions both in the formation solid and in the borehole fluid (Biot, 1952; Cheng and Toksöz, 1981). The two solutions are matched at the borehole wall using continuity conditions. Consequently, the elastic motion of the wall is specified. The known wall motion may be treated as a boundary condition prescribed at the borehole boundary. In the presence of the vertical fracture, this boundary condition will be perturbed. To know the extent to which the boundary condition is changed, one needs to study the fluid motion in the fracture and its interaction with the borehole fluid motion. The effect of this change in the boundary condition on the borehole Stoneley propagation will be investigated by means of the boundary condition perturbation technique.

4.3 Boundary Condition Without Fracture

For a fluid-filled borehole of radius R in an unfractured elastic formation, the elastic motion at the wall may now be prescribed as a boundary condition for the borehole fluid motion. According to equations 4.2, 4.3, and 4.4, one may relate the potential

$\psi(r,\theta)$ and its radial derivative through the following equation

$$\frac{\partial\psi}{\partial r} - (\rho_f\omega^2\frac{U}{P})\psi = 0 \ . \tag{4.7}$$

where U is the radial fluid displacement. At the radial boundary $r = R$, one has the continuity of radial stress and displacement. These conditions can be expressed through a match of the wall impedance (Biot, 1952)

$$\frac{P}{U} = -\frac{\sigma}{U_w} \ , \tag{4.8}$$

where σ and U_w are the elastic radial stress and displacement at the borehole wall, respectively. Equation 4.8, together with the condition that the elastic shear stress vanish at the wall, leads to a dispersion equation given by (Cheng et al., 1982)

$$\frac{I_0(fR)}{fI_1(fR)} = \frac{\rho}{\rho_f l}\left\{\frac{2V_s^2 lg}{k_z^2c^2}\left[\frac{1}{gR} + \frac{2V_s^2}{c^2}\frac{K_0(gR)}{K_1(gR)}\right] - (\frac{2V_s^2}{c^2} - 1)^2\frac{K_0(lR)}{K_1(lR)}\right\} \ , \tag{4.9}$$

with the radial wavenumbers l, g, and f given as

$$l = k_z\sqrt{1 - \frac{c^2}{V_p^2}} \ , \quad g = k_z\sqrt{1 - \frac{c^2}{V_s^2}} \ , \quad f = k_z\sqrt{1 - \frac{c^2}{V_f^2}} \ , \tag{4.10}$$

where I_0 and I_1 are the first kind, and K_0 and K_1 are the second kind modified Bessel functions of order zero and one, respectively. The parameters V_p, V_s, V_f, ρ, ρ_f, and R have all been defined previously. The phase velocity of wave modes is c. Equation 4.9 has an infinite number of solutions for c, giving rise to different wave modes. Specifically, for a hard formation, an infinite number of pseudo-Rayleigh (or normal) modes exist (Biot, 1952; Cheng and Toksöz, 1981), while for a soft formation, an infinite number of leaky-P modes exist (Paillet and Cheng, 1986). In both situations, a fundamental mode – Stoneley mode exists for all frequencies. Depending on whether the mode velocity c is greater or smaller than the fluid acoustic velocity V_f, equation 4.7, evaluated at $r = R$, can be written as

$$\frac{\partial\psi}{\partial r} - \left[\frac{fI_1(fR)}{I_0(fR)}\right]\psi = 0 \ , (c < V_f, \quad \text{Stoneley mode}) \tag{4.11}$$

$$\frac{\partial\psi}{\partial r} + \left[\frac{fJ_1(fR)}{J_0(fR)}\right]\psi = 0 \ , (c > V_f, \quad \text{other modes}) \tag{4.12}$$

where J_0 and J_1 are the first kind Bessel functions of order zero and one, respectively. Equations 4.11 and 4.12 can be readily derived by noting that the solution for ψ is

$$\psi = CI_0(fr) \ , \qquad (c < V_f)$$
$$\psi = CJ_0(fr) \ , \qquad (c > V_f)$$

where C is an arbitrary constant. Substitution of the given function of ψ into equations 4.2 and 4.3 gives the wall impedance P/U in equation 4.7, from which equations 4.11 and 4.12 are obtained. It is noted that equation 4.11 or 4.12 has the form of the conventional mixed (or the third) boundary condition. A somewhat "unconventional" point in this boundary condition is that the coefficient in front of ψ assumes different values depending on different wave modes determined by equation 4.9. However, as one will see later, since the perturbation theory applies to one particular wave mode (e.g., Stoneley mode in the present study), equation 4.11 or 4.12 can still be treated as the conventional mixed boundary condition for this particular wave mode.

4.4 Boundary Condition With Fracture

In the presence of the vertical fracture, the boundary condition at the borehole wall will be perturbed. It is assumed here that significant change in the boundary condition occurs mainly at the fracture opening, so that the boundary condition (for the Stoneley) away from the fracture can still be approximated by equation 4.11. This assumption is based on the laboratory experimental observation (which will be shown later) that the Stoneley velocity along a fractured borehole does not differ significantly from that along an unfractured borehole. This indicates that the boundary condition as a whole is not significantly changed and the change should be mainly at the fracture opening. Therefore, for the solid part of the borehole wall one can still write

$$\frac{\partial \psi}{\partial r} - h_0 \psi = 0 \ , \quad \text{(solid part of the wall)} \tag{4.13}$$

where $h_0 = fI_1(fR)/I_0(fR)$. Whereas for the fluid part of the wall where the fracture opening is located, the boundary condition will be determined by the interaction between the borehole and the fracture fluid systems. When a borehole acoustic wave propagates along the fracture opening, wave motion will be excited in the fracture, which in turn will affect the borehole propagation. For this reason, one needs to know how much motion is excited. Using the theory of dynamic conductivity developed in Chapter 2, a quantitative measure is given for the amount of fluid flow conducted into the fracture opening.

$$Q = -\bar{C}\frac{\partial P}{\partial y} \ , \tag{4.14}$$

where Q is the volume flow rate per unit fracture length, $\frac{\partial P}{\partial y}$ is the dynamic pressure gradient normal to the fracture opening. $\bar{C}$ is the dynamic conductivity governed by both effects of viscous shear at the fracture surface and wave propagation along the fracture. It has been shown in Chapter 2 that, when the viscous skin depth $\delta = \sqrt{2\nu/\omega}$ (ν = kinematic viscousity) is small compared to the fracture aperture L, $\bar{C}$ is given by a simple formula (equation 2.38)

$$\bar{C} = \frac{iL}{\omega\rho_f} \ , \ (L \gg \delta) \ . \tag{4.15}$$

As discussed in section 2.4 of Chapter 2, this equation holds true regardless whether the fracture surface is rigid or elastic. At logging frequencies between [0.1-8] kHz for the Stoneley wave, δ is the order of 10 μm to 100 μm, depending on viscosity. The fracture aperture of interest here is the order of millimeter to centimeter. Thus the use of equation 4.15 is well justified. Therefore, viscous effects will be neglected for the present study. The determination of the pressure gradient in equation 4.14 needs the knowledge of fluid motion in the fracture which will be studied in the following section.

4.4.1 Fracture Wave Excited by Borehole Propagation

Consider the Cartesian coordinate system (x, y, z) shown in Figure 4-1, where the fracture surfaces are located at $x = -L/2$ and $x = L/2$, z is parallel with the borehole axis, and y is measured from the fracture opening and is pointed into the fracture. The fracture fluid pressure P_f satisfies the scalar wave equation

$$\nabla^2 P_f + k_0^2 P_f = 0 \ , \tag{4.16}$$

where

$$\nabla^2 = \frac{\partial^2}{\partial x^2} + \frac{\partial^2}{\partial y^2} + \frac{\partial^2}{\partial z^2} \ .$$

In terms of P_f, the fluid displacement is given by

$$\vec{U}_f = \frac{\nabla P_f}{\rho_f \omega^2} \ . \tag{4.17}$$

In the elastic solid bonding the fracture, a general solution to the vector equation of motion can be written as (Pilant, 1979)

$$\vec{u} = \nabla\Phi - \nabla \times \nabla \times (\vec{e}_x \Omega) + \nabla \times (\vec{e}_x \Lambda) \ , \tag{4.18}$$

where $\vec{u}$ is the elastic displacement, $\vec{e}_x$ is the unit vector along x axis, and Φ, Ω, and Λ satisfy the following wave equations:

$$\begin{aligned} \nabla^2\Phi + \frac{\omega^2}{V_p^2}\Phi &= 0 \ , \\ \nabla^2\Omega + \frac{\omega^2}{V_s^2}\Omega &= 0 \ , \\ \nabla^2\Lambda + \frac{\omega^2}{V_s^2}\Lambda &= 0 \ . \end{aligned} \tag{4.19}$$

They represent P-wave, SV-wave, and SH-wave motions, respectively. The elastic stresses σ_{ij} are given by the constitutive relation for an isotropic elastic solid:

$$\sigma_{ij} = \lambda(\frac{\partial u_k}{\partial x_k})\delta_{ij} + \mu(\frac{\partial u_i}{\partial x_j} + \frac{\partial u_j}{\partial x_i}) \ , \tag{4.20}$$

where δ_{ij} is the Krokener delta and λ and μ are elastic moduli; $x_1 = x$, $x_2 = y$, and $x_3 = z$; σ_{ij} $(i, j = 1, 2, 3)$ represents the stress system (σ_{xx}, σ_{yy}, σ_{zz}, σ_{xy}, σ_{xz},

σ_{yz}). Because of a propagating borehole pressure wave $P(\omega)\exp(ik_z z)$ along the fracture opening, the propagation in the fracture has two components. The first is the propagation along z direction to comply with the borehole propagation, given by $\exp(ik_z z)$. The second is the propagation towards y direction, denoted by $\exp(ik_y y)$. The latter propagation is initiated by the pressure difference between the borehole and the fracture fluid. Taking this two-dimensional propagation into account and considering the fact that the borehole pressure $P(\omega)$ is symmetric with respect to x, one has solutions to equations 4.16 and 4.19 in the form of

$$\begin{bmatrix} P_f \\ \Phi \\ \Omega \\ \Lambda \end{bmatrix} = \begin{bmatrix} P_{f0}\cos qx \\ \Phi_0 e^{-q_p|x|} \\ \Omega_0 e^{-q_s|x|} \\ \Lambda_0 e^{-q_s|x|} \end{bmatrix} \exp(ik_y y)\exp(ik_z z) \ , \tag{4.21}$$

where

$$q = \sqrt{\frac{\omega^2}{V_f^2} - k_y^2 - k_z^2} \ , \quad q_p = \sqrt{k_y^2 + k_z^2 - \frac{\omega^2}{V_p^2}} \ , \quad q_s = \sqrt{k_y^2 + k_z^2 - \frac{\omega^2}{V_s^2}} \ .$$

Substitution of the solutions in equations 4.21 into equations 4.17, 4.18, and 4.20 yields fluid displacement in fracture and elastic stresses and displacement in solid. The boundary conditions at solid-fluid interfaces $x = \pm L/2$ are the vanishing of shear stresses

$$\begin{aligned} \sigma_{xy} &= 0 \ , \\ \sigma_{xz} &= 0 \ , \end{aligned} \tag{4.22}$$

and the continuity of normal stress and displacement. This continuity condition can be expressed by an impedance equation (Ferrazzini and Aki, 1987)

$$\frac{P_f}{U_f} = -\frac{\sigma_{xx}}{u_x} \ , \quad (x = \pm L/2) \ . \tag{4.23}$$

Equations 4.22 result in the vanishing of SH-wave motion in the elastic solid (i.e., $\Lambda_0 = 0$). This is to be expected since the type of coupling between solid and fluid as stated in equations 4.22 and 4.23 only allows P-SV waves to exist. Equations 4.22

and 4.23 lead to the following dispersion equation:

$$\cot\left(\frac{L\omega}{2v}\sqrt{\frac{v^2}{V_f^2}-1}\right)=\frac{\rho V_s^4\sqrt{v^2/V_f^2-1}}{\rho_f v^4\sqrt{1-v^2/V_p^2}}\left[\left(2-\frac{v^2}{V_s^2}\right)^2-4\sqrt{1-\frac{v^2}{V_s^2}}\sqrt{1-\frac{v^2}{V_p^2}}\right], \tag{4.24}$$

where v is the phase velocity of the wave modes existing in the fracture and cot represents the cotangent function. The same dispersion equation has been obtained by several authors (Ferrazzini and Aki, 1987; Paillet and White, 1982) for one-dimensional propagation cases. As the above derivations show, this dispersion equation holds true for general two-dimensional propagation cases. One only needs to notice that the fracture wavenumber k determined by equation 4.24 is related to k_y and k_z via

$$k=\frac{w}{v}=\sqrt{k_y^2+k_z^2}\ . \tag{4.25}$$

The wave modes determined by the dispersion equation (equation 4.24) have been experimentally confirmed by a laboratory measurement (Tang and Cheng, 1988). Analogous to the dispersion equation (equation 4.9) for the borehole modes, equation 4.24 results in an infinite number of normal or leaky-P wave modes, depending on whether the solid is hard or soft with respect to the fracture fluid. In particular, a fundamental mode analogous to the borehole Stoneley mode exists for all frequencies. However, the velocity of this fundamental mode goes to zero at very low frequencies (see Tang and Cheng, 1988) while the velocity of the borehole Stoneley mode approaches a finite value. Although a number of wave modes may exist in the fracture, the fundamental mode is the most important one which one is interested in. It is assumed that the borehole pressure is nearly uniform over the fracture aperture, since the aperture is generally small compared to the borehole perimeter. If the formation is rigid, the uniform pressure at the opening excites only the fundamental mode in the fracture. It is reasonable to assume that the borehole pressure will mostly excite the fundamental fracture wave mode when the formation is elastic. This assumption has been verified by numerically evaluating the amplitude of each mode excited by an uniform pressure at the opening. It was found that the fundamental mode indeed

dominates even in the case of a soft elastic formation. One therefore needs only to consider the interaction of the fundamental fracture wave mode with the borehole propagation. When the fundamental mode velocity is found by solving equation 4.24, the fracture fluid wavenumber is given by

$$k_{fr} = \frac{\omega}{v} \ . \tag{4.26}$$

Like what was done for the fracture fluid pressure in Chapter 2, the fracture pressure in equation 4.21 is averaged over the fracture aperture L and is matched with the borehole pressure $P(\omega, R)$ at the fracture opening. By doing so, it is readily shown that the pressure gradient in equation 4.14 (averaged over the fracture aperture) is given by

$$\frac{\partial P}{\partial y} = ik_y P(\omega, R) \ , \tag{4.27}$$

where

$$k_y = \sqrt{k_{fr}^2 - k_z^2} \ . \tag{4.28}$$

A few remarks will help to illustrate the interaction between the fundamental fracture wave and the borehole propagation. The wave front in the fracture has an angle $\alpha = sin^{-1}(k_y/k_{fr})$ with respect to the wave front in the borehole. As has been mentioned before, at very low frequencies, the fracture wave velocity goes to zero, while the (unfractured) borehole Stoneley velocity approaches a finite value. Thus $k_{fr} \gg k_z$ and $\alpha \rightarrow \pi/2$. The borehole pressure pushes the fluid radially into the fracture, causing strong interaction between the two fluid systems. Whereas at high frequencies, both the fracture and the borehole velocities approach the Stoneley velocity along the fluid-solid interface (i.e., Scholte velocity, for the borehole case see Cheng and Toksöz, 1981; for the fracture case see Ferrazzini and Aki, 1987). Thus $k_y \sim 0$ and $\alpha \rightarrow 0$; the fracture wave motion is nearly in phase with the borehole propagation, resulting in minimal interaction. It is therefore expected that the effects of the fracture will be more significant at low frequencies than at higher frequencies.

4.4.2 Boundary Condition for Entire Wall

With $\bar{C}$ and $\frac{\partial P}{\partial y}$ known, equation 4.14 can be used to determine the average radial fluid displacement $\overline{U}$ at the fracture opening. Since Q, the unit-length flow rate, is the integral of flow velocity (given by $-i\omega U$) over the aperture L, the average displacement is given by

$$\overline{U} = \frac{Q}{-i\omega L} = \frac{ik_y}{\rho_f \omega^2} P(\omega, R) \ . \tag{4.29}$$

By using equation 4.7, equation 4.29 can be expressed in terms of the displacement potential ψ.

$$\frac{\partial \psi}{\partial r} - ik_y \psi = 0 \ , \quad \text{(at fracture opening)} \ . \tag{4.30}$$

Combining equations 4.13 and 4.30, one can write the boundary condition for the entire borehole wall as

$$\frac{\partial \psi}{\partial r} - h_0 \psi + (-ik_y + h_0) W(\theta) \psi = 0 \ , \quad (\text{at } r = R) \tag{4.31}$$

where

$$W(\theta) = \begin{cases} 1 \ , & -L/(2R) \leq \theta \leq L/(2R) \\ 1 \ , & \pi - L/(2R) \leq \theta \leq \pi + L/(2R) \\ 0 \ , & \text{otherwise} \end{cases}$$

Because the coefficient in front of ψ is the function of the azimuthal variable θ in this boundary condition, equation 4.5 cannot be solved using the conventional method of separation of variables. One therefore has to seek approximate solutions using the perturbation theory.

4.5 Formulation of Boundary Condition Perturbation

For a perturbation theory, the term $(-ik_y + h_0)W(\theta)$ in equation 4.31 may be treated as a perturbation to the original boundary condition $\partial_r \psi - h_0 \psi = 0$. Although this

term may not be a small quantity at the fracture opening, the fracture aperture is generally small compared to the borehole perimeter, such that its overall effect on the borehole propagation is a perturbation. It is therefore convenient to consider the solutions to the unperturbed boundary value problem as basis functions

$$\begin{cases} \nabla_t^2 \phi_{mn} + \kappa_{mn}^2 \phi_{mn} = 0 & , \\ \partial_r \phi_{mn} - h_0 \phi_{mn} = 0 & , \ (\text{at } r = R) \end{cases} \tag{4.32}$$

where κ_{mn}'s are the eigenvalues of the problem, and ϕ_{mn} are the associated eigen functions that form a complete orthogonal set. Using the conventional method of separation of variables (Morse and Feshbach, 1953), solutions of equation 4.32 are readily found, as given by

$$\phi_{mn} = \frac{1}{\sqrt{\pi N_{mn} \epsilon_m}} \left\{ \begin{array}{c} \cos m\theta \\ \sin m\theta \end{array} \right\} J_m(\gamma_{mn} \frac{r}{R}) \ , \tag{4.33}$$

with

$$\left\{ \begin{array}{ll} m = & 0, 1, 2, \cdots \\ n = & 1, 2, 3, \cdots \end{array} \right. \quad \text{and} \quad \epsilon_m = \left\{ \begin{array}{ll} 2 & m = 0 \\ 1 & m > 0 \end{array} \right. ,$$

where

$$N_{mn} = \frac{R^2}{2} \left\{ [J'_m(\gamma_{mn})]^2 + (1 - \frac{m^2}{\gamma_{mn}^2})[J_m(\gamma_{mn})]^2 \right\} \tag{4.34}$$

is the normalization factor, J_m is the mth order Bessel function of the first kind, and

$$\gamma_{mn} = \kappa_{mn} R$$

is the nth root of the following equation:

$$\gamma \frac{dJ_m(\gamma)}{d\gamma} - h_0 R J_m(\gamma) = 0 \ . \tag{4.35}$$

This equation is obtained from the boundary condition of equation 4.32. Equation 4.35 gives a set of eigenvalues κ_{mn} and determines their associated eigen functions ϕ_{mn} (equation 4.33). Note that $h_0 R$ in this equation has to be found by solving the borehole dispersion equation for the Stoneley mode. Consequently, the set $\{\phi_{mn}\}$

can be regarded as the sub-set (or sub-modes) of the Stoneley mode (Analogously, there are sub-modes for the pseudo-Rayleigh modes and leaky-P modes). The non-dimensional quantity $h_0R = fRI_1(fR)/I_0(fR)$ depends on the formation and fluid properties. In fact, it characterizes the compliance of the borehole wall with respect to the borehole fluid. Figure 4-2 shows h_0R as the function of frequency for both hard and soft formations surrounding a fluid-filled borehole of a given radius. As shown in this figure, h_0R is small for a hard formation and large for a soft formation. In the extremely hard formation case, h_0R approaches zero and equation 4.35 corresponds to the rigid boundary condition. For this case, the roots of $J'_m(\gamma) = 0$ are available (Abramowitz and Stegun, 1970). For an elastic formation of finite rigidity, h_0R has a finite value and the roots of equation 4.35 have to be determined for the different values of h_0R. What makes equation 4.11 or 4.35 special is the negative sign in front of the coefficient of ψ or of $J_m(\gamma)$. In this place, the commonly encountered third boundary condition has a positive sign. Doak and Vaidya (1970) have studied the behavior of the roots of the equation 4.35 type equation. Based on their results, one can draw the following two useful properties.

- For $n = 1$, γ_{m1} is imaginary if $h_0R > m$ and is real if $h_0R \leq m$.
- For $n > 1$, all γ_{mn}'s are real regardless whether $h_0R > m$ or $h_0R \leq m$. They are interplaced with the roots of $J'_m(\gamma) = 0$.

Thus if γ_{mn}'s are real, they can be found by solving equation 4.35 using the roots of $J'_m(\gamma) = 0$ as an initial guess. While when $\gamma_{m1} = i\bar{\gamma}_m$ is imaginary, $\bar{\gamma}_m$ can be found as the single root of

$$\bar{\gamma}\frac{dI_m(\bar{\gamma})}{d\bar{\gamma}} - h_0RI_m(\bar{\gamma}) = 0 \ , \tag{4.36}$$

where I_m is the mth order modified Bessel function of the first kind, resulting from the imaginary argument of J_m. The fact that γ_{mn} has imaginary solutions indicates the presence of the Stoneley type modes in the sub-set $\{\phi_{mn}\}$ (the Stoneley has a radial function of I instead of J). In this case, $\{\phi_{mn}\}$ still forms a complete, orthogonal real

set (Watson, 1941). With a slight modification, this set can be written as

If γ_{mn} is real:

$$\phi_{mn} = \sqrt{\frac{2}{\pi R^2 \epsilon_m}} \frac{\gamma_{mn}}{\sqrt{\gamma_{mn}^2 + (h_0 R)^2 - m^2}} \left\{ \begin{array}{c} \cos m\theta \\ \sin m\theta \end{array} \right\} \frac{J_m(\gamma_{mn} r/R)}{J_m(\gamma_{mn})} \quad . \tag{4.37}$$

If γ_{m1} is imaginary:

$$\phi_{m1} = \sqrt{\frac{2}{\pi R^2 \epsilon_m}} \frac{\bar{\gamma}_m}{\sqrt{\bar{\gamma}_m^2 - (h_0 R)^2 + m^2}} \left\{ \begin{array}{c} \cos m\theta \\ \sin m\theta \end{array} \right\} \frac{I_m(\bar{\gamma}_m r/R)}{I_m(\bar{\gamma}_m)} \quad . \tag{4.38}$$

In equation 4.37 or 4.38, equation 4.35 or 4.36 has been used in the normalization factor N_{mn} given by equation 4.34. Having obtained the unperturbed eigen functions ϕ_{mn}, one now uses them to formulate the boundary condition perturbation theory. To develop, one employs the two-dimensional Green's function $G(\vec{r}, \vec{r}_0; \omega)$ satisfying the same mixed boundary condition as in equation 4.32 at the borehole boundary $r = R$.

$$\left\{ \begin{array}{ll} \nabla_t^2 G + \kappa^2 G = -4\pi\delta(\vec{r} - \vec{r}_0) & , \\ \partial_r G - h_0 G = 0 & , \quad (\text{at } r = R) \end{array} \right. \tag{4.39}$$

where ∇_t^2 has been defined in equation 4.6, $\delta(\vec{r} - \vec{r}_0)$ represents the two-dimensional Dirac function, and the two-dimensional vectors

$$\vec{r}_0 = \left\{ \begin{array}{c} r_0 \cos\theta_0 \\ r_0 \sin\theta_0 \end{array} \right\} \quad \text{and} \quad \vec{r} = \left\{ \begin{array}{c} r\cos\theta \\ r\sin\theta \end{array} \right\}$$

are the source and field positions, respectively. Using the eigen functions $\{\phi_{mn}\}$, one expands the Green's function with waiting-to-be-determined coefficients and the Dirac function with known coefficients. Substituting the expansions into the partial differential equation in equation 4.39 and comparing the coefficients on both sides of the equation, one obtains the series solution for the Green's function:

$$\begin{aligned} G(\vec{r}, \vec{r}_0; \omega) &= 4\pi \sum_{m,n} \frac{\cos[m(\theta - \theta_0)]}{(\kappa_{mn}^2 - \kappa^2) N_{mn}} J_m(\gamma_{mn} \frac{r_0}{R}) J_m(\gamma_{mn} \frac{r}{R}) \\ &= 4\pi \sum_{m,n} \frac{\phi_{mn}(\vec{r}) \phi_{mn}(\vec{r}_0)}{\kappa_{mn}^2 - \kappa^2} \quad . \end{aligned} \tag{4.40}$$

Applying the two-dimensional Green's theorem

$$\iint_A [G \bigtriangledown_t^2 \psi - \psi \bigtriangledown_t^2 G] dA = \oint_S [G \frac{\partial \psi}{\partial r} - \psi \frac{\partial G}{\partial r}] dS \ , \tag{4.41}$$

where

$$A : \text{borehole area}; \quad S : \text{borehole boundary } r_0 = R$$

to equations 4.5 and 4.39, one gets

$$4\pi\psi(\vec{r},\omega) = \oint_S [G \frac{\partial \psi}{\partial r} - \psi \frac{\partial G}{\partial r}] dS \ . \tag{4.42}$$

Note that the integrand in equation 4.42 is evaluated with the source point on the borehole boundary $r_0 = R$. Thus the respective boundary conditions for ψ and G (equations 4.31 and 4.39) can be used. Substituting $\partial_r G = h_0 G$ and $\partial_r \psi = h_0\psi - (-ik_y + h_0)W(\theta)\psi$ into equation 4.42 and letting $\vec{r}$ approach $\vec{r}_0$ on the boundary, one obtains the following integral equation for $\psi(\vec{r}_0)$:

$$\psi(\vec{r}_0,\omega) = -\frac{1}{4\pi} \oint_S h(S) G(\vec{r}_0, \vec{r}_0; \omega) \psi(\vec{r}_0, \omega) dS \ , \tag{4.43}$$

with

$$h(S) = (-ik_y + h_0)W(\theta) \ , \ (S = R\theta) \ . \tag{4.44}$$

Equation 4.43 is a second kind homogeneous Fredholm integral equation and can be solved by series expansions. It is assumed that $\psi(\vec{r}_0,\omega)$, being the perturbed wave function, can be expanded using the unperturbed eigen functions (or sub-modes)

$$\psi(\vec{r}_0,\omega) = \sum_{m,n} C_{mn} \phi_{mn}(\vec{r}_0,\omega) \ , \tag{4.45}$$

where C_{mn}'s are the expansion coefficients. In the unfractured borehole case, the Stoneley mode itself suffices to satisfy the axial-symmetric boundary condition (equation 4.11), whereas in the fractured borehole case, the Stoneley sub-modes combine to form a wave packet, in order to satisfy the azimuthally varying boundary condition (equation 4.31). Substitution of equations 4.40 and 4.45 into equation 4.43 results in

$$\sum_{m,n} C_{mn} \phi_{mn} = \sum_{m,n} \left(\frac{\sum_{p,q} C_{pq} h_{mnpq}}{\kappa^2 - \kappa_{mn}^2} \right) \phi_{mn} \ , \tag{4.46}$$

where

$$h_{mnpq} = \oint_S h(S)\phi_{mn}(\vec{r}_0)\phi_{pq}(\vec{r}_0)dS \ .$$

An analysis of the fracture and borehole geometry shown in Figure 4-1 indicates that the fluid motion in the borehole is symmetric with respect to the diameters coinciding with $\theta = 0$ and $\theta = \pi/2$, so that the azimuthal function of ϕ_{mn} (equation 4.33 or 4.37 and 4.38) has only $\cos m\theta$ component, and the integer m must be even numbers. Using this fact and the $h(S)$ given in equation 4.44, h_{mnpq} can be readily integrated out as

$$h_{mnpq} = \frac{4(-ik_y + h_0)}{\pi R\sqrt{\epsilon_m \epsilon_p}} \frac{\gamma_{mn}\gamma_{pq}}{\sqrt{[\gamma_{mn}^2 + (h_0R)^2 - m^2][\gamma_{pq}^2 + (h_0R)^2 - p^2]}}$$
$$\times \begin{cases} \sin[(m-p)L/(2R)]/(m-p) + \sin[(m+p)L/(2R)]/(m+p) & , \quad m \neq p \\ L/(2R) + \sin(mL/R)/(2m) & , \quad m = p \neq 0 \\ L/R & , \quad m = p = 0 \end{cases} \tag{4.47}$$

with

$$\begin{cases} m, p = & 0, 2, 4, \cdots \\ n, q = & 1, 2, 3, \cdots \end{cases}$$

where γ_{mn} and γ_{pq} can be real or imaginary depending on the solution to equation 4.35. From equation 4.46, one obtains a set of linear simultaneous equations for the coefficients C_{mn}.

$$\sum_{p,q}[(\kappa^2 - \kappa_{mn}^2)\delta_{mp}\delta_{nq} - h_{mnpq}]C_{pq} = 0 \ . \tag{4.48}$$

The matrix of this equation is of infinite dimension because m, n, p, and q can go to infinity. In practice, however, this problem can be approximately solved by making the matrix finite dimensional (Bender and Orzag, 1978). The series in equation 4.46 is truncated at $m = M$ (M is an even number) and $n = N$. Equation 4.48 may thus be written as

$$\mathbf{HC} = \mathbf{0} \ , \tag{4.49}$$

where $\mathbf{H}$ is a $(M/2+1)N \times (M/2+1)N$ symmetric square matrix, given as

$\mathbf{H} =$

$$\begin{pmatrix} \kappa^2 - \kappa_{01}^2 - h_{0101} & -h_{0102} & -h_{0103} & \cdots & -h_{01MN} \\ -h_{0201} & \kappa^2 - \kappa_{02}^2 - h_{0202} & -h_{0203} & \cdots & -h_{02MN} \\ -h_{0301} & -h_{0302} & \kappa^2 - \kappa_{03}^2 - h_{0303} & \cdots & -h_{03MN} \\ \vdots & \vdots & \vdots & & \vdots \\ -h_{MN01} & -h_{MN02} & -h_{MN03} & \cdots & \kappa^2 - \kappa_{MN}^2 - h_{MNMN} \end{pmatrix} ,$$

and $\mathbf{C}$ is the vector representation of the coefficients C_{mn} having $(M/2+1) \times N$ elements, given by

$$\mathbf{C}^T = [C_{01} \cdots C_{0N}\, C_{21} \cdots C_{2N} \cdots C_{M1} \cdots C_{MN}] \ .$$

The condition that there be nontrivial solutions $\mathbf{C}$ is that the determinant of $\mathbf{H}$ vanishes.

$$det\ \mathbf{H} = \mathbf{0} \ . \tag{4.50}$$

This results in a series of perturbed eigenvalues for κ^2. The complicated boundary value problem is therefore reduced to a perturbative eigenvalue problem (Bender and Orzag, 1978).

4.5.1 Borehole Stoneley Wave

Because of the effects of the fracture, the sub-modes $\{\phi_{mn}\}$ are perturbed, and their associated eigenvalues κ_{mn} are modified, as given by the solutions of equation 4.50. The eigenvalue corresponding to the perturbed borehole Stoneley mode is the lowest order one of all the eigenvalues determined by equation 4.50. This lowest order eigenvalue is designated by κ_{ST}^2. When κ_{ST}^2 is found by solving equation 4.50, the borehole Stoneley wavenumber k_z is given by

$$k_z = \sqrt{k_0^2 - \kappa_{ST}^2} \ , \tag{4.51}$$

and the Stoneley phase velocity c_{ST} and attenuation coefficient α_{ST} are obtained from the real and imaginary part of k_z as

$$\begin{aligned} c_{ST} &= \omega / Re\{k_z\} \ , \\ \alpha_{ST} &= Im\{k_z\} \ . \end{aligned} \tag{4.52}$$

The attenuation of the perturbed Stoneley mode results from the loss of wave energy into the fracture. To illustrate how the presence of the fracture affects the borehole Stoneley propagation, one expresses κ_{ST}^2 with a series expansion of the secular determinant in equation 4.50 (Morse and Feshbach, 1953).

$$\begin{aligned} \kappa_{ST}^2 &= \kappa_{01}^2 + h_{0101} + \sum_{\substack{p\neq 0 \\ q\neq 1}} \frac{h_{01pq} h_{pq01}}{\kappa_{ST}^2 - \kappa_{pq}^2 - h_{pqpq}} \\ &+ \sum_{\substack{p,r\neq 0;\ q,s\neq 1 \\ r\neq p;\ q\neq s}} \frac{h_{01pq} h_{pqrs} h_{rs01}}{(\kappa_{ST}^2 - \kappa_{pq}^2 - h_{pqpq})(\kappa_{ST}^2 - \kappa_{rs}^2 - h_{rsrs})} + \cdots \ . \end{aligned} \tag{4.53}$$

Thus if the fracture does not exist (i.e., $h_{mpnq} = 0$), κ_{ST} is given by $\kappa_{01} = \bar{\gamma}_0 / R$, where $\bar{\gamma}_0$ is the root of equation 4.36 for $m = 0$. In fact, for $m = 0$ equation 4.36 reduces to the borehole dispersion equation (equation 4.9), and $\bar{\gamma}_0$ corresponds to the radial fluid wave number f in equations 4.10. This gives the unperturbed Stoneley wavenumber

$$k_z^{(0)} = \sqrt{k_0^2 - \kappa_{01}^2} = \frac{\omega}{c} \ , \tag{4.54}$$

where c is the borehole Stoneley velocity determined by equation 4.9. In the presence of the fracture, κ_{ST}^2 is given by the perturbation series in equation 4.53, with κ_{01} as the zero-order solution. The perturbations are in ascending orders of h_{mpnq}. From equation 4.47, one has, approximately,

$$h_{mpnq} \propto \frac{\omega L}{\pi R^2} \ .$$

Therefore, at low frequencies or small fracture apertures, h_{mpnq} is small and κ_{ST}^2 can be well approximated by taking only the zero and first order terms. Thus

$$k_z = \sqrt{\frac{\omega^2}{c^2} + \frac{2L(-ik_y + h_0)[I_0(fR)]^2}{\pi R^2 \{[I_0(fR)]^2 - [I_1(fR)]^2\}}} \ , \tag{4.55}$$

where the expression for h_{0101} given by equation 4.47 has been used. With increasing frequency (or aperture), κ_{ST}^2 in equation 4.53 involves higher order perturbation terms. In this situation, one must increase M and N in equation 4.48 to yield accurate results. Physically, this means that the effects of higher frequency or larger fracture aperture will involve higher degree of azimuthal (characterized by M) and radial (characterized by N) fluid motions. For a given frequency range and fracture aperture, M and N can be practically determined by comparing the numerical result at M, N with that at $M+1$, $N+1$. When the two results are sufficiently close, one may then reckon that the perturbation series in equation 4.53 converges to its true value at M and N. Since κ_{ST}^2 is the lowest order eigenvalue, it converges to its limit more rapidly than any other eigenvalues as M and N increase (Bender and Orzag, 1978). Therefore, moderate values of M and N will be sufficient to yield accurate results.

4.6 Theoretical Results

In this section, theoretical results are presented for the effects of a vertical borehole fracture on the Stoneley propagation. Cases of both a hard and a soft formation are investigated, and the behavior of these effects will be illustrated in both low and higher frequency ranges.

4.6.1 Hard Formation

The effects of the fracture in the presence of a hard formation are first investigated. Figure 4-3 shows the results for a radius $R = 10$ cm borehole with a $L = 1$ cm fracture in a low frequency range of [0-2] kHz. For the formation, the compressional and shear velocities are V_p =5 km/s and V_s =3 km/s, respectively. Its density ρ =2.5 g/cm^3. For the fluid, the acoustic velocity $V_f = 1.5$ km/s and the density $\rho = 1$ g/cm^3. Figure 4-3a shows the velocity dispersion of the Stoneley wave in the fractured borehole,

plotted against the velocity of an unfractured borehole having the same radius. A prominent feature in this figure is the drastic decrease of the perturbed Stoneley velocity as frequency approaches zero while the unperturbed Stoneley velocity remains relatively unchanged. As discussed previously, this behavior is associated with the slow wave behavior of the fracture fundamental mode at low frequencies (Ferrazzini and Aki, 1987; Tang and Cheng, 1988). That is, the decrease in fracture wave velocity creates a large pressure gradient between the borehole and the fracture fluid, which drives the bore fluid effectively into the fracture, resulting in the retardation of wave propagation in the borehole. Figure 4-3b shows the calculated Stoneley wave attenuation coefficient in the same frequency range. The attenuation drastically increases with frequency to reach a maximum at low frequencies, then decreases with increasing frequency. In fact, the behaviors of Stoneley dispersion and attenuation at very low frequencies are well predicted by the first order theory given by equation 4.55. For a check of the theory, both results from the first order theory (equation 4.55) and from the complete perturbation theory (equation 4.50) are plotted in Figure 4-3b. The later theoretical result is calculated by setting $M = 16$ and $N = 5$ in equation 4.48. Corresponding to equation 4.53, this result involves the summation of $(M/2+1) \times N = 45$ perturbation terms, and should be regarded as quite accurate. As expected, the first order theory does not differ from the complete theory in the low frequency range. As frequency increases, they begin to show some discrepancy, the attenuation from the first order theory being slightly higher than that from the complete theory. At higher frequencies, this discrepancy will be non-negligible and one should rely on the complete theory to yield accurate theoretical results. Figure 4-4 shows the Stoneley wave dispersion (a) and attenuation (b) in a higher frequency range ([0-20] kHz) calculated using the complete perturbation theory. The parameters for the numerical evaluation are the same as those of Figure 4-3. In Figure 4-4a, the Stoneley dispersion curve of the fractured borehole is plotted against that of a unfractured borehole of the same radius. Drastically increasing from small values at low frequencies, the

perturbed Stoneley velocity becomes slightly higher than the unperturbed velocity in the medium frequency range. As will be discussed later, this effect is to be expected since the opening of the fracture reduces the guiding effects of the borehole and the Stoneley velocity tends to move towards the free space velocity of the fluid. At high frequencies, both velocities approach the Scholte wave velocity (i.e., Stoneley velocity along a planar fluid-solid interface). Figure 4-4b shows the Stoneley attenuation coefficient as the function of frequency. Starting from a maximum at very low frequencies (see Figure 4-3b), the attenuation monotonically decreases with increasing frequency. From Figures 4-3 and 4-4, it can be seen that the overall effects of a vertical fracture on the borehole Stoneley waves are very similar to those of a permeable borehole with a porous formation as studied in Chapter 3. Both types of effects involve dynamic fluid flow at the borehole wall and are more important in the very low frequency range than at higher frequencies.

To show the effects of the fracture thickness on the Stoneley wave, Figure 4-5 plots the Stoneley velocities (a) and attenuations (b) for a set of fracture apertures in a borehole with a 20 cm diameter. They are L = 0.2, 1, and 3 cm, respectively. The frequency range is [0-4] kHz. The fluid and formation properties for the calculations are the same as those used in Figures 4-3 and 4-4. Figure 4-5a shows that the decrease of Stoneley velocity at low frequencies is more pronounced for a big fracture (L=3 cm) than for a small fracture (L=0.2 cm). But they all approach the same limit at high frequencies (see also Figure 4-4a), where the effects of a fracture become minimal. Figure 4-5b shows that the Stoneley attenuation increases with increasing fracture aperture, especially at low frequencies. But the increase is not linearly proportional to the fracture aperture. This can be explained by the behavior of the fracture slow wave. Although the increase in aperture results in a linear increase of fracture conductivity (equation 4.15), the velocity of the slow wave is also increased. According to equation 4.28, this means that the fracture-borehole interaction tends to be reduced. Therefore, although the overall effects are increased by increasing the

fracture aperture, they are not linearly proportional to it.

4.6.2 Soft Formation

In the case of a soft formation whose shear velocity is less than the acoustic velocity of the fluid, the Stoneley wave velocity in the borehole and the fundamental mode velocity in the fracture are considerably lower than those in the case of a hard formation (for the fracture wave velocity, see Tang and Cheng, 1988). These effects are reflected in the term h_{mnpq} in equation 4.47, which governs the perturbation by the fracture. The soft formation or the slower Stoneley velocity causes the wall compliance $h_0 R$ to be much larger than that of a hard formation, particularly at high frequencies (Figure 4-2). On the other hand, the slower fracture wave velocity makes k_y have a larger value, especially at low frequencies. This results in the increase in the dynamic pressure gradient at the fracture opening and produces stronger borehole-fracture interaction. It is therefore expected that in the low frequency range, the effect of a given fracture in the soft formation case will be more prominent than that in the hard formation case.

Figure 4-6 shows the Stoneley wave dispersion (a) and attenuation (b) in a low frequency range of [0-2] kHz. The borehole radius and the fracture aperture are the same as those in Figure 4-3. They are $R = 10$ cm and $L = 1$ cm. The formation and fluid velocities are: $V_p = 3$ km/s, $V_s = 1.4$ km/s, and $V_f = 1.5$ km/s. The formation and fluid densities are 2.5 g/cm^3 and 1 g/cm^3, respectively. As seen from Figure 4-6a, the perturbed Stonely velocity exhibits a similar behavior as has been seen and discussed in Figure 4-3a, except that the difference between the perturbed and the unperturbed velocities are more significant than that in Figure 4-3a between 0.5 kHz and 2 kHz. The attenuation shown in Figure 4-6b also has the similar behavior as that shown in Figure 4-3b. But the former is higher than latter, because of the effects of a soft formation. In addition, one also notices that the attenuation given by the first order theory begins to significantly differ from the one by the complete pertur-

bation theory at about 1 kHz, because of the increased wall compliance. Figure 4-7 shows the Stoneley dispersion (a) and attenuation (b) in the frequency range of [0-20] kHz. The borehole radius and fracture aperture as well as the formation and fluid parameters are the same as those of Figure 4-6. The Stoneley velocity of a fractured borehole is significantly higher than the velocity of an unfractured borehole in the lower frequency range of Figure 4-7a. As frequency increases, both velocities approach the Scholte wave velocity corresponding to a soft solid-fluid interface. In Figure 4-7b, the attenuation of Stoneley wave has its maximum value at very low frequencies (see also Figure 4-6b), then it rapidly decreases with increasing frequency. Beyond 10 kHz, the attenuation becomes very small. In the hard formation case shown in Figure 4-4b, the Stoneley attenuation is still significant even at 20 kHz. The fact that the Stoneley attenuation due to a fracture is most significant at low frequencies allows it to be separated from the intrinsic attenuation of the formation and fluid. The latter attenuation is small or negligible in the low frequency range.

To show the effects of the fracture thickness on the Stoneley wave in the presence of a soft formation, Figure 4-8 plots the Stoneley velocities (a) and attenuations (b) for a set of fracture apertures in borehole with a 20 cm diameter. They are $L = 0.2$, 1, and 3 cm, respectively. The frequency range is [0-4] kHz. The fluid and formation properties for the calculations are the same as those used in Figures 4-6 and 4-7. As in the hard formation case (Figure 4-5), Figure 4-8a shows that increasing fracture aperture increases the dispersion of Stoneley velocity at low frequencies. In addition, for a big fracture, the tendency for the Stoneley velocity to increase towards the free space velocity is pronounced (see the L=3 cm curve). As mentioned previously, this is related to the reduction of the solid-fluid coupling by the fracture. The borehole fluid is more intimately coupled with a soft formation than with a hard formation (see Figure 4-2), so that the Stoneley velocity is significantly lower in a soft formation than in a hard formation. Once this coupling effect is reduced, the Stoneley velocity increases towards the free space velocity. But the increase from the low velocity

(the soft formation case) is more significant than the increase from the high velocity (the hard formation case), because in the hard formation case the Stoneley velocity is already close to the free space velocity (see Figures 4-4 and 4-5). However, this phenomenon occurs only in the medium frequency range. At very low frequencies, the strong interaction of the borehole fluid with the fracture drastically reduces the Stoneley velocity. At very high frequencies, the borehole acts like a planar surface and the Stoneley velocity approaches the Scholte velocity. Figure 4-8b shows that the attenuation coefficient in the presence of a soft formation is generally higher than in the presence of a hard formation (see Figure 4-5b). The attenuation increases with increasing fracture aperture. At higher frequencies, the attenuation decreases with increasing frequency. The bigger the fracture is, the faster the attenuation decreases, so that the attenuation of the 3 cm fracture drops below that of the 1 cm fracture above 3.5 kHz. This is related to the fact that the slow wave effects become less significant as frequency and fracture thickness increase. When the slow wave velocity approaches the borehole Stoneley wave velocity at high frequencies or large fracture apertures, the fracture wave is almost in phase with the borehole wave motion, resulting in the decrease of fluid flow into the fracture. This effect is more pronounced for a soft formation than for a hard formation.

4.7 Laboratory Experimental Study

The characteristics of Stoneley wave propagation in a borehole with a vertical fracture have been theoretically analyzed. It is desirable to test the validity of these analyses. For this purpose, ultrasonic modeling experiments are carried out to measure Stoneley propagation in laboratory fracture borehole models.

4.7.1 Experimental Procedure

In the ultrasonic laboratory experiment, one must ensure that the borehole diameter lies in the range of ultrasonic wavelengths, so that the guided wave effects are easily measurable. Thus to simulate an in-situ Stoneley wave of peak frequency 5 kHz in a 20 cm diameter borehole, the model borehole diameter is scaled to the order of 1 cm for a laboratory Stoneley wave with peak frequency around 100 kHz. The vertical fracture is simulated by a saw cut in the model, which crosses the borehole diametrically and has an aperture on the order of 1 mm. Aluminum is used to simulate the hard formation and lucite is used to model the soft formation. They are shaped into cylinders. The aluminum cylinder is 20 cm in diameter and 25 cm in height. The lucite one is 15 cm in diameter and 18 cm in height. Water is used as the borehole fluid. The acoustic properties of the three media are given in Table 4.1.

A diagram of the experimental setup is shown in Figure 4-9. An acoustic transducer is mounted at the bottom of the borehole model. The signal receiver is a small transducer located some distance above the source. During the experiment, the model assembly designed in Figure 4-9 is submerged in a water tank. The ultrasonic wave is generated at the source transducer by a Panametrics 5055PR pulser. The received signals are first amplified by a Panametrics 5660B preamplifier, then filtered by a Krohn-Hite 3203R filter, and finally digitized by a Data Precision DATA 6000 digital oscilloscope with 12-bit amplitude resolution. The digital oscilloscope and the step motor controller are interfaced with IBM PC-AT computer by the IEEE-488 interface bus. Digitized data are first stored in the IBM PC-AT. After experiment, they are transferred to a VAX 8800 computer for data processing. When a received waveform is digitized at a 0.4 μs sampling rate at a receiver position, the receiver is automatically moved to the next receiving position at a 1.8 mm step by the step motor controller. With about 50 receiver positions, a waveform array is obtained. The array data are then processed using the refined Prony's method (Ellefsen et al., 1989). Assuming the homogeneity of the formation and fluid along the array, this method of array

processing involves changing the data from the time domain to frequency domain by applying a fast Fourier transform to each trace and then estimating the amplitude and phase for a propagating wave mode at every frequency using the method of least squares. The decay of amplitude along the array gives attenuation coefficient while the phase yields the phase velocity of the wave mode. Since it is desired to measure the Stoneley wave attenuation and dispersion along the fractured borehole, this array processing technique is ideal for this purpose. For the velocity estimate, this technique yields accurate results, even when wave amplitude is small. For the attenuation estimate, one obtains reasonably accurate results when the signal-to-noise ratio of the wave is high. But the quality of the results will be degraded when this ratio is low.

4.7.2 Experimental Results

The results of the hard formation fracture model experiment are first presented. Figure 4-10 shows the waveform array data for the aluminum model. The borehole radius R=1 cm and the fracture aperture L=1.1 mm. The high frequency arrivals are water wave propagating in the bore fluid (Biot, 1952; Winbow, 1988). The fact that its propagation is virtually unaffected by the presence of the fracture indicates that the effects of the fracture is minimal at high frequencies – a behavior that is predicted by the theory. Following the water arrivals is the Stoneley wave (indicated by ST in this figure). This wave moves across the array at almost no noticeable dispersion. However, one can notice the decay of wave amplitude as source-receiver distance increases, particularly in the low frequency portion of the waves. This indicates that the Stoneley wave gradually loses its energy into the fracture in the propagation. The array data shown in Figure 4-10 are then processed using Prony's method. Figure 4-11 shows the estimated wave amplitude spectrum (a), attenuation coefficient (b), and the phase velocity (c) for the Stoneley wave. The attenuation and velocity are plotted versus the theoretical predictions calculated by solving equation 4.50 using the parameters in Table 4.1 for the aluminum. As shown in Figure 4-11b, in a

broad frequency range of [0-250] kHz, both the predicted and measured attenuations decrease with increasing frequency. From 70 kHz to 250 kHz in which the wave has most of its energy (see Figure 4-11a), the agreement is very good, although the measured values are a little higher than those of the theory towards the low frequency range. The theoretical and experimental velocity dispersions shown in Figure 4-11c show very good agreement throughout the frequency range. In particular, the decrease of velocity at very low frequencies — a characteristic of the effect of fracture as predicted by the theory — is detected by the experiment. Only in this very low frequency range, does the perturbed Stoneley velocity have noticeable difference from the unperturbed (i.e., the intact borehole) Stoneley velocity (dashed line in Figure 4-11c) in this particular case.

Next, the results of the soft formation fracture model experiment are presented. Figure 4-12 shows the waveform array data for the lucite model in which the borehole radius is 0.53 mm and the fracture aperture is 1.4 mm. The full waveform consists of a leaky-P (P) wave, a water wave (W), and a Stoneley wave (ST), as indicated in this figure. The leaky-P and water waves are typical of a soft formation (Chen, 1988) but they are of little interest at present. The Stoneley wave moves out approximately at a velocity of 1070 m/s, nearly the same as the Stoneley velocity without the effect of fracture. However, as one can notice from the figure, the Stoneley wave amplitude rapidly attenuates as the wave moves across the array. The array data shown in Figure 4-12 are then processed using Prony's method. Figure 4-13 shows the estimated wave amplitude spectrum (a), attenuation coefficient (b), and velocity dispersion (c). The theoretical predictions for the attenuation (b) and dispersion (c) are also plotted. Considering the fact that lucite is an attenuative medium, the intrinsic attenuation for the Stoneley wave is calculated using the theory of partition coefficient developed by Cheng et al. (1982). In this calculation, the presence of the fracture is neglected and a shear quality factor $Q_s = 40$ is used for the lucite. As shown in Figure 4-13b, the intrinsic attenuation is linearly superimposed on the fracture attenuation

(solid curve) to give the total attenuation (dashed curve). As expected, the total attenuation does not differ significantly from the fracture attenuation in the lower frequency range. As seen from the same figure, in the frequency range of [60-180] kHz in which the wave amplitude is the most significant, the measured attenuation shows little scatter and falls between the fracture attenuation and total attenuation curves. The agreement of the experiment with the theory is fairly good. The velocity estimate is shown in Figure 4-13c. The measured velocities are in very good agreement with the theory. Particularly, in the range of [60-180] kHz, the experimental results closely follow the theoretical velocity curve for a fractured borehole (solid curve), which is slightly higher than the velocity corresponding to an unfractured borehole with a soft (lucite) formation (dashed curve). At low frequencies, the measured velocities show the tendency to decrease with decreasing frequency, as predicted by the theory, although this tendency appears to occur at slightly higher frequencies.

4.8 Conclusions

This chapter has presented a quantitative analysis of the Stoneley wave propagation in a fluid-filled borehole with a vertical fracture. This analysis is based on a boundary condition perturbation technique developed for the borehole situation, in which the change in the boundary condition due to the fracture is treated as the perturbation to the fluid-solid boundary condition at the borehole wall. To find this change in the boundary condition, the fracture fluid motion excited by the borehole propagation was studied. The boundary condition at the fracture opening can thus be specified by the interaction between the borehole wave and the fracture fundamental wave. The boundary condition perturbation technique reduces the complicated boundary value problem to a perturbative eigenvalue problem. The Stoneley wavenumber is obtained from the lowest order perturbed eigenvalue, giving the attenuation and velocity of the Stoneley wave as a function of frequency. Whatever the formation, hard or

soft, significant Stoneley wave attenuation is produced because of the dynamic fluid flow occurring at the fracture opening. The attenuation is more significant at low frequencies than at higher frequencies. In the presence of intrinsic attenuation that is small at low frequencies, this behavior allows one to separate the two effects. The effects of a fracture on the Stoneley velocity is generally not very significant at higher frequencies. But they drastically reduce the Stoneley velocity at very low frequencies because of the increased borehole-fracture interaction. The theoretical predictions were tested with laboratory experimental results for both hard and soft formation situations. The theory and experiment are in good agreement. Specifically, the decrease of Stoneley velocity at very low frequencies is observed by the experiment and the measured Stoneley attenuation is close to the theoretical values in the frequency range where the wave amplitude is high. The theoretical results of this study provide the quantitative relationship between Stoneley propagation and the character of a vertical fracture in connection with acoustic properties of the formation and fluid. The boundary condition perturbation technique developed in this study can be modified to study the effects of a vertical fracture on the propagation of other wave modes that exist in a borehole environment, such as pseudo-Rayleigh mode, leaky-P mode, and flexural wave mode.

Medium	ρ (g/cm^3)	V_p (m/sec)	V_s (m/sec)
Aluminum	2.7	6410	3180
Lucite	1.2	2740	1330
Water	1.0	1480	0

Table 4.1: Density ρ, compressional velocity V_p, and shear velocity V_s of the fluid and solid used in the measurement.

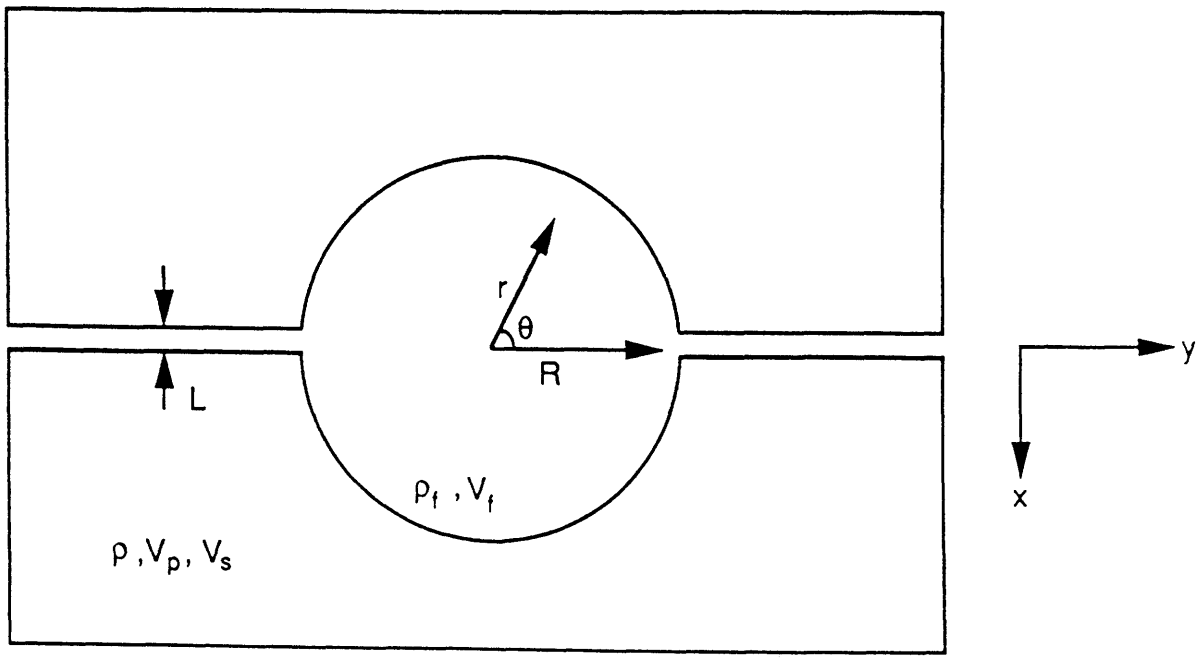

Figure 4-1: A cross-section of the borehole and fracture systems and their corresponding coordinates (r, θ, z) and (x, y, z). The z axes of the two systems are respectively at $r = 0$ and $x = y = 0$ and are pointing outwards from the figure.

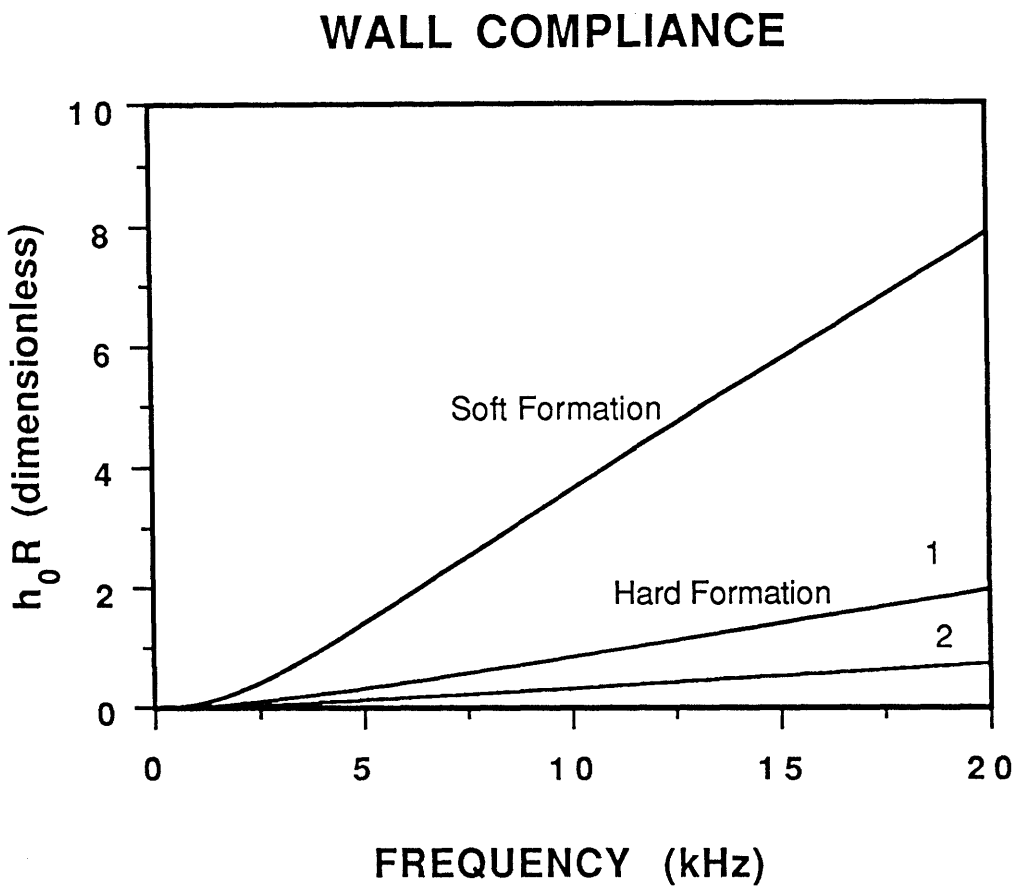

Figure 4-2: Wall compliance h_0R of hard and soft formations versus frequency. The parameters are: $V_p = 3$ km/s and $V_s = 1.2$ km/s for the soft formation; $V_p = 5$ km/s and $V_s = 3$ km/s for hard formation (1) and $V_p = 4$ km/s and $V_s = 2$ km/s for hard formation (2). In all cases the formation density $\rho = 2.5$ g/cm^3, the borehole has a radius of $R = 10$ cm and is filled with a fluid of $V_f = 1.5$ km/s and $\rho_f = 1$ g/cm^3. Note that the compliance of a soft wall is much greater than that of hard walls.

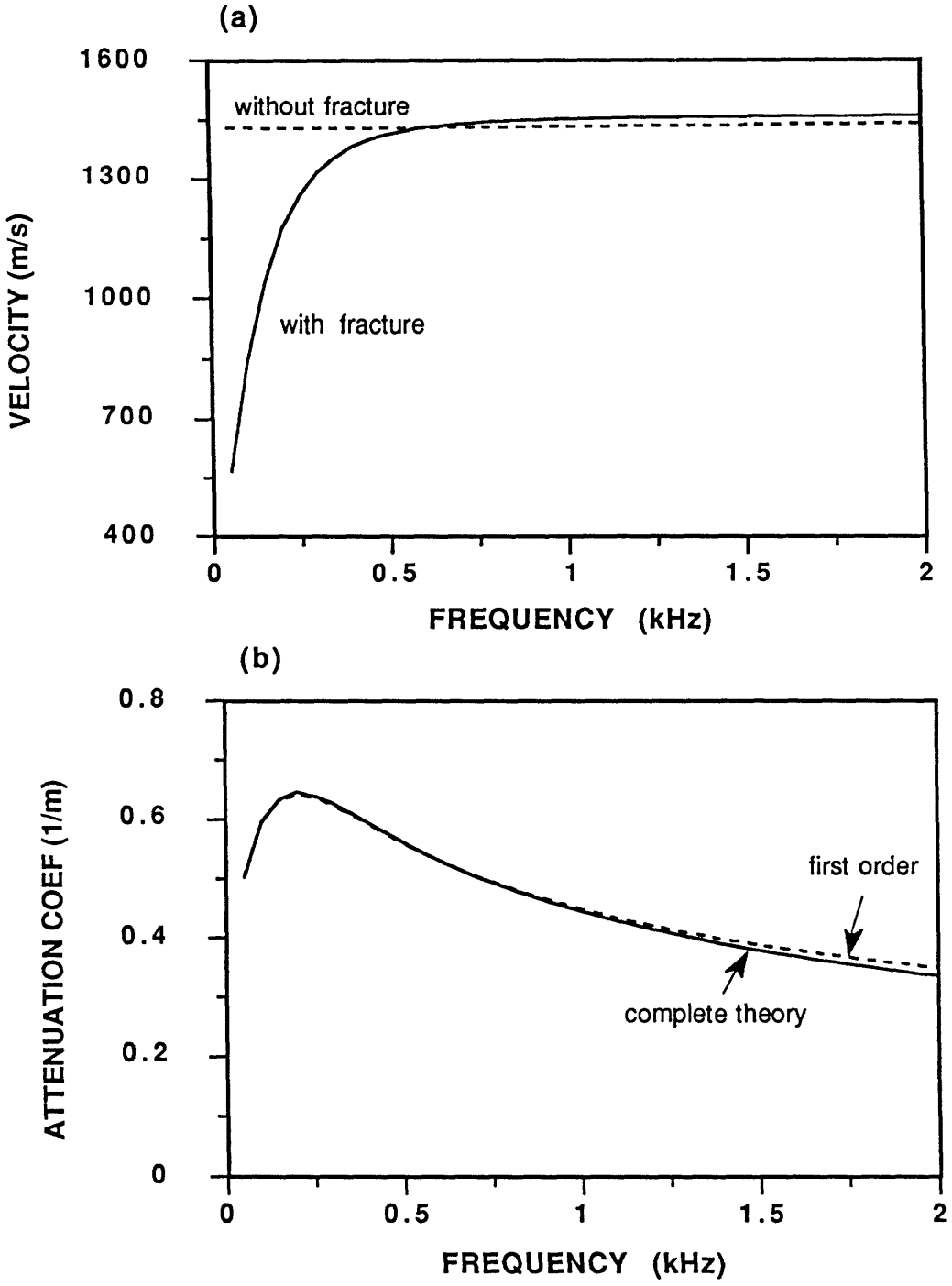

Figure 4-3: Stoneley wave dispersion (a) and attenuation (b) in the low-frequency range for the hard formation case. As indicated in (a), the Stoneley velocity of a fractured borehole drastically decreases at very low frequencies. In (b) the Stoneley attenuations from the first order theory and from the complete perturbation theory are plotted. The two results are identical at low frequencies and begin to differ as frequency increases.

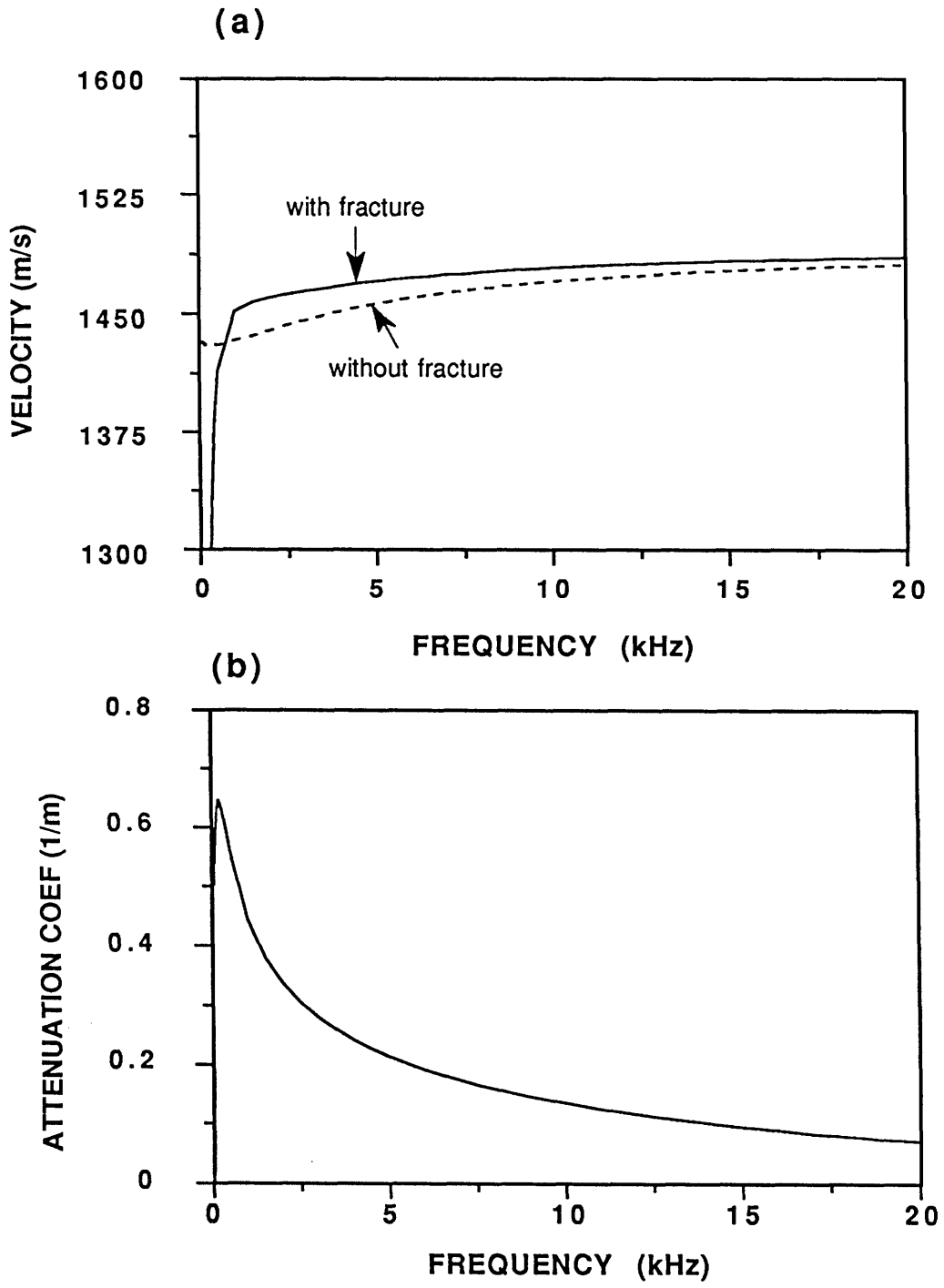

Figure 4-4: Stoneley dispersion (a) and attenuation (b) of Figure 4-3 in a higher frequency range. In (a) the perturbed velocity drastically increases to become slightly higher than the unperturbed velocity in the lower frequency range. Both velocities approach Scholte velocity as frequency increases. In (b) the Stoneley attenuation is the most significant at low frequencies and decreases as frequency increases.

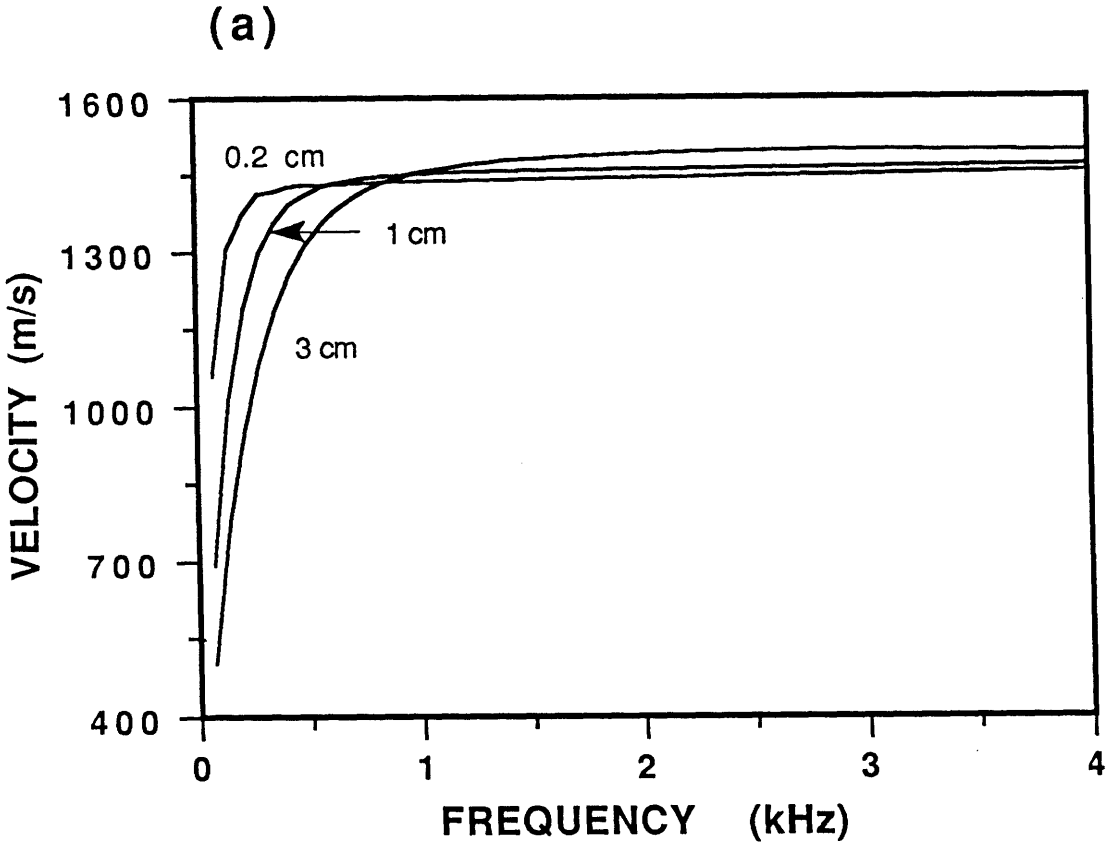

Figure 4-5: Stoneley wave velocity (a) and attenuation (b) for three different fracture apertures, which are 0.2 cm, 1 cm, and 3 cm, as indicated on the curves. Other model parameters are the same as those used in Figures 4-3 and 4-4. This figure demonstrates that the effects of a fracture increase with increasing fracture thickness.

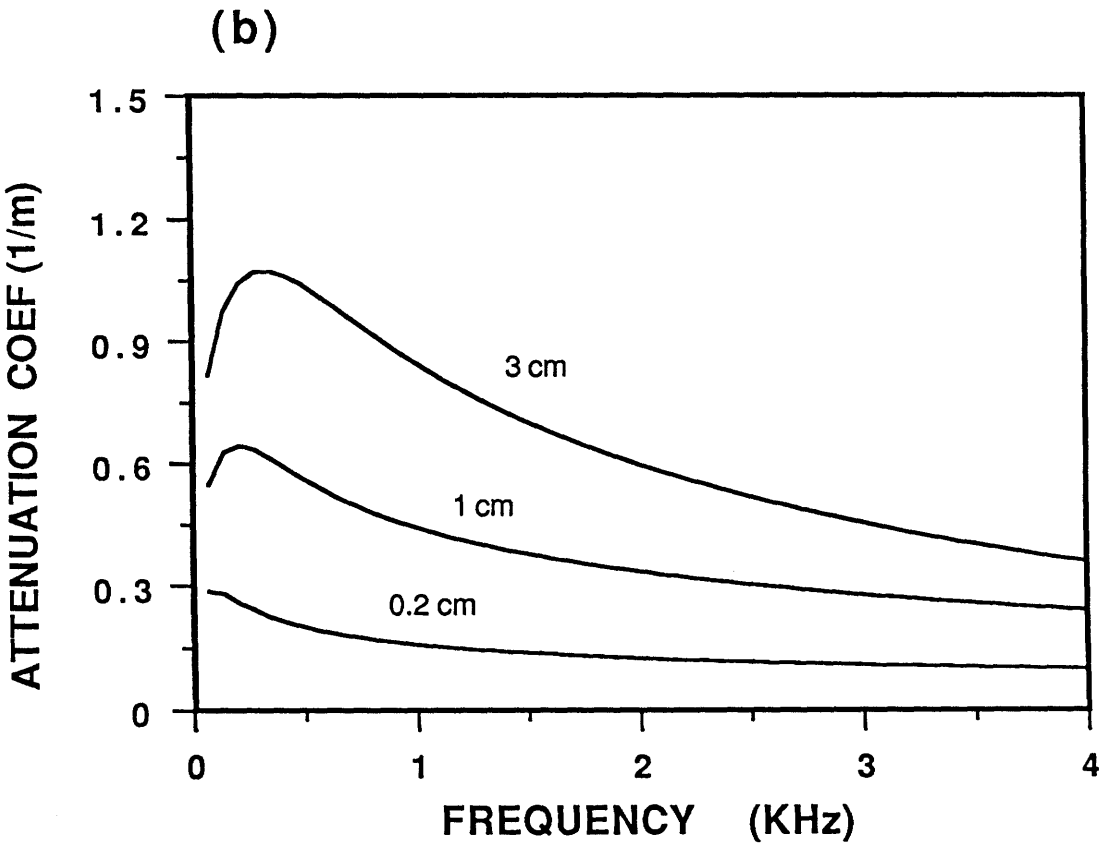

Figure 4-5: (b) Stoneley attenuation coefficient associated with (a).

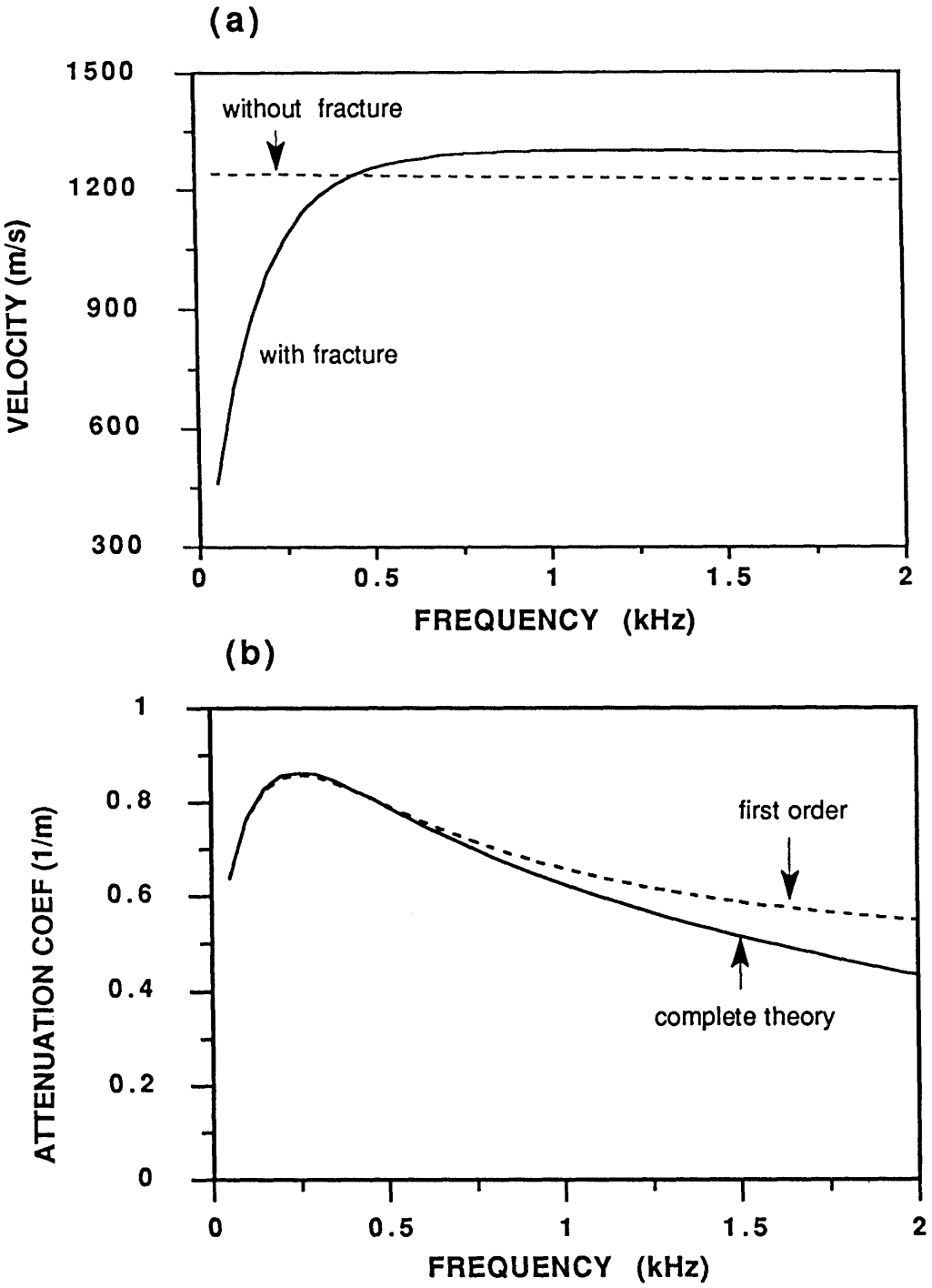

Figure 4-6: Stoneley dispersion (a) and attenuation (b) in the low frequency range for the soft formation case. In (a) the perturbed velocity exhibits the same behavior as in Figure 4-3a. In (b) the attenuation from the first order theory begins to diverge from that from the complete theory even in the low frequency range, because of the effects of the soft wall.

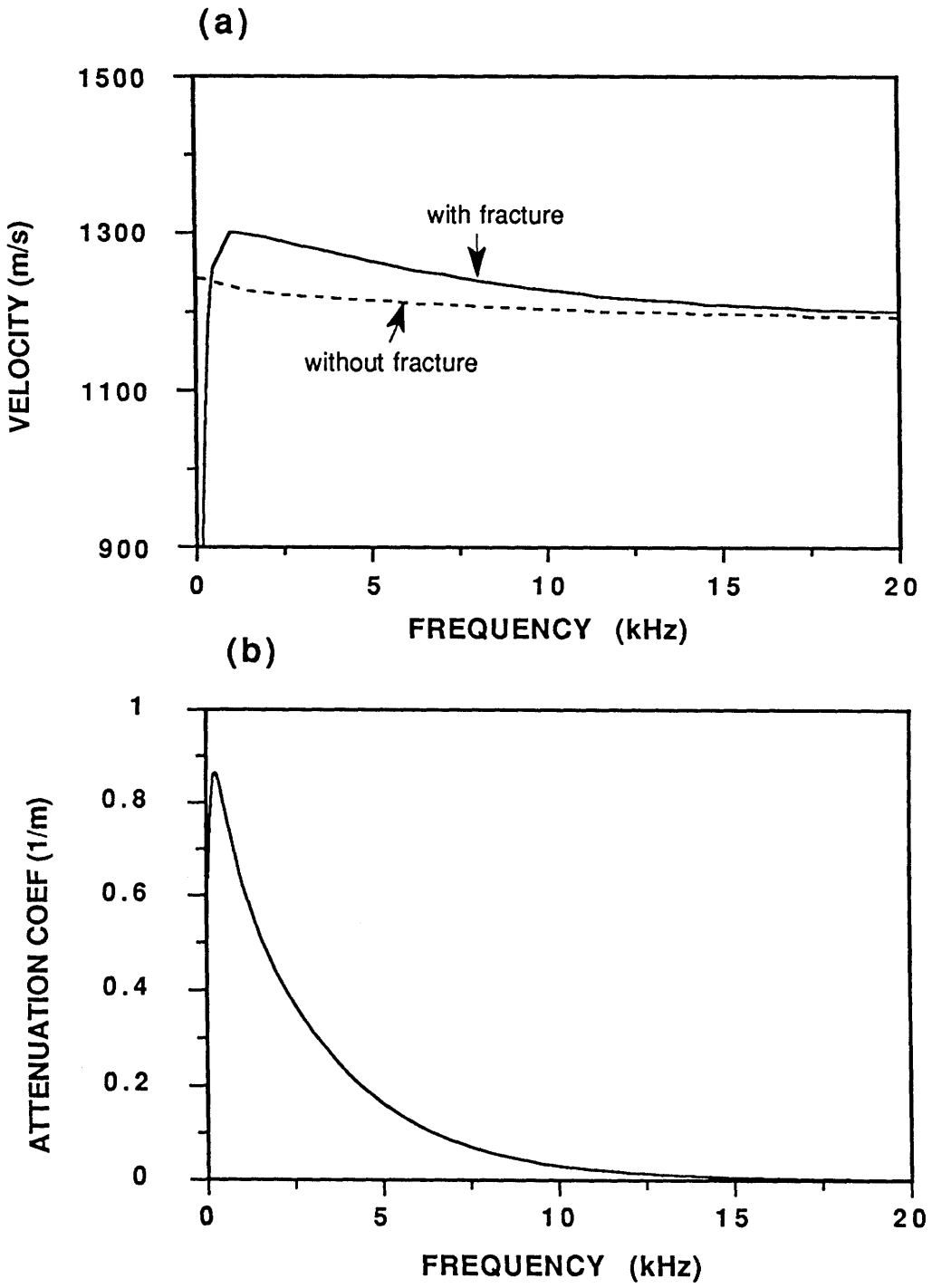

Figure 4-7: Stoneley dispersion (a) and attenuation (b) of Figure 4-6 in a higher frequency range. As shown in (a), the perturbed velocity becomes higher than the unperturbed velocity in the lower frequency range. Both velocities approach Scholte velocity along a soft solid-fluid interface as frequency increases. In (b) the attenuation is the most significant at low frequencies and rapidly decreases with increasing frequency.

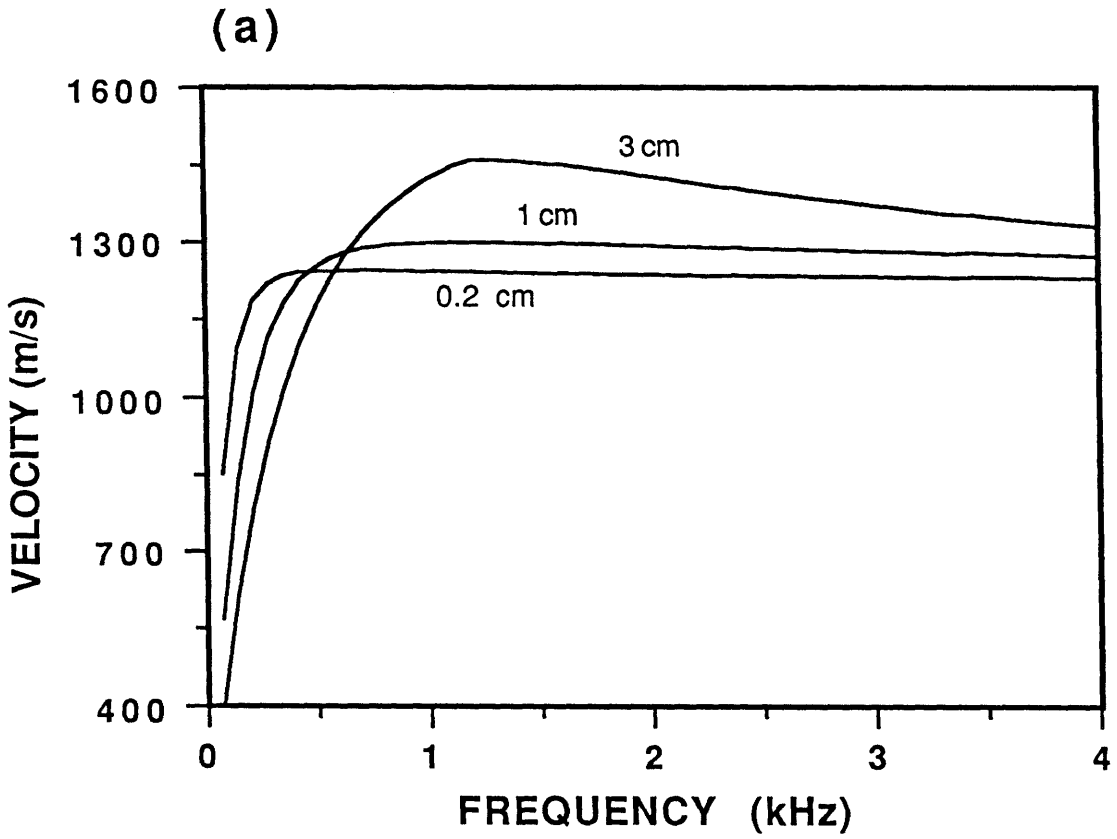

Figure 4-8: Stoneley wave velocity (a) and attenuation (b) for three different fracture apertures in the presence of a soft formation. The apertures are 0.2 cm, 1 cm, and 3 cm, as indicated on the curves. Other model parameters are the same as those used in Figures 4-6 and 4-7. In (a) the tendency for the velocity to reach the free space velocity becomes pronounced as the aperture of the fracture increases.

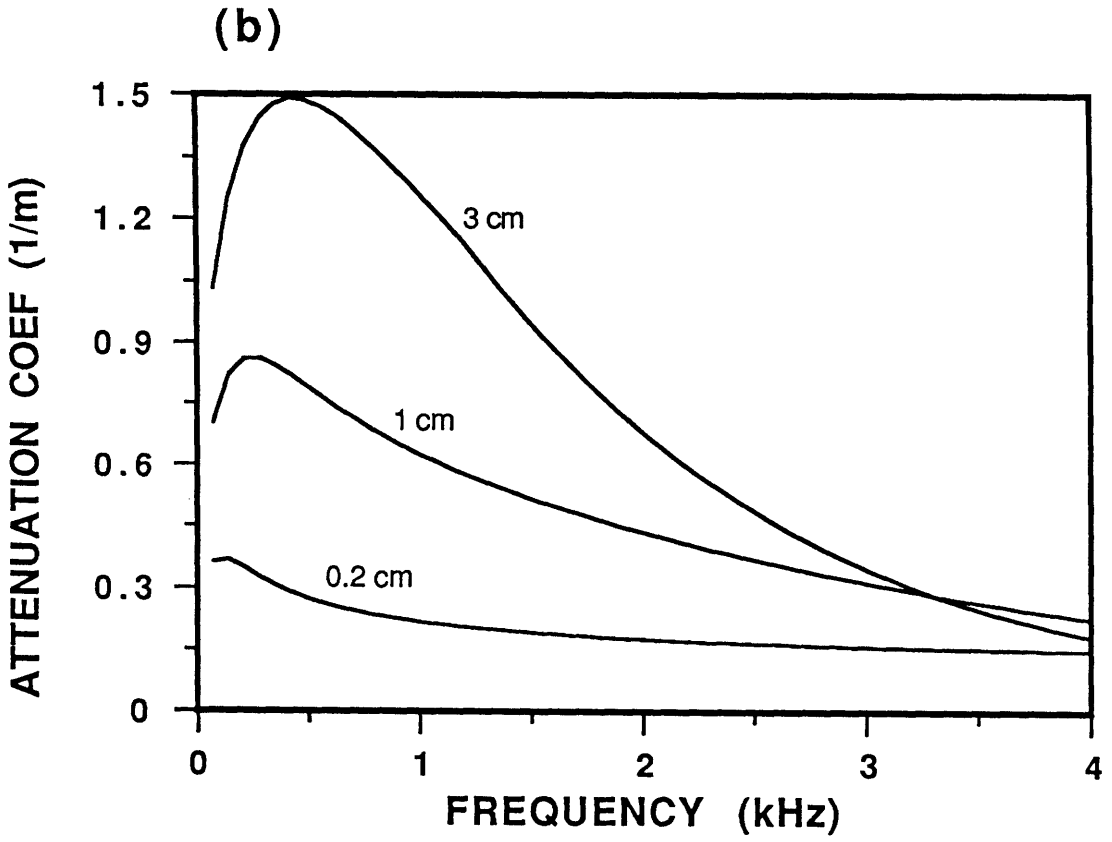

Figure 4-8: (b) Stoneley attenuation coefficient associated with (a). The attenuations are generally higher than those shown in Figure 4-5a for a given fracture aperture. For a big fracture, the attenuation decreases rapidly with increasing fracture (see the 3 cm curve).

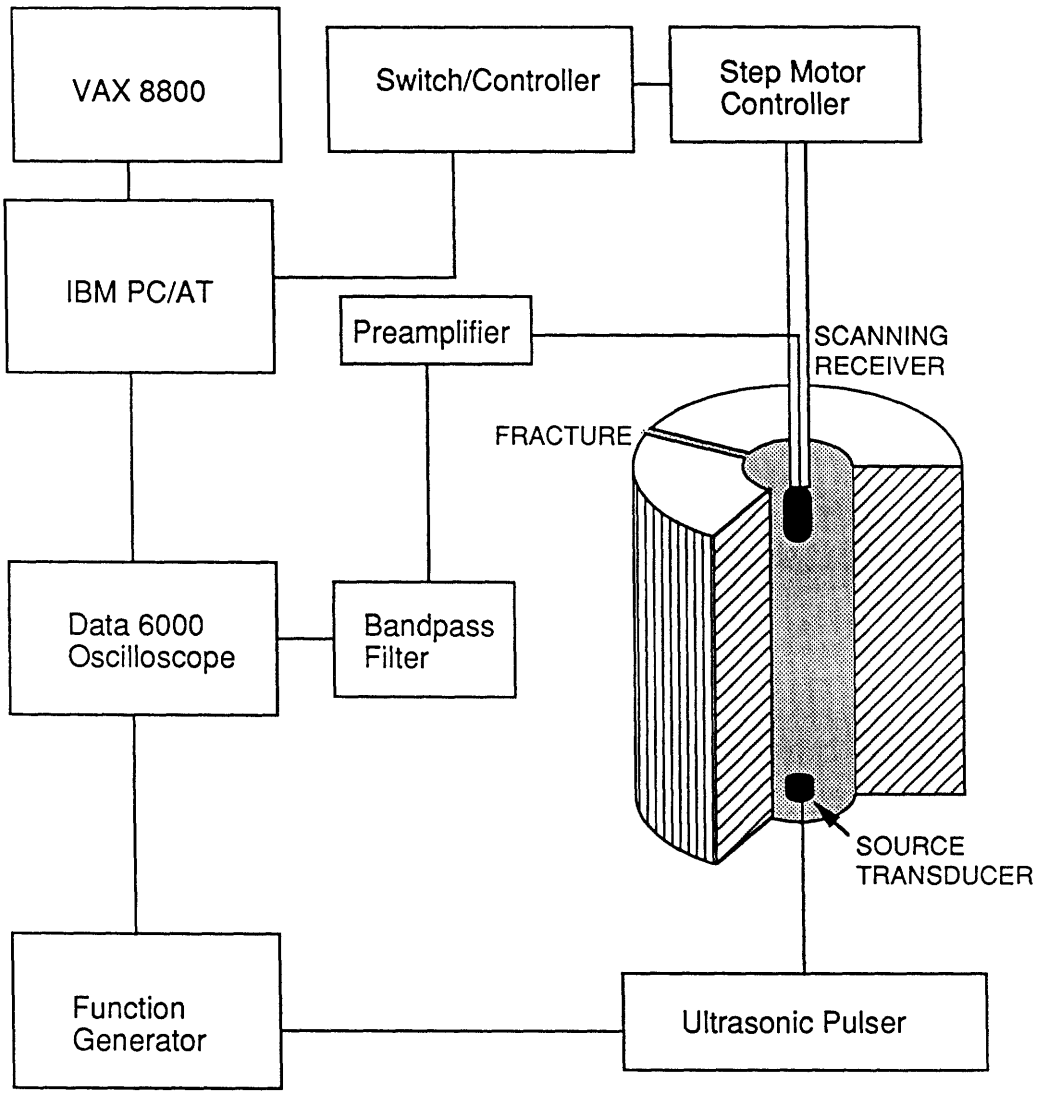

Figure 4-9: Block diagram of the laboratory experimental setup for measuring wave propagation in a fluid-filled borehole with a vertical fracture. The fracture is simulated by a saw-cut in the model. A transducer source is mounted at the bottom of the model while a receiver is placed into the borehole to measure the waves.

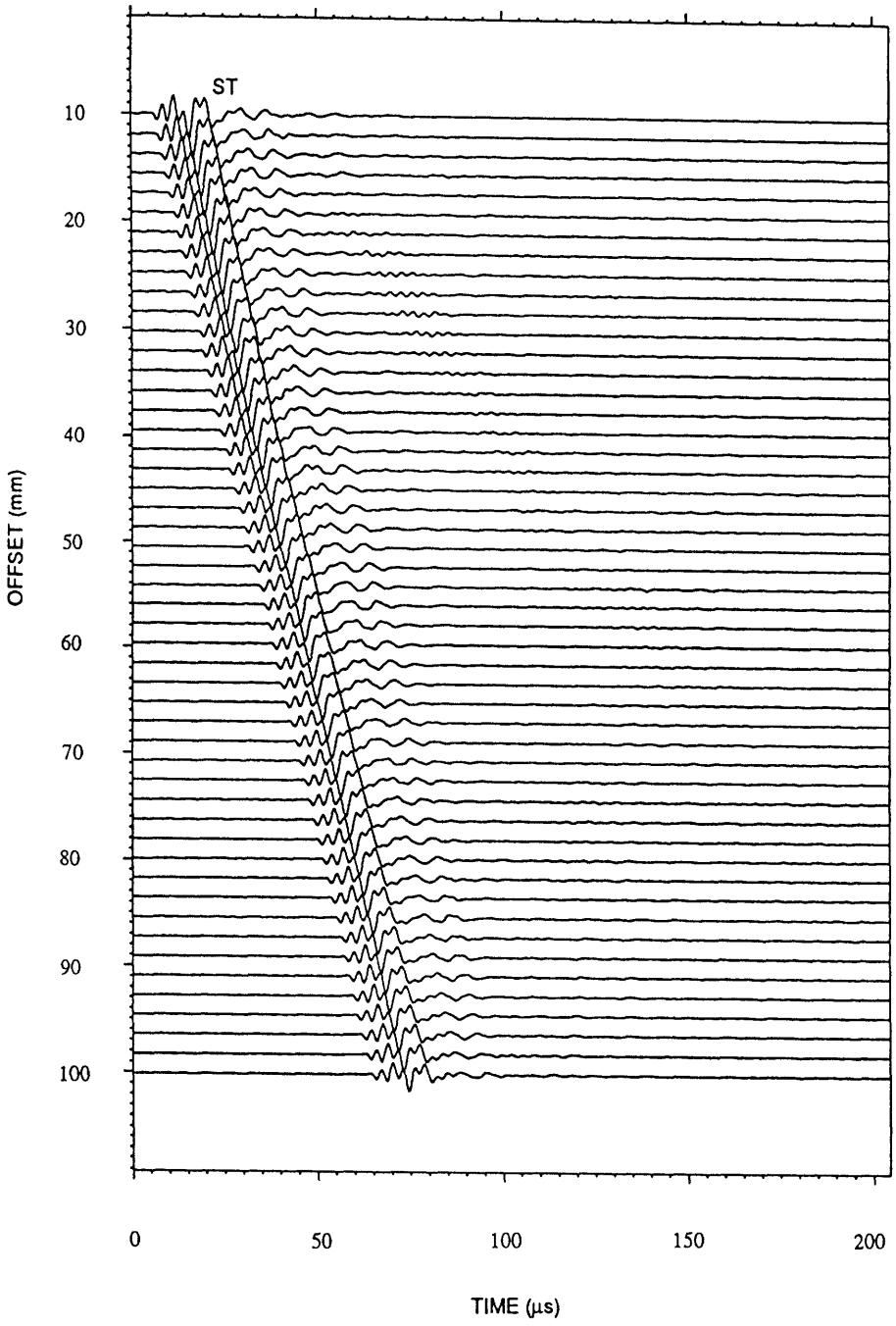

Figure 4-10: Experimental waveform array data received in the aluminum model at varying source-receiver distances. Note that the wave amplitude, particularly that of the lower frequency waves, gradually decreases as the source-receiver distance increases.

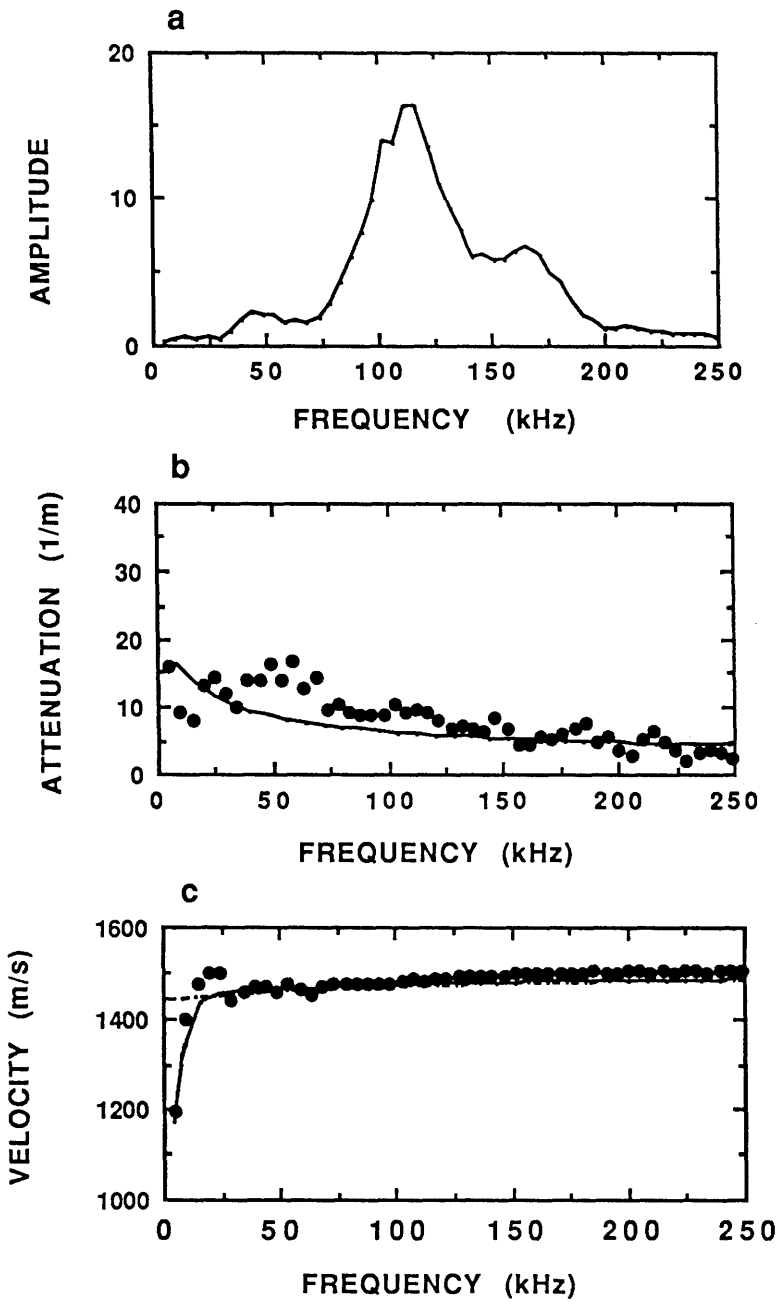

Figure 4-11: Experimental results versus theoretical predictions for the hard formation (aluminum) model. (a) Wave amplitude spectrum. (b) Measured Stoneley attenuation (dots) and the theoretical attenuation (solid curve). (c) Measured Stoneley velocity (dots) versus theory (solid curve). Note that in (c), at very low frequencies the experimental velocity decreases with decreasing frequency, as predicted by the theory.

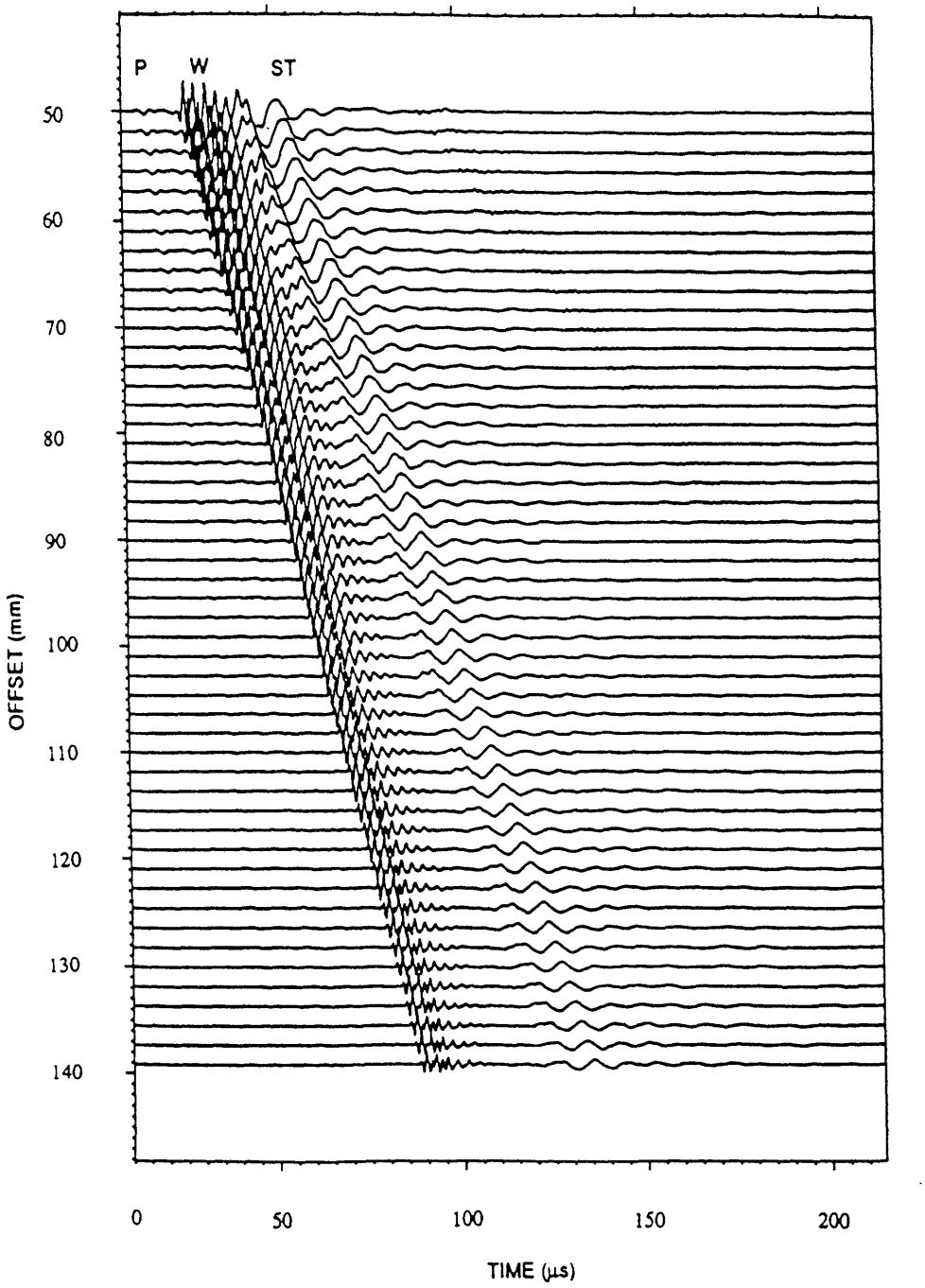

Figure 4-12: Waveform array data received in the lucite model. The labels are: P: leaky-P waves, W: "water" waves, and ST: Stoneley waves. Note that the Stoneley wave rapidly attenuates with increasing source-receiver distance.

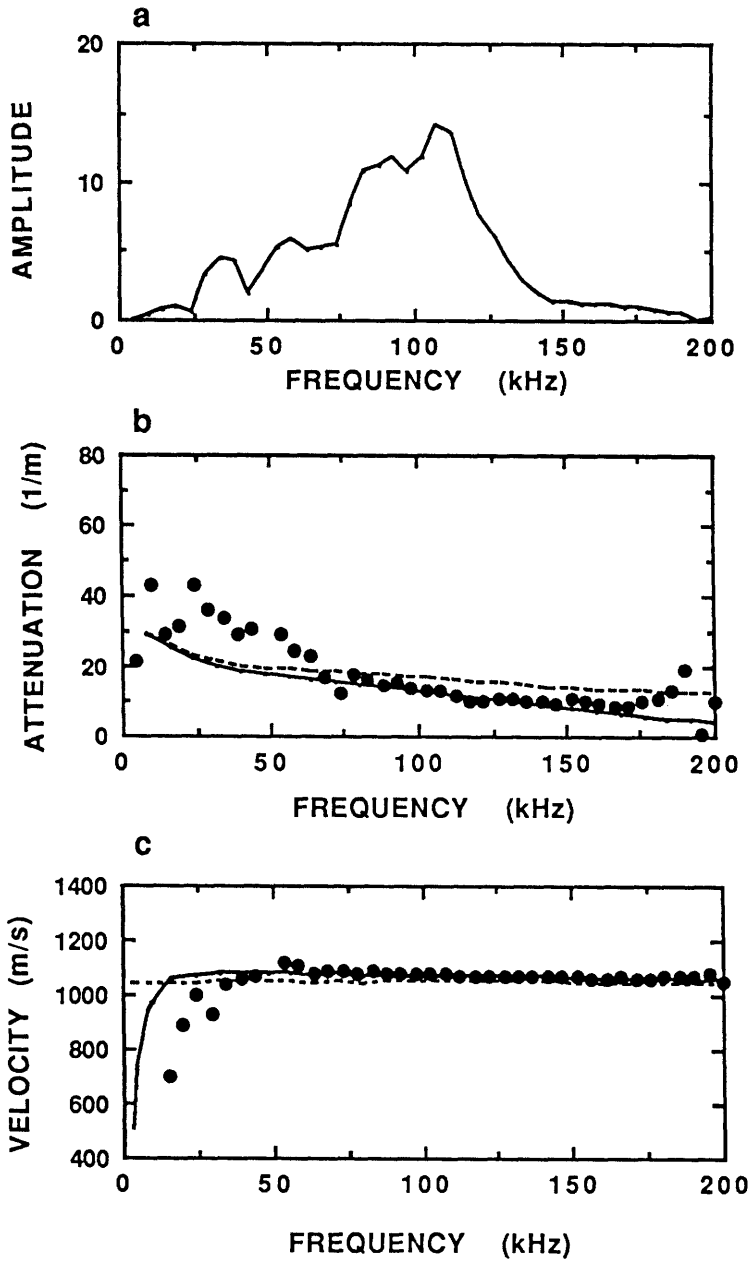

Figure 4-13: Experimental results versus theory for the soft formation (lucite) model. (a) Wave amplitude spectrum. (b) Measured Stoneley attenuation (dots) and the theoretical attenuation (solid curve). (c) Measured Stoneley velocity (dots) versus theory (solid curve). The Stoneley velocity of an unfractured borehole (dashed curve) is also plotted.

Chapter 5

Acoustic Wave Propagation in a Fluid-filled Borehole With a Horizontal Fracture

5.1 Introduction

The characterization of borehole fractures is important in reservoir evaluation and hydrocarbon production. Full waveform acoustic logs provide a means of fracture detection and characterization. Field measurements have shown effects of permeable fractures on the attenuation of borehole acoustic waves (Paillet, 1980; Hsu et al., 1985; Hardin et al., 1987; Brie et al., 1988). Borehole Stoneley (or tube) waves have been of special interest because these waves dominate the low frequency portion of the acoustic logs. In Chapter 4, the effects of a vertical borehole fracture on the Stoneley propagation have been studied. It was shown that the major effects are the Stoneley attenuation due to fluid flow into the fracture. In the present chapter, the problem of borehole guided wave propagation across a horizontal fracture will be treated. This problem has been treated by several authors using finite-difference modeling (Stephen, 1986; Stephen et al., 1985; Bhashvanija, 1983). These calculations require

large fracture apertures in the modeling because of the number of nodal points needed to resolve effects of the fracture. In addition, although these calculations display the wave characteristics in the vicinity of the fracture, the response of each individual wave component, such as pseudo-Rayleigh or Stoneley mode, to the fracture is not easy to resolve because of the overlap of the waveforms in the time domain. Therefore, the major purpose of the present study is to analyze the effects of fractures with different apertures on the borehole guided waves. The results are expected to provide useful information for fracture detection and characterization using acoustic logging techniques.

The borehole guided waves, or Stoneley and pseudo-Rayleigh waves, are the dominant waves on an acoustic log. Their response to the effects of a fracture will be easily recognized in terms of changes in the wave amplitude. In the presence of a horizontal fracture, the problem becomes more complicated than the case of a vertical fracture because, in addition to the fluid flow into the fracture, the scattering effects of the fracture should also be considered. A borehole guided wave is coupled with the wave motion in the formation. This coupling will be affected when the formation wave energy encounters a discontinuity (the fracture). For the fluid flow effects, a simple model has been developed in Chapter 2 to account for the Stoneley attenuation due to these effects. Hornby et al. (1989) have also presented a similar model for this problem. The two models are identical when the viscosity of the fluid is neglected. In both models, the fracture surfaces were modeled as rigid and Stoneley wave attenuation occurs because of the fluid flow into the fracture. In the present study, the treatment will be extended to incorporate scattering effects of the fracture by matching the boundary conditions at the fracture surfaces. Borehole pseudo-Rayleigh waves will also be included.

The present problem involves treating a discontinuity that intersects the direction of borehole wave propagation. Because of the discontinuity, the problem cannot be solved using the conventional wavenumber integration technique (Cheng and Toksöz,

1981). The difficulty lies in the necessity that the solutions must satisfy conditions at two perpendicular boundaries, i.e., the borehole boundary and the fracture surfaces. However, if modal solutions for the borehole propagation are used, the boundary conditions at the borehole boundary are automatically satisfied and one can use the sum of the modes to match boundary conditions at the fracture surfaces. Although the combination of the borehole leaking modes can be used for this purpose, the multivaluedness of these modal functions will force one to perform integrations along contours on the complex frequency and wavenumber planes (Haddon, 1987, 1989), which is inconvenient for the present problem where boundary conditions at the fracture are matched for each real frequency. This study will adopt a hybrid method used by Tsang (1985, 1987) and Nolet et al. (1989). An artificial boundary is introduced at a radial distance that is large compared to the borehole radius. This boundary generates discrete wave modes, which form a basis for the solutions in the regions separated by the fracture. Boundary conditions at the fracture surfaces then couple the solutions in the two regions. This coupling results in the transmission and reflection of the incident borehole acoustic waves.

5.2 Theoretical Formulation

Consider the borehole and fracture configuration shown in Figure 5-1. The fracture is modeled as a horizontal fluid layer with thickness L, which crosses the borehole perpendicularly. The fracture separates the domain of propagation into two regions. If taking the borehole axis as z, the upper region is the $z < 0$ region, while the lower one is the $z > L$ region. The formation for the two regions is an isotropic homogeneous elastic solid, with compressional and shear velocities V_p and V_s, and density ρ. The borehole and the fracture are filled with the same fluid having acoustic velocity V_f and density ρ_f. In either the upper or lower region, the borehole fluid displacement potential ϕ_f and the formation compressional and shear displacement potentials ϕ_s

and ψ_s satisfy the following wave equations:

$$\begin{aligned} \nabla^2\phi_f + k_f^2\phi_f &= 0 \ , \\ \nabla^2\phi_s + k_p^2\phi_s &= 0 \ , \\ \nabla^2\psi_s + k_s^2\psi_s &= 0 \ , \end{aligned} \tag{5.1}$$

where

$$\nabla^2 = \frac{\partial^2}{\partial r^2} + \frac{1}{r}\frac{\partial}{\partial r} + \frac{\partial^2}{\partial z^2}$$

is the cylindrical Laplace operator, r is the radial variable, $k_f = \omega/V_f$, $k_p = \omega/V_p$, $k_s = \omega/V_s$, and ω is the angular frequency. In this problem, the azimuthal symmetry is assumed. From the potentials, the fluid and formation displacement vectors $\vec{u}_f$ and $\vec{u}_s$ are calculated using

$$\begin{aligned} \vec{u}_f &= \nabla\phi_f \ , \\ \vec{u}_s &= \nabla\phi_s + \nabla \times (\psi_s \vec{e}_\theta) \ , \end{aligned} \tag{5.2}$$

where $\vec{e}_\theta$ is the unit vector tangential to a circle of radius r (Biot, 1952). In the frequency domain, the fluid stresses are simply

$$\sigma_{rrf} = \sigma_{zzf} = -\rho_f \omega^2 \phi_f \ , \tag{5.3}$$

and the formation stress components are calculated using

$$\begin{aligned} \sigma_{rrs} &= \lambda[\frac{1}{r}\frac{\partial}{\partial r}(ru_{rs}) + \frac{\partial u_{zs}}{\partial z}] + 2\mu\frac{\partial u_{rs}}{\partial r} \ , \\ \sigma_{zzs} &= \lambda[\frac{1}{r}\frac{\partial}{\partial r}(ru_{rs}) + \frac{\partial u_{zs}}{\partial z}] + 2\mu\frac{\partial u_{zs}}{\partial z} \ , \\ \sigma_{rzs} &= \mu(\frac{\partial u_{rs}}{\partial z} + \frac{\partial u_{zs}}{\partial r}) \ , \end{aligned} \tag{5.4}$$

where λ and μ are Lamé constants of the formation and can be calculated from the given V_p, V_s, and ρ of the formation.

5.2.1 Construction of Modal Solutions

In order to generate modal solutions for the problem, one places an artificial boundary at $r = d$ ($d \gg a$). At this boundary, the displacement components u_{rs} and u_{zs} are let

to vanish so that it represents a rigid boundary. At the borehole boundary $r = a$, one has the continuity of the normal stress and radial displacement, and the vanishing of the formation shear stress. With the given radial boundaries, the solutions to equations 5.1 can be written as

$$\begin{aligned} \phi_f &= AI_0(fr)\exp(ikz) \ , \\ \phi_s &= [BK_0(lr) + B'I_0(lr)]\exp(ikz) \ , \\ \psi_s &= [CK_1(mr) + C'I_1(mr)]\exp(ikz) \ , \end{aligned} \tag{5.5}$$

with radial wavenumbers given as

$$f = \sqrt{k^2 - k_f^2} \ , \quad l = \sqrt{k^2 - k_p^2} \ , \quad m = \sqrt{k^2 - k_s^2} \ , \tag{5.6}$$

where k is the axial wave number, I_n and K_n $(n = 0, 1)$ are the first and second kind modified Bessel functions of order n, respectively, and A, B, B', C, and C' are constants to be determined. From the potentials in equations 5.5, the stress and displacement components can be calculated using equations 5.2, 5.3, and 5.4. They are given in Appendix A. By using the boundary conditions at $r = a$ and $r = d$, a system of equations for determining the constants in equations 5.5 is obtained as follows

$$\begin{bmatrix} a_{11} & a_{12} & a_{13} & a_{14} & a_{15} \\ a_{21} & a_{22} & a_{23} & a_{24} & a_{25} \\ 0 & a_{32} & a_{33} & a_{34} & a_{35} \\ 0 & a_{42} & a_{43} & a_{44} & a_{45} \\ 0 & a_{52} & a_{53} & a_{54} & a_{55} \end{bmatrix} \begin{bmatrix} A \\ B \\ B' \\ C \\ C' \end{bmatrix} = 0 \ , \tag{5.7}$$

where the matrix elements a_{ij} are given by

$$\begin{aligned} a_{11} &= k_f^2 I_0(fa) \ , \\ a_{12} &= [(\lambda/\lambda_f)(l^2 - k^2) + 2(\mu/\lambda_f)l^2]K_0(la) + 2(\mu/\lambda_f)(l/a)K_1(la) \ , \\ a_{13} &= 2(\mu/\lambda_f)ikm[K_0(ma) + K_1(ma)/(ma)] \ , \\ a_{14} &= [(\lambda/\lambda_f)(l^2 - k^2) + 2(\mu/\lambda_f)l^2]I_0(la) - 2(\mu/\lambda_f)(l/a)I_1(la) \ , \end{aligned}$$

$$
\begin{aligned}
a_{15} &= -2(\mu/\lambda_f)ikm[I_0(ma) - I_1(ma)/(ma)] \ , \\
a_{21} &= fI_1(fa) \ , \\
a_{22} &= lK_1(la) \ , \\
a_{23} &= ikK_1(ma) \ , \\
a_{24} &= -lI_1(la) \ , \\
a_{25} &= ikI_1(ma) \ , \\
a_{32} &= -2iklK_1(la) \ , \\
a_{33} &= (k^2 + m^2)K_1(ma) \ , \\
a_{34} &= 2iklI_1(la) \ , \\
a_{35} &= (k^2 + m^2)I_1(ma) \ , \\
a_{42} &= ikK_0(ld) \ , \\
a_{43} &= -mK_0(md) \ , \\
a_{44} &= ikI_0(ld) \ , \\
a_{45} &= mI_0(md) \ , \\
a_{52} &= -lK_1(ld) \ , \\
a_{53} &= -ikK_1(md) \ , \\
a_{54} &= lI_1(ld) \ , \\
a_{55} &= -ikI_1(md) \ ,
\end{aligned}
$$

where $\lambda_f = \rho_f V_f^2$ is the fluid modulus. The condition that there be nontrivial solutions for A, B, B', C, and C' requires that the determinant of equation 5.7 (denoted by D) vanish. This leads to

$$D(k,\omega) = 0 \ . \tag{5.8}$$

For a given frequency ω, equation 5.8 determines M number of values for k, denoted by k_α ($\alpha = 1, 2, \cdots, M$). Each k_α is associated with a wave mode. As already shown by Tsang (1987), for real ω these k values are located at the real and imaginary k axes. The mode with $k_\alpha > k_f$ is the well known Stoneley wave; the modes with

$k_f > k_\alpha > k_s$ are the pseudo-Rayleigh modes. The Stoneley and pseudo-Rayleigh are guided waves that are trapped in the borehole and are therefore insensitive to the boundary at $r = d$ if $d \gg a$. The modes with $Re\{k_\alpha\} < k_s$ are radiation modes. The fact that their locations coincide with the Sommerfeld branch cut indicates that the mode locations represent the discretization of the branch cut, and the sum of the modes approximates the contribution from this branch cut (Tsang, 1987). Therefore, the total modes form a basis for the solution to the borehole wave motion. The wave motion of each mode is distributed both in the borehole and in the formation, as shown in equations 5.5. The constants in equations 5.5 govern this distribution. After k_α is evaluated, the normalized eigenvector for the constants is found by solving equation 5.7 with A set to 1. The αth eigenvector is denoted by [1, B_α, B'_α, C_α, C'_α].

It is worthwhile to mention some of the numerical manipulations that are required to calculate the roots of equation 5.8 and their associated eigenvectors. Because the radial boundary $r = d$ is a large number, the modified Bessel functions I_n $(n = 0, 1)$ evaluated at this boundary may create overflow problems. To overcome this difficulty, one makes the following substitutions:

$$\begin{aligned} B'' &= B' I_0(ld) \quad , \quad (\text{if } k > k_p) \\ C'' &= C' I_0(md) \quad , \quad (\text{if } k > k_s) \, . \end{aligned} \tag{5.9}$$

When equations 5.9 are used, the the fourth and fifth columns of the matrix in equation 5.7 are modified as:

$$\begin{aligned} a_{i4} &\rightarrow a_{i4}/I_0(ld) \, , \quad (\text{if } \; k > k_p) \\ a_{i5} &\rightarrow a_{i5}/I_0(md) \, , \quad (\text{if } \; k > k_s) \end{aligned}$$

where i =1,2,3,4, and 5. Once B'' and C'' are found from the modified equation 5.7, equations 5.9 are used to recover B' and C'. The overflow problem is thus overcome.

Another manipulation is in the root finding procedure of equation 5.8. The modes are generally close together around k_p and k_s (Tsang, 1987). This behavior poses some difficulty in locating these modes. It is therefore advisable to locate the modes using l

instead of k when k is around k_p, and using m when k is around k_s. This can be seen by noting a relation that can be derived from equations 5.6, i.e., $dl = kdk/\sqrt{k^2 - k_p^2}$; when k is close to k_p, the separation dl on the l axis is much bigger than dk on the k axis. The same is true for dm.

Tsang (1987) has shown that the modes so determined satisfy the following orthogonality relation

$$\begin{aligned} W(k_\beta)\delta_{\alpha\beta} &= \int_0^a \sigma_{zzf}(k_\beta, r) u_{zf}(k_\alpha, r) r dr \\ &+ \int_a^d [\sigma_{zzs}(k_\beta, r) u_{zs}(k_\alpha, r) - \sigma_{rzs}(k_\alpha, r) u_{rs}(k_\beta, r)] r dr \ , \end{aligned} \tag{5.10}$$

where $\delta_{\alpha\beta}$ is the Kronecker delta. The normalization constant $W(k_\alpha)$ is given by (Tsang, 1987)

$$W(k_\alpha) = -\frac{i\rho_f \omega^2}{2} \frac{(\partial D/\partial k_\alpha)(\omega, k_\alpha)}{N(\omega, k_\alpha)} \ , \tag{5.11}$$

where $N(\omega, k_\alpha)$ is the determinant of a 5×5 matrix. This matrix is obtained from the one in equation 5.7 by replacing a_{11} with $-k_f^2 K_0(fa)$ and a_{21} with $fK_1(fa)$, respectively. Equation 5.11 can be readily derived from the evaluation of the mode amplitude using the theorem of residues (see Tsang, 1987). The factor $-i\rho_f\omega^2/2$ in equation 5.11 was given as $-\rho_f\omega^2/\pi$ in Tsang's (1987) equation 9. This is because Hankel and Bessel functions were used in Tsang's (1989) formulation, and here the first and second kind modified Bessel functions are used in the present formulation. The orthogonality equation given in equation 5.10 is an important relation that will later be used to determine the mode coupling at the fracture surfaces.

5.2.2 Solution of Wave Motion in the Fracture Fluid Layer

The solution for the fracture fluid wave motion is needed in order to couple the wave motions in the two regions separated by the fracture. The fracture fluid displacement potential ϕ satisfies the wave equation

$$\frac{1}{r}\frac{\partial}{\partial r}(r\frac{\partial \phi}{\partial r}) + \frac{\partial^2 \phi}{\partial z^2} + k_f^2 \phi = 0 \ , \quad (0 < r < d \ , \ 0 < z < L) \ . \tag{5.12}$$

In terms of ϕ, the fluid displacement $\vec{u}$ and pressure p are given by

$$\begin{aligned} \vec{u} &= \nabla\phi \ , \\ p &= \rho_f \omega^2 \phi \ . \end{aligned} \tag{5.13}$$

At $r = d$, the fluid motion is let to satisfy the same rigid boundary condition as in either the upper or lower region, i.e.,

$$\frac{\partial \phi}{\partial r} = 0 \ , \ (\text{at } r = d) \ . \tag{5.14}$$

At the fracture surfaces $z = 0$ and $z = L$, one prescribes the values of ϕ, which are related to the normal stresses σ_{zzf} and σ_{zzs} of the two regions through the continuity of these stresses. To find the solution of equation 5.12 with the given boundary conditions, one first solves the Green's function determined by the following boundary value problem.

$$\frac{1}{r}\frac{\partial}{\partial r}(r\frac{\partial G}{\partial r}) + \frac{1}{r^2}\frac{\partial^2 G}{\partial \theta^2} + \frac{\partial^2 G}{\partial z^2} + k_f^2 G = -\frac{4\pi}{r}\delta(r - r_0)\delta(\theta - \theta_0)\delta(z - z_0) \ , \tag{5.15}$$

with

$$G = 0 \ , \ (\text{at } z = 0 \text{ and } L) \ ; \ \frac{\partial G}{\partial r} = 0 \ , \ (\text{at } r = d)$$

where θ is the azimuthal variable, (r_0, θ_0, z_0) and (r, θ, z) are source and field points, respectively, and δ is the Dirac delta function. Following the procedures for finding Green's function (Morse and Feshbach, 1953), the solution to equation 5.15 is found to be

$$\begin{aligned} &G(r, \theta, z, \omega; r_0, \theta_0, z_0) = \\ &\frac{4}{d^2}\sum_{m,n} \frac{e^{im(\theta - \theta_0)} J_m(\zeta_{mn} r) J_m(\zeta_{mn} r_0)}{(1 - m^2/\zeta_{mn}^2) J_m^2(\zeta_{mn} d)} \frac{\sinh(\sqrt{\zeta_{mn}^2 - k_f^2}\ z_<) \sinh[\sqrt{\zeta_{mn}^2 - k_f^2}(L - z_>)]}{\sqrt{\zeta_{mn}^2 - k_f^2}\ \sinh(\sqrt{\zeta_{mn}^2 - k_f^2} L)} \ , \end{aligned} \tag{5.16}$$

where

$$z_< = \min(z, z_0) \ , \text{ and } \ z_> = \max(z, z_0) \ ,$$

the symbol sinh represents the hyperbolic function, J_m is the mth order Bessel function, and $\zeta_{mn}d$ is the nth root of

$$J'_m(\zeta_{mn}d) = 0 \ , \quad n = 1,2,3,\cdots \ , \tag{5.17}$$

where the prime denotes taking the derivative. By using Green's theorem, ϕ is expressed as

$$\phi = \frac{1}{4\pi}\iint_{S_0}(G\frac{\partial\phi}{\partial n_0} - \phi\frac{\partial G}{\partial n_0})dS_0 \ , \tag{5.18}$$

where n_0 is the outward normal to the boundary surface S_0, which now includes the upper and lower surfaces of the fluid layer, as well as the circular strip at $r = d$. Using the respective boundary conditions for ϕ and G at $z = 0$ and L, and $r = d$, one can express ϕ using the surface integrals over the upper and lower surfaces of the fracture fluid layer.

$$\phi = \frac{1}{4\pi}\iint_{z_0=0}\phi\frac{\partial G}{\partial z_0}dS_0 - \frac{1}{4\pi}\iint_{z_0=L}\phi\frac{\partial G}{\partial z_0}dS_0 \tag{5.19}$$

Because of the azimuthal symmetry in ϕ and the orthogonality of the function $\exp(im\theta_0)$ over the interval [0-2π], the integration over S_0 knocks out all the $m \neq 0$ terms in the Green's function given in equation 5.16. Thus one only needs to use the $m = 0$ terms of this equation. In addition, for $m = 0$, equation 5.17 becomes

$$J_1(\zeta_n d) = 0 \ , \quad n = 1,2,3\cdots \ . \tag{5.20}$$

Without using all the roots of equation 5.17, the summation in equation 5.16 is now only over the positive roots (including the root $\zeta d = 0$) of equation 5.20. In the following, equation 5.19 will be used to couple the wave motions at both sides of the fracture.

5.2.3 Determination of Transmission and Reflection of Incident Waves

One now lets a borehole wave be incident on the fracture and determines transmission and reflection. In the $z < 0$ region there are incident and reflected waves, while in

the $z > L$ region, there are only transmitted waves. The reflected waves propagate in negative z direction and have $\exp(-ik_\alpha z)$ dependencies. It has been shown (Tsang, 1987) that replacing k_α with $-k_\alpha$ will not change the sign of σ_{zzs}, σ_{zzf}, and u_{rs} but will reverse the sign of u_{zf}, u_{zs}, and σ_{rzs}. In the following, this property will be used to write the boundary conditions at the $z = 0$ surface. At this surface, one has the continuity of normal stress and displacement, and the vanishing of shear stress. In the $z < 0$ region, these quantities are expressed by the linear combination of the incident and reflected modes, while in the fracture fluid layer the pressure and displacement are derived from equations 5.13 and 5.19. One therefore has the following equations for the $z = 0$ surface:

For $0 < r \leq a$

$$\sum_\alpha (b_\alpha^+ - b_\alpha^-) u_{zf}(k_\alpha, r) = \frac{\partial \phi}{\partial z} , \tag{5.21}$$

$$\sum_\alpha (b_\alpha^+ + b_\alpha^-) \sigma_{zzf}(k_\alpha, r) = -\rho_f \omega^2 \phi . \tag{5.22}$$

For $a < r \leq d$

$$\sum_\alpha (b_\alpha^+ - b_\alpha^-) u_{zs}(k_\alpha, r) = \frac{\partial \phi}{\partial z} , \tag{5.23}$$

$$\sum_\alpha (b_\alpha^+ + b_\alpha^-) \sigma_{zzs}(k_\alpha, r) = -\rho_f \omega^2 \phi , \tag{5.24}$$

$$\sum_\alpha (b_\alpha^+ - b_\alpha^-) \sigma_{rzs}(k_\alpha, r) = 0 , \tag{5.25}$$

where b_α^+ and b_α^- are amplitude coefficients of the αth incident and reflected wave modes, respectively. One then makes use of the orthogonality relation (equation 5.10) to relate these equations. Multiply equation 5.21 by $\sigma_{zzf}(k_\beta, r)r$ and integrate from 0 to a. Next, multiply equation 5.23 by $\sigma_{zzs}(k_\beta, r)r$ and equation 5.25 by $-u(k_\beta, r)r$ and integrate from a to d. Add the equations together and apply equation 5.10 to the left hand side of the resulting equation. One obtains

$$W(k_\beta)(b_\beta^+ - b_\beta^-) = \int_0^d \sigma_{zz}(k_\beta, r) \left. \frac{\partial \phi}{\partial z} \right|_{z=0} r dr , \tag{5.26}$$

where the normal stress σ_{zz} equals σ_{zzs} in the formation and σ_{zzf} in the borehole. Similarly, one matches boundary conditions at the lower boundary $z = L$ using the

transmitted wave modes and the fracture fluid pressure and displacement.

For $0 < r \leq a$

$$\sum_{\alpha} c_{\alpha}^{+} u_{zf}(k_{\alpha}, r) = \frac{\partial \phi}{\partial z} \ , \tag{5.27}$$

$$\sum_{\alpha} c_{\alpha}^{+} \sigma_{zzf}(k_{\alpha}, r) = -\rho_f \omega^2 \phi \ . \tag{5.28}$$

For $a < r \leq d$

$$\sum_{\alpha} c_{\alpha}^{+} u_{zs}(k_{\alpha}, r) = \frac{\partial \phi}{\partial z} \ , \tag{5.29}$$

$$\sum_{\alpha} c_{\alpha}^{+} \sigma_{zzs}(k_{\alpha}, r) = -\rho_f \omega^2 \phi \ , \tag{5.30}$$

$$\sum_{\alpha} c_{\alpha}^{+} \sigma_{rzs}(k_{\alpha}, r) = 0 \ , \tag{5.31}$$

where c_{α}^{+} is the amplitude coefficient of the αth transmitted wave mode. In equations 5.27 through 5.31, a factor $\exp(ik_{\alpha}L)$ is absorbed in c_{α}^{+} because these equations are evaluated at the $z = L$ surface. Again, following the same procedure as for the upper boundary $z = 0$, one obtains

$$W(k_{\beta}) c_{\beta}^{+} = \int_0^d \sigma_{zz}(k_{\beta}, r) \left. \frac{\partial \phi}{\partial z} \right|_{z=L} r dr \ . \tag{5.32}$$

To get $\frac{\partial \phi}{\partial z}$ needed in equations 5.26 and 5.32, one differentiates equation 5.19 with respect to z. This results in

$$\frac{\partial \phi}{\partial z} = \frac{1}{4\pi} \iint_{z_0=0} \phi \frac{\partial^2 G}{\partial z \partial z_0} dS_0 - \frac{1}{4\pi} \iint_{z_0=L} \phi \frac{\partial^2 G}{\partial z \partial z_0} dS_0 \ . \tag{5.33}$$

At this stage, however, mathematical difficulty arises when one lets $z \rightarrow 0$ and $z \rightarrow L$ to obtain the surface values of $\frac{\partial \phi}{\partial z}$. This is because the kernel of the integrals $\frac{\partial^2 G}{\partial z \partial z_0}$ is strongly singular in view of the discontinuity in G as a function of the field point, when the source point is on the boundary surface (Morse and Feshbach, 1953). The integrals are therefore non-integrable in the classical sense. Nevertheless, multiplying equations like equation 5.33 by a regularizing function and integrating over the field points may regularize this kind of problem (Delves and Walsh, 1974), providing that this function has good behavior over the domain of integration. In the present case,

the regularizing function is $\sigma_{zz}(k_\beta, r)$ in equations 5.26 and 5.32. However, the integrals in these two equations are still singular because σ_{zz} is discontinuous at $r = a$ [$\sigma_{zzf}(k, a) \neq \sigma_{zzs}(k, a)$]. One therefore defines a continuous stress function

$$\sigma^1_{zz}(k_\beta, r) = \begin{cases} \sigma_{zzs}(k_\beta, r) & , \ (a < r \leq d) \\ \sigma_{zzf}(k_\beta, r) + [\sigma_{zz}(k_\beta, a)]H(a - r) & , \ (0 < r \leq a) \end{cases} \tag{5.34}$$

where $[\sigma_{zz}(k, a)] = \sigma_{zzs}(k, a) - \sigma_{zzf}(k, a)$ is the normal stress discontinuity at the borehole boundary $r = a$ and $H(a - r)$ is the step function. By using σ^1_{zz}, the integrals in equations 5.26 and 5.32 become

$$\int_0^d \sigma_{zz}(k_\beta, r)\frac{\partial \phi}{\partial z} r dr = \int_0^d \sigma^1_{zz}(k_\beta, r)\frac{\partial \phi}{\partial z} r dr - [\sigma_{zz}(k_\beta, a)] \int_0^a \frac{\partial \phi}{\partial z} r dr \ . \tag{5.35}$$

Because the discontinuity is removed from σ^1_{zz}, the first term of equation 5.35 is now regular. By substituting $\phi|_{z_0=0}$ given in equations 5.22 and 5.24 and $\phi|_{z_0=L}$ in equations 5.28 and 5.30 into equation 5.33, this term, evaluated at $z = 0$ and L, may now be respectively written as

$$\begin{aligned} \int_0^d \sigma^1_{zz}(k_\beta, r)\frac{\partial \phi}{\partial z}\bigg|_{z=0} r dr &= \sum_\alpha (b^+_\alpha + b^-_\alpha)\Theta_{\alpha\beta} - \sum_\alpha c^+_\alpha \Theta'_{\alpha\beta} \ , \\ \int_0^d \sigma^1_{zz}(k_\beta, r)\frac{\partial \phi}{\partial z}\bigg|_{z=L} r dr &= \sum_\alpha (b^+_\alpha + b^-_\alpha)\Theta'_{\alpha\beta} - \sum_\alpha c^+_\alpha \Theta_{\alpha\beta} \ , \end{aligned} \tag{5.36}$$

with

$$\begin{pmatrix} \Theta_{\alpha\beta} \\ \Theta'_{\alpha\beta} \end{pmatrix} = \frac{2}{d^2 \rho_f \omega^2} \sum_{\zeta_n} \frac{I(k_\alpha, \zeta_n) I_1(k_\beta, \zeta_n)}{J_0^2(\zeta_n d)} \frac{\sqrt{\zeta_n^2 - k_f^2}}{\sinh(\sqrt{\zeta_n^2 - k_f^2}\, L)} \begin{pmatrix} \cosh(\sqrt{\zeta_n^2 - k_f^2}\, L) \\ 1 \end{pmatrix} , \tag{5.37}$$

where the summation in equations 5.37 is over the roots of equation 5.20 and

$$I(k_\alpha, \zeta_n) = \int_0^d \sigma_{zz}(k_\alpha, r) J_0(\zeta_n r) r dr \tag{5.38}$$

$$I_1(k_\beta, \zeta_n) = \int_0^d \sigma^1_{zz}(k_\beta, r) J_0(\zeta_n r) r dr \tag{5.39}$$

can be analytically integrated out and are listed in Appendix B. The second term in equation 5.35 carries the singularity of the problem (using equations 5.16 and

5.33, one can show that this term is divergent). Since the integration of this term is over the borehole area, it can be regularized using a physical model based on the conservation of mass. From equation 5.13, one can see that $\frac{\partial \phi}{\partial z}\Big|_{z=L}$ is the axial borehole fluid displacement at the lower boundary $z = L$. Multiplying this term by $-i\omega$ and integrating over the borehole area gives the borehole fluid flux through the boundary. Based on the conservation of mass, the difference between the flux through the $z = L$ boundary and that through the $z = 0$ boundary equals the fluid flux into the fracture. Thus one has

$$-i\omega 2\pi \int_0^a \frac{\partial \phi}{\partial z}\Big|_{z=L} r dr + i\omega 2\pi \int_0^a \frac{\partial \phi}{\partial z}\Big|_{z=0} r dr = 2\pi a q \ , \tag{5.40}$$

where q is the volume flow rate per unit fracture length. According to the theory of dynamic conductivity of an open fracture, as studied in Chapter 2 , q is given by (equation 2.35)

$$q = -\bar{C}\frac{\partial p}{\partial r} \ , \ (r = a) \tag{5.41}$$

where $\bar{C}$ is the fracture dynamic conductivity and $\frac{\partial p}{\partial r}$ is the dynamic pressure gradient at the fracture opening. If one assumes that the viscous skin depth of the fluid is small compared to the fracture aperture L, $\bar{C}$ is then given by (equation 2.38)

$$\bar{C} = \frac{iL}{\omega \rho_f} \ . \tag{5.42}$$

As discussed in section 2.4 of Chapter 2, this formula holds true even though the formation bounding the fracture is elastic. In addition, as in the case of a vertical fracture studied in Chapter 4, it is assumed that the fluid flux is carried away mainly by the fracture fundamental wave mode. The pressure associated with this wave is given by the Hankel function $p_0 H_0^{(1)}(k_{fr} r)/H_0^{(1)}(k_{fr} a)$, where p_0 is the pressure at the fracture opening and the fracture wavenumber k_{fr} is found by solving the fracture wave dispersion equation (equation 4.24) for the fundamental mode. The pressure gradient at the fracture opening is obtained as

$$\frac{\partial p}{\partial r} = -p_0 k_{fr} \frac{H_1^{(1)}(k_{fr} a)}{H_0^{(1)}(k_{fr} a)} \ . \tag{5.43}$$

As an approximation, one can assume that p_0 is the average of the borehole pressures of the upper and lower surfaces evaluated at $r = a$. Using equations 2.22 and 2.28, one has

$$p_0 = \frac{1}{2}\rho_f\omega^2(\phi|_{z=0} + \phi|_{z=L})|_{r=a} = -\frac{1}{2}\sum_\alpha (b_\alpha^+ + b_\alpha^- + c_\alpha^+)\sigma_{zzf}(k_\alpha, a) \ . \tag{5.44}$$

With q determined, equation 5.40 is used to regularize the second term of equation 5.35. To couple the fluid flow at $z = 0$ and $z = L$, one expresses the flux through $z = 0$ using q and the flux through $z = L$. The latter flux is calculated with $\frac{\partial\phi}{\partial z}\Big|_{z=L}$ given in equation 5.21. Similarly, one expresses the flux through $z = L$ using q and the flux through $z = 0$. The latter flux is calculated using the surface value of $\frac{\partial\phi}{\partial z}\Big|_{z=0}$ given in equation 5.27. Finally, the following coupled matrix equations are obtained for vectors $\mathbf{b}^-$ and $\mathbf{c}^+$, which respectively contain the reflected and transmitted amplitude coefficients.

$$\begin{aligned} \mathbf{W}\mathbf{c}^+ &= \mathbf{\Theta}'(\mathbf{b}^+ + \mathbf{b}^-) - \mathbf{\Theta}\mathbf{c}^+ - \mathbf{N}(\mathbf{b}^+ + \mathbf{b}^- + \mathbf{c}^+) - \mathbf{K}(\mathbf{b}^+ - \mathbf{b}^-) \ , \\ \mathbf{W}(\mathbf{b}^+ - \mathbf{b}^-) &= \mathbf{\Theta}(\mathbf{b}^+ + \mathbf{b}^-) - \mathbf{\Theta}'\mathbf{c}^+ + \mathbf{N}(\mathbf{b}^+ + \mathbf{b}^- + \mathbf{c}^+) + \mathbf{K}\mathbf{c}^+ \ , \end{aligned} \tag{5.45}$$

where $\mathbf{W}$ is a diagonal matrix with the $\beta\beta$ element equal to $W(k_\beta)$, $\mathbf{\Theta}$ and $\mathbf{\Theta}'$ have been defined in equations 5.37, and $\mathbf{K}$ and $\mathbf{N}$ are $M \times M$ square matrices whose elements are as follows

$$\begin{aligned} K_{\alpha\beta} &= (ik_\alpha a/f_\alpha)I_1(f_\alpha a)[\sigma_{zz}(k_\beta, a)] \ , \\ N_{\alpha\beta} &= (aL/2)I_0(f_\alpha a)[\sigma_{zz}(k_\beta, a)]k_{fr}H_1^{(1)}(k_{fr}a)/H_0^{(1)}(k_{fr}a) \ , \end{aligned} \tag{5.46}$$

where f_α is calculated by replacing k in f given in equations 5.6 with k_α. To solve the coupled matrix equations (equations 5.45), one can use the auxiliary vectors

$$\begin{aligned} \mathbf{x} &= (\mathbf{b}^- + \mathbf{c}^+)/\mathbf{2} \ , \\ \mathbf{y} &= (\mathbf{b}^- - \mathbf{c}^+)/\mathbf{2} \ , \end{aligned} \tag{5.47}$$

and obtains the following decoupled matrix equations for $\mathbf{x}$ and $\mathbf{y}$, respectively.

$$\begin{aligned} (\mathbf{W} - \mathbf{\Theta} - \mathbf{\Theta}' + \mathbf{K})\mathbf{b}^+ &= (\mathbf{W} + \mathbf{\Theta} + \mathbf{\Theta}' + \mathbf{K})\mathbf{x} \ , \\ (\mathbf{W} - \mathbf{\Theta} + \mathbf{\Theta}' - \mathbf{K} - \mathbf{2N})\mathbf{b}^+ &= (\mathbf{W} + \mathbf{\Theta} - \mathbf{\Theta}' - \mathbf{K} + \mathbf{2N})\mathbf{y} \ . \end{aligned} \tag{5.48}$$

Once $\mathbf{x}$ and $\mathbf{y}$ are found by independently solving the above equations, the vectors $\mathbf{b}^-$ and $\mathbf{c}^+$ are obtained using equations 5.47, and the transmission and reflection of the incident wave are thus determined.

It is convenient here to give a short discussion on the present theory and its relevance to previous model given in Chapter 2, as well as the one developed by Hornby et al., (1989). In the above theoretical development, one balances the fluid flow across and into the fracture in order to overcome the singularity problem. This technique has been used in Chapter 2, and by and Hornby et al. (1989) in the modeling of Stoneley attenuation across a fracture. In addition to the fluid flow feature of the previous models, the present theory includes effects of mode conversion at the fracture by matching the boundary condition at fracture surfaces. Thus it is expected that there are similarities and differences between the present model and previous models. In addition, the balance of fluid flow is appropriate for the incidence of guided waves that are trapped in the borehole, since these waves can produce an effective borehole pressure to drive the flow into the fracture. Therefore, the present study is primarily concerned with the determination of the transmission and reflection for the guided wave incidence.

Let a guided wave mode with amplitude coefficient b_α^+ be incident on the fracture, one can calculate the resulting transmitted and reflected amplitude coefficients c_α^+ and b_α^- corresponding to the same mode (Stoneley or pseudo-Rayleigh). This defines the transmission and reflection coefficients of this wave mode.

$$\begin{aligned} T_{rs} &= c_\alpha^+ / b_\alpha^+ \ , \\ R_{fl} &= b_\alpha^- / b_\alpha^+ \ , \end{aligned} \tag{5.49}$$

where the subscript α refers to either Stoneley or pseudo-Rayleigh wave mode. In addition, synthetic microseismograms can also be calculated to show the effects of the fracture on the incident wave mode. Given a guided wave mode generated at a distance h above the fracture in the region I, one lets this mode be incident on the fracture. At the source, the amplitude coefficient is $1/W(k_{in})$ (Tsang, 1987), where

k_{in} is the wavenumber of the incident mode. At the upper fracture surface, this coefficient becomes

$$b_{in}^{+} = \frac{e^{ik_{in}h}}{W(k_{in})} \quad . \tag{5.50}$$

Upon interacting with the fracture, the incident wave energy is partly reflected and partly transmitted, together with some converted wave energy originating from the fracture. Thus in region I, the total borehole fluid pressure wave field is

$$P^{I} = \rho_f \omega^2 [b_{in}^{+} \phi_f(k_{in}, r) e^{ik_{in}z} + \sum_{\alpha} b_{\alpha}^{-} \phi_f(k_{\alpha}, r) e^{-ik_{\alpha}z}] \quad , \quad (z < 0) \quad . \tag{5.51}$$

In region II, this pressure field is

$$P^{II} = \rho_f \omega^2 \sum_{\alpha} c_{\alpha}^{+} \phi_f(k_{\alpha}, r) e^{ik_{\alpha}z} \quad , \quad (z > L) \quad . \tag{5.52}$$

In equations 5.51 and 5.52, the sum is over all the modes found from equation 5.8, and the axial distance z is measured from the upper fracture surface. In calculating the synthetics, equations 5.51 and 5.52 are convolved with a wave source. A Kelly source (Kelly et al., 1976; Stephen et al., 1985) is used in this study. Given a center frequency ω_0 of the source, one can choose the maximum frequency ω_{max} as $2.5\,\omega_0$. Starting from ω_{max}, one calculates the amplitude coefficients b_{α}^{-} and c_{α}^{+} of each wave mode for each decreasing frequency. After equations 5.51 and 5.52 are evaluated for each frequency, they are multiplied with the source spectrum and the products are transformed by the fast Fourier transform (FFT) into time domain to generate waveforms for each given distance z in regions I and II. In this way, synthetic microseismograms are obtained which display the wave characteristics in the vicinity of the fracture.

5.3 Theoretical Results and Discussion

In this section, the theoretical results are presented for the Stoneley and pseudo-Rayleigh waves, respectively. In the theoretical calculations, the borehole radius is $a = 10$ cm and the rigid boundary is set at $d = 130$ cm. The formation properties

are $V_p = 5$ km/s, $V_s = 3$ km/s, and $\rho = 2.5$ g/cm^3. The borehole fluid velocity and density are $V_f = 1.5$ km/s and $\rho_f = 1$ g/cm^3, respectively. In the summation of the modes, the mode series is truncated by neglecting those modes whose k_α values are on the imaginary k axis, since they are not traveling waves (see Nolet et al., 1989 and Tsang, 1985, 1987).

5.3.1 Stoneley Wave

The effects of the fracture on the incidence of Stoneley waves are first investigated. Before presenting the results in more detail, it is instructive to compare the present theory with the previous model given in Chapter 2. Figure 5-2 plots the transmission coefficients from the two models in a low frequency range of [0-5] kHz for a set of fracture apertures ranging from 0.5 cm to 5 cm. The two models are qualitatively similar in this low frequency range. Both models predict that the transmission across the fracture is reduced as the fracture aperture increases. The major significant difference is at low frequencies. Although both models show the decrease of transmission with decreasing frequency for each given aperture, the present theory predicts a greater decrease than the previous theory does. This discrepancy is due to the assumption of the rigid fracture wall in the previous theory. The present theory takes into account the elasticity of the wall by using equation 5.43, in which the wavenumber k_{fr} is found by solving a period equation corresponding to the elastic fracture (equation 4.24). The effects of mode conversion have also been checked. It is found that the number of modes found from equation 5.8 decreases with decreasing frequency, as pointed out by Tsang (1985, 1987), and that the amplitude of the radiation modes is considerably smaller compared with that of the Stoneley mode at low frequencies. This means that the energy converted to radiation is small. One therefore concludes that, at low frequencies, the transmission of Stoneley waves across a fracture is mainly controlled by the amount of fluid flow into the fracture.

Next, the theoretical results are presented in a higher frequency range of [0-15]

kHz. Figure 5-3 shows the transmission (a) and reflection (b) coefficients of Stoneley waves in this frequency range for a set of fracture thicknesses, the thicknesses being indicated on each curve of this figure. At low frequencies, the characteristic decrease in transmission and increase in reflection indicate the fluid flow effects, as discussed previously. At higher frequencies (above 5 kHz), the transmission decreases and reflection increases. These effects are closely related to the increasing coupling of the Stoneley mode with radiation modes, since the number and amplitude of the latter modes increase as frequency increases. These effects are not predicted by the previous theory since mode coupling was not considered. As frequency crosses the cut-off frequency of the first pseudo-Rayleigh mode, the transmission and reflection coefficients exhibit a discontinuous feature across the cut-off. The discontinuity is small for small fracture thickness (one can see this from the 0.5 cm and 1 cm curves), but becomes prominent as thickness increases. This discontinuity indicates the strong coupling of the Stoneley mode with the pseudo-Rayleigh mode. Because both modes are guided waves trapped in the borehole, the conversion of Stoneley wave energy to pseudo-Rayleigh energy is more efficient than the conversion to radiation modes, for the latter conversion occurs mostly at the fracture surfaces where the Stoneley energy is not as significant as in the borehole. To illustrate Stoneley wave characteristics due to a fracture as a function of frequency, synthetic microseismograms with different source center frequencies are calculated and the results are shown in Figures 5-4 and 5-5. In Figure 5-4, the source center frequency is 12 kHz, while the cut-off frequency of the first pseudo-Rayleigh wave mode is 8.36 kHz for the model used. Thus the coupling of the Stoneley with this wave mode is expected. Figure 5-4a shows the synthetics for a 1 cm thick fracture whose location is indicated by an arrow on the fracture-receiver offset axis. A Stoneley wave is generated at $z = -1.2$ m from the fracture and then incident on it from the negative z direction. In both (a) and (b) of Figure 5-4, the scale for the amplitude is expanded to show the small amplitude converted waves. As can be seen from Figure 5-4a, the Stoneley wave impinging

on the fracture is largely transmitted and partly reflected, in accordance with the transmission and reflection coefficients shown on Figure 5-3. In addition, there is some small amplitude wave energy originating from the fracture. The early portions of these waves move out above and below the fracture at the formation shear velocity (indicated by the solid lines). Following them are the dispersive pseudo-Rayleigh waves. The noise in the seismogram is due to the approximation of the branch cut integration using a finite number of modes (see also Nolet et al.'s (1989) seismograms). In addition, the use of the fast Fourier transform (FFT) assumes a periodic signal, so that signals which arrive outside the time window $1/\Delta f$, with Δf the frequency spacing, will fold over into this time window (Nolet et al., 1989). However, the noise is small compared to the Stoneley and pseudo-Rayleigh waves. This example shows that, in addition to the transmission and reflection effects, a small portion of the Stoneley waves is converted to pseudo-Rayleigh waves at the fracture. In the next example, the fracture aperture is increased to 4 cm and other parameters are kept unchanged. The resulting synthetics are shown in Figure 5-4b. This figure exhibits much stronger converted pseudo-Rayleigh waves than those shown on Figure 5-4a, because of the increased Stoneley to pseudo-Rayleigh conversion due to the much thicker fracture. Using the synthetic examples, it has been demonstrated that the discontinuity in transmission and reflection coefficients shown in Figure 5-3 is due to the coupling of Stoneley with pseudo-Rayleigh waves. Below the cut-off frequency, there are no pseudo-Rayleigh waves, and the only guided wave that exists in the borehole is the Stoneley wave. In Figure 5-5a, the fracture aperture is still 4 cm, as used in Figure 5-4b, but the source center frequency is reduced to 5 kHz. Around this frequency, the waves existing in the borehole are the Stoneley wave and a number of small amplitude radiation modes. The synthetics in Figure 5-5a show that, at low frequencies, the major effects are the transmission and reflection of the Stoneley mode according to the the coefficients given in Figure 5-3a and Figure 5-3b. the mode conversion effects are minimal and the converted radiation waves are not visible on the seismograms.

As an extremal example, Figure 5-5b shows the synthetics corresponding to very low frequency tube (Stoneley) waves. In this figure, the source frequency is only 300 Hz, and the fracture aperture is 2 cm. A Stoneley wave is generated at $z = -13$ m from the fracture and incident on it from the negative z direction. One can notice the strong Stoneley reflection from the fracture and the significant attenuation of the transmitted waves across the fracture. These phenomena are commonly observed in VSP measurements where low frequency tube waves are often excited (Hardin et al., 1987). The important implication of this example to field measurements is that the strong, coherent low frequency tube wave reflections are often associated with a fracture. Thus they may be used to provide useful information for fracture detection and characterization.

5.3.2 Pseudo-Rayleigh Wave

Pseudo-Rayleigh waves comprise an important portion of full waveform acoustic logs following the onset of formation of shear arrivals. Because these wave modes are more intimately coupled with the formation than the Stoneley (Stephen et al., 1985), they may be more sensitive to a formation fracture than the Stoneley wave.

Figure 5-6 shows the transmission (a) and reflection (b) coefficients of the first two pseudo-Rayleigh modes in the frequency range of [7-21] kHz for three different fracture apertures, which are 0.1 cm, 1 cm, and 2 cm, respectively. The apertures are chosen to model very thin ($L = 0.1$ cm) and relatively thick ($L = 2$ cm) borehole fractures. The parameters for the calculations are the same as those used for the Stoneley wave calculations. A prominent feature shown in Figure 5-6a is that, for all apertures, thin or thick, the pseudo-Rayleigh waves are strongly attenuated across the borehole fracture, the second mode being more attenuated than the first one. This behavior of pseudo-Rayleigh waves is very different from that of the Stoneley wave shown in Figure 5-3a. This difference can be expected from the wave motion characteristics of the two waves and from the analysis of partition coefficients of these waves

(Cheng et al., 1982). In general, in the presence of a hard formation, the Stoneley wave energy is mostly confined in the borehole fluid and its particle motion is dominantly in the axial direction. Because of this, the Stoneley is not sensitive to the formation shear property (Cheng et al., 1982). As has been shown previously, apart from some energy loss due to mode coupling at higher frequencies, the attenuation of the Stoneley by a fracture is due largely to the fluid flow into the fracture driven by this wave motion. Whereas for the pseudo-Rayleigh wave, the particle motion at the borehole interface is of elliptical shape and is dominated by horizontal motion (Stephen et al., 1985). The partition coefficient due to the formation shear property primarily controls the pseudo-Rayleigh wave at lower frequencies above the cut-off (see Cheng et al., 1982). Therefore, the pseudo-Rayleigh wave motion requires the formation shear strength to sustain its propagation. Consequently, when this wave motion encounters a crack filled with material of zero shear strength, this motion picture will be destroyed. Thus, as long as there is no shear coupling between the fracture surfaces, pseudo-Rayleigh waves will be significantly affected, whatever the fracture thickness. This is what one has seen in Figure 5-6a. Moreover, for the transmitted energy, it may take a while for this energy to organize its elliptically shaped wave motion and become reguided. Thus, after being transmitted across a fracture, the pseudo-Rayleigh wave may disappear for a while before it reappears as a guided wave, leaving a blank part on the acoustic logs. This characteristic will later be illustrated with laboratory examples. Another interesting feature in Figure 5-6a is that as the frequency decreases to approach the cut-off frequency, the transmission coefficients also decrease, the first mode being more drastic. This behavior can also be expected from analyzing the partition coefficient (Cheng et al., 1982). Because the partition coefficient due to the shear property is the most significant towards the cut-off, the pseudo-Rayleigh wave that is controlled by this coefficient is affected the most with the vanishing of shear strength at the fracture. This decrease in transmission will make the severely attenuated pseudo-Rayleigh waves even weaker near the

cut-off frequencies. This characteristic has been observed in the laboratory and will be shown in the next section. This characteristic may also have some implications in detecting borehole fractures using acoustic logs. Because the phase and group velocities of the pseudo-Rayleigh wave reach their maximum value at the cut-off frequency, which is the formation shear velocity V_s (Cheng and Toksöz, 1981), the early arrivals of this wave are the wave energy near the cut-off frequencies. Therefore, on an acoustic log, if one traces the formation shear arrival times across a fracture, the lack of wave energy following these arrival times may be a very good indication of the existing fracture. One now takes a look at the reflection coefficients shown on Figure 5-6b. The reflection of the pseudo-Rayleigh waves by a fracture is strong even for the very thin fracture with thickness of 0.1 cm. The reflection increases towards the cut-off, corresponding to the decrease of the transmission coefficient shown in Figure 5-6a. However, as the aperture varies from the very thin to relatively thick fractures, the reflection coefficient does not change significantly, especially for the first mode at higher frequencies. This is in agreement with the finite difference modeling of Stephen (1986). In his modeling, the source frequency is between the cut-off of the first pseudo-Rayleigh mode and that of the second mode. For different fracture apertures, he obtained reflected pseudo-Rayleigh waves with practically the same amplitude. Thus, thin fractures are practically as effective as thick fractures in decoupling the pseudo-Rayleigh waves from the lower formation. The reflected pseudo-Rayleigh waves, when not seriously contaminated by later arrivals of incident waves, may also be an indication of the existence of borehole fractures.

5.4 Laboratory Experimental Studies

Laboratory experiments were performed to study the propagation characteristics of borehole guided waves across a horizontal fracture. These experiments also provide a test of the theoretical analysis of this study.

5.4.1 Experimental Procedure

The laboratory setup for acoustic logging experiments have been described in Chapter 4, where borehole models with a vertical fracture were used. For the present study, one only needs to replace the vertical fracture model in Figure 4-9 with a horizontal fracture model shown in Figure 5-1 in the experimental setup. Two aluminum cylinders were used, each having a height of 12 cm and diameter of 20 cm. The compressional and shear velocities of this material are $V_p = 6.4$ km/s and $V_s = 3.1$ km/s, respectively. Its density is 2.7 g/cm^3. A borehole of 1 cm diameter was drilled at the center of each cylinder. A horizontal fracture is simulated by a gap between the smooth ends of the two cylinders, as shown in Figure 5-1. By varying the thickness of the gap, one can measure the effects of the fracture aperture on the borehole acoustic waves. In the experiment, an acoustic transducer is mounted at the bottom of the model and a receiver with a diameter of 0.9 cm is placed in the borehole to measure the waves. Because of its size, the receiver measures the average incoming wave field over the borehole area and, when the source and receiver are on the same side of the fracture, the receiver is not sensitive to the waves reflected back from the fracture. In other words, the experiment detects the effects of the fracture by measuring the transmission of borehole acoustic waves. During the experiment, the model assembly is submerged in a water tank. The water acoustic velocity is 1.5 km/s and its density 1 g/cm^3. The receiver is initially placed below the fracture. After a waveform is recorded, the receiver is moved to next position by a step motor controller at a step length of 0.18 mm. In this process, the receiver passes the fracture and eventually moves above it. The whole process generates a waveform array. This array is processed by stacking the desired signal at its move-out velocity. If the desired signal is not the dominant wave in the data (for example, the pseudo-Rayleigh wave may be followed by strong Stoneley arrivals), windowing the signal may become necessary. The stacked signals below and above the fracture give the average incident and transmitted waves. The amplitude spectral ratio of the incident wave relative to

that of the transmitted wave in the frequency range of interest gives the transmission coefficient across the fracture in that frequency range.

5.4.2 Experimental Results

The experimental results for the Stoneley waves are first presented. Figure 5-7 shows the experimental array waveform data of Stoneley waves. The waves were recorded below the cut-off frequency of the first pseudo-Rayleigh wave (which is about 174 kHz for the model used), so that the Stoneley waves are the strongest phase in the data. For this example, the fracture has an aperture of 2.8 mm. Its location is indicated in Figure 5-7 on the source-receiver offset axis. It can be seen that the transmitted wave amplitude is reduced by the fracture. Figure 5-8a shows the averaged incident and transmitted wave spectra obtained by respectively stacking the wave traces above and below the fracture. The reduction of the transmitted wave amplitude is clearly seen in the frequency range of about [90-180] kHz, in which the wave amplitudes are the strongest. Figure 5-8b shows the ratio of the transmitted amplitude relative to the incident amplitude in the same frequency range. The theoretical transmission coefficient is also plotted. The measured data and the theory are in good agreement. In addition, Figure 8 also shows the incident and transmitted wave spectra and the measured transmission coefficient versus the theoretical coefficient obtained for 5.1 mm (c and d), 1.0 mm (e and f), and 0.2 mm (g and h) thick laboratory model fractures. Again, in the same frequency range, the measured transmission coefficient and the theoretical transmission coefficient are in good agreement, although there are some scatter in the experimental results due to the noise in the data. The experiments were performed for a set of model fractures with thickness ranging from 0.2 to 5.1 mm. The theoretical and experimental transmission coefficients were averaged in the frequency range around 135 kHz, as shown in (b) and (d) of Figure 5-8. The averaged results are plotted versus fracture thickness in Figure 5-9 . They agree very well. As can be seen from this figure, the transmission coefficient decreases with increasing

fracture aperture. This result agrees with those of the previous experiments given in Tang and Cheng (1989) and Hornby et al. (1989).

In the experiment, the pseudo-Rayleigh waves were also measured to study their response to the effects of a fracture and to test the theoretical predictions. In order to effectively excite pseudo-Rayleigh waves, the experiments were performed in a higher frequency range around 340 kHz. Figures 5-10 and 5-11 show the array waveforms for the laboratory measurements with fracture aperture equal to 0.3 mm (Figure 5-10) and 2.5 mm (Figure 5-11), respectively. In these two figures, the scale is expanded for the wave amplitude to highlight the pseudo-Rayleigh waves (denoted by P-R in this figure), particularly the transmitted waves. A line across the array (denoted by S) indicates the formation shear arrival time of each trace. The location of the fracture is indicated by an arrow on offset axis. In fact, the array waveforms for the two very different fracture apertures are very similar. For the upper part of the array (incident waveforms), the pseudo-Rayleigh waves are effectively excited. Following them are some high-frequency fluid arrivals which are mixed up with the pseudo-Rayleigh waves. However, right after being transmitted across the fracture, the pseudo-Rayleigh portion of the waveforms is drastically attenuated, leaving a region with very emergent wave energy. At some distance farther from the fracture, the waves become reguided and reappear as coherent pseudo-Rayleigh waves. One may also notice that the early part of these waves following the formation shear arrival times (indicated by the line across the array) is very weak compared with the early part of the incident waves. The fact that the above described phenomena are common for both the thin (L=0.3 mm, Figure 5-10) and the thick (L=2.5 mm, Figure 5-11) fractures agrees with the theoretical prediction that a thin fracture is as effective as a thick fracture in affecting pseudo-Rayleigh waves. As discussed previously, after the elliptically-shaped particle motion is destroyed at the fracture, the propagating pseudo-Rayleigh energy may take a while to organize its original motion and become reguided. This is demonstrated by the almost blank region across

the fracture in both Figure 5-10 and Figure 5-11. For analyzing the waveforms in Figures 5-10 and 5-11, Figure 5-12 plots the phase (solid line) and group (dashed line) velocities of the first and the second pseudo-Rayleigh modes for the laboratory borehole model (aluminum). As can be seen from this figure, in the experimental frequency range around 340 kHz, the phase velocity of the first mode is close to the fluid velocity (1.5 km/s), and its group velocity is lower than the fluid velocity. The phase velocity of the second mode around this frequency is close to the formation shear velocity (3.1 km/s) and is fairly flat. Its group velocity is significantly higher than the fluid velocity. Thus in Figure 5-10 or Figure 5-11, the early part of the waveforms before the fluid arrivals is mainly composed of the second mode. This can also be evidenced by tracing the one particular phase (trough or peak) of the early waveforms across the upper part of the array. The phase moves out at a velocity close the the shear velocity and there is no significant dispersion of the waves (see the flat dispersion curve of the second mode around 340 kHz in Figure 5-12), showing the the waves are indeed from the second mode. The weak early arrivals of the transmitted waves are the wave energy near the second cut-off frequency. Their small amplitude compared with that of the incident waves also agrees with the theoretical result that the transmission coefficient is generally the smallest near the cut-off frequencies. To make a quantitative comparison between the experiment and the theory, one needs to process the data of Figures 5-10 and 5-11. The pseudo-Rayleigh waves before the fluid arrivals were windowed. As shown by previous discussion, the windowed signal is mainly composed of the second pseudo-Rayleigh mode. Then upper part of the windowed array was stacked to obtain the average incident waveform. For the lower part that corresponds to the transmitted waves, the last 9 traces which consist of coherent pseudo-Rayleigh energy were stacked. This gives the average transmitted waveform. The results of the processing are shown in Figure 5-13 for the L=0.3 mm (a) and L=2.5 mm (b) fractures. In this figure, the formation shear arrival times are marked on each waveform, and the transmitted wave amplitude is

scaled relative to the maximum incident amplitude. As can be seen from this figure, the relative amplitudes of the transmitted and the incident waves in both (a) and (b) are very similar, despite the fact the one fracture (L=2.5 mm) is more than 8 times as thick as the other (L=0.3 mm). Moreover, for the transmitted waves in both (a) and (b), there is some weak energy following the formation shear arrival times, indicating the strong attenuation of pseudo-Rayleigh waves near the cut-off frequencies. Figure 5-14 shows the amplitude spectra (a and c) of the waves shown in Figures 5-10 and 5-11 and the resulting transmission coefficients (open circles on (b) and (d) of Figure 5-14) obtained from the spectral ratio of the transmitted spectrum relative to the incident spectrum. The theoretical transmission coefficients (solid line) calculated for the second mode are also shown. As shown on Figure 5-14b and (d), theory and experiment agree in both cases. Both results show the same amount of amplitude attenuation of the transmitted waves and the general decreasing tendency of the transmission coefficient towards the cut-off frequency. The experiments on the pseudo-Rayleigh waves have shown the wave characteristics across an open horizontal fracture and confirmed theoretical analysis on these waves.

5.5 Conclusions

In this chapter, the propagation of borehole guided waves across an open horizontal fracture has been investigated. The theoretical analysis was based on a hybrid method (Tsang, 1985, 1987). This method generates wave modes which are summed to match the boundary conditions at the fracture surfaces. To overcome the singularity problem in matching the surface conditions, the borehole fluid flow across and into the fracture were balanced, as has done for the Stoneley waves in Chapter 2. The coupling at the fracture surfaces results in the transmission and reflection of an incident borehole guided wave. Based on the analysis, one can calculate the transmission and reflection coefficients due to a fracture for the Stoneley and pseudo-Rayleigh waves. At low

frequencies, the effects of the fracture on the Stoneley wave are controlled by the amount of fluid flow into the fracture. This has been confirmed by comparison with the flow model developed in Chapter 2 and by laboratory measurements on Stoneley waves. As frequency increases, the effects of mode conversion at the fracture become important. Particularly above the the cut-off frequency of the first pseudo-Rayleigh mode, the conversion to pseudo-Rayleigh wave is significant, especially for a thick fracture, as has been shown by synthetic microseismograms. For the pseudo-Rayleigh wave, an open fracture, whatever the thickness, drastically reduces the transmitted wave amplitude and produces strong reflection, these effects being more significant towards the cut-off frequencies than away from these frequencies. As shown by the laboratory measurements performed using thin and thick fractures, because of the destruction of its elliptically-shaped particle motion at the fracture, the transmitted pseudo-Rayleigh wave leaves a region with very weak wave energy in the vicinity of the fracture. This characteristic may be an important indication of the existence of an open fracture on an acoustic log. In addition, laboratory experiments indicated the weak early arrivals of the transmitted pseudo-Rayleigh waves, as predicted by the theory. In general, the theory and experiment agree quite well. The guided wave characteristics due to a fracture described in this study may provide useful information for the fracture detection and characterization using acoustic logs.

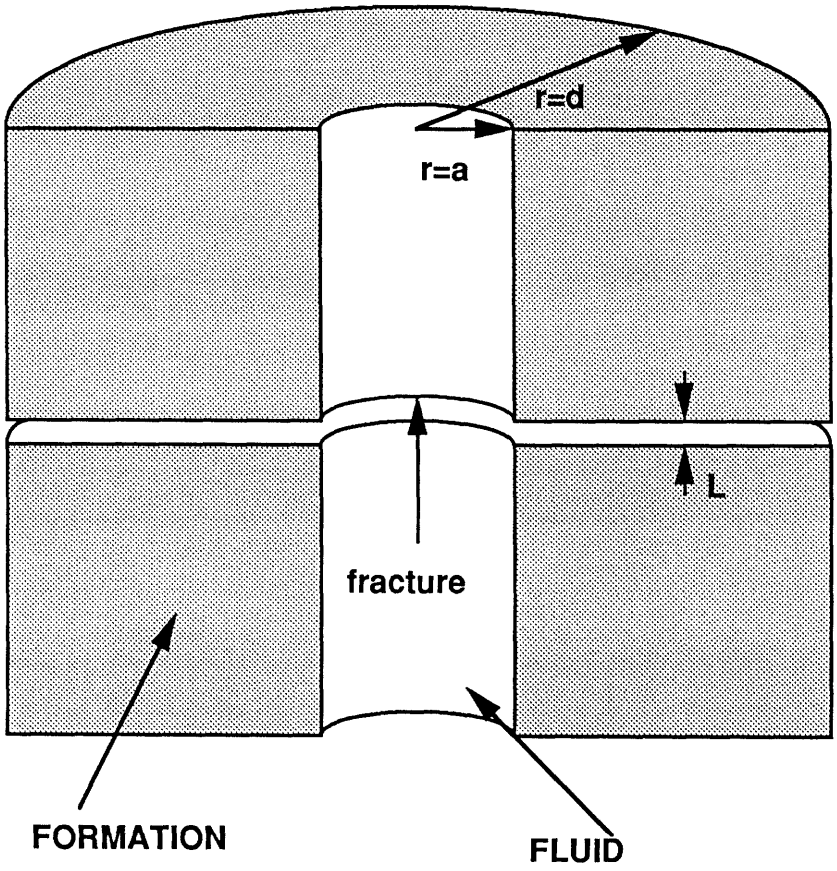

Figure 5-1: Borehole intersected by a horizontal fracture with thickness L. For the hybrid method, a rigid boundary is placed at $r = d \gg a$. The formation at both sides of the fracture is an elastic solid. The borehole and the fracture are filled with the same fluid.

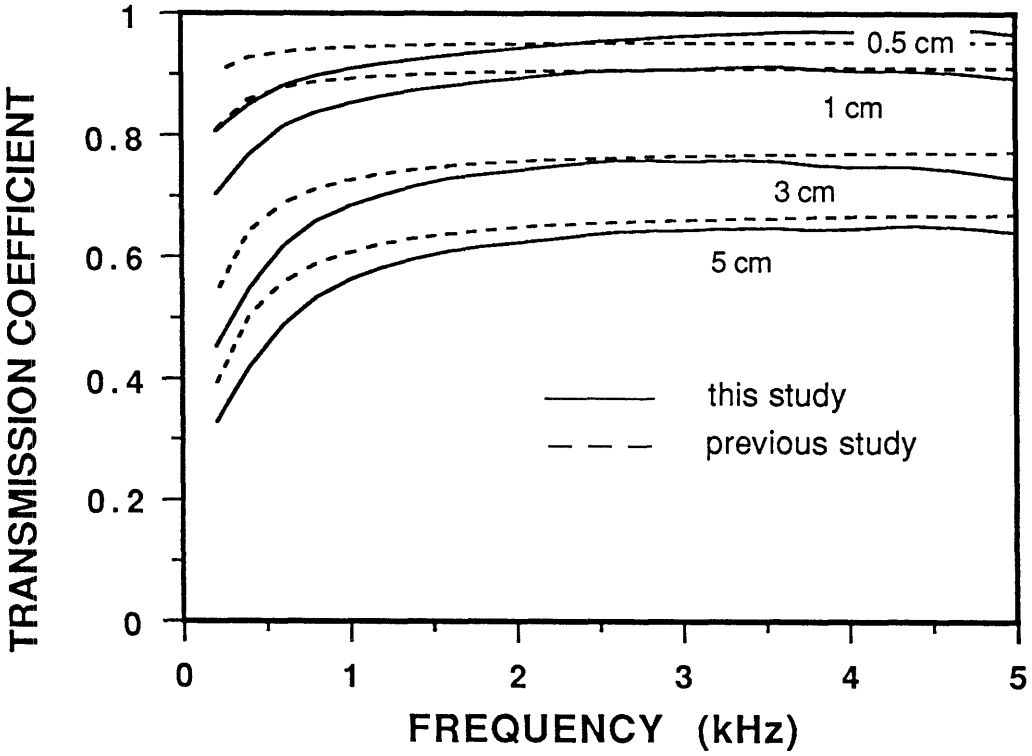

Figure 5-2: Comparison of the present theory (solid line) with the previous one dashed line) for the transmission of Stoneley waves in he low frequency range. The model parameters are given in the text and the fracture apertures are indicated on the curves. At low frequencies, the present theory shows more attenuation than the previous theory.

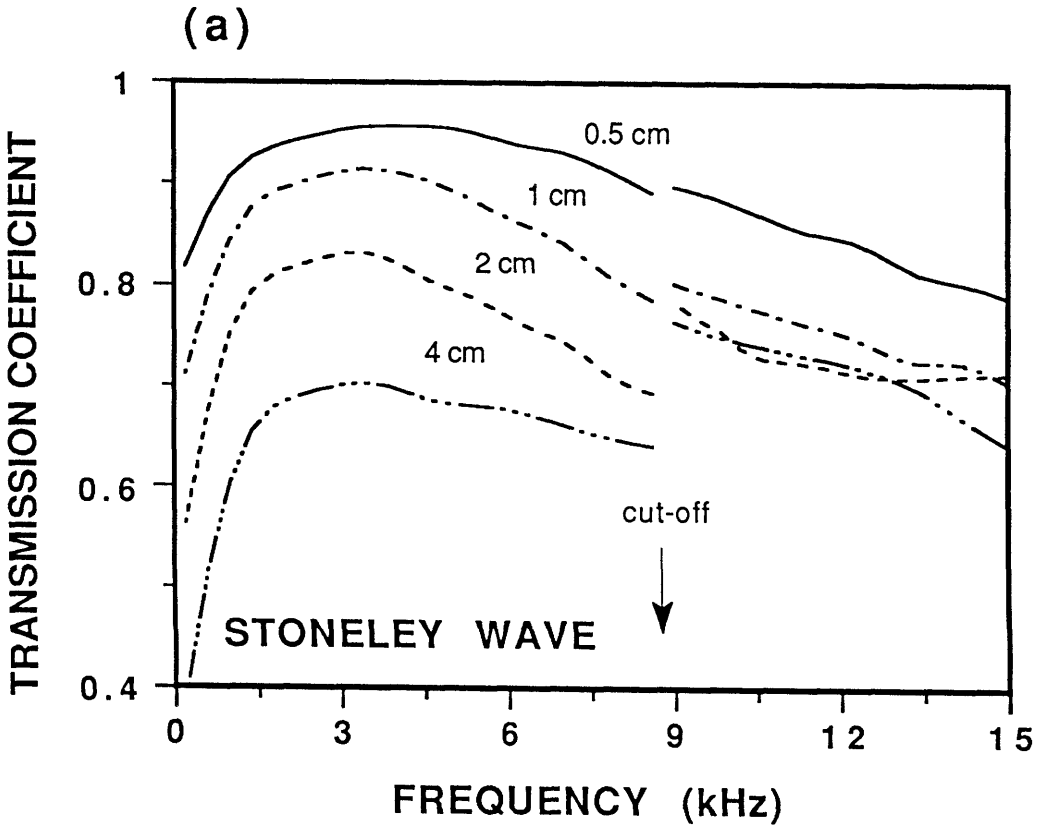

Figure 5-3: Transmission (a) and reflection (b) of Stoneley waves in the frequency range of [0-15] kHz. Above 5 kHz, the transmission decreases and reflection increases with frequency because of the coupling with radiation modes. At the cut-off frequency (marked by an arrow) the coefficients are discontinuous, indicating the coupling of the Stoneley with pseudo-Rayleigh waves.

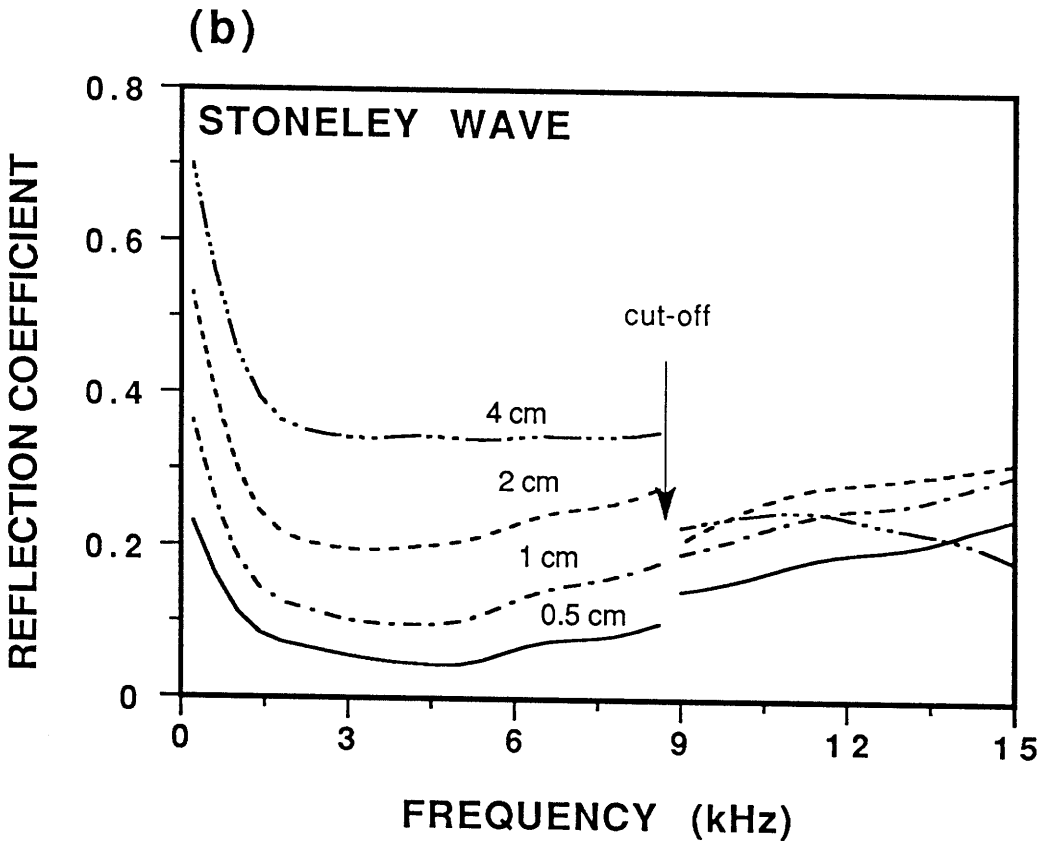

Figure 5-3: (b) Stoneley wave reflection coefficient associated with (a).

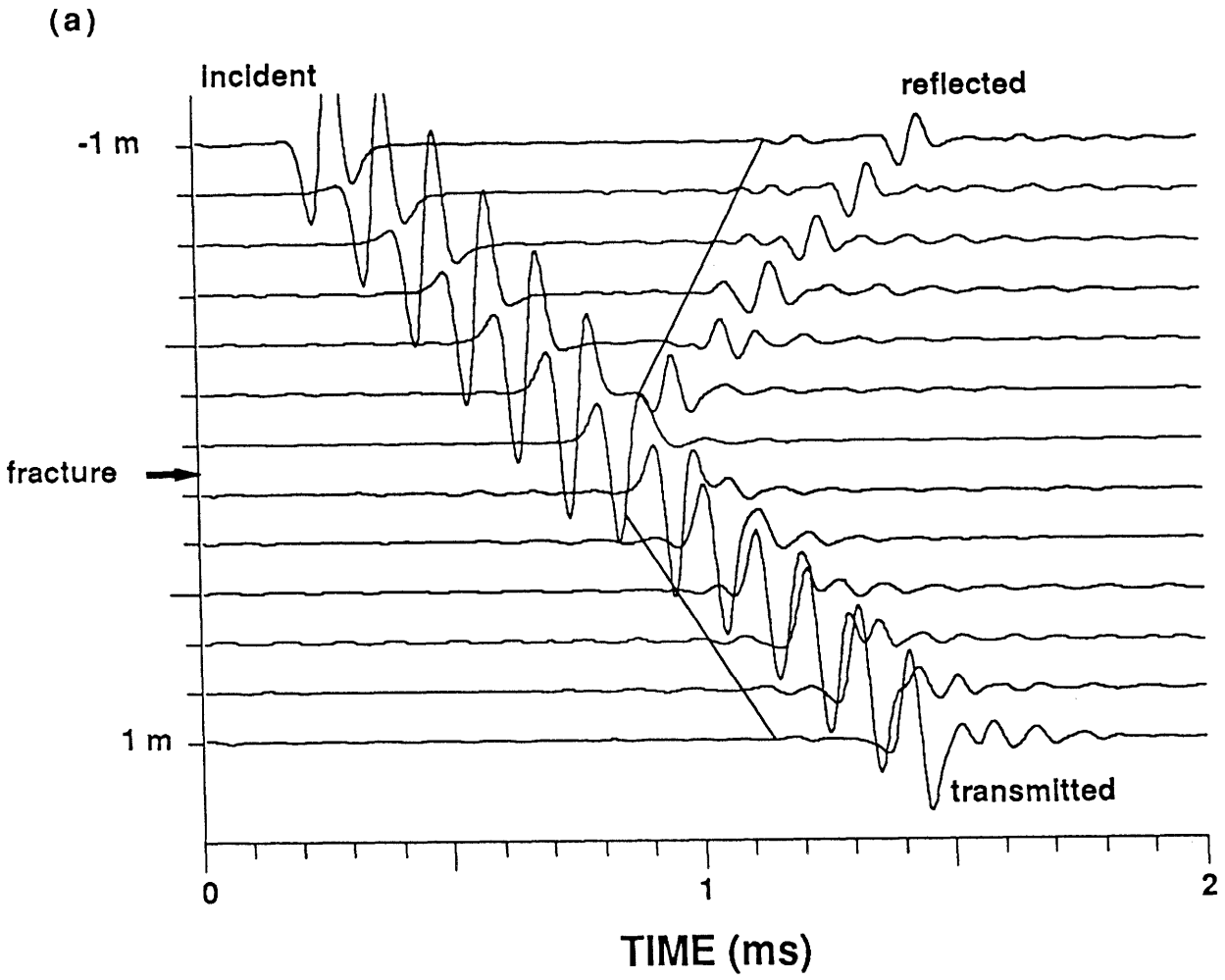

Figure 5-4: Synthetic microseismograms showing the conversion of Stoneley waves to pseudo-Rayleigh waves above the cut-off frequency. The Stoneley is the incident wave. In (a), the fracture aperture is 1 cm. In (b), it is 4 cm. The solid lines indicate the move-out of the formation shear signals originating from the fracture. Following them are the converted pseudo-Rayleigh waves.

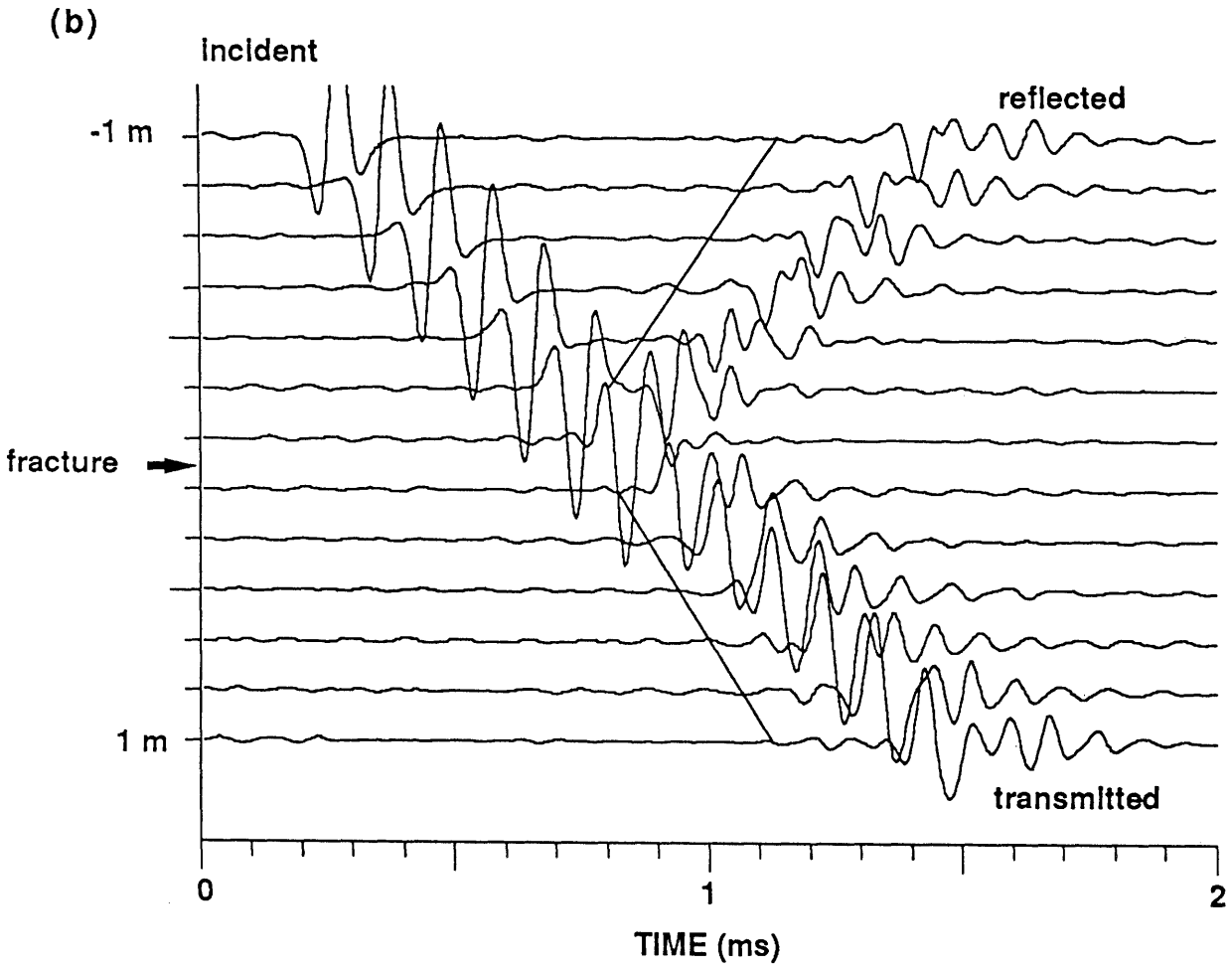

Figure 5-4: (b) Seismograms with a 4 cm thick fracture. For the thicker fracture, the converted waves become stronger.

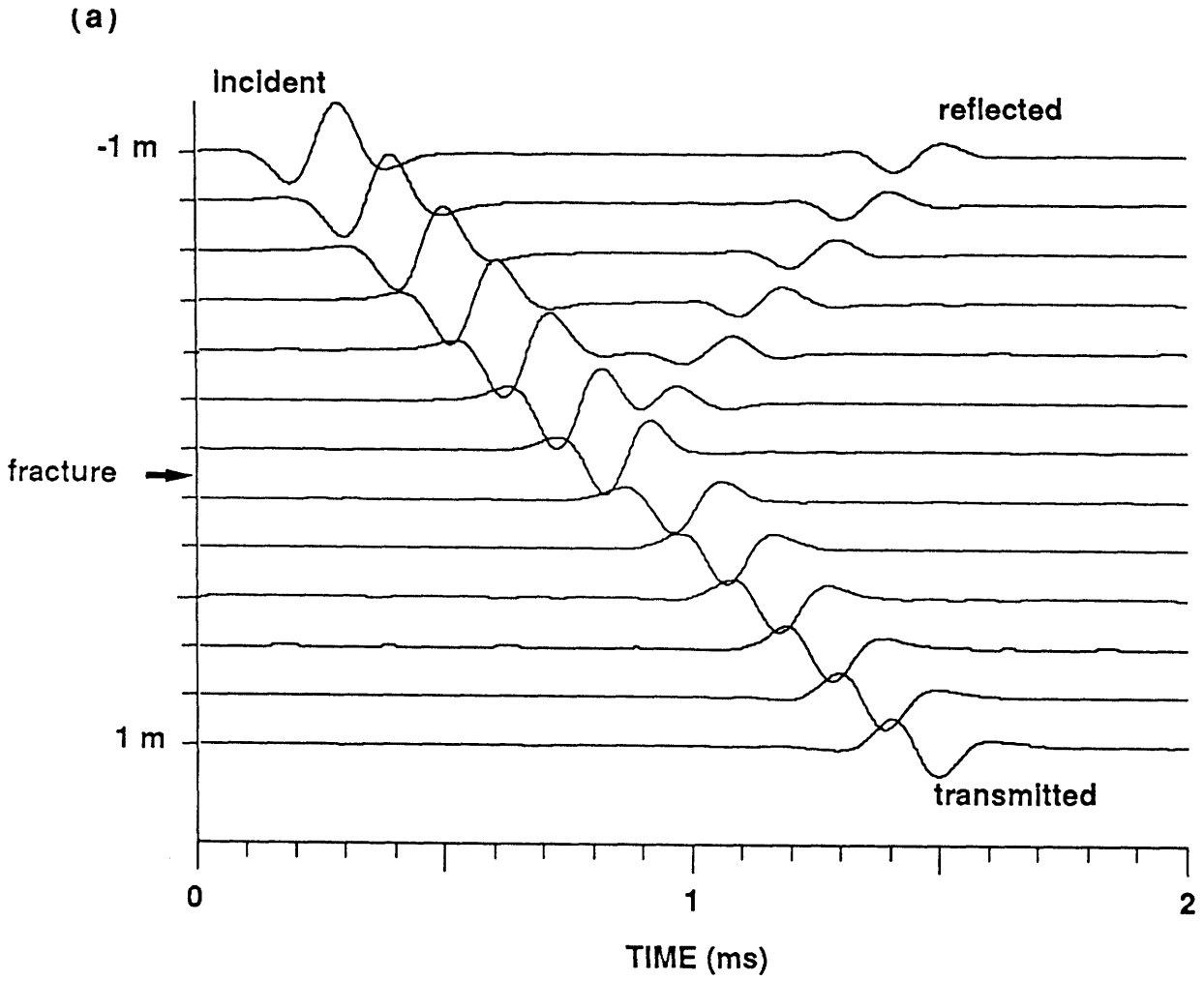

Figure 5-5: Stoneley waves below the cut-off frequency. In (a), the fracture aperture is 4 cm and source center frequency is 5 kHz. The Stoneley is simply transmitted and reflected at the fracture with little mode conversion effects.

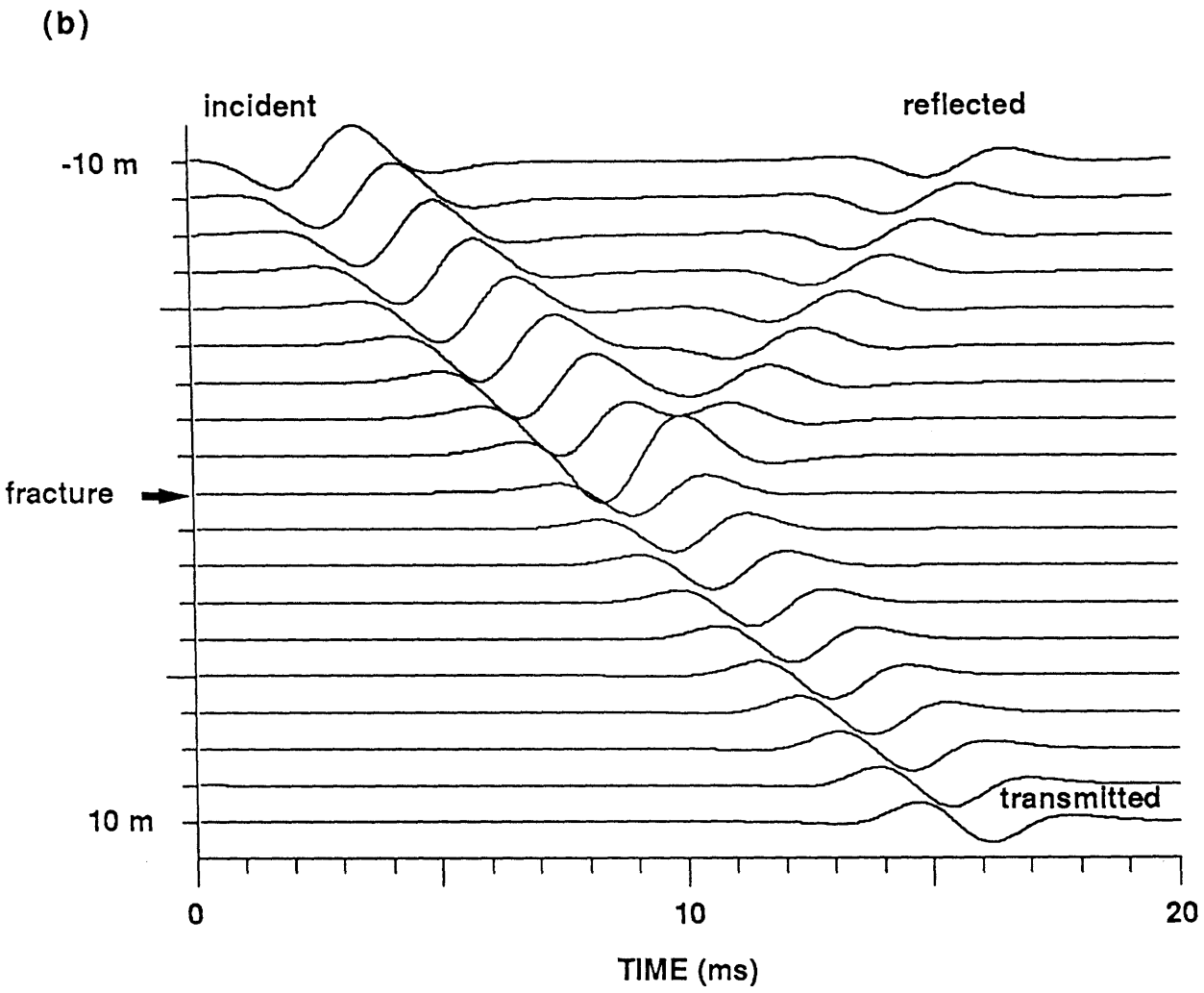

Figure 5-5: (b) Stoneley waves in the VSP frequency range. The fracture is 2 cm thick and the center frequency is down to 300 Hz to model tube waves observed in VSP measurements. The strong reflection and attenuation of the tube wave due to a fracture are common in such measurements.

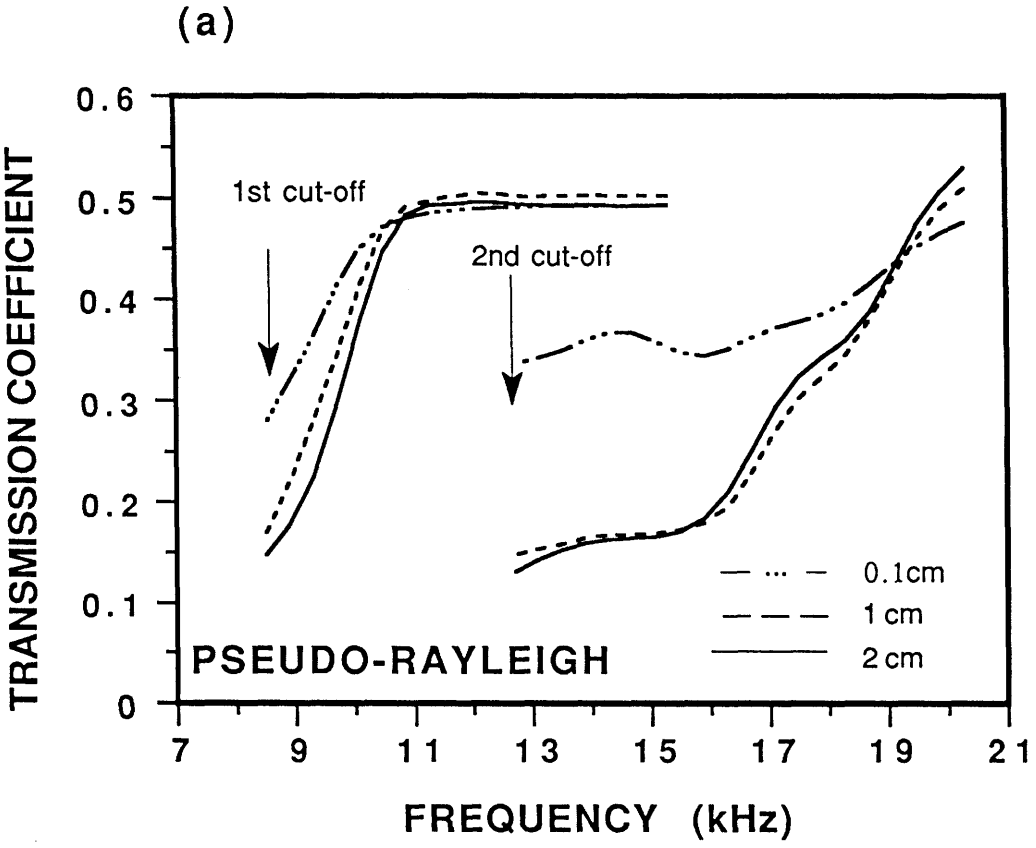

Figure 5-6: Transmission (a) and reflection (b) of the first two pseudo-Rayleigh modes as a function of frequency and fracture thickness. These types of wave modes are strongly attenuated and reflected by thin as well as thick fractures. Near the cut-off frequencies, the attenuation is generally the strongest.

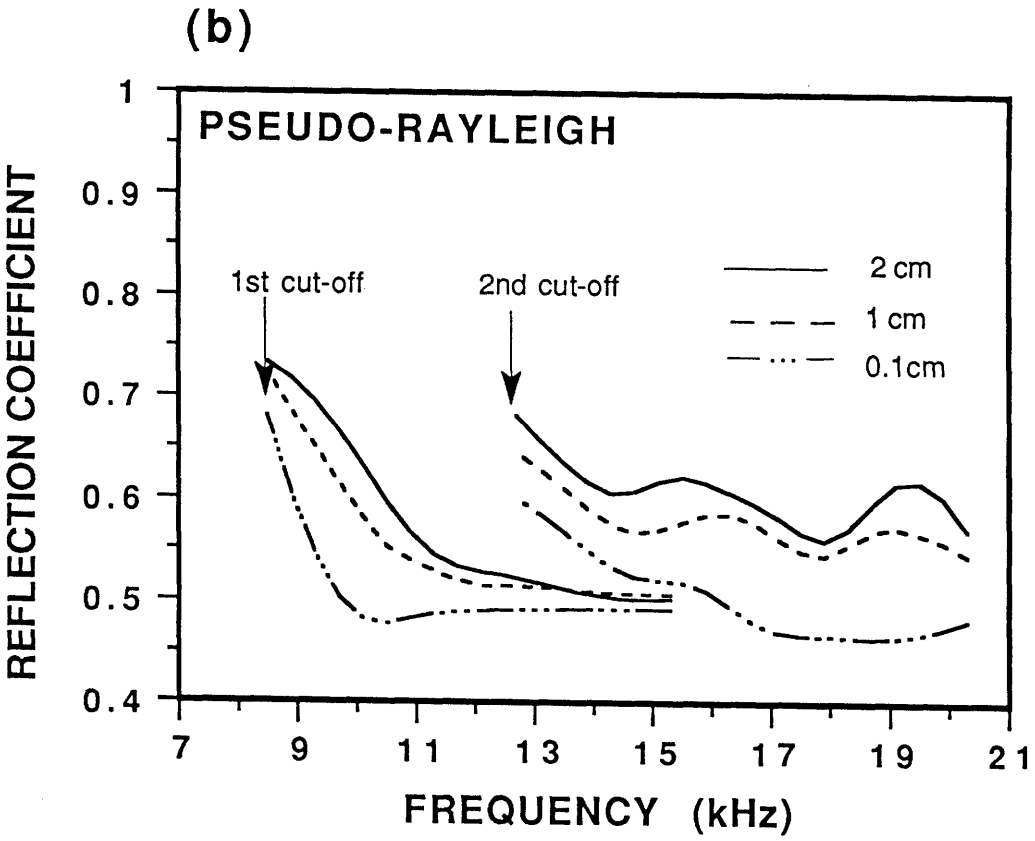

Figure 5-6: (b) Pseudo-Rayleigh wave reflection coefficient associated with (a).

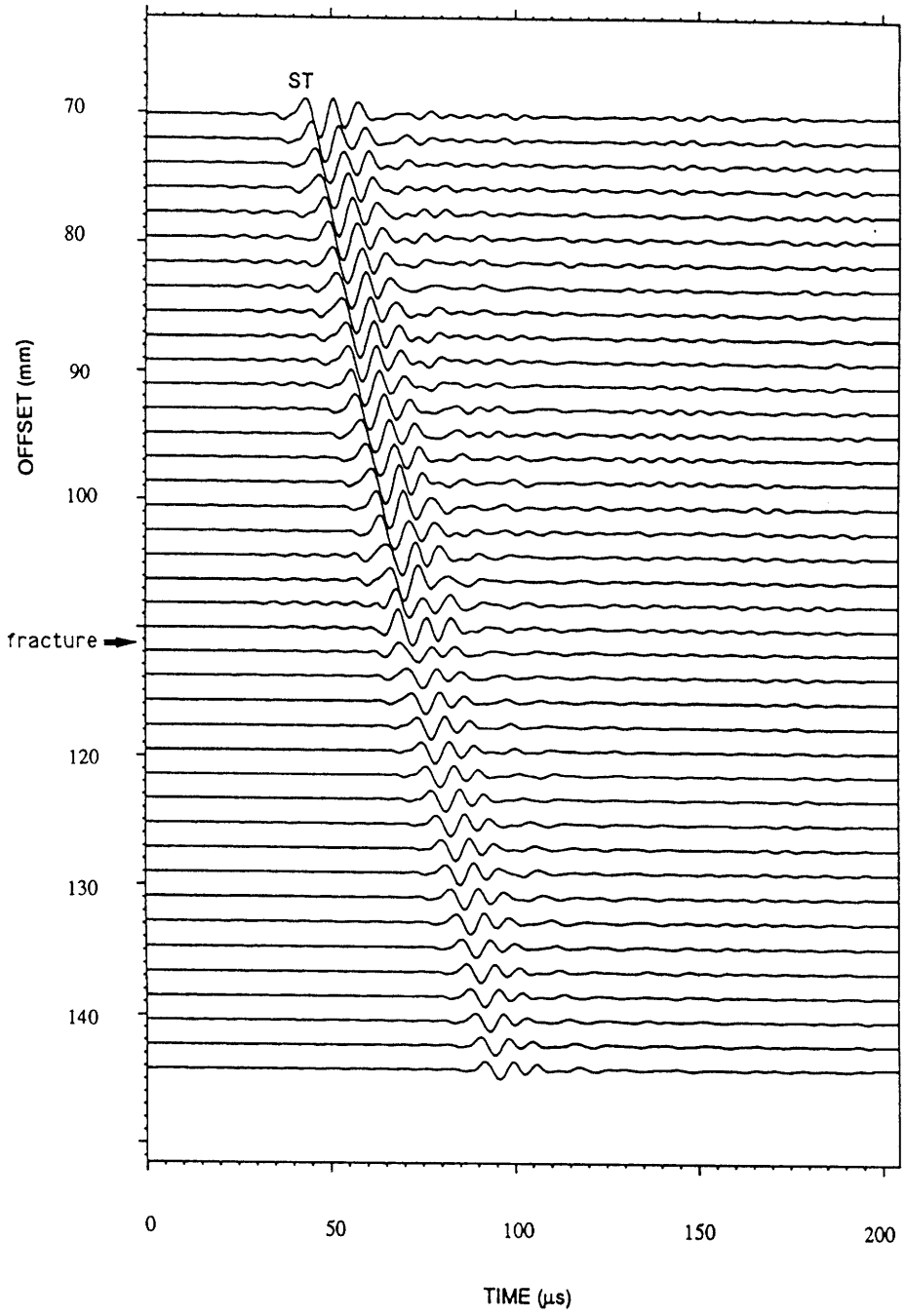

Figure 5-7: Experimental array waveform data for Stoneley waves. A fracture of 2.8 mm thick in the model is indicated on the offset axis. The Stoneley amplitude is reduced across the fracture.

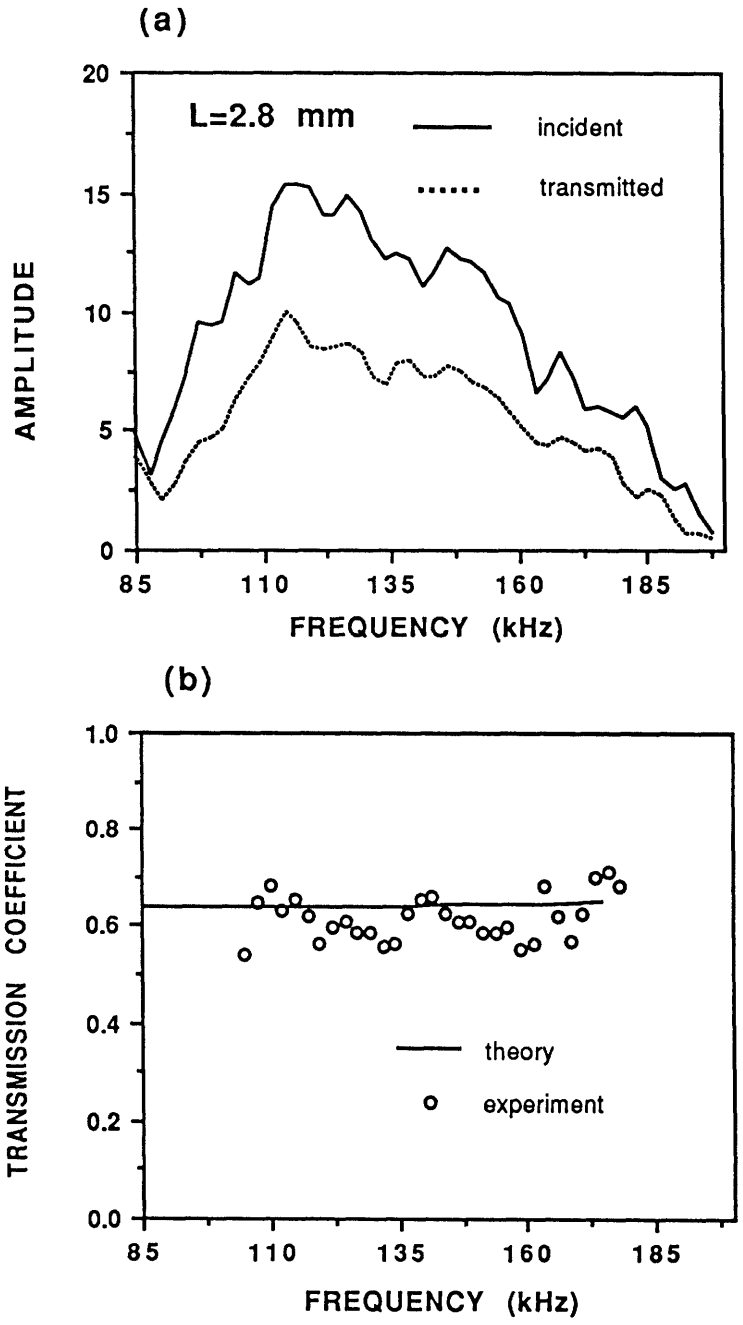

Figure 5-8: Measured incident and transmitted spectra (top figures) and transmission coefficient (bottom figures). For (a) and (b), the fracture thickness is 2.8 mm.

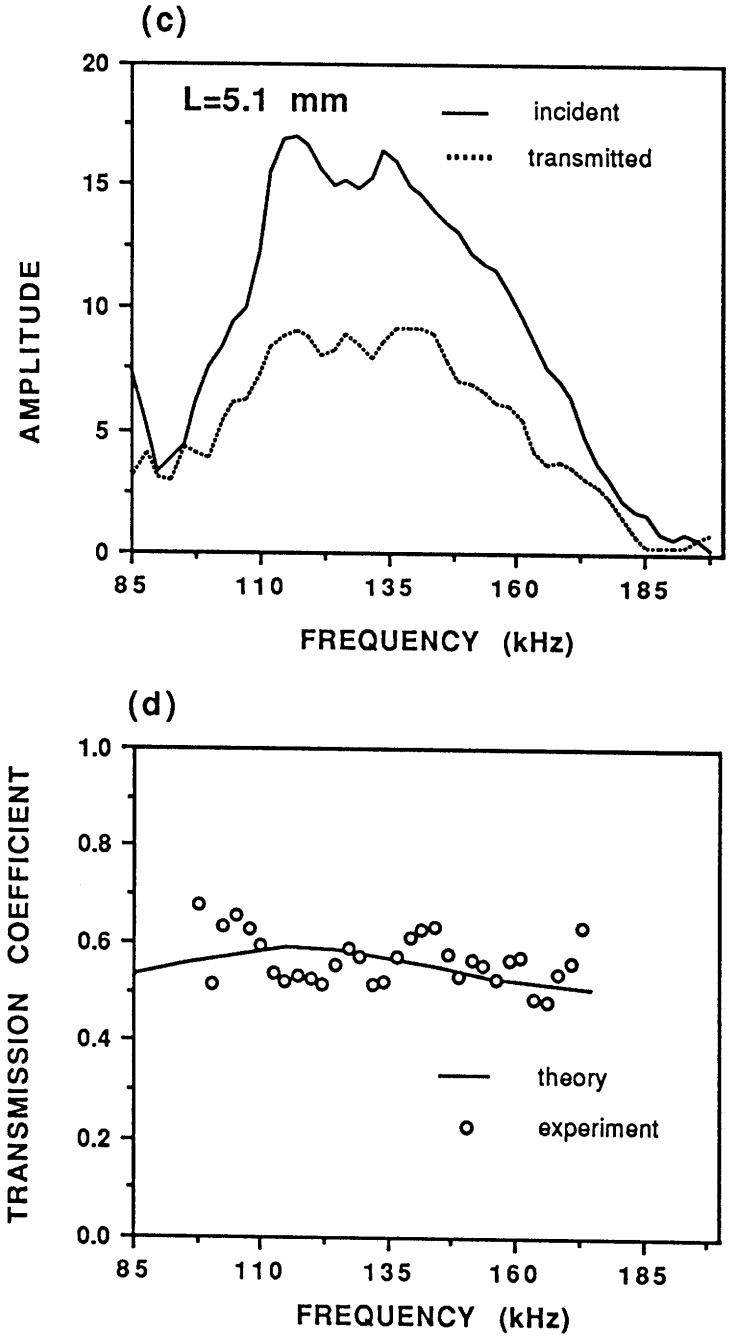

Figure 5-8: (c) and (d) For a 5.1 mm fracture.

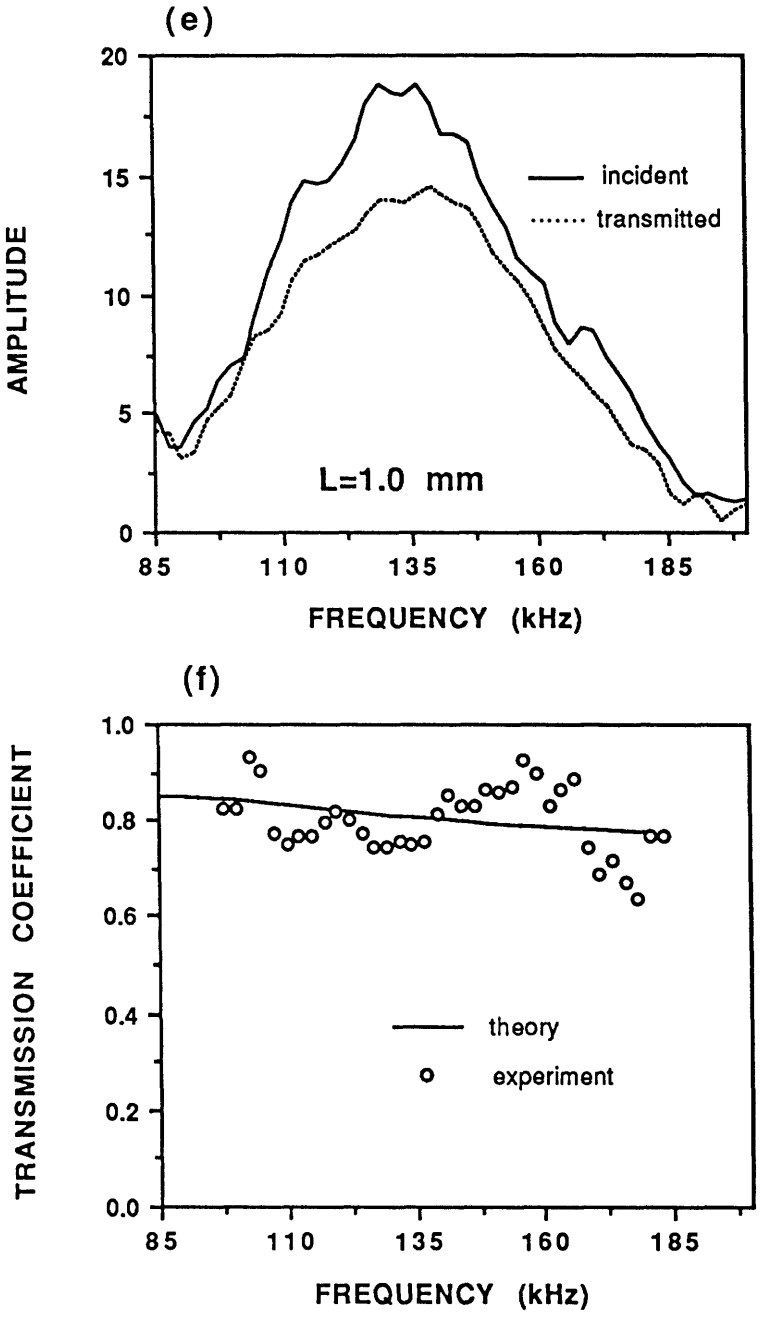

Figure 5-8: (e) and (f) For a 1 mm fracture.

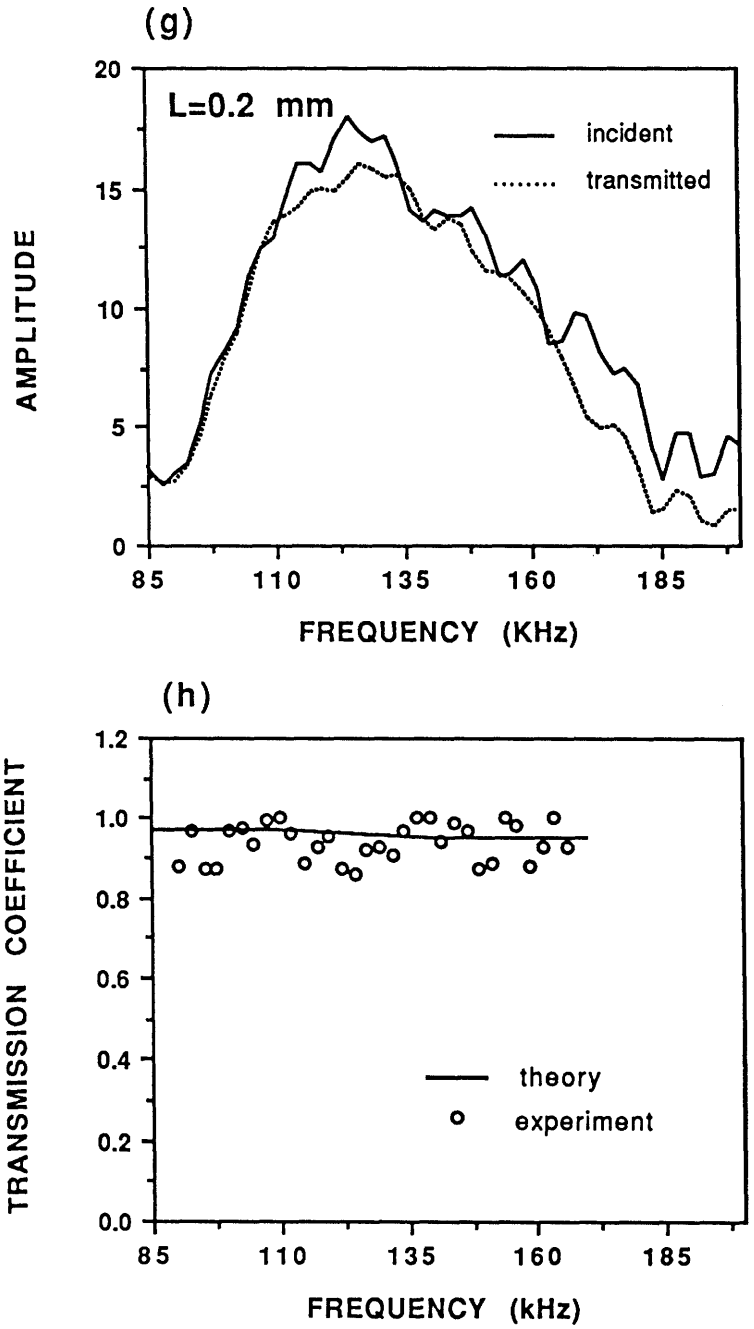

Figure 5-8: (g) and (h) For a 0.2 mm fracture.

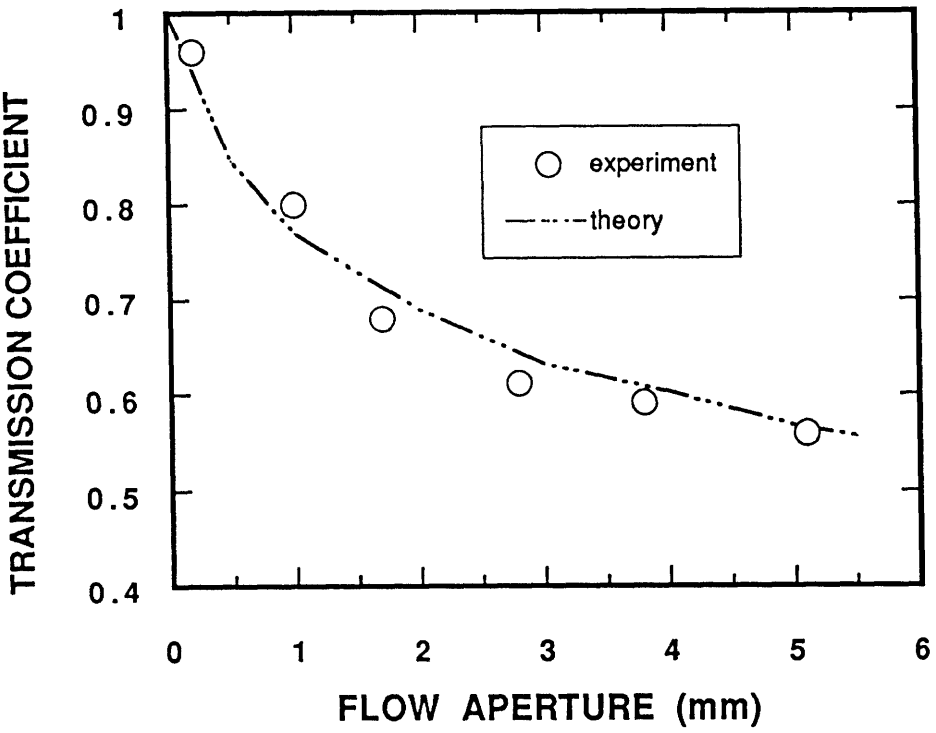

Figure 5-9: Experimental and theoretical transmission coefficients versus fracture thickness. These coefficients are averaged over the frequency range shown in Figure 5-8.

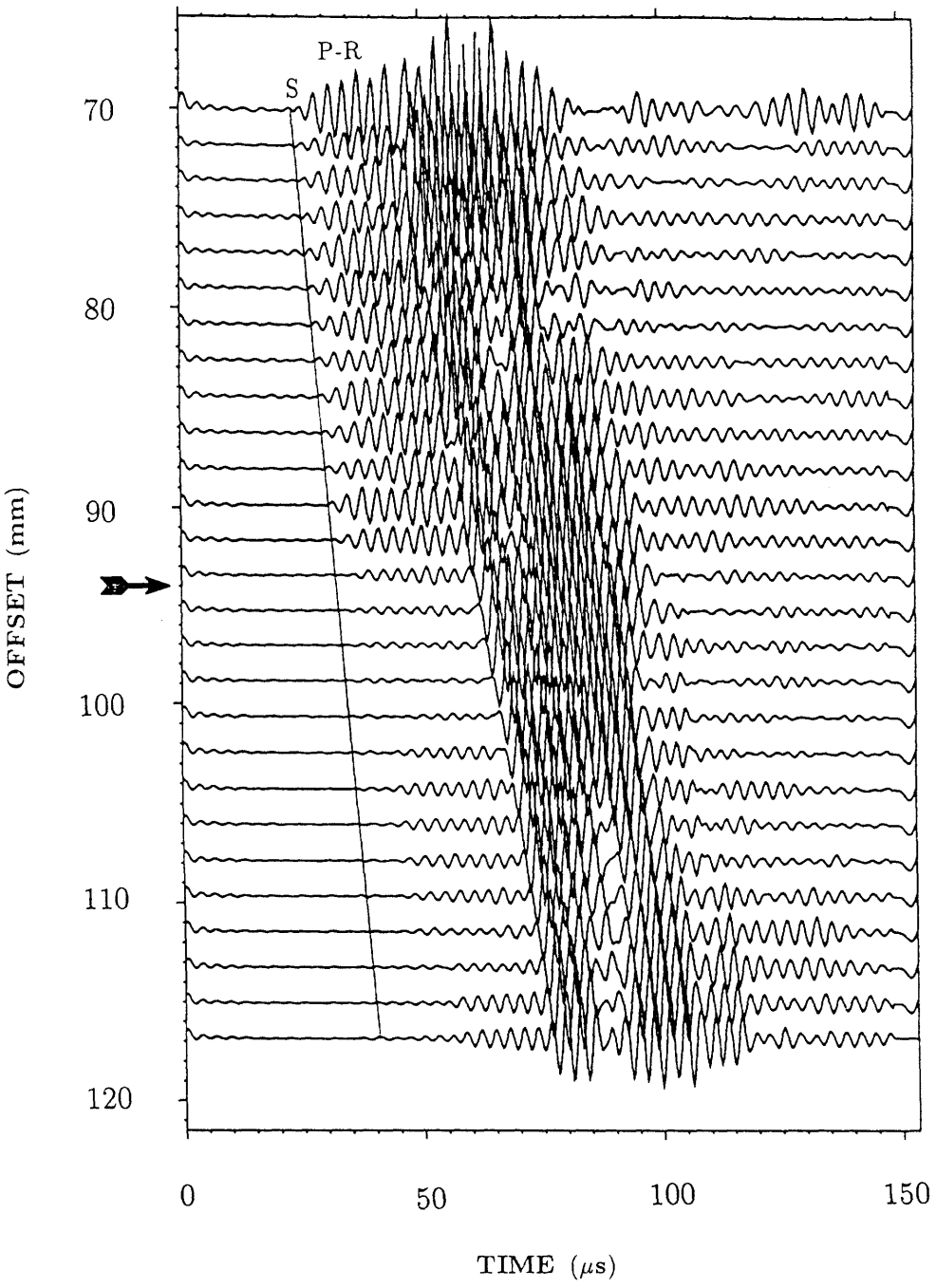

Figure 5-10: Experimental array waveform data for pseudo-Rayleigh waves. The fracture thickness is 0.3 mm. Fracture location is indicated by an arrow. The pseudo-Rayleigh waves are denoted by P-R. A line across the array denoted by S indicates formation shear arrival times. Note the waves are missing across the fracture and become reguided at some distance away from it. Note also the lack of wave energy in the early part of the transmitted waves.

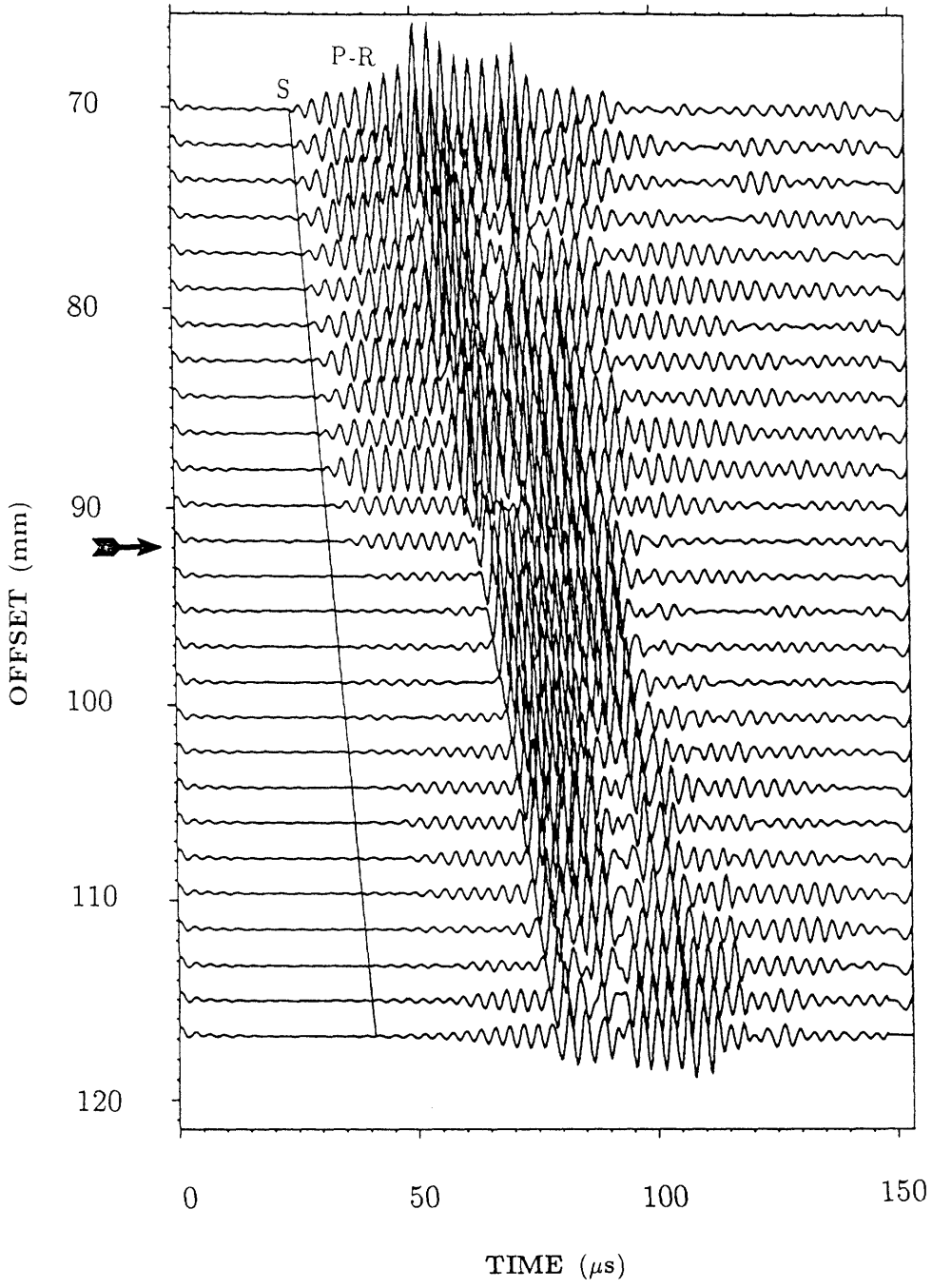

Figure 5-11: Experimental array waveform data. The fracture thickness is 2.5 mm.

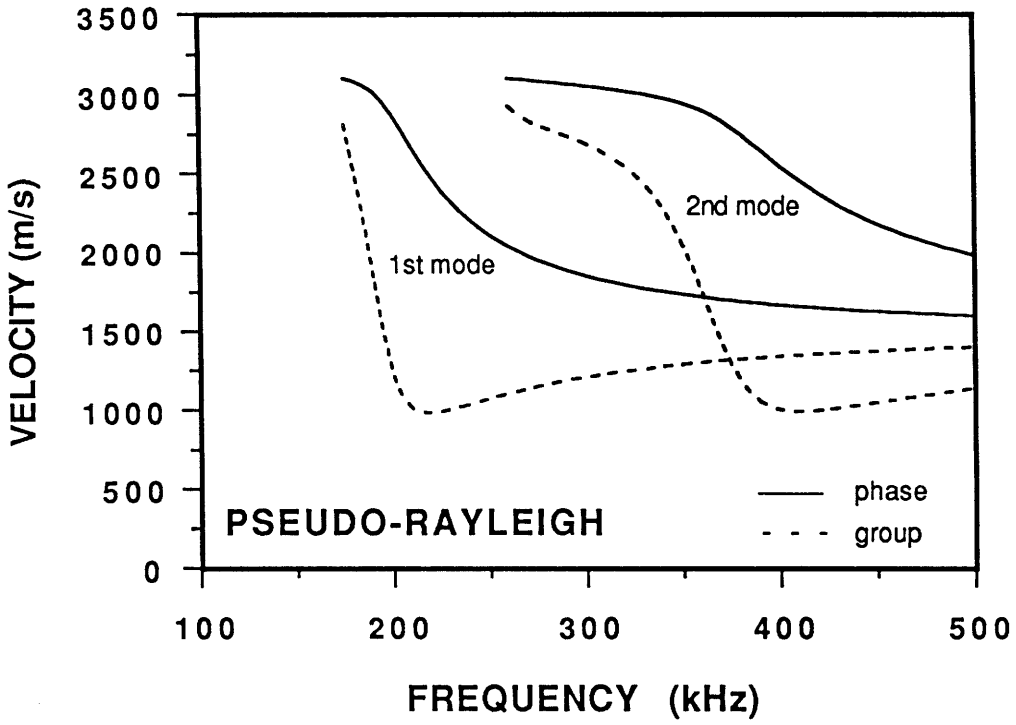

Figure 5-12: Phase (solid line) and group (dashed line) velocities of the first and second pseudo-Rayleigh modes for the laboratory aluminum borehole model.

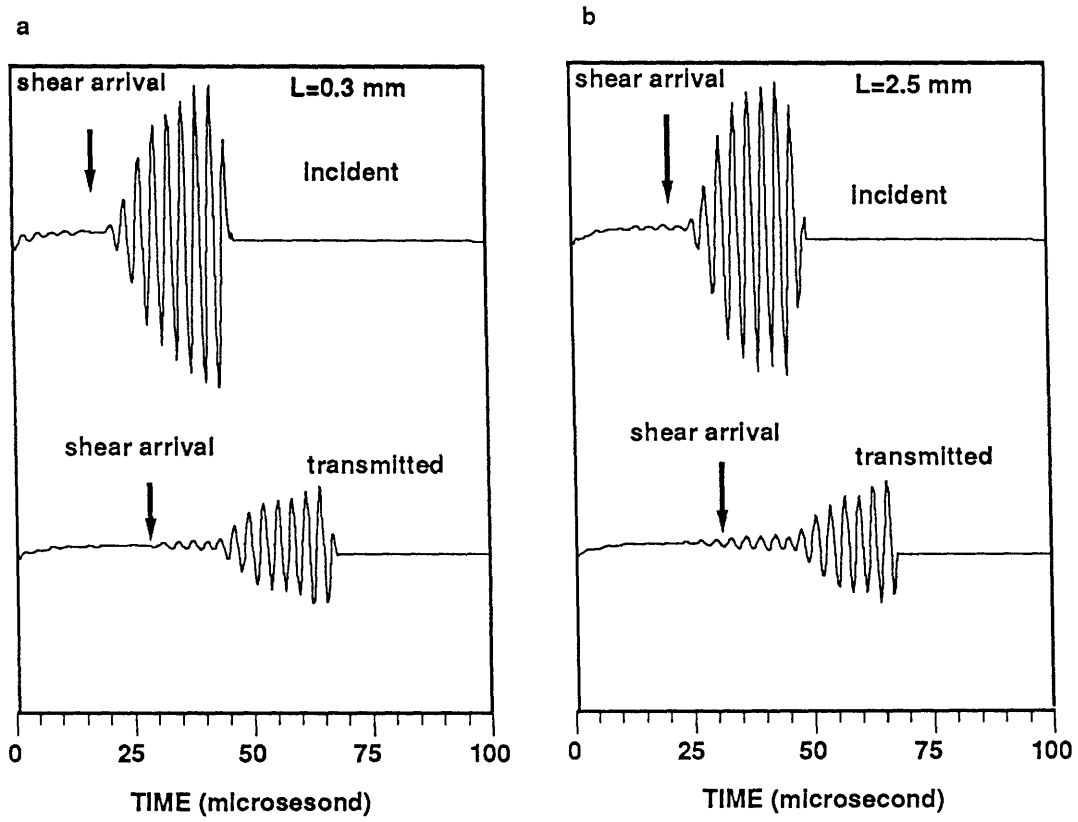

Figure 5-13: Averaged incident and transmitted pseudo-Rayleigh waveforms. They are obtained from the data shown in Figures 5-10 and 5-11 by windowing the signal before the fluid arrivals and stacking the traces above and below the fracture. For the transmitted waves, only the last 9 traces of Figures 5-10 and 5-11 which have coherent wave energy are used. Note the similarity between the waveforms in (a) and (b) and the weak early part of the transmitted waves.

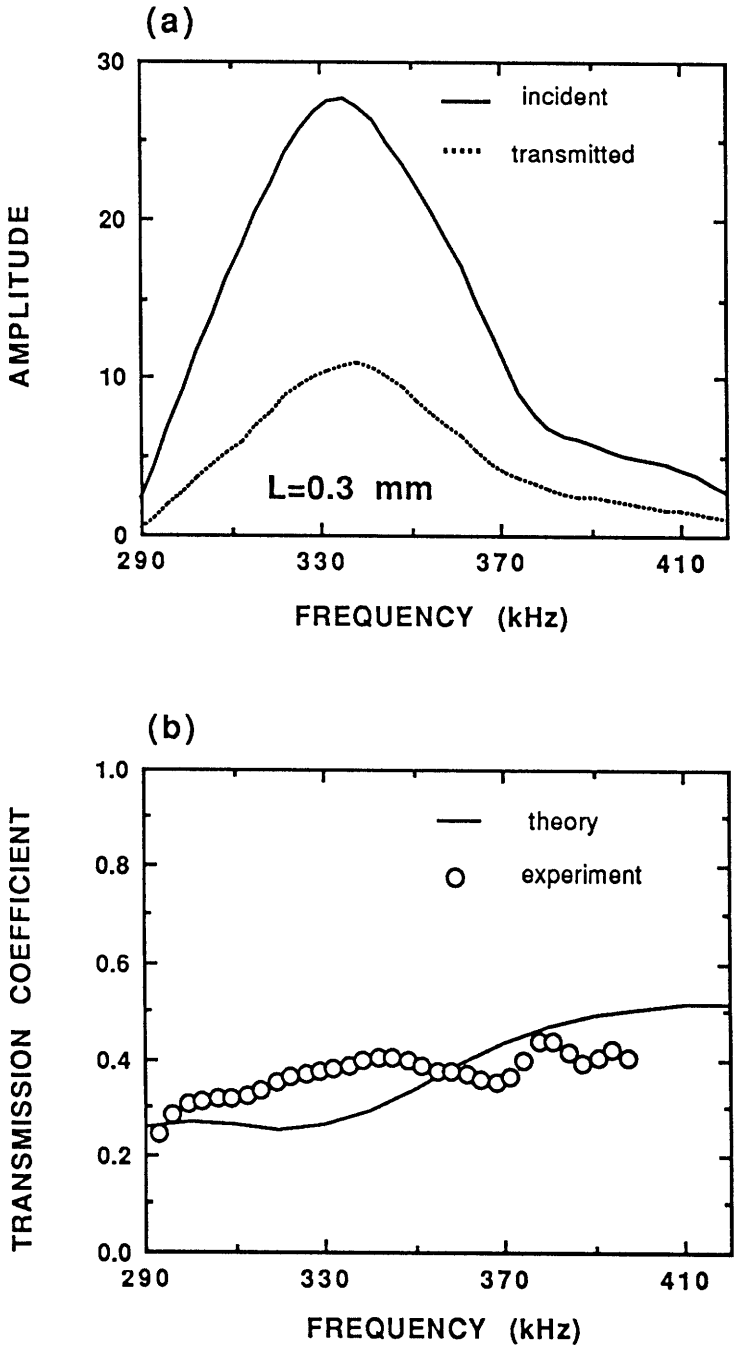

Figure 5-14: Experimental results obtained from the waveforms shown in Figure 5-13. The spectra in (a) and (c) show almost the same substantial amplitude reduction for the two very different fractures. The open circles in (b) and (d) are the measured transmission coefficients and the solid lines are the theoretical coefficients. Theory and experiment agree well.

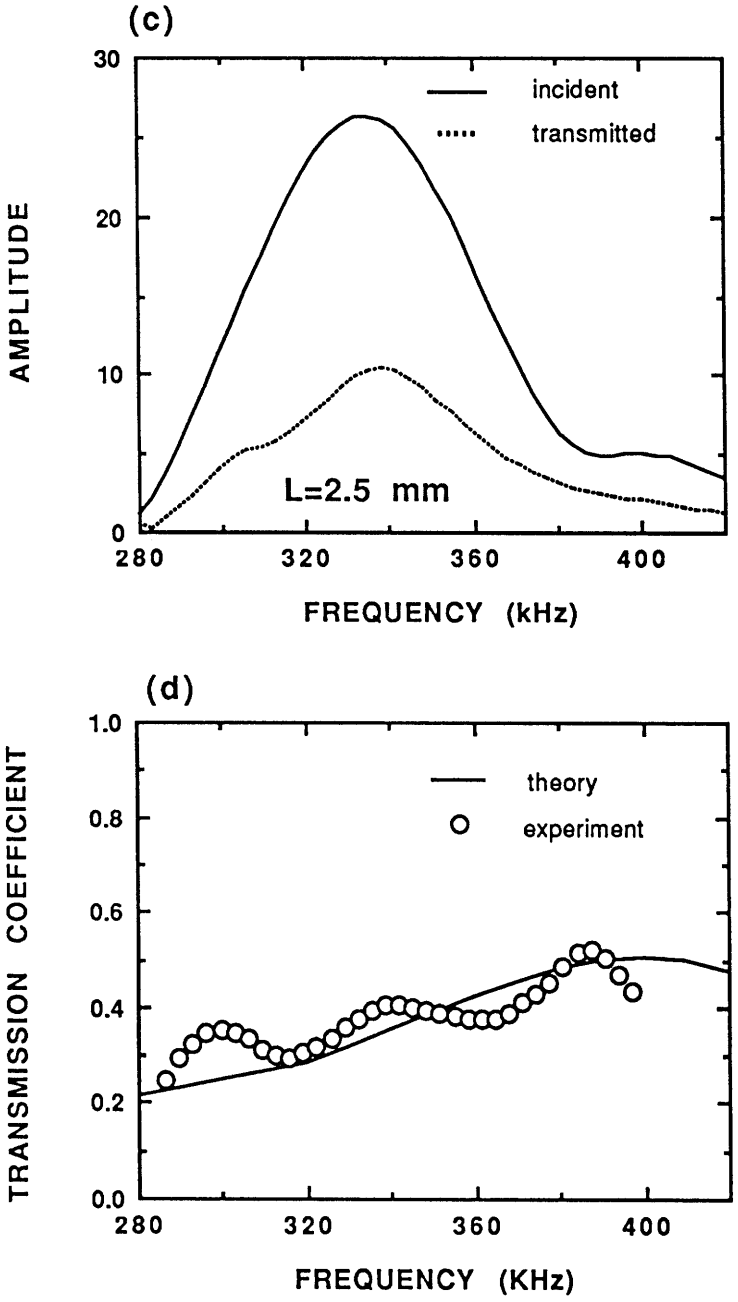

Figure 5-14: (c) and (d) Experimental results for the 2.5 mm fracture.

Chapter 6

Summary and Conclusions

The purpose of this thesis was to study how the fluid flow in pores and fractures of a formation responds to the excitation of borehole acoustic waves and how these effects can be detected with acoustic logging techniques. To this end, the thesis addressed two major issues. The first is the characteristics of dynamic fluid flow in conduits of rocks. The second is the application of the dynamic fluid flow theory to acoustic logging in porous and fractured formations.

The general behavior of dynamic fluid flow in hydraulic conduits of rocks was studied. Using a plane parallel fracture model, the dynamic conductivity of a fracture was derived. Although an actual fracture may differ from this simple model, the physics of dynamic fluid flow is clearly illustrated by this model. It is this same physics that governs the dynamic fluid flow in hydraulic conduits of rocks. The excellent agreement between the theory of dynamic conductivity and the theory of dynamic permeability of a porous medium shows the general physical principle governing the dynamic fluid motions. That is, the distinction between the static fluid motion (Darcy's law) and the dynamic motion is whether the viscous skin depth, $\delta = \sqrt{2\mu/\omega}$, is small or large compared to the sizes of the pores or the thickness of the fracture. With this result, the the behavior of dynamic fluid-flow in a natural fracture can be addressed. A natural fracture is characterized by its surface roughness (Brown, 1987). When

the height of the surface roughness is small compared to the viscous skin depth, its effects are accounted for by using an effective aperture for the fracture, and the fluid flow is governed by the dynamic permeability at low frequencies. When the average height of the roughness is large compared to the viscous skin depth, the fluid flow is also characterized by the dynamic permeability. The effects of the rough surfaces are accounted for by the tortuosity and an effective fracture aperture in the dynamic permeability. These quantities describe the tortuous, widing fracture flow channels. In either cases, the dynamic flow properties are characterized by the dynamic permeability. This illustrates that the theory of dynamic permeability has tremendous predictive power in the sense that the dynamic fluid flow in a given sample, regardless whether it is a porous medium or contains a fracture, can be characterized by various input parameters in the dynamic permeability. The important conclusion is that in acoustic logging measurements performed in a typical frequency range of [2-20] kHz, the dynamic fluid flow theory, instead of the conventional Darcy's law, is the appropriate theory for the fluid flow induced in the formation flow system (pores or fractures).

The validity of the dynamic flow theory was verified through the application of it to the important problem of acoustic logging in permeable porous formations. The application of the concept of dynamic permeability to charactering formation fluid flow not only points to the physical process involved in the problem but also yields a simple, useful theory that will be of significant applicability to both forward and inverse problems concerning Stoneley wave propagation in permeable boreholes. For example, for the forward problem, this model can be used to study the effects of a permeable zone on the borehole Stoneley propagation. Because of the predictive power of the dynamic permeability, this permeable zone can be characterized by such parameters as permeability, porosity, tortuosity, and fluid viscosity, regardless whether it is composed of a porous medium or fractures. Thus the simple model is also a useful theory in the fracture characterization using acoustic logging techniques. For

an inverse problem, the simple model can be used to formulate an inversion procedure, analyze its sensitivity to each model parameter, and finally invert for the parameters (particularly the permeability) using available Stoneley measurement data.

For fractures that are parallel to the borehole axis (vertical fractures), the results of Chapter 4 showed that the effects on the Stoneley wave propagation are primarily due to the dynamic fluid flow in the fracture. The resulting Stoneley wave characteristics are similar to those of a Stoneley wave in a permeable borehole, as studied in Chapter 3. As in the permeable borehole case, the dynamic fluid flow occurring at the fracture opening results in significant attenuation and decrease of velocity at low frequencies. This indicates that the gradual decay in amplitude of low-frequency Stoneley waves across a certain part of a borehole may be diagnostic of the existing fracture, as have been illustrated by the laboratory experimental examples in Chapter 4. A special feature of an open fracture is that in the medium frequency range, the Stoneley velocity has the tendency to reach the free space acoustic velocity of the fluid. As frequency increases, the velocity decreases to approach the Scholte velocity along a planar solid-fluid interface. This effect is especially pronounced for a thick fracture in the presence of a soft formation. In addition, the study of the vertical fracture in Chapter 4 assumed the planar plate surfaces for an open fracture. Although an in-situ fracture may differ from the parallel fracture model, the general wave characteristics in a leaky wave guide are demonstrated by this model. This can be seen from the similarity between the wave characteristics of the vertically fractured borehole and those of a permeable borehole. This similarity is due to the fact that as long as fluid flow occurs at the borehole wall, the borehole Stoneley wave will lose energy into the formation, regardless whether the flow is into the fracture or pores. Furthermore, the study of a fracture that differs from the parallel plate model can be carried out based on the studies of this thesis. An in-situ fracture may be composed of multiple fractures, or it may be a major fracture filled with materials like gravel or clay. To model the effects of such a fracture on the Stoneley propagation, one can

use the dynamic permeability to characterized the fluid flow into the fracture. The boundary condition perturbation theory developed in Chapter 4 can then be applied to study the resulting effects on the Stoneley propagation. In conclusion, because the effects of vertical fractures are initiated by the dynamic flow along the fractures, the vertical fractures can best be characterized as a permeable zone or channel and their flow properties can be determined from the measured Stoneley wave propagation characteristics, such as attenuation and dispersion.

In the case of acoustic propagation across fractures that intersect the borehole, the propagation of borehole guided waves in the vicinity of the fracture was theoretically analyzed and tested with laboratory experimental results. The theoretical results showed that at low frequencies, the Stoneley wave attenuation across an open horizontal fracture is due largely to the fluid flow into the fracture. As frequency increases, the coupling of the Stoneley wave with the radiation waves at the fracture becomes important. Above the cut-off frequency of the first pseudo-Rayleigh wave mode, the Stoneley is strongly coupled with the pseudo-Rayleigh wave at the fracture. This coupling is pronounced when the thickness of the fracture increases. Pseudo-Rayleigh waves are strongly attenuated by thin as well as thick fracture. The reason for this is that the pseudo-Rayleigh wave depends on the formation shear strength to sustain its propagation. Once it encounters a fracture of zero shear strength, its propagation is greatly affected. The effects of a fracture on pseudo-Rayleigh waves have been verified in the laboratory by experimenting with thin and thick fracture models. Although these results were obtained for a horizontal fracture, the physics involved is also true for an inclined fracture. Consequently, the lack of pseudo-Rayleigh energy across a borehole fracture may be a very good indication of the existing fracture. Moreover, the theory also predicts that the effects of a fracture on pseudo-Rayleigh waves are more pronounced towards the cut-off frequencies than away from these frequencies. Because the early arrivals of the pseudo-Rayleigh wave are the energy near the cut-off frequency, the missing of wave energy of these early arrivals may also

be an indication of the existing fracture. These examples were demonstrated by the laboratory experimental studies in Chapter 5. Again, as in Chapter 4, the parallel plate analogy was used to model the borehole fracture. By modeling the fracture as a crack without shear strength, this model was quite successful in explaining the strong attenuation of pseudo-Rayleigh waves across a borehole fracture. In many cases, an in-situ fracture is characterized as a discontinuity that lacks shear strength. Therefore, the result for the pseudo-Rayleigh waves is applicable to the field situation. For the Stoneley waves, however, this model requires a rather large fracture aperture (on the order of centimeters) to attenuate the Stoneley wave significantly. However, fractures with such apertures are rarely found in the field (Hornby et al., 1989), but Stoneley wave attenuation (up to 50% or more) across in-situ fractures is commonly observed (Paillet, 1980). This means that an in-situ fracture may be quite complicated. It may be a very permeable zone intersecting the borehole, or it may be a major discontinuity with its surfaces loosely bounded. Therefore, realistic fracture models need to be developed to model in-situ fractures. For the permeable zone case, the model developed in Chapter 3 can be employed. If the the fracture is a fracture with its surfaces in contact, the boundary condition at the fracture surfaces may be modeled as a slip boundary condition (Murty, 1976). The hybrid method of Tsang (1987) can then be used to treat this problem. In conclusion, acoustic logging can be used as an effective tool in the detection and characterization of horizontal or inclined fractures. Specifically, the pseudo-Rayleigh waves that are sensitive to formation fracturing can be used to detect and locate the fractures, while the Stoneley waves, which are sensitive to permeability of the formation, can be used to find the flow properties of the fractures.

Appendix A

Dispacement and Stress Components for the Hybrid Method

In this appendix, the displacement and stress components for the formation and borehole fluid are listed. Given the solutions in equations 5.5, these components are calculated using equations 5.2, 5.3, and 5.4. The components are:
For the fluid:

$$u_{zf} = ikAI_0(fr) \ , \tag{A.1}$$

$$u_{rf} = fAI_1(fr) \ , \tag{A.2}$$

$$\sigma_{zzf} = -\rho_f^2\omega^2 AI_0(fr) \ . \tag{A.3}$$

For the formation:

$$u_{rs} = l[-BK_1(lr) + B'I_1(lr)] - ik[CK_1(mr) + C'I_1(mr)] \ , \tag{A.4}$$

$$u_{zs} = ik[BK_0(lr) + B'I_0(lr)] + m[-CK_0(mr) + C'I_0(mr)] \ , \tag{A.5}$$

$$\begin{aligned} \sigma_{zzs} = & -(\rho\omega^2 + 2\mu l^2)[BK_0(lr) + B'I_0(lr)] \\ & +2\mu ikm[-CK_0(mr) + C'K_0(mr)] \ , \end{aligned} \tag{A.6}$$

$$\begin{aligned}
\sigma_{rzs} &= 2\mu ikl[-BK_1(lr) + B'I_1(lr)] \\
&\quad +(k^2+m^2)\mu[CK_1(mr) + C'I_1(mr)] \ , \qquad \text{(A.7)} \\
\sigma_{rrs} &= B[(-\rho\omega^2 + 2\mu k^2)K_0(lr) + 2\mu(l/r)K_1(lr)] \\
&\quad +B'[(-\rho\omega^2 + 2\mu k^2)I_0(lr) - 2\mu(l/r)I_1(lr)] \\
&\quad +2\mu ikmC[K_0(mr) + K_1(mr)/(mr)] \\
&\quad -2\mu ikmC'[I_0(mr) - I_1(mr)/(mr)] \ . \qquad \text{(A.8)}
\end{aligned}$$

Note that every equation in this Appendix has the $\exp(ikz)$ dependencies.

Appendix B

Analytical Expressions for the Integrals in Equations 5.38 and 5.39

In this appendix, the analytical expressions are given for the integrals in equations 5.38 and 5.39. For the first integral, one makes use of the expressions of σ_{zzf} and σ_{zzs} which are respectively listed in equation A.3 and equation A.6 of Appendix A. Multiply them by $J_0(\zeta r)r$ (here the subscripts α and n omitted) and integrate over from 0 to a and a to d. The resulting expression contains integrals involving products of Bessel and modified Bessel functions of the zero order, which can be analytically integrated out as (Gradshteyn and Ryzhik, 1963)

$$\begin{aligned}\int_x^y I_0(\gamma r)J_0(\zeta r)rdr &= (\gamma^2+\zeta^2)^{-1}\left[\zeta y I_0(\gamma y)J_1(\zeta y)-\zeta x I_0(\gamma x)J_1(\zeta x)\right.\\ &\quad \left.+\gamma y J_0(\zeta y)I_1(\gamma y)-\gamma x J_0(\zeta x)I_1(\gamma x)\right]\ , \qquad \text{(B.1)}\\ \int_x^y K_0(\gamma r)J_0(\zeta r)rdr &= (\gamma^2+\zeta^2)^{-1}\left[\zeta y K_0(\gamma y)J_1(\zeta y)-\zeta x K_0(\gamma x)J_1(\zeta x)\right.\\ &\quad \left.-\gamma y J_0(\zeta y)K_1(\gamma y)+\gamma x J_0(\zeta x)K_1(\gamma x)\right]\ , \qquad \text{(B.2)}\end{aligned}$$

where the limits of integration x can be 0 and a, and y can be a and d; the symbol γ can be each one of the radial wavenumbers f, m, and l. As a result, the integral

given in equation 5.38 is found as

$$\begin{aligned} I(k,\zeta) &= \zeta a J_1(\zeta a)[a_0/(\zeta^2+f^2)+a_1/(\zeta^2+l^2)+a_2/(\zeta^2+m^2)] \\ &\quad +J_0(\zeta a)[b_0/(\zeta^2+f^2)+b_1/(\zeta^2+l^2)+b_2/(\zeta^2+m^2)] \\ &\quad +J_0(\zeta d)[c_1/(\zeta^2+l^2)+c_2/(\zeta^2+m^2)] \ , \end{aligned} \tag{B.3}$$

where

$$a_0 = -\rho_f \omega^2 I_0(fa) \ , \tag{B.4}$$

$$a_1 = (\rho\omega^2 + 2\mu l^2)[BK_0(la) + B' I_0(la)] \ , \tag{B.5}$$

$$a_2 = 2\mu ikm[CK_0(ma) - C' I_0(ma)] \ , \tag{B.6}$$

$$b_0 = -\rho_f \omega^2 fa I_1(fa) \ , \tag{B.7}$$

$$b_1 = (\rho\omega^2 + 2\mu l^2) la[-BK_1(la) + B' I_1(la)] \ , \tag{B.8}$$

$$b_2 = -2\mu ikm^2 a[CK_1(ma) + C' I_1(ma)] \ , \tag{B.9}$$

$$c_1 = (\rho\omega^2 + 2\mu l^2) ld[BK_1(ld) - B' I_1(ld)] \ , \tag{B.10}$$

$$c_2 = 2\mu ikm^2 d[CK_1(md) + C' I_1(md)] \ . \tag{B.11}$$

For the integral in equation 5.39, one uses the σ^1_{zz} defined in equation 5.34. Applying the identity

$$J_0(\zeta r) = \frac{d}{dr}[rJ_1(\zeta r)]/(\zeta r) \tag{B.12}$$

to equation 5.39 and integrating by part, one gets

$$I_1(k,\zeta) = \zeta^{-1}[rJ_1(\zeta r)\sigma^1_{zz}(k,r)]\Big|_0^d - \zeta^{-1}\int_0^d \frac{d}{dr}[\sigma^1_{zz}(k,r)]J_1(\zeta) r dr \ . \tag{B.13}$$

Because σ^1_{zz} is continuous at $r = a$ and $J_1(\zeta d) = 0$ (equation 5.20), the first term vanishes. From equation 5.34, one can see that the derivative of σ^1_{zz} equals that of σ_{zz}. Using σ_{zz} given in Appendix A (equations A.3 and A.6) and completing the integration of the second term, one obtains

$$\begin{aligned} I_1(k,\zeta) &= J_1(\zeta a)/\zeta[a_0'/(\zeta^2+f^2)+a_1'/(\zeta^2+l^2)+a_2'/(\zeta^2+m^2)] \\ &\quad +aJ_0(\zeta a)[b_0'/(\zeta^2+f^2)+b_1'/(\zeta^2+l^2)+b_2'/(\zeta^2+m^2)] \\ &\quad +dJ_0(\zeta d)[c_1'/(\zeta^2+l^2)+c_2'/(\zeta^2+m^2)] \ , \end{aligned} \tag{B.14}$$

where

$$a_0' = \rho_f \omega^2 f^2 a I_0(fa) \ , \tag{B.15}$$

$$a_1' = -(\rho\omega^2 + 2\mu l^2) l^2 a [B K_0(la) + B' I_0(la)] \ , \tag{B.16}$$

$$a_2' = 2\mu i k m^3 a [-C K_0(ma) + C' I_0(ma)] \ , \tag{B.17}$$

$$b_0' = -\rho_f \omega^2 f I_1(fa) \ , \tag{B.18}$$

$$b_1' = -(\rho\omega^2 + 2\mu l^2) l [B K_1(la) - B' I_1(la)] \ , \tag{B.19}$$

$$b_2' = -2\mu i k m^2 [C K_1(ma) + C' I_1(ma)] \ , \tag{B.20}$$

$$c_1' = (\rho\omega^2 + 2\mu l^2) l [B K_1(ld) - B' I_1(ld)] \ , \tag{B.21}$$

$$c_2' = 2\mu i k m^2 [C K_1(md) + C' I_1(md)] \ . \tag{B.22}$$

References

Abramowitz, M., and I. A. Stegun, 1970, *Handbook of Mathematical Functions*, New York, Dover Publications, Inc.

Arditty, P. C. and P. Staron, 1987, Lithologic analysis and fracture detection in open and cased holes, Sonic Full Wave Research Workshop, *Soc. Expl. Geophys. 57th Ann. Mtg. and Exposition*, New Orleans, LA.

Bamber, C. L., and J. R. Evans, 1967, $\phi - k$ log (permeability definition from acoustic amplitude and porosity): *Am. Inst. Min. Metalurg., Petr. Eng.*, Midway U.S.A. Oil and Gas Symp., Paper SPE 1971.

Bear, J., 1972, *Dynamics of Fluids in Porous Media*, Elsevier, New York.

Bender, C. M., and S. A. Orzag, 1978, *Advanced Mathematical Methods for Scientists and Engineers*, New York, McGraw-Hill Book Company.

Beydoun, W. B., C. H. Cheng, and M. N. Toksöz, 1985, Detection of open fractures with vertical seismic profiling, *J. Geophys. Res., 90,* 4557–4566.

Bhashvanija, K., 1983, A finite difference model of an acoustic logging tool: The borehole in a horizontal layered geologic medium, PhD Thesis, Colorado School of Mines, Golden, CO.

Biot, M. A., 1952, Propagation of elastic waves in a cylindrical bore containing a fluid; *J. Appl. Phys., 23*, 977–1005.

Biot, M. A., 1956a, Theory of propagation of elastic waves in a fluid-saturated porous solid, I: Low frequency range, *J. Appl. Phys., 33*, 1482–1498.

Biot, M. A., 1956b, Theory of propagation of elastic waves in a fluid-saturated porous solid, II: Higher frequency range, *J. Acoust. Soc. Am., 28*, 168–178.

Biot, M. A., 1962a, Mechanics of deformation and acoustic wave propagation in porous media, *J. Appl. Phys., 33*, 1482–1498.

Biot, M. A., 1962b, Generalized theory of aocustic propagation in porous dissipative media, *J. Acoust. Sco. Am.*, 1254–1264.

Boussinesq, 1868, J., Mḿoire sur l'inflience des frottements dans les movements réguliers des fluides, *J. Math. Pure Appl., Ser. 2, 13*, 377–424.

Brie, A., K., Hsu, and C. Eckersley, 1988, Using the Stoneley normalized differential energies for fractured reservoir evaluation; *Trans., Soc. Prof. Well Log Analysts, 29th Ann. Log. Symp.*, San Antonio, TX, XX1-XX25.

Brown, S., 1987, Flow through rock joints: the effects of surface roughness, *J. Geophys. Res., 92*, 1337–1347.

Burns, D. R., and C. H. Cheng, 1986, Determination of in-situ permeability from tube wave velocity and attenuation, *Trans., Soc. Prof. Well Log Analysts, 27th Ann. Log. Symp.*, paper KK.

Burns, D. R., Viscous fluid effects on guided wave propagation in a borehole, *J. Acoust. Soc. Am., 83,* 463–469, 1988.

Burns, D. R., 1986, *Formation Property Estimation from Guided Waves in a Borehole*, PhD thesis, Massachusetts Institute of Technology.

Chan, A. K. and L. Tsang, 1983, Propagation of acoustic waves in a fluid-filled borehole surrounded by a concentrically layered transversely isotropic formation, *J. Acoust. Soc. Am., 74*, 1605–1616.

Chang, S. K., H. L. Liu, and D. L. Johnson, 1988, Low-frequency tube waves in permeable rocks, *Geophysics, 53*, 519–527.

Chen, S. T. and D. E. Willen, 1984, Shear wave logging in slow formations, *Trans., Soc. Prof. Well Log Analysts, 25th Ann. Log. Symp.*, paper DD.

Chen, S. T., 1988, Shear-wave logging with dipole sources; *Geophysics, 53*, 659–667.

Cheng, C. H., and M. N. Toksöz, 1981, Elastic wave propagation in a fluid-filled borehole and synthetic acoustic logs, *Geophysics, 46*, 1042–1053.

Cheng, C. H., M. N. Toksöz, and M. E. Willis, 1982, Determination of in-situ attenuation from full-waveform acoustic logs, *J. Geophys. Res., 87*, 5447–5484.

Cheng, C.H., M. N. Toksöz, 1983, Determination of shear velocity in "soft" formations, *Trans., Soc. Prof. Well Log Analysts, 24th Ann. Log. Symp.*, paper V.

Cheng, C.H., J. Z. Zhang, and D. R. Burns, 1987, Effects of in-situ permeability on the propagation of Stoneley (tube) waves in a borehole, *Geophysics, 52*, 1297–1289.

Cleary, M. P., 1978, Elastic and dynamic response regimes of fluid impregnated solids with diverse microstructures, *Int. J. Solids Structures, 14*, 795–819.

Cleary, M. P., 1980, Wave propagation in fluid-infiltrated porous media – some review and analysis, *Report to the Solid Mechanics Program of the National Science Foundation, under Grant No. ENG-76-82007 to M.I.T.*

Darcy, H., 1856, Les fontaines publiques de la ville de Dijon.

Delves, L. M. and J. Walsh, 1974, *Numerical Solution of Integral Equations*, Oxford: University Press.

Doak, P. E. and P. G. Vaidya, 1970, Attenuation of plane wave and higher order mode sound propagation in lined ducts, *J. Sound Vib., 12*, 201–224.

Dutta, N. C., 1980, Theoretical analysis of observed second bulk compressional wave in a fluid-saturated porous solid at ultrasonic frequencies, *Appl. Phys. Lett., 37*, 898–900.

Ellefsen, K. J., C. H. Cheng, and K. M. Tubman, 1989, Estimating phase velocity and attenuation of guided waves in acoustic logging data, *Geophysics, 54*, 1054–1059.

Ellefsen, K. J., 1990, *Elastic wave propagation along a borehole in an anisotropic medium*, PhD thesis, Massachusetts Institute of Technology.

Ferrazzini, V. and K. Aki, 1987, Slow waves trapped in a fluid-filled infinite crack: implication for volcanic tremor, *J. Geophys. Res., 92*, 9215–9223.

Gassmann, F., 1951, Über die Elastizität Poröser Medien, *Vierteljahrsschr Naturforsch Ges Zürich, 96*, 1–23.

Gradshteyn, I. and I. Ryzhik, 1980, *Tables of integrals, series, and products*, Academic Press, corrected and enlarged by A. Jeffreys edition.

Güler, F. and M. N. Toköz, 1987, Ultrsonic laboratory study of full waveform acoustic logs in boreholes with farctures, *M.I.T. Full Waveform Acoustic Logging Consortium Annual Report.*

Haddon, R. A., 1987, Numerical evaluation of Green's function for axisymmetric boreholes using leaking modes, *Geophysics, 52*, 1099–1105.

Haddon, R. A., 1989, Exact Green's functions using leaking modes for solid elastic media, *Geophysics, 54*, 609–620.

Hardin, E.L., C.H. Cheng, F.L. Paillet, and J.D. Mendelson, 1987, Fracture characterization by means of attenuation and generation of tube waves in fractured crystalline rock at Mirror Lake, New Hampshire; *J. Geophys. Res., 92*, 7989–8006.

Hsu, K., A. Brie, and R. A. Plumb, 1985, A new method for fracture identification using array sonic tools, *Rep. 14397*, Soc. of Petrol. Engineer.

Hsui, A. T., and M. N. Toksöz, 1986, Application of an acoustic model to determine in-situ permeability, *J. Acoust. Soc. Am., 79*, 2055–2059.

Hornby, B.E., D.L. Johnston, K.H. Winkler, and R.A. Plumb, 1989, Fracture evaluation using reflected Stoneley-wave arrivals, *Geophysics, 54*, 1274–1288.

Jackson, J. D., 1962, *Classical Electrodynamics*, John Wiley & Sons, New York.

Johnson, D. L., J. Koplik, and R. Dashen, 1987, Theory of dynamic permeability and tortuosity in fluid-saturated porous media, *J. Fluid Mech., 176,* 379–400.

Kelly, K. R., R. W. Ward, S. Treitel, and R. M. Alford, 1976, Synthetic microseismograms: A finite-difference approach, *Geophysics, 41*, 2–27.

Lakey, K. G., 1985, *Physical modeling of the full acoustic wave train in a borehole with a perpendicular fracture*, Master's thesis, Washington State University, Pullman, Washington.

Landau, L. D. and E. M. Lifshitz, 1959, *Fluid Mechanics*, Pergamon.

Liu, O. Y., 1984, Stoneley wave-derived Δt shear log, *Trans., Soc. Prof. Log Well Analysts, 25th Ann. Sypm.*, paper ZZ.

Louis, C. A., 1969, A study of groundwater flow in jointed rock and its influence on the stability of rock masses, *Rock Mech. Res. Rep. 10*, Imp. Coll., London.

Mathieu, F., 1984, *Application of full waveform acoustic logging data to the estimation of reservoir permeability*, Master's thesis, Massachusetts Institute of Technology.

Morse, P. M., and H. Feshbach, 1953, *Methods of theoretical Physics*, McGraw-Hill Book Company, New York.

Murty, G. S., 1976, Reflection, Transmission and Attenuation of Elastic waves at a loosely-bounded interface of two half spaces, *Geophys. J. Roy. Astr. Soc., 44*, 389–404.

Nolet, G., R. Sleeman, V. Nijhof, and B. L. N. Kennett, 1989, Synthetic reflection microseismograms in three dimensions by a locked-mode approximation, *Geophysics, 54*, 350–358.

Norris, A. N., 1989, Stoneley-wave attenuation and dispersion in permeable formations, *Geophysics, 54*, 330–341.

Paillet, F. L., 1980, Acoustic propagation in the vicinity of fractures which intersect a fluid-filled borehole, *Trans., Soc. Prof. Well Log Analysts, 21th Ann. Symp.*, Paper DD.

Paillet, F. L. and C. H. Cheng, 1986, A numerical investigation of head waves and leaky modes in fluid-filled boreholes, *Geophysics, 51*, 1438–1449.

Paillet, F. L. and J. E. White, 1982, Acoustic modes of propagation in the borehole and their relationship to rock properties, *Geophysics, 47*, 1215–1228.

Peterson, E. W., 1974, Acoustic Wave propagation along a fluid-filled cylinder, *J. Appl. Phys., 45*, 3340–3350.

Pilant, W. L., 1979, *Elastic Waves in the Earth*, Elsevier.

Plona, T. J., 1980, Observation of a second bulk compressional wave in a porous medium at ultrasonic frequencies, *Appl. Phys. Lett., 36*, 259–261.

Poeter, E. P., 1987, Characterizing fractures at potential nuclear waste repository sites with acoustic waveform logs, *Log Analyst, 28*, 453–461.

Rayleigh, J. B., 1945, *The Theory of Sound*, Dover, Mineola, New York.

Roever, W. L., J. H. Rosenbaum, and T. F. Vining, 1974, Acoustic waves from an impulsive source in a fluid-filled borehole, *J. Acoust. Soc. Am., 55*, 1144–1157.

Rothman, D. H., 1987, Cellular-automaton fluids: A model for flow in porous media, *Geophysics, 53*, 509–518.

Romm, E. S., 1966, *Flow Characteristics of Fractured Rocks* (in Russian), Nedra, Moscow.

Rosenbaum, J. H., 1974, Synthetic microseismograms: logging in porous formations, *Geophysics, 39*, 14–32.

Schmitt, D. P., 1985, *Simulation numérique de diagraphies acoustiques. Propagation d'ondes dans des formations cylindriques axisymétriques radialement stratifiées incluant des milieux élastiques et/ou poreux saturés.* PhD thesis, University of Grenoble.

Schmitt, D. P., 1986, Full wave synthetic acoustic logs in saturated porous media; Part I: A review of Biot's theory; Part II: Simple configuration; Part III: Pore shape and pore geometry effects, *M.I.T. Full Waveform Acoustic Logging Consortium Annual Report.*

Schmitt, D. P., M. Bouchon, and G. Bonnet, 1988, Full-waveform synthetic acoustic logs in radially semiinfinite saturated porous media, *Geophysics, 53*, 807–823.

Schmitt, D. P., 1989, Acoustic multipole logging in transversely isotropic poroelastic formations, *J. Acoust. Soc. Am., 86*, 2397–2421.

Schoenberg, M., T. Marzetta, J. Aron, and R. Porter, 1981, Space-time dependence of acoustic waves in a borehole, *J. Acoust. Soc. Am., 70*, 1496–1507.

Staal, J. J., and J. D. Robinson, 1977, Permeability profiles from acoustic logging: Presented at the *52th Ann. Fall Conf., Soc. Petr. Engr. of the Am. Inst. Min. Metalurg.*, paper SPE 6821.

Snow, D. T., 1965, *A parallel plate model of fractured permeability media*, PhD thesis, Univ. of Calif., Berkeley.

Stephen, R. A., F. Pardo-Casas, and C. H. Cheng, 1985, Finite difference synthetic acoustic logs, *Geophysics, 50*, 1588–1609.

Stephen, R. A., 1986, Synthetic acoustic logs over bed boundaries and horizontal fissures, *M.I.T. Full Waveform Acoustic Logging Consortium Annual Report*, 365–414.

Stevens, J. L. and S. M. Day, 1986, Shear velocity logging in slow formations using the Stoneley wave, *Geophysics, 50*, 1588–1609.

Tang, X. M. and C. H. Cheng, 1988, Wave propagation in a fluid-filled fracture–an experimental study, *Geophy. Res. Lett., 15*, 1463–1466.

Tang, X. M. and C. H. Cheng, 1989, A dynamic model for fluid flow in open borehole fractures, *J. Geophys. Res., 94*, 7567–7576.

Tsang, L., 1985, Solution of the fundamental problem of transient acoustic propagation in a borehole with the hybrid method; *J. Acoust. Soc. Am., 77*, 2024–2032.

Tsang, L., 1987, Transient acoustic waves in a fluid-filled borehole with a horizontal bed boundary separating two solid formations; *J. Acoust. Soc. Am., 81*, 844–853.

Tsang, L. and D. Radar, 1979, Numerical evaluation of trasient acoustic waveform due to a point source in a fluid-filled borehole, *Geophysics, 44*, 1706–1720.

Tubman, K. M., C. H. Cheng, and M. N. Toksöz, 1984, Synthetic full-waveform acoustic logs in cased boreholes, *Geophysics, 49*, 1051–1059.

Tubman, K. M., C. H. Cheng, and M. N. Toksöz, 1986, Synthetic full-waveform acoustic logs in cased boreholes, II–Poorly bonded casing, *Geophysics, 51*, 902–913.

Watson, G. N., 1941, *A Treatise on the Theory of Bessel Functions*, London, Cambridge University Press.

White, J. E., 1983, *Underground sound*, Elsevier Science Publ. Co., Inc.

White, J. E. and R. E. Zechman, 1968, Computed response of an acoustic logging tool, *Geophysics, 33*, 302–310.

Witherspoon, J. S., Y. Wang, K. Iwai, and J.E. Gale, 1980, Validity of cubic law for fluid flow in a deformable rock fracture, *Water Resour. Res., 15(5)*, 1016–1024.

Williams, D. M., J. Zemanek, F. A. Angona, C. L. Denis, and R. L. Caldwell, 1984, The long space acoustic logging tool, *Trans., Soc. Prof. Well Log Analysts, 25th Ann. Log. Symp.,* paper T.

Winbow, G. A., 1980, How to separate compressional and shear arrivals in a sonic log, *Expd. Abst., Soc. Expl. Geophs., 50th Ann. Int. Mtg.*, Dallas, TX.

Winbow, G. A., 1988, A theoretical study of acoustic S-wave and P-wave velocity logging with conventional and dipole sources in soft formations, *Geophysics, 53*, 1334–1342.

Winkler, K. W., H. L. Liu, and D. L. Johnson, 1989, Permeability and borehole Stoneley waves: Comparison between experiment and theory, *Geophysics, 54*, 66–75.

Zemanek, J., D. M. Williams, R. L. Caldwell, C. L. Denis, and F. A. Angona, 1985, New developments in acoustic logging, presented at the Indonesian Petr. Assoc. 14th Ann. Conv.

Zhang, J. Z. and C. H. Cheng, 1984, Numerical studies of body wave amplitudes in full waveform acoustic logs, *M.I.T. Full Waveform Acoustic Logging Consortium Annual Report*, 75–102.

Zhu, X. H. and G. A. McMechan, 1989, Numerical simulation of wave propagation in a porous elastic solid using Biot theory, *Expd. Abst., Soc. Expl. Geophys., 59th Ann. Int. Mtg. and Exposition*, Dallas, TX.